CFD INVESTIGATIONS OF THERMAL HYDRAULIC CHARACTERISTICS AND CONSEQUENCES OF FLOW BLOCKAGE IN FAST REACTOR FUEL SUBASSEMBLIES

By

NAVEEN RAJ M

Enrollment number: ENGG02201204001

Indira Gandhi Center for Atomic Research, Kalpakkam

A thesis submitted to the Board of Studies in Engineering Sciences

In partial fulfillment of requirements

for the Degree of

DOCTOR OF PHILOSOPHY

of

HOMI BHABHA NATIONAL INSTITUTE

September, 2018

Homi Bhabha National Institute

Recommendations of the Viva Voce Committee

As members of the Viva Voce Committee, we certify that we have read the dissertation prepared by **Mr. Naveen Raj M** entitled **"CFD Investigations of Thermal Hydraulic Characteristics and Consequences of Flow Blockage in Fast Reactor Fuel Subassemblies"** and recommend that it may be accepted as fulfilling the thesis requirement for the award of Degree of Doctor of Philosophy.

S. Murugan	20.9.2018
Chairman- **Dr. S. Murugan**	**Date:**
	20/9/2018
Guide / Convener - **Dr. K. Velusamy**	**Date:**
	20-9-2018
Examiner - Dr. Ashwin W. Patwardhan	**Date:**
	20-9-2018
Member 1- **Dr. Anil Kumar Sharma**	**Date:**
	20/9/18
Member 2- **Dr. Anish Kumar**	**Date:**

Final approval and acceptance of this thesis is contingent upon the candidate's submission of the final copies of the thesis to HBNI.

I hereby certify that I have read this thesis prepared under my direction and recommend that it may be accepted as fulfilling the thesis requirement.

Date: 20/9/2018

Place: Indira Gandhi Center for Atomic Research (IGCAR) Kalpakkam

Dr. K. Velusamy
(Guide)

STATEMENT BY AUTHOR

This dissertation has been submitted in partial fulfillment of requirements for an advanced degree at Homi Bhabha National Institute (HBNI) and is deposited in the Library to be made available to borrowers under rules of the HBNI.

Brief quotations from this dissertation are allowable without special permission, provided that accurate acknowledgement of source is made. Requests for permission for extended quotation from or reproduction of this manuscript in whole or in part may be granted by the Competent Authority of HBNI when in his or her judgment the proposed use of the material is in the interests of scholarship. In all other instances, however, permission must be obtained from the author.

Naveen Raj
20-9-2018

Naveen Raj. M

DECLARATION

I, hereby declare that the investigation presented in the thesis has been carried out by me. The work is original and has not been submitted earlier as a whole or in part for a degree / diploma at this or any other Institution / University.

Naveen Raj M
20-9-2018

Naveen Raj. M

List of Publications Arising from the Thesis

International Journal Papers

1. **Naveen Raj, M.**, Velusamy, K., 2018. Investigations on thermal hydraulic consequences of planar blockage in a prototype sodium cooled fast reactor fuel subassembly. Progress in Nuclear Energy, 104, 47-59.

2. **Naveen Raj, M.,** Velusamy, K., Ram Kumar Maity, 2016. Thermal hydraulic investigation on porous blockage in a prototype sodium cooled fast reactor fuel pin bundle. Nuclear Engineering and Design, 303, 88-108.

3. **Naveen Raj, M.,** Velusamy, K., 2016. Characterization of velocity and temperature fields in a 217 pin wire wrapped fuel bundle of sodium cooled fast reactor. Annals of Nuclear Energy, 87, 331–349.

Conference Proceedings

1. **Naveen Raj, M.**, Velusamy, K., 2017. CFD Simulation of Sodium Boiling in heated Pipe using RPI Model. 2nd International Conference on Multiphase Flow and Heat transfer, International-ASET, Barcelona, Spain. ISSN: 2371-5316, DOI: 10.11159/icmfht17.114.

2. **Naveen Raj, M.,** Velusamy, K., 2015. Study of fuel bundle geometry on inter-subchannel flow in a 19 pin wire wrapped bundle. 1st International ISHMT-ASTFE Heat and Mass Transfer Conference, ISRO, Thiruvananthapuram.

Naveen Raj M
20-9-2018

Naveen Raj. M

Dedicated to my loving mom, encouraging dad, very supportive guide, kind & caring brothers, sisters and friends, and to my dear friend Prakash, for all those scientific discussions, which inspire me ever, even after his disappearance into the nature's womb.

ACKNOWLEDGEMENTS

I feel greatly delighted to have this chance to express my thanks to all those who have been with me during the pursuit of my research and helped me to successfully complete this thesis.

At first, I deeply thank my Guide **Dr. K. Velusamy**, Associate Director, Nuclear Systems Analysis Group, Reactor design group (RDG), IGCAR for his persistent encouragement, everlasting patience, very caring nature and insightful guidance, which in all the ways led to the completion of my thesis. I am highly grateful to my Doctoral Committee (DC) chairman, **Dr. S. Murugan**, DC members (**Dr. Anil Kumar Sharma,** and **Dr. Anish Kumar**) and former chairmen (**Dr. S. Venugopal** and **Dr. U. Kamachi Mudali)** for their valuable inputs, continuous monitoring of my progress and valuable support throughout the course of my research. I sincerely thank **Shri Puthiyavinayagam. P**, Director, RDG and former directors (**Dr. P. Chellapandi, Shri G. Srinivasan** and **Dr. P. Selvaraj**) for their perpetual support and encouragement. I thank **Dr. A.K. Bhaduri**, Director, IGCAR, **Dr. Srikumar Banerjee,** Chancellor, **Dr. P.R.Vasudeva Rao**, Vice Chancellor, and **Dr. B. K. Dutta**, Dean, HBNI, Mumbai for all the amenities I have enjoyed at IGCAR and for providing the funding for my foreign travel. I sincerely thank our former Dean of students affairs **Dr. M. Sai Baba**, the current Dean **Dr. Lakshmi Narasimhan** and Dean of Engineering Sciences **Dr. G. Sasikala**, for their care and support.

I endow my special gratitude to **Mr. Ram Kumar Maity** SO (E**)** and my immediate senior **Dr. Ravi. L**, as both of them were supporting me next to my guide, providing me moral and technical supports, and also helped me in understanding the fundamentals of CFD during my initial days. My special thanks are due to the officers of Reactor Design Group **Mr**. **M. Asokkumar, Mr. U. Partha Sarathy, Mr. K. Natesan, Dr. R. Gajapathy, Mr. M. Rajendra Kumar, Mr. Juby Abraham, Mr. Arulbaskar. R, Mr. Nandakumar. R, Mr. Bhagwanaram Manda, Mr. Sudharshan. V, Mr. Amit Kumar. C, Mr. Aravindan. S, Mr. Niraj Jamdade, Mr. Vikram. G** and the Research scholar at IIT-Madras, **Mr. Harish. P**, for their kind help, encouragement and sharing their scientific and technical knowledge. I would like to acknowledge **Smt. R. Vijayashree, Mr. P.A. Sasidhran** and **Mr. B. Madhavan** for providing an excellent work environment. I also thank **Mr. Jehadeesan. R,** Head, Computer Division and **Mrs. Sundari** for providing High performance computational facility and for helping me in its usage. I also acknowledge the support of **Mrs. M. Banumathi**, **Mr. Dass**, Streno Gr-I, **Mr. S. Jaisankar, Mr. A. Sivakumar**, DM/D, and **Mr. S. Sundarlingam**, Tech./C, during the thesis work. I also thank my seniors **Dr. Satpathy. K** and **Dr. Govindha Rasu. N**, for all the motivations they have given me, when I joined as a fresher. Further, I thank all the training school staff who helped me during my course work. I also thank Council for Scientific and Industrial Research (CSIR) for providing me with the partial air fare for attending International Conference.

I also deeply thank my friends, **Mr. M. Thangam, Mr. R. Balakrishnan, Ms. Sravanthi. S, Mr. Chandan Bhagat, Mr. Balasundaram. G, Mr. Abuthahir. J, Ms. Sumathi. V, Ms. Prema. S, Mr. Santosh, Mr. Barath. S, Mr. Ragavendra. K.G, Mr. Srinivasan. K, Mrs. Sumathi. G, Mr. Sanjay, Mr. Prasanna. G, Dr. Thiyagarajan, Dr. Mohandass. R, Mr. Chandan Reddy, Mr. Vishnu, Mr. Anuj Dubey, Mr. Ronit Panda. K, Dr. Varun Hassija, Mr. Rajneesh Pal, Mr. Prasanth, Mr. Mohit Rajput** and all my batch mates and research scholars for making my days at Kalpakkam very colorful.

I should also be very grateful to my father **Mr. Manoharan**, mother **Mrs. Vijayalakshmi**, brothers **Mr. M. Varun Raj, Mr. M. Karthik Raja, Mr. C. Raagesh** and sister **Ms. C. Sindhu Priya,** for the support and cheer they have given me, even during the turbulent days of my life. And above all, I thank Mother Nature, for all her blessings, and for keeping me safely on this beautiful planet.

CONTENTS

SYNOPSIS

Sodium cooled fast reactors (SFR) form the second stage of Indian nuclear power program. A typical medium size prototype SFR, has ~180 hexagonal fuel subassemblies, each with width across flats as ~130 mm. Every fuel subassembly generates ~ 8 MW thermal powers and encloses 217 fuel pins. There are over 480 subchannels (coolant flow space between the pins) in each subassembly. The space between the pins are maintained by the helically wound spacer wires. Apart from supporting the fuel pins against flow induced vibrations, the spacer wires induce prominent transverse flow which enhances coolant mixing among the subchannels. As consequences of these, there are periodic spatial flow variations in the subchannels along the stream-wise direction. Also, the fuel clad is subjected to significant temperature variations around the circumference leading to thermal stress in the clad. Presence of a large number of tiny subchannels (hydraulic diameter ~ 3 mm) combined with helical wire wrap enhances the possibility of flow blockages in fuel subassemblies. Any possible blockage would have adverse impact on availability and safety of the reactor. Understanding the local flow and heat transfer features of a SFR subassembly and the consequences and detectability of possible blockages is essential for improvement in core design and enhance safety. Towards this, RANS based CFD simulation is performed on 217 pin wire wrapped fuel bundle with a structured mesh having over 36 million grid points and solved using 84 processors in parallel.

At the outset, CFD simulations on unblocked pin bundle under normal operating condition were carried out. Based on the predicted data, correlations have been proposed for calculation of transverse flow, which forms an important input for development of subchannel analysis codes. Peak to peak axial flow rate variation of ~21% and 50 % is observed in the central and peripheral subchannels respectively. The transverse flow in the faces of central subchannels follows a cosine profile, with a phase lag of 120° among the three lateral faces that bound the subchannel. In the peripheral subchannels, a strong unidirectional transverse flow prevails in the faces perpendicular to the hexcan wall. On the other hand, the transverse flow in the face parallel to the hexcan follows a square wave pattern. The CFD results indicate that the swirl velocity in the peripheral subchannel is non-uniform, contrary to that considered in the traditional subchannel models. The mean clad temperature is seen to exhibit a non-monotonic increase along the flow direction. This phenomenon is more dominant in the peripheral pins due to large gradient in subchannel temperature and the square wave profile of the transverse flow.

To understand the consequences of various local blockage scenario, wide parametric ranges for blockage radius, porosity, mean particle diameter and location of blockage have been considered. Critical length of blockage that would result in local sodium boiling as a function of aforementioned blockage parameters has been estimated and the parametric zone posing risk of sodium boiling has been identified. Attention has been paid to coolant mixing and flow and temperature fields downstream of the blockage zone. Fuel-clad that are partly exposed to blockage are subjected to large circumferential temperature variation and the associated thermal stress. Further, for a six subchannel blockage with 40% porosity and 0.5 mm mean particle diameter, the critical length is determined to be 80 mm, whereas for the same blockage the critical length reduces to < 7 mm when its porosity reduces to 5%. Six subchannel blockage with 60% porosity and 0.5 mm mean particle diameter, does not induce boiling even up to a blockage height of 400 mm. For a single subchannel blockage with one helical pitch length, there is no risk of sodium boiling even for porosity as low as 5%. In the case of planar blockage, it is found that inception of sodium boiling is likely if 3 or more rows are obstructed by a blockage located either in the center or in the corner of the subassembly. Even when the blockage is symmetric about the subassembly axis, large asymmetry in temperature field is observed within the blockage. This asymmetry is observed to be strongly dependent on the wire orientation in the upstream of blockage. In the case of corner planar blockage, a larger reverse flow zone and a higher sodium temperature are found in its downstream, than that of central planar blockage. This suggests that, sodium boiling is more likely in the case of corner blockage. It is seen that for a prototype subassembly with various sections contributing to pressure loss, the total flow reduction is < 3 % for all blockages that can lead to local sodium boiling. This leads to the conclusion that global bulk sodium temperature monitoring at subassembly outlet is unlikely to detect slowly growing blockages. Comparing the sodium flow and temperature fields in unblocked and blocked bundles, it is found that the wake induced temperature non-uniformity persists even upto 3 helical pitch lengths downstream, highlighting that the sodium temperature non-uniformity at the bundle exit can serve as an efficient blockage indicator, provided that the cross section temperature is mapped by a proper instrumentation.

LIST OF FIGURES

LIST OF TABLES

1 INTRODUCTION

1.0 FOREWORD

Growing population, along with the escalating domestic and industrial loads, propels the need for a steady growth in the electricity generation, worldwide. International Energy Agency (IEA) has reported that in the year 1973, the world electricity generation was at 6070 TWh, whereas it rose to 24164 TWh by 2015 (IEA, 2017). Over these years, India, to support for its huge infrastructure development, increased electricity generation dramatically from 67 TWh to 1105 TWh which crossed 1230 TWh at the beginning of 2017 (Central Electricity Authority (CEA), 2017). Currently worldwide, coal and natural gas are the primary source for power production. But, considering their depletion status in near future and sizable environmental impact, prompt attention is paid to other means of electricity generation with minimal carbon footprints. Among them nuclear energy stands as the potential candidate for a long term power production. Right from the middle of the 20th century, nuclear energy has been contributing a reasonable share to the electricity production in developed nations. Worldwide, nuclear share in overall electricity generation has increased from 3.3 % in 1973 to 10.6% in 2015 (IEA, 2017). In India, the present installed nuclear power capacity of ~ 6.8 GWe contributes to ~ 3% of overall electricity production (CEA, 2017). India's natural uranium reserve constitutes < 1% of the global reserves (Nuclear Energy Agency (NEA) and International Atomic Energy Agency (IAEA), 2016). By utilizing the indigenous natural uranium reserves on once through fuel cycle, the country's nuclear power programme would to be limited to a maximum of ~ 10 GWe (Diwan and Parag, 2009).

Natural uranium consists of 0.7% of fissile U_{235} and 99.3 % of fertile U_{238} isotopes. Hence, in thermal reactors only a 0.7% will undergo fission to support the power generation. But, within a thermal reactor, a small proportion of U_{238} will be transmuted into fissile Pu_{239}. However, in fast reactor, the amount of such generation can exceed the fuel consumed. By reprocessing the spent fuel, this plutonium can be separated out and used in another reactor as fresh fuel. But considering the limited availability of indigenous natural uranium, even this uranium plutonium closed loop cycle would not be adequate in the very long run. But on the other hand, India has a large reserves of Th_{232} which amounts to >30% of global reserves. The fertile Th_{232} can be converted into fissile U_{233} in a reactor and its vast availability can support for a long term energy programme. Considering these, Dr. Homi Bhaba drafted the Indian three stage nuclear program (Venkataram, 1994).

In this programme, the first stage starts with Pressurized Heavy Water Reactor (PHWR) which uses oxide fuel made form natural uranium. While generating electricity, it also transmutes U_{238} into fissile Pu_{239}. The current establishment of first stage PHWRs produces ~ 5 GWe and the construction projects in progress will double this capacity in near future. The second stage is deployment of Fast Breeder Reactor (FBR), where Uranium Plutonium mixed oxide fuel obtained from reprocessing the spent fuel in first stage is utilized. In the third stage, reactors working on Th_{232}-U_{233} cycle will be deployed which will fulfill the long term energy demand for India.

1.1 FAST BREEDER REACTOR

Globally, there is renewed interest in FBR technology due to its large breeding capacity, high burn up and strong potential to transmute heavy long living isotopes. In India, FBR stands as a potential workhorse for the second stage of nuclear program. Despite many potential merits, the FBR design is very complex. The core of an FBR is compact in order to maintain an optimum fast neutron economy, which is necessary for breeding and for effective actinide management. The large power density (peek power density ~ 650 MW/m^3) and need for fast neutron economy makes sodium with its high thermal conductivity and poor moderation properties as the most widely chosen coolant material for FBR. Sodium with its high boiling point (~1155 K at atmospheric pressure) reduces the need for high pressure primary vessel as in the case of PHWR. But apart from this, handling sodium has other added challenges.

Sodium cooled fast reactors (SFR) in general will have three loops, i.e., primary sodium loop, secondary sodium loop and steam water loop, each connected to their next successive loops (Ref. Fig.1.1).

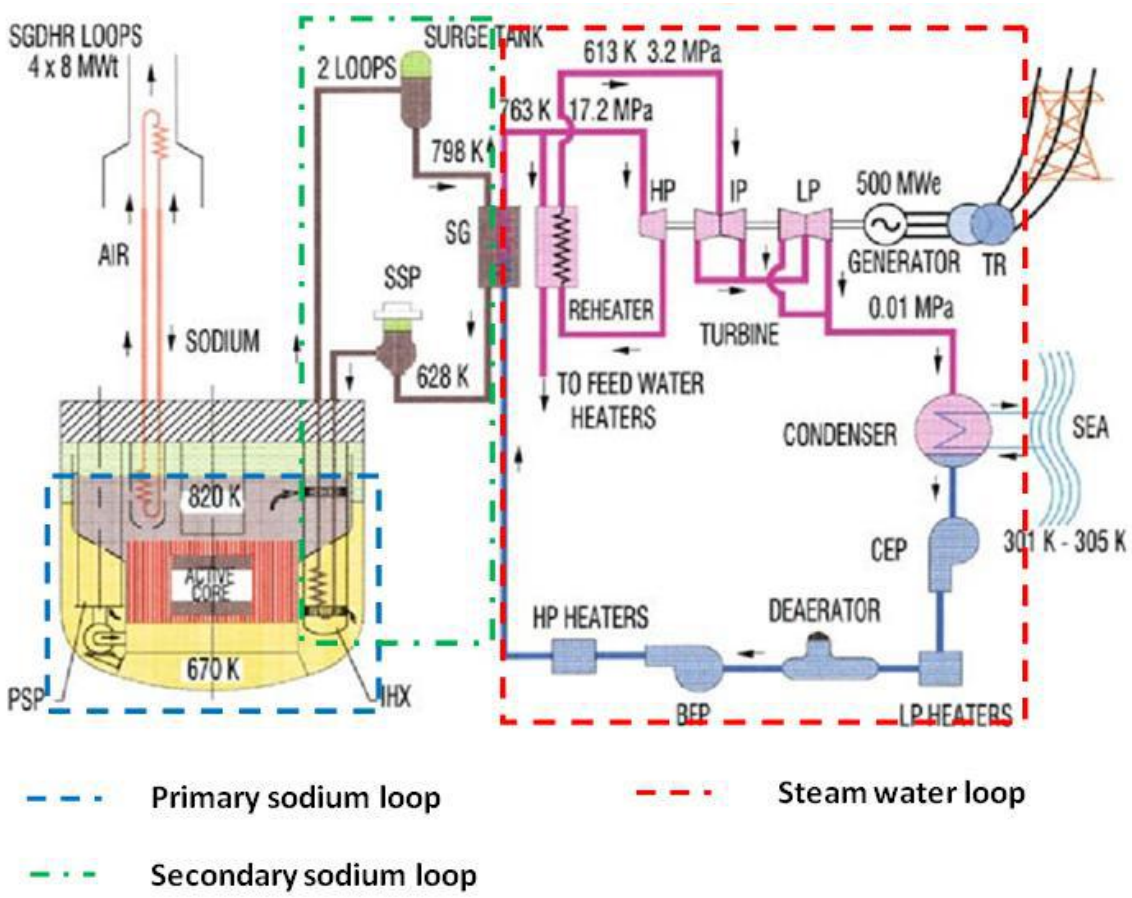

Fig 1.1 Plant layout of Sodium cooled Fast Reactor (SFR).

In typical prototype SFR the primary loop is of pool type (Ref. Fig. 1.2), where the entire primary system components are immersed in a large sodium pool contained in main vessel. Here, the pool is divided into hot pool and cold pool by an inner vessel. Sodium from the cold pool is pumped through the bottom of the core, and while flowing through the core it removes the nuclear heat and reaches the hot pool. Then due to level difference between hot and cold pool, it flows through the intermediate heat exchanger after transferring the heat to the secondary sodium loop.

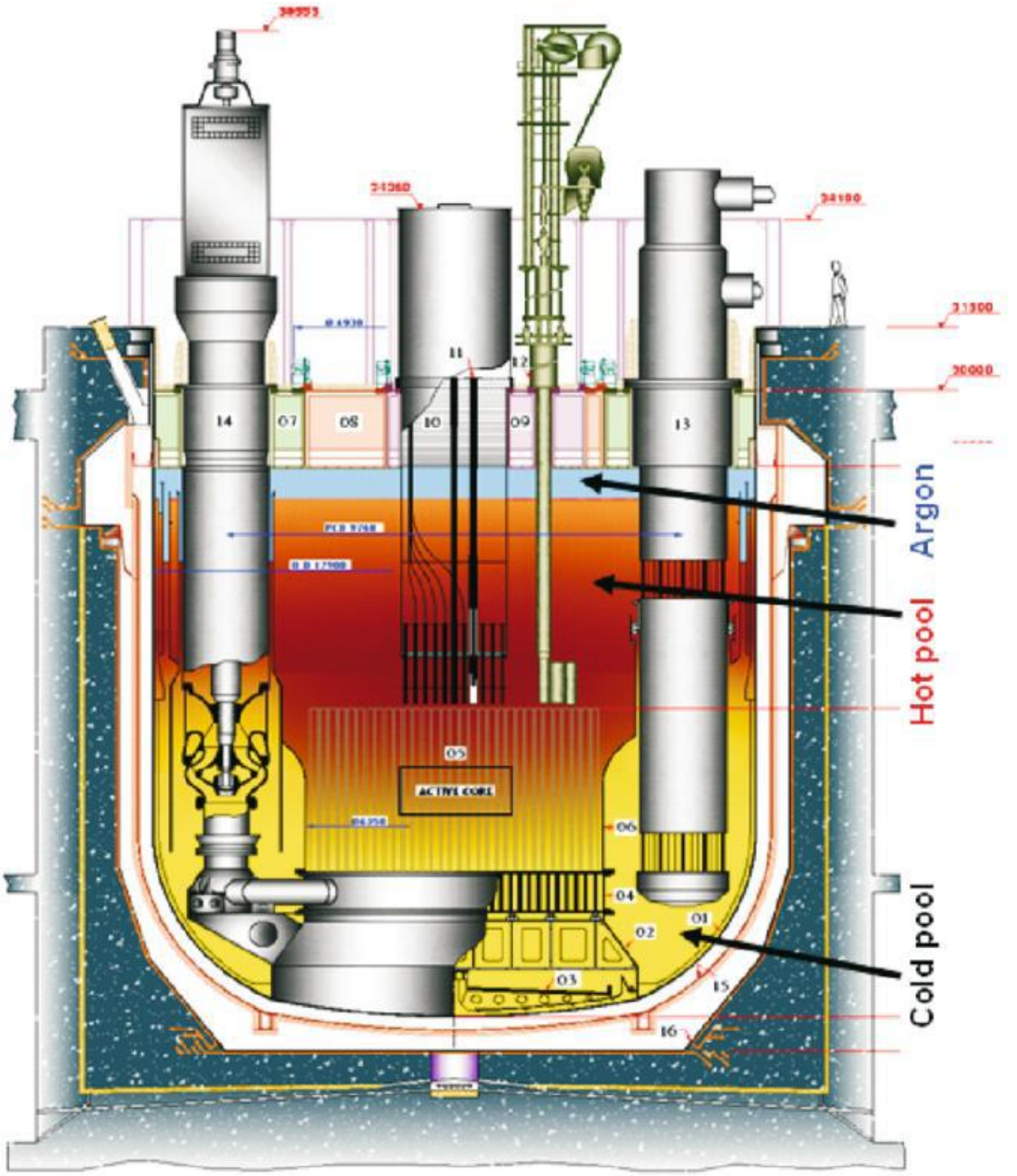

LEGEND

01. MAIN VESSEL	09. SMALL ROTATABLE PLUG
02. CORE SUPPORT STRUCURE	10. CONTROL PLUG
03. CORE CATCHER	11. CONTROL & SAFETY ROD MECHANISM
04. GRID PLATE	12. IN-VESSEL TRANSFER MACHINE
05. CORE	13. INTERMEDIATE HEAT EXCHANGER
06. INNER VESSEL	14. PRIMARY SODIUM PUMP
07. ROOF SLAB	15. SAFETY VESSEL
08. LARGE ROTATABLE PLUG	16. REACTOR VAULT

Fig 1.2. Reactor assembly of a pool type SFR.

The reactor core consists of over 1700 subassemblies. A horizontal section of a prototype SFR core showing various types of subassemblies is depicted in the Fig. 1.3. The subassemblies are placed vertical in the core with their feet supported by sleeves in a high pressure plenum, called Grid plate. Sodium from the primary pump, first enters the grid plate, then through these sleeves to enter the subassemblies and finally to reach the hot pool. A typical medium sized prototype SFR with 1200 MWt power has ~180 hexagonal fuel subassemblies and ~120 blanket subassemblies each with width across flats as ~130 mm. There are other subassemblies such as control, reflector, B_4C, internal storage and neutron shielding subassemblies.

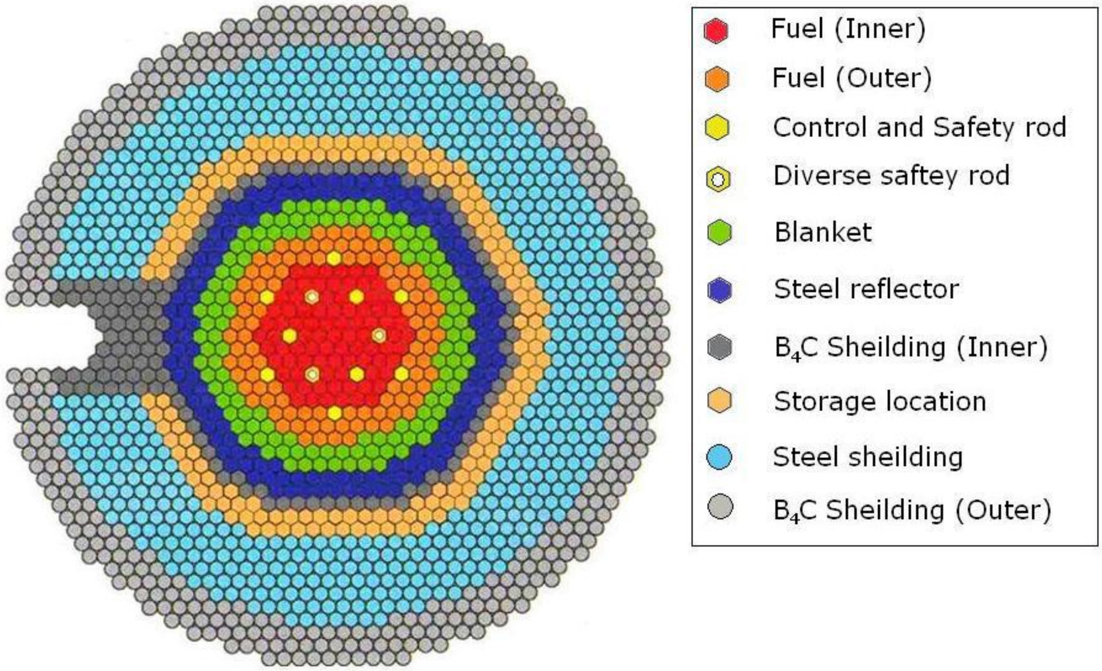

Fig 1.3. Horizontal cross section of core with various subassemblies.

A peak rated fuel subassembly generates ~8 MWt power and encloses 217 pins with helically wound spacer wires. Vertical section of a fuel subassembly and fuel pin is depicted in Fig. 1.4. The coolant flow space between the fuel pins is called subchannel and there are over 480 subchannels in each fuel subassembly. The gap between the pins is maintained by helically wound wire wrap. This highly compact core with large specific power necessitates heat removal by a high thermal conductive coolant (liquid sodium) flowing through these small subchannels of ~ 3 mm hydraulic diameter.

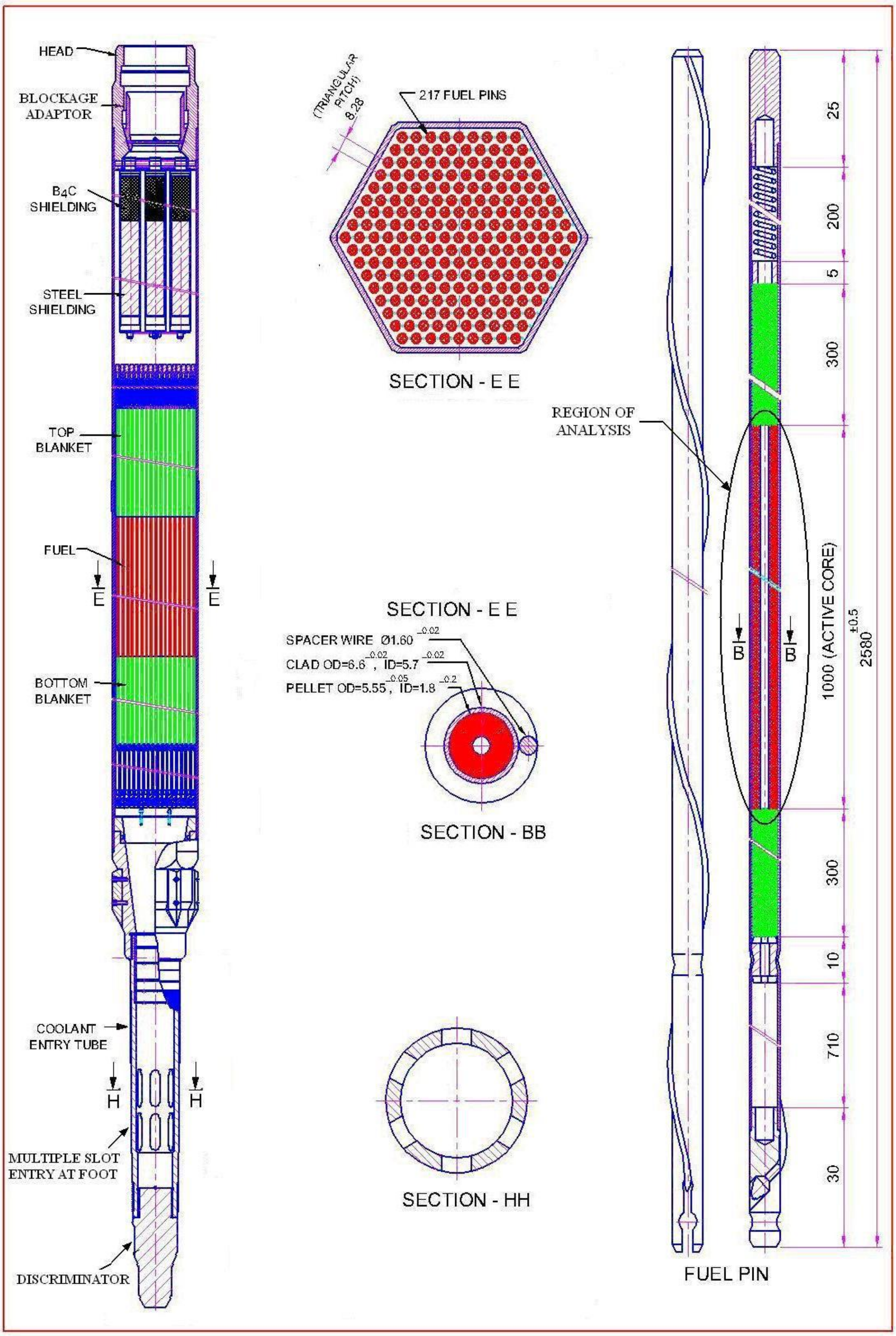

Fig. 1.4: Schematic of SFR fuel subassembly and fuel pin.

Apart from supporting the fuel pins against flow induced vibrations, the spacer wires induce prominent transverse flow which enhances coolant mixing among the subchannels. As consequences of these, there are periodic spatial flow variations in the subchannels along the stream-wise direction. Also, the clad is subjected to significant temperature variations around the circumference leading to thermal stress in the clad. Understanding the local flow and heat transfer features of a SFR subassembly is essential for improvement in core design in the direction of improved economy and enhanced safety. But experimental routes to determine the thermal hydraulic characteristics of a SFR subassembly are highly constrained by the small hydraulic diameter of subchannels (~3mm), elevated temperature (~ 500°C), reactive and opaque nature of sodium coolant.

It may be highlighted that, large number of subchannels enhances the possibility of blockages in fuel subassemblies. Compared to helical wire spacer the grid spacers have a greater possibility of blockage development and the resulting blockage is typically planar type. But, the helical wires also lead to blockage as the external debris/particles get lodged in the crevice between pin and wire. Then, subsequent particles get deposited over the initially deposited particles leading to a columnar porous blockage. Any possible blockage would have adverse impact on availability and safety of the reactor. Blockages in pin bundle could be initiated by different mechanisms such as, loading of blocked subassembly, foreign particles (weld spatter) present in the primary circuit, clogging by broken spacer wire and irradiation swelling of fuel pins.

There is a strong need to understand the consequences of possible blockages (Roychowdhury et al. 2000). If the consequences are manageable, the reactor could even be operated until the subsequent scheduled shutdown. It may be highlighted that, partial blockage in a subassembly is a Design Basis Event (DBE). The blockage that leads to a hotspot clad temperature of 800°C is termed as category-2 type blockage. The blockage that leads to a hotspot clad temperature of 900°C is termed as category-3 type blockage. However, a complete blockage of a subassembly is a Beyond Design Basis Event

(BDBE). Complete blockage is made as a low probability event due to the design provisions in the reactor, such as (i) multiple radial entry holes in the sleeves, (ii) multiple slots in the subassembly foot, and (iii) provision of blockage adaptor in the subassembly head with radial holes in all the faces of the Hexcan. Any partial blockage at the entry to the subassembly will lead to flow reduction in the subassembly, but the flow distribution in the active fuel zone will not get altered. An inlet blockage that leads to a flow reduction of 3% will increase the bulk coolant exit temperature by ~ 5°C and a flow reduction of 6% will increase the bulk coolant temperature by ~10°C. The coolant exit temperature is continuously monitored by core monitoring thermocouple. The former leads to an alarm and the later leads to automatic reactor trip. The increase in the clad temperature during these flow reductions will be very marginal (only ~20°C). But, in the case of internal blockage, the flow distribution in the pin bundle gets altered. This can lead the clad to attain category-2/ catogory-3 Design Safety Limit.

It is known that the clad temperature at the instant of sodium boiling is ~ 880°C which is well in the creep regime. Further, sodium boiling leads to thermal cycling in the clad. Due to these, the clad is expected to fail within a short time depending on its previous resident time in the core and fission gas pressure. This is important because even small amount of molten fuel mixing with sodium can result in huge amount of energy release (Hicks and Menzies 1965). Local fuel melting due to blockage and propagation of fuel melting can promote core compaction and the consequent large positive reactivity addition (Kleijn, 1970). Thus, sodium boiling is an important consideration and detection of sodium boiling before fuel clad failure is essential. Han (1977) reported the relevance of fast response thermocouple at subassembly exit of SUPER-PHENIX reactor in detecting minor temperature disturbances during the event of internal blockage. Seung et al. (2006) found that the temperature fluctuation at the upper plenum can provide information on the presence of local partial blockage. Further, during the event of sodium boiling, identification of extent of sodium vapor occupying the core is essential from both heat transfer and reactor physics perspectives. Hence, the present thesis is focused on (i) characterizing the partial internal blockage that can lead to the category-3 DBE and (ii) efficacy of the core monitoring thermocouple (provided in the present designs of FBR) to detect such a blockage. It may be reiterated that in these events, the Delayed Neutron Detectors (DND) located in the hot plenum will protect the reactor when clad fails.

1.2 MOTIVATION AND SCOPE OF THE STUDY

Since the dawn of FBR era, series of experimental and computational investigations have been carried out on reactor core and specifically on fuel pin bundle. But most of the studies were devoted to engineering parameters such as friction factor and Nusselt number and their dependence on pin bundle geometrical parameters. The reported understanding of local flow features within a subassembly is still limited. An exclusive study on the relationship between the local axial and transverse flow features and correlations for inter-channel transverse flow as a function of bundle dimensions and number of pins in the bundle have not been reported. But characterization of local flow physics is very important for development of improved subchannel analysis codes.

In the area of blockage investigation, a few experimental and numerical studies on small size pin bundles were reported. However their scalability to 217 pin bundle is not yet demonstrated. Also, the effect of blockage configuration, blockage location and its influence on sodium boiling are not well understood. Further, experimental (or) subchannel models cannot capture 3 dimensional temperature and velocity distributions within the bundle, specifically behind the blocked zone as well as at bundle exit. Such thermal hydraulic features are important for improving the detectability of blockage and improvement in subassembly design. Further, it could be seen that internal blockage can also be detectable by monitoring temperature fluctuation at the upper plenum which requires fast response thermocouple installed at upper plenum. To identify the design parameters of such thermocouple, local temperature fluctuation in the upper plenum has to be identified, which requires the appropriate outlet temperature of the blocked pin bundle. These form the inspiration for the present research work.

The present thesis attempts to understand (i) flow and temperature characteristics in a prototype fuel subassembly during normal condition, (ii) thermal hydraulic consequences of porous internal blockage, (iii) critical length of the internal blockages that would lead to sodium boiling, (iv) thermal hydraulic consequences of planar internal blockage and (v) detectability of flow blockages by core monitoring thermocouple. Towards these, RANS based CFD simulation of flow and temperature fields in a wire wrapped 217 pin fast reactor fuel subassembly for 7 helical pitch lengths has been carried out.

1.3 ORGANISATION OF THE THESIS

The present thesis is divided into four major parts. The first part includes the first three chapters, which is introduction to the research problem (chapter-1), critical review of existing literature (chapter-2) and mathematical modeling (chapter-3). In the second part, the characterization of velocity and temperature fields in a 217 pin wire wrapped fuel bundle (chapter-4) is discussed. Third part comprises the 5th and 6th chapters, where the investigation of thermal hydraulic consequences of partial internal blockages (porous & planar blockage) in a 217 pin bundle is discussed. The final part of the thesis (chapter-7) comprises the summary of the major finding of the thesis and scope for future research.

2 LITERATURE SURVEY

2.0 INTRODUCTION

From the very beginning of FBR program, large volumes of experimental studies to understand the thermal hydraulic behavior of fuel subassemblies and various aspects of flow blockage within the pin bundle have been reported in the open literature. Trailing them, cost effective analysis based on numerical simulations was on rise with the advent of faster computers. In the past decade, more sophisticated numerical simulations based on CFD technique are being pursued. Most of these literatures were dedicated to identify the engineering parameters such as friction factor and Nusselt number. Further, blockage analyses were mostly carried out on pin bundle with a small number of pins. Some of the significant literature in this field is discussed in the flowing sections.

2.1 PIN BUNDLE THERMAL HYDRAULICS

2.1.1 Experimental Investigations

Many of the experimental investigations are focused on pressure drop characterization, while a few of them were dedicated to study the intricate flow features. For example Lafay et al., (1975), conducted experiments in 19 pin wire wrap bundles, to study local pressure and peripheral flow distributions. They found that the measured value of transverse velocity is higher than that calculated by the assumption that the flow follows the helical wire. Further, they also highlighted the importance of understanding the local flow field in developing accurate mixing models for wire wrapped bundles.

Lorenz and Ginzberg (1977) performed water experiment in a 91 pin wire wrapped bundle to understand the flow distribution. They identified that, whenever the wire is inside the edge subchannel the coolant attains the maximum axial velocity for that pitch. They found that the peripheral swirl velocity is 1.2 times that predicted by helix angle. Patch et al., (1979) performed experimental investigation on a 5:1 scale sector of Clinch River Breeder Reactor Plant (CRBRP) blanket subassembly using air as working medium. The experiments were conducted on a non symmetric cut out portion of CRBRP blanket subassembly with 48 rods. They measured the subchannel cross flow velocities at interior, edge and corner subchannels at a Reynolds number of 22000. They observed that the ratio of gap average interior subchannel velocity to that predicted with helix angle reaches the maximum value of 1.1. Roidt et al., (1980) performed experiments in scaled up 1/6th sectors of fuel and blanket subassemblies with air as the working fluid. They established the static pressure gradient and transverse velocity field within various subchannels. Fernandez and Carajilescov (2000) considered a 7-pin bundle for understanding static pressure and wall shear stress distributions using air as the working medium. They found that dependence of wall shear stress on Reynolds number is negligible and the wire generated cross flow greatly masks any secondary flow that is induced by the turbulence. Bogoslovskaya et al., (2000) measured the transverse flow of liquid metal in a 19 pin bundle. They observed a sinusoidal pattern in the transverse flow field.

Extensive experiments have been performed by many researchers to derive suitable pressure drop correlations for wire wrapped rod bundles. These include the works of Novendstern (1972), Rehme (1973), Engel et al., (1979), Baxi and Dalle-Donne (1981), Cheng and Todreas (1986), Choi et al., (2003), Bubelis and Schikorr (2008) etc. Recently, Chen et al., (2014) made a detailed comparison of these correlations and evaluated their applicable ranges. Correlations for fully developed Nusselt number in wire wrapped rod bundle were proposed by Kazimi and Carelli (1976).

2.1.2 Subchannel Code Based Investigations

Most of the previous works investigated the thermal hydraulics of subassemblies using the subchannel approach as detailed by Wantland (1974), Basehore and Todreas (1980), Kim et al., (2002), Memmott et al., (2010), Wu et al., (2013), Syeilendra and Minoru (2013) and Liu and Scarpelli (2015). In the subchannel approach, the chief assumption is axial flow is dominant compared to transverse flow. So, the axial flow is rigorously treated by solving the governing equations, whereas the transverse flow is handled with a simplified model in the form of algebraic expressions. This approach is very handy and is well suited for parametric studies as the computational time required is relatively small compared to a CFD simulation. SUPERENERGY, MANTRA-LMR, RELAP5-3D and COBRA-LM are some of the popular subchannel codes used in SFR core design. In most of the subchannel codes for wire wrapped bundle, the effect of helical wire is axially averaged and the diversion effect of wire in peripheral region is modeled employing an analytical expression for the unidirectional swirl (Chiu et al., 1978a). Subchannel code by Wantland (1974) considered the diversion effect of wire in the inner regions using an analytical expression for transverse velocity. The transverse velocity model was derived from the assumptions that (i) only the wire passing through a face of a subchannel induces cross flow in that face, (ii) the maximum transverse flow occurs when the wire blocks the face, and (iii) the wire acts as a vane. However, the validity of these assumptions has not been explicitly established. Further, the mass exchange between any two subchannels varies along the axial direction depending on the position of the helical wire, location of the pin in the bundle and the type of subchannel under consideration. Thanks to the advancements in CFD simulations, transverse velocity distribution can be properly predicted by 3-dimensional calculations.

2.1.3 CFD Based Investigations

In the recent past, the number of CFD investigations on pin bundle thermal hydraulics has been on the rise. Ahmad and Kim (2006) carried out thermal hydraulic analysis on 7 and 19 pin wire wrapped bundles by solving the RANS equations over one pitch length, using the periodic boundary condition. They found that in wire wrapped fuel subassemblies, subchannel fluid temperatures surrounding the central pin are not identical. Further, this temperature gradient around the pin is periodically repeated for every pitch. Raza and Kim (2008) compared thermal hydraulic characteristics of 7 and 19 pin wire wrapped bundles. They found that the temperature gradient among interior subchannels is higher in 19 pin bundle than that in a 7 pin bundle. Sreenivasulu and Prasad (2009) investigated thermal hydraulics of wire wrapped single pin in an annular duct. Gajapathy et al., (2009) studied the characteristics of flow mixing among the peripheral and central zones in 7, 19 and 37 pin bundles. Then, the characteristics were extended to a 217 pin bundle. Pointer et al., (2009) compared the results of transverse velocity in the inter-channel gap of 7 pin wire wrapped bundle obtained from RANS and LES simulations and found that the flow prediction by RANS simulation is reasonably accurate. They also performed RANS simulation in 217 pin bundle and presented the temperature and transverse velocity fields at a cross section. Fanning et al., (2009) compared thermal hydraulic performance of a 217 pin bundle using RANS simulation as well as a subchannel model. They observed the necessity for a multi-resolution approach, where higher resolution models such as RANS could provide accurate modeling parameter, such as inter-channel cross flow, which is a necessary input for low resolution model such as subchannel approach. Peniguel et al., (2010) performed RANS simulations on 7, 19 and 271 pin bundles, with conjugate heat transfer at the pin walls. They compared the performances of the two equation k-ε and Reynolds stress turbulence models in predicting friction factor and Nusselt number. They found that both the models have good agreement with the experimental correlations. Roelofs et al., (2012) reported the results of a low resolution CFD approach with and without the requirement of sub-grid modeling. They observed that the low resolution modeling can be adopted to provide necessary modeling parameters required in the subchannel approach. Later, a complete CFD simulation of 127 pin bundle with headers and footers has been reported by Roelofs et al., (2013). Govindha Rasu et al., (2013), investigated entrance flow characteristics in a simultaneously developing flow for bundles with a maximum of 37 pins. They found that the flow is developed within an axial length of ~125 hydraulic diameters, but temperature development is achieved only when pin diameter is small or the number of pins is low. For bundles with large number of pins, temperature development is not achieved, even after a length of 1000 hydraulic diameters. Amit et al., (2013) studied the effect of eccentricity on thermal hydraulic characteristics of rod bundle. Gopala et al., (2014) performed RANS based CFD simulation of lead bismuth eutectic flow and heat transfer through a 19 pin bundle to understand flow development length. Govindha Rasu et al., (2014a), investigated development of cross stream velocity as a function of helical pitch length and number of pins. They found the existence of periodic spatial oscillations in friction factor and Nusselt number. Recently, Gajapathy et al., (2015) conducted a CFD based computation on a 217 pin bundle and analyzed the effect of helical pitch on the flow and temperature distributions and the variation in friction factor and Nusselt number as a function of helical wire parameters.

2.2 BLOCKAGE ANALYSIS ON SFR SUBASSEMBLIES

2.2.1 Experimental Investigations

Blockage characterization has been approached through experimental studies using water (or) sodium as coolant. Fontana et al. (1973) conducted blockage studies in a 19 pin bundle and found that even in 24 subchannel inlet blockages, the temperature in the vicinity of blockage does not exceed the outlet temperature in unblocked case and they stay, however undetectable. They noted that the distorted exit temperature distribution could act as a means for early detection of blockage. They also found that extrapolation of 19 pin blockage results to 217 pin prototype bundle under-predicts the local temperature. Porous central blockage in a 19 pin bundle was studied by Olive and Jolas (1990). The focus of their study was to determine the size and characteristics of blockage that would cause sodium boiling. They found that six subchannel porous blockage with a length of 60 mm would not cause boiling in a 19 pin bundle.

Kirsch (1973) conducted pin bundle blockage experiments in water and observed that the maximum temperature in the downstream of the blockage occurs at the edge of the blocked region. In a planar blockage experiment on a grid spaced bundle, Huber and Peppler (1985) observed that the peak temperature occurs in the vortex center of recirculating zone in the downstream of the blockage. In the case of grid spaced bundle though the peak temperature occurs in the periphery of the blocked region, the temperature field is symmetric about the axis. They noted that temperature field becomes toroidal in the downstream of blockage. Similar results were found in blockage study using subchannel analysis by Jeong et al. (2009). Han (1977) presented a comprehensive review of various pin bundle blockage experiments and simulations. He concluded that water experiments are in good agreement with sodium experiment in obtaining resident time in the wake region of the blockage.

The boiling superheat of liquid metals may vary largely and it depends on parameters such as dissolved gas content, flow rates and the boundary conditions. To understand this, sodium boiling experiments were carried out by Uotani and Haga (1984) on a partially blocked 37-pin wire wrapped bundle. They found that in both the cases of central and corner blockages the boiling superheat is very low and it decreases with increase in flow velocity. Schlieiziek (1970) has identified that for high heat flux value and low Peclet number, the boiling superheat tends to lie in the range of 40 – 125 ºC. Holtz and Fauske (1971) found that a loop type reactor system has nearly zero boiling superheat, but a pool type reactor has higher boiling superheat, which would reduce in the case of possible cover gas entrainment.

2.2.2 Analysis Based on 1-D Models and Subchannel Codes

Marr and Crawford (1972) performed parametric studies to find the critical thickness of porous heat generating blockage as a function of particle diameter and porosity using a one dimensional heat flow model. Their study considers particle size from 0.1 to 1 mm and porosity value in the range of 0.35 to 0.45. Chang et al. (2011) studied 271 pin wire wrapped bundle with blockage located at different radial locations using a subchannel code MANTRA-LMR-FB. They reported that even for six subchannel blockage, the wake behind blockage extents up to subassembly exit. A two dimensional computational fluid dynamic simulation of flow channel area reduction due to buckling of pin bundle is carried out by Amgad and Salah (2012). They found that there is no risk of sodium boiling up to 100% and 90 % flow reduction in an average channel and hot channel respectively.

2.2.3 CFD Based Investigations

Di Piazza et al. (2014) performed CFD investigation on a 127 pin bundle with planar blockage, and found that clad temperature exceeding 1000 ºC is reached if blockage occupies more than 30% of flow area. Govindha et al. (2014b) predicted the flow and temperature fields within a blocked 19 pin bundle using CFD. They reported the influence of various blockage parameters on the initiation of sodium boiling, but the exact limit of parameters has not been reported. Roelofs et al. (2012) investigated the consequences of partial inlet and internal blockages in a lead cooled 169 pin bare bundle. Further, as an upper bound of local blockage, complete flow blockage in fuel subassembly has been studied by Ravi et al. (2013) and Marie et al. (2015). While the total blockage studies are useful for safety evaluation, understanding of realistic scenario demands local blockage investigations.

Through a LES simulation of upper plenum, Seung et al. (2006) found that the temperature fluctuation at the upper plenum can provide information on the presence of partial blockage. The output from a subchannel analysis of the bundle served as input for the LES study. They identified that a fast response thermocouple located within 25 cm from the subassembly exit would be optimum to detect the blockage. A summary of the literature review is given in Table 2.1.

Table 2.1: Summary of literature review.

Reference	**Investigation method**	**Number of pins**	**Prime findings**
Pin bundle thermal hydraulics studies			
Novendstern (1972), Rehme (1973), Engel et al., (1979), Baxi and Dalle-Donne (1981), Cheng and Todreas (1986), Choi et al., (2003), Bubelis and Schikorr (2008)	Experiment	---	Established the correlation for the pin bundle friction factor. These correlations are presented in the Appendix-1.
Kazimi and Carelli (1976)	Liquid metal experiment	----	Established the correlation for the pin bundle Nusselt number. This correlation is depicted in the Appendix -1.
Lafay et al., (1975)	Water experiment	19	Measured transverse velocity is found to be higher than that calculated by the assumption that the flow follows the helical wire.
Lorenz and Ginzberg (1976)	Water experiment	91	Whenever the spacer wire is inside the edge subchannel the axial velocity attains maximum value. The measured peripheral swirl velocity is found to be 1.2 times that predicted by helix angle.
Chiu et al., (1978a)	Water experiment	61	Identified analytical expression for the unidirectional swirl. This correlation is presented in the Appendix-1.
Patch et al., (1979)	Water experiment	49	The ratio of measured average interior transverse velocity to that predicted with helix angle attains a maximum value of

			1.1.
Roidt et al., (1980)	Air experiment	1/6th sector	Established the static pressure gradient and transverse velocity field within the various subchannels.
Fernandez and Carajilescov (2000)	Air experiment	7	Wire generated cross flow greatly masks any secondary flow that is induced by the turbulence.
Bogoslovskaya et al., (2000)	Liquid metal experiment	19	Observed a sinusoidal pattern in the transverse flow field.
Wantland (1974),	Subchannel code	19	Proposed the use of analytical expression for transverse velocity in subchannel code.
Basehore and Todreas (1980),	Subchannel code	37 and 61.	Developed SUPERENERGY subchannel code to study on the steady state thermal hydraulics of fast reactor fuel subassemblies. They employed a swirl flow model to account for peripheral swirl, proposed by Chiu et al., (1978a).
Ahmad and Kim (2006)	CFD	7 and 19	Observed that temperature gradient around the pin is periodically repeated for every helical wire pitch.
Raza and Kim (2008)	CFD	7 and 19	Observed that the radial temperature is higher in a 19 pin bundle than that in a 7 pin bundle.
Sreenivasulu and Prasad (2009)	CFD	7	Influence of friction factor and Nusselt number on the pin bundle dimensions is identified and an optimum geometry for heat exchange is proposed.
Gajapathy et al., (2009)	CFD	7,19 and 37	Identified characteristics of flow mixing among the peripheral and central zones in 7, 19 and 37 pin bundles. Then, the characteristics were extended to a 217 pin bundle.
Pointer et al., (2009)	CFD	7 and 217	Performed RANS and LES simulations to obtain transverse velocity in the inter-channel gap of 7 pin bundle and found

			that the flow prediction by RANS simulation is reasonably accurate.
Fanning et al., (2009)	CFD	7 and 217	Observed the necessity for a multi-resolution approach, where higher resolution models such as RANS could provide accurate modeling parameter, such as inter-channel cross flow, which is a necessary input for low resolution model such as subchannel approach.
Peniguel et al., (2010)	CFD	7, 19 and 271	Found that two equation k-ε and Reynolds stress turbulence models have good agreement with the experimental correlations.
Roelofs et al., (2012)	CFD	127	Reported that the results of a low resolution CFD approach with and without the requirement of sub-grid modeling. They observed that the low resolution modeling can be adopted to provide necessary modeling parameters required in the subchannel approach.
Govindha Rasu et al., (2013),	CFD	7, 37	For bundles with large number of pins, temperature development is not achieved, even after a length of 1000 hydraulic diameters.
Amit et al., (2013)	CFD	19	Studied the thermal hydraulic consequences of eccentricity of rod bundle with respect to its sheath. They identified that the pin surface temperature increase by ~ 250 % for an eccentricity value of 0.7.
Gopala et al., (2014)	CFD	19	Investigated flow and temperature development characteristics, in Lead Bismuth Eutectic coolant. They observed that changing the shape of the wire does not affect the velocity field, but change in helix angle largely influence the temperature field.

Govindha Rasu et al., (2014a),	CFD	19	Found the existence of periodic spatial oscillations in friction factor and Nusselt number.
Gajapathy et al., (2015)	CFD	217	Studied the effect of helical pitch on the flow and temperature distributions and the variation in friction factor and Nusselt number as a function of helical wire parameters.
Pin bundle blockage studies			
Fontana et al. (1973)	Sodium experiment	19	Found that extrapolation of 19 pin blockage results to 217 pin prototype bundle under-predicts the local temperature.
Kirsch (1973).	Water experiment	169	Observed that the maximum temperature in the downstream of the blockage occurs at the edge of the blocked region.
Huber and Peppler (1985)	Sodium experiment	169	Observed that the peak temperature occurs in the vortex center of the recirculating zone in the downstream of planar blockage. In the case of grid spaced bundle through the peak temperate occurs in the periphery of the blocked region, the temperature field was symmetric about the axis.
Olive and Jolas (1990).	Sodium experiment	19	Noted that six subchannel porous blockage with a length of 60 mm would not cause boiling in a 19 pin bundle.
Uotani and Haga (1984)	Sodium experiment	37	In both the case of central and corner blockage the boiling superheat is very low and it decreases with increase in flow velocity.
Schlieiziek (1970)	Sodium experiment	---	For high heat flux value and low Peclet number, the boiling superheat tends to be in the range of 40 – 125 ºC. Further, the boiling superheat tends to decrease with increase in sodium velocity and decrease

			in heat flux.
Holtz and Fauske (1971)	Analytical	---	Loop type reactor system have nearly zero boiling superheat, but pool type reactor has higher boiling superheat, which would reduce in the case of possible cover gas entrainment.
Han (1977)	Review	---	Performed a comprehensive review of various pin bundle blockage experiments and simulations. He concluded that water experiments are in good agreement with sodium experiment in obtaining resident time in the wake region of the blockage.
Marr and Crawford (1972)	1-D analysis	---	Identified the critical thickness of porous heat generating blockage as a function of particle diameter and porosity using a one dimensional heat flow model.
Jeong et al. (2009).	Subchannel code	19	Observed that the maximum temperature in the downstream of the blockage occurs at the edge of the blocked region.
Chang et al. (2011)	Subchannel code	271	Reported that even for six subchannel blockage, the wake behind blockage extents up to subassembly exit.
Seung et al. (2006)	CFD	---	Found that the temperature fluctuation at the upper plenum can provide information on the presence of local partial blockage.
Amgad and Salah (2012).	CFD	2D	Reported that no risk of sodium boiling up to 100% and 90 % flow reduction in an average channel and hot channel respectively
Roelofs et al. (2012)	CFD	169	Investigated the consequences of partial inlet and internal blockages in a lead cooled 169 pin bare bundle.
Di Piazza et al. (2014)	CFD	127	Clad temperature exceeding 1000 ºC is reached if planar blockage occupies more

			than 30% of flow area.
Govindha et al. (2014b)	CFD	19	Reported the influence of various blockage parameters on the initiation of sodium boiling, but the exact limit of parameters has not been reported.
Ravi et al. (2013) and Marie et al. (2015).	Lumped codes	---	Studied the consequences of complete flow blockage in fuel subassemblies.

2.3 CLOSURE

From the literature survey, it is clear that though many experimental and computational investigations have been carried out, the reported understanding of local flow features within a subassembly is still limited. Most of the studies were devoted to engineering parameters such as friction factor and Nusselt number and their dependence on pin bundle geometrical parameters. Though a handful of RANS simulations on 217 pin bundle have been reported, only a few of them reported transverse flow profile in the inter channel gap. The relationship between the local axial and transverse flow features and correlations for inter-channel transverse flow have not been reported. A comprehensive quantification/characterization of local flow physics is very important for development of improved subchannel analysis codes. Further the influence of local flow field on temperature distributions in a prototype fuel subassembly is to be identified.

Many experimental and numerical blockage studies have been reported on bundles with small number of pins, but the blockage study on a prototype bundle is limited. Blockage analysis on a 217 pin wire wrapped bundle using CFD has not yet been reported. Most of the studies were with impermeable blockage, which is less likely to occur. Though, a parametric study of porous heat generating blockage has been conducted by Marr and Crawford (1972) with one dimensional model, clear identification of safe and unsafe regimes of blockage parameters for non heat generating blockages by a three dimensional model is not reported. Further, experimental (or) subchannel models cannot capture three dimensional temperature and velocity distributions within the bundle, specifically behind the blocked zone as well as at bundle exit. Such thermal hydraulic features are important for improving the detectability of blockage and improvement in subassembly design. As reported by Seung et al. (2006) the internal blockage could be detectable with appropriate fast response thermocouple installed at upper plenum. These studies required the appropriate outlet temperature of the blocked subassembly as its input boundary condition.

These form the motivation for the present investigations where the focus is on the local flow features within the subassembly and their effect on overall flow and temperature distributions in the subassembly. Further, the focus is on determination of permissible axial length of porous blockage that excludes the risk of sodium boiling as a function of blockage parameters and to identify the consequences of planar blockages. Finally, it is essential to assess the possibility of blockage detection by core monitoring thermocouple.

3 MATHEMATICAL MODELING

3.0 INTRODUCTION

In the present study numerical analysis are performed to understand the flow and temperature fields within the pin bundle under unblocked and blocked conditions. Hence, in this chapter the equations which govern the fluid flow and heat transfer, along with the turbulence model used are discussed in detail.

3.1 GOVERNING EQUATIONS

Heat transfer and flow characteristics of liquid sodium within the fuel subassembly of a FBR are governed by 3 dimensional, steady state, incompressible, Reynolds averaged conservation equations of mass, momentum and energy. The turbulence is modeled by the standard high Reynolds number version of *k*-ε model (Launder and Spalding, 1974). All the unblocked and blocked subassembly cases studied in the present thesis are at Re ~ 90000, which are in the valid range of k-ε model, viz., Re > 10000. The 3-dimensional conservation equations that govern steady incompressible sodium flow and heat transfer (with symbols provided in nomenclature) are:

Continuity

$$\nabla \cdot \left(\vec{v} \right) = 0 \qquad \text{--------------- (Eq.3.1)}$$

Conservation of momentum

$$\nabla \cdot \left(\rho \vec{v}\vec{v} \right) = -\nabla p + \nabla \cdot \left[\left(\mu + \mu_t \right) \left(\nabla \vec{v} + \nabla \vec{v}^T \right) \right] + S_{por} \qquad \text{--------------- (Eq.3.2)}$$

Conservation of energy

$$\nabla \cdot \left(\rho \vec{v} c_p T\right) = \nabla \cdot \left(\lambda_m \nabla T + \frac{c_p \mu_t}{\Pr_t} \nabla T\right)$$ --------------- (Eq.3.3)

Conservation of Turbulent kinetic energy (*k*)

$$\nabla \cdot \left(\rho \vec{v} k\right) = \nabla \cdot \left(\left(\mu + \frac{\mu_t}{\sigma_k}\right) \nabla k\right) + G_k - \rho\varepsilon$$ --------------- (Eq.3.4)

Conservation of Turbulent dissipation rate (*ε*)

$$\nabla \cdot \left(\rho \vec{v} \varepsilon\right) = \nabla \cdot \left(\left(\mu + \frac{\mu_t}{\sigma_\varepsilon}\right) \nabla \varepsilon\right) + \frac{C_{1\varepsilon}\varepsilon}{k} G_k - \frac{C_{2\varepsilon}\rho\varepsilon^2}{k}$$ --------------- (Eq.3.5)

where,

$$G_k = \frac{\mu_t}{2}\left[\left(\nabla\vec{v} + \nabla\vec{v}^T\right) \cdot \left(\nabla\vec{v} + \nabla\vec{v}^T\right)\right]$$ --------------- (Eq.3.6)

And the turbulent viscosity is derived from,

$$\mu_t = \rho C_\mu k^2 / \varepsilon$$ --------------- (Eq.3.7)

The standard wall function approach with turbulent Prandtl number of 0.85 has been adopted based on the experience of Govindha Rasu et al. (2014a,b).

$$u^+ = y^+ \quad for \;\; y^+ \leq y_m^+$$ ---------- (Eq. 3.8a)

$$u^+ = \frac{1}{\kappa}\ln(Ey^+) \quad for \;\; y^+ > y_m^+$$ ---------- (Eq. 3.8b)

Critical y plus, $y_m^+ = 11.32$

$$u^+ = \frac{u}{u_\tau}$$ --------- (Eq. 3.9)

$$y^+ = \frac{y\, u_\tau}{\nu}$$ ---------- (Eq. 3.10)

The friction velocity u_τ is calculated by solving equations, 3.8-3.10.

$$u_\tau = \sqrt{(\tau_w/\rho)}$$ ---------- (Eq. 3.11)

Where, u is the first cell velocity and y is the perpendicular distance of the first cell centroid from the wall. Using the friction velocity in equation 3.11 the wall shear stress τ_w is calculated.

Blockage modeling

The effect of blockage is modeled by a porous body model adopting superficial velocity formulation. To account for the excess pressure drop due to porous blockage, an additional sink term S_{por} is added to the momentum equations. This excess pressure drop is calculated from the correlation proposed by Ergun (1952), which is expressed as,

$$S_{por} = -\frac{|\nabla p|}{\nabla z} = -\left(150\frac{(1-\beta)^2}{\beta^3}\frac{\mu u_s}{d_p^2} + 1.75\frac{(1-\beta)}{\beta^3}\frac{\rho u_s^2}{d_p}\right) \quad \text{--------------- (Eq.3.12)}$$

Where, β and d_p are porosity and mean particle diameter of the blockage respectively, u_s is the superficial velocity of fluid and $(|\Delta P|/\Delta Z)$ is pressure drop per unit length. Blockage particles are assumed to be made of stainless steel. Effective or mean thermal conductivity (λ_m) for all the control volumes within the blockage is calculated by arithmetic averaging of the conductivity of blockage material (λ_b) and coolant material (λ_s).

$$\lambda_m = \lambda_s\beta + \lambda_b(1-\beta) \quad \text{--------------- (Eq.3.13)}$$

The above conservation equations are solved using a pressure based CFD solver, CFD-Expert (2009). Even though all the cells are hexagonal and built originally based on multi-block structured approach, the solver converts the mesh into an unstructured format. The SIMPLE algorithm is used to resolve the pressure-velocity coupling (Patankar, 1980) and it is done through Rhie-Chow interpolation method, which ensures that there is no checkerboard effect in staggered unstructured grid. Hybrid differencing scheme is used to combine the convection and diffusion terms. The set of algebraic equations are solved using a combination of Gauss-Seidel and conjugate gradient methods.

The residue in the discretized equation of a variable in each cell is computed at the end of the each iteration. Then the absolute sum of the residues in all the cells is computed, which is then divided by the total number of cells. This error value is computed for all the momentum, energy, continuity and turbulent equations. To declare convergence, the error value for all the transport equations is set as $< 10^{-4}$. But in the case of planar blockage in a few cases the residue stabilized after reaching $< 2x10^{-4}$.

3.2 TURBULENCE MODEL VALIDATION

3.2.1 Validation with published experimental data

Towards verifying the performance of high Reynolds number turbulence model combined with the standard wall function for the present application in rod bundle, sodium flow and heat transfer in an annular pipe have been simulated adopting the same model. The mesh used in this validation study has a y^+ value of ~130, which is very close to the y^+ value of ~120 in the 217 pin bundle simulations for similar Reynolds number (Re) value. The mesh considered for annular pipe flow simulation is presented in Fig. 3.1. The fully developed Nusselt number and friction factor obtained from CFD simulation are compared with the correlations proposed by Rensen (1981) and Blasius (1913) in Figs. 3.2a and 3.2b. It is seen that for nearly similar Re (~96000) and Peclet number (Pe) (~460), the deviations in Nusselt number and friction factor are < 2.5% and < 4% respectively.

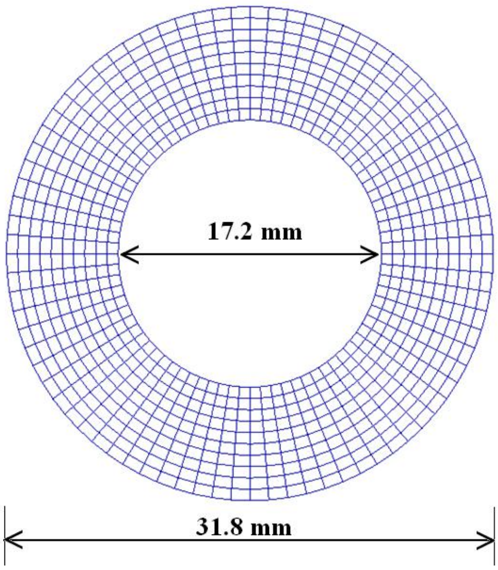

Fig. 3.1: Mesh considered for simulating sodium flow in an annulus.

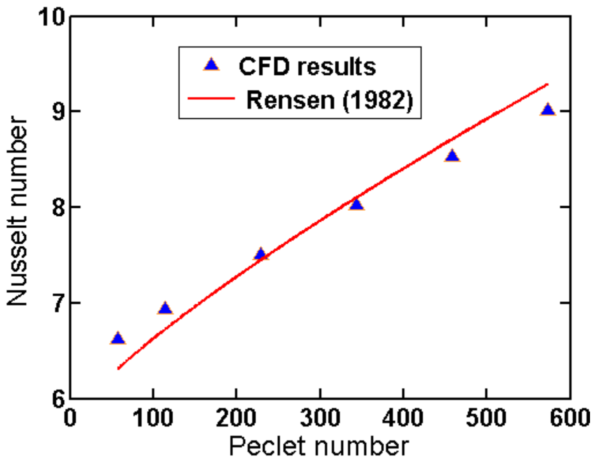

Fig. 3.2a: Comparison of predicted fully developed Nusselt number with Rensen's correlation.

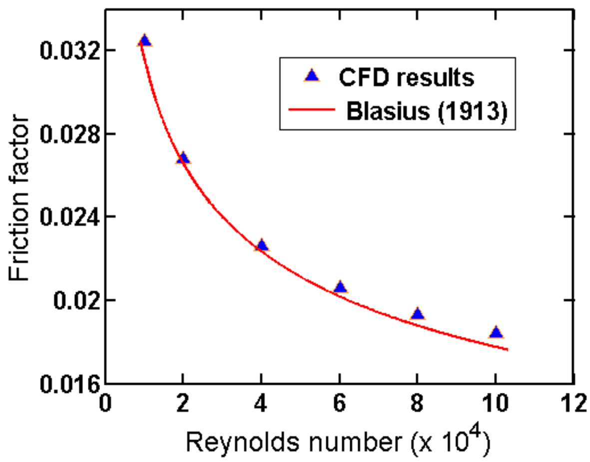

Fig. 3.2b: Comparison of predicted fully developed friction factor with Blasius's correlation.

3.2.2 Comparison among various turbulence models

In addition to the observed comparison of the experimental results with CFD results obtained employing high Reynolds number k-ε turbulence model, further investigation has been carried out to understand the prediction capability of other turbulence models for wire wrap pin bundle. The simulations for a 19 pin bundle were carried out at Re ~ 100000 and Pe ~ 470. Comparison of friction factor and Nusselt number along the length of the bundle obtained by employing various turbulence models is depicted in Figs 3.3a and 3.3b. Further, comparison of the friction factor and Nusselt number at an axial position of 0.15 m from the inlet of the bundle is presented in Table 3.1. It could be seen that in the case of friction factor, except SST k-ω model all the turbulence models have a deviation of < 5%. In the case of Nusselt number, except for the RNG k-ε turbulence model, all the other models compare within 5%. Comparison of normalized transverse velocity in the central subchannel along the length of the bundle obtained by employing various turbulence models is depicted in Fig. 3.4. It could be seen that there is a very good comparison among various turbulence models in predicting the transverse flow. Thus the thermal hydraulic results are found to be less sensitive to the turbulence model employed.

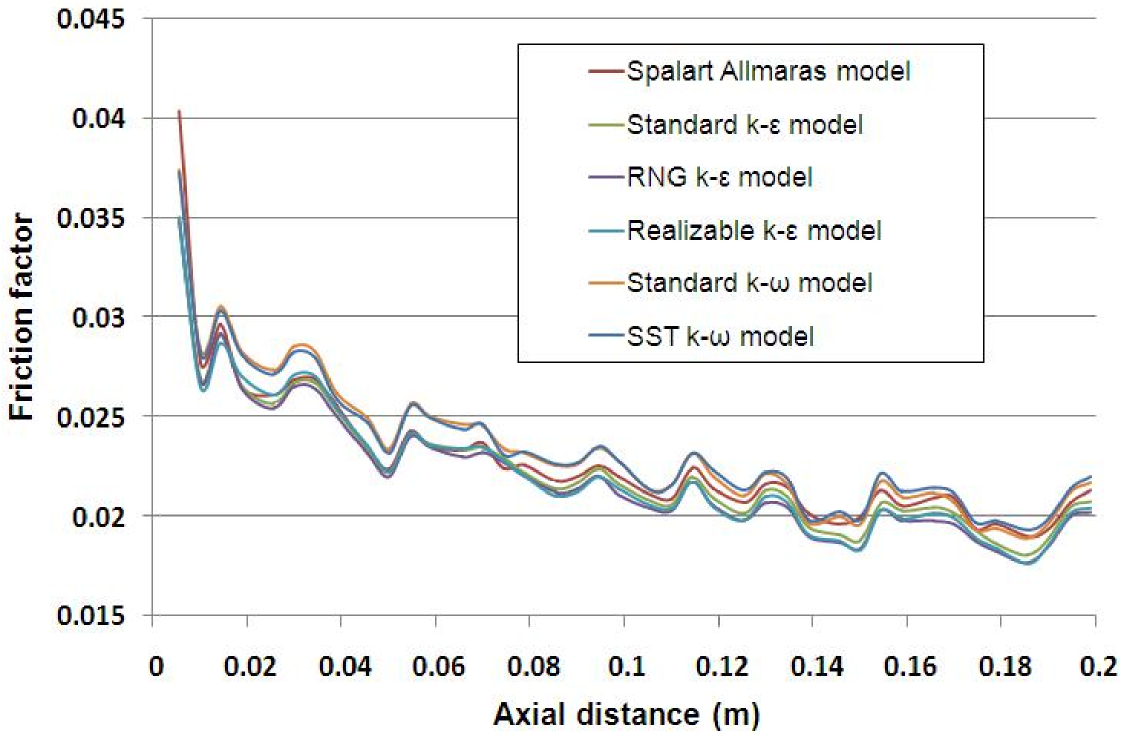

Fig. 3.3a: Comparison of Friction factor along the bundle length predicted by various turbulence models (Re ~100000, Pe ~470).

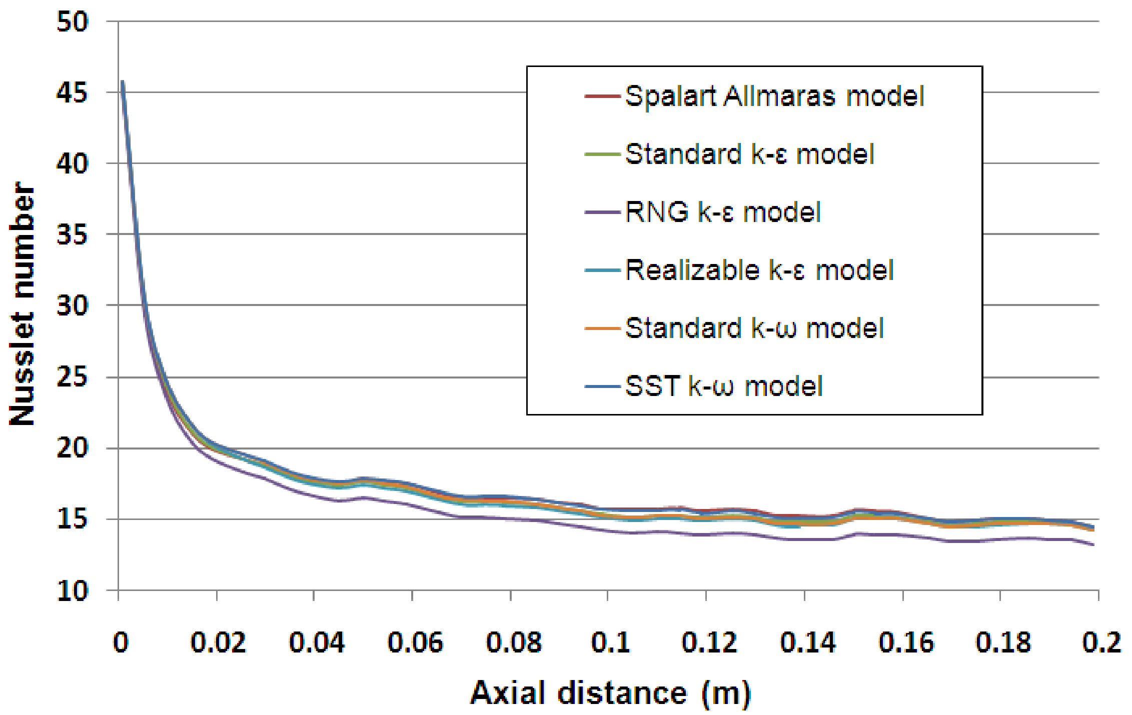

Fig. 3.3b: Comparison of Nusselt number along the bundle length predicted by various turbulence models (Re ~100000, Pe ~470).

Table 3.1: Comparison of friction factor and Nusselt number predicted by various turbulence models (axial length = 0.15 m).

Turbulent models	**Friction factor**	**Nusselt number**	**% Deviation in friction factor**	**% Deviation In Nusselt number**
Spalart Allmaras model	0.0200	15.61	-6.39	-2.65
Standard k-ε model	0.0188	15.21	0	0
RNG k-ε model	0.0184	13.90	2.19	8.63
Realizable k-ε model	0.0183	14.97	2.62	1.57
Standard k-ω model	0.0196	15.04	-4.19	1.10
SST k-ω model	0.0199	15.48	-5.56	-1.74

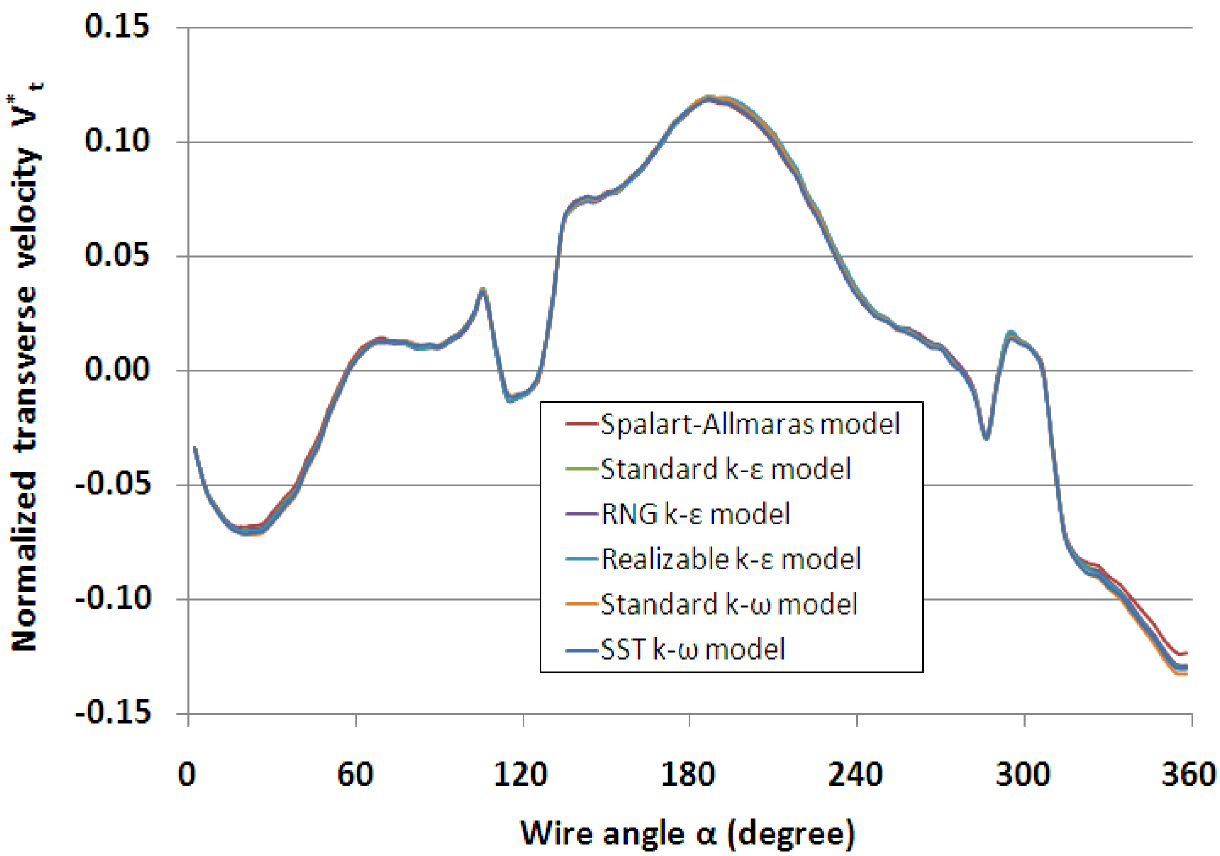

Fig. 3.4: Comparison of Normalized transverse velocity along the bundle length predicted by various turbulence models.

3.3 DEFINITION OF FRICTION FACTOR AND NUSSELT NUMBER

The friction factor f_z at any axial distance z from inlet is defined as

$$f_Z = \frac{2D_h}{\rho V_a^2}\left(\frac{dP}{dz}\right)_z \qquad \text{--------------- (Eq.3.14)}$$

Where, $\left(\frac{dP}{dz}\right)_z$ is the axial pressure gradient at any distance z from the entrance.

The Nusselt number (Nu_z) at any distance z from inlet is defined by

$$Nu_Z = \frac{h_z D_e}{K_s} \qquad \text{--------------- (Eq.3.15)}$$

The heat transfer coefficient is determined from,

$$h_z = \frac{q^{"}}{(T_{cz} - T_{bz})} \qquad \text{--------------- (Eq.3.16)}$$

Where, the definitions of various symbols are provided in Nomenclature.

3.4 GEOMETRY AND BOUNDARY CONDITIONS FOR THE PIN BUNDLE STUDY

In the case of a prototype fuel subassembly, the active fuel zone length is 5 helical pitches (Chetal et al., 2006). There is considerable heat generation in the axial blanket region at one pitch length below the fuel zone and one pitch length above the fuel zone. Liquid sodium enters the subassembly through the lateral slots at its foot from where the coolant travels vertically upwards and extracts the nuclear heat generated in the fuel / blanket regions before leaving the subassembly through the top. In the present analysis, 1.4 m of effective heat generating bundle height (1 m active core and 0.2 m of top and bottom axial blankets) is modeled. The dimensions of the pin bundle are: 6.6 mm pin diameter, 1.65 mm wire diameter, 8.28 mm triangular pin pitch, and 200 mm helical wire pitch (Table 3.2). The nominal mass flow rate of sodium is 35.8 kg/s. The inlet temperature is 670 K. The details of the boundary conditions are presented in Table 3.3. A schematic of pin bundle and boundary conditions are depicted in Fig. 3.5a. The heat flux profile that is applied over the pins is a function of the neutron flux density and neutronic properties of the reactor material. Detailed reactor physics calculations have been carried out and the resulting heat generation rate in the central subassembly pins is found to follow a cosine profile (Ref. Fig. 3.5b). The heat generation rate is converted into heat flux in the present study. The total heat input to the bundle is 8 MW. More details regarding neutronic calculation procedures can be found in in Walter and

Reynolds (1981). For the flow characterization studies the fluid properties are taken at 670 K (sodium inlet temperature to the bundle). For the blockage analysis the fluid properties are taken at bulk mean temperature (757K). In the present study buoyancy effect and neutron flux density variation due to variation in sodium density are not accounted. Through a study on 19 pin bundle with blocked central subchannels, the influence of buoyancy was found to be minimal (deviation in the peak clad temperature is < 4 K). Further, in the present study all the pins were supplied with identical power. This is valid only for central fuel subassembly.

Table 3.2: Dimensional details of 217 pin bundle.

Parameters	**Values**
Pin diameter (**D**)	6.6 mm
Wire diameter ($\mathbf{D_w}$)	1.65 mm
Triangular Pitch (**P**)	8.28 mm
Helical Wire Pitch (**H**)	200 mm
Pin to hexcan wall gap ($\mathbf{g_{hex}}$)	1.75 mm
Pin pitch type	Triangular
Total axial length	1400 mm

Table 3.3: Boundary conditions of 217 pin bundle.

Parameters	**Values**
Inlet mass flow rate	35.8 kg/s
Inlet temperature of coolant	670 K
Coolant used	Sodium
Outlet pressure	0 bars
Pin walls	Constant or space dependent heat flux.
Wire walls	Adiabatic
Hexcan wall	Adiabatic

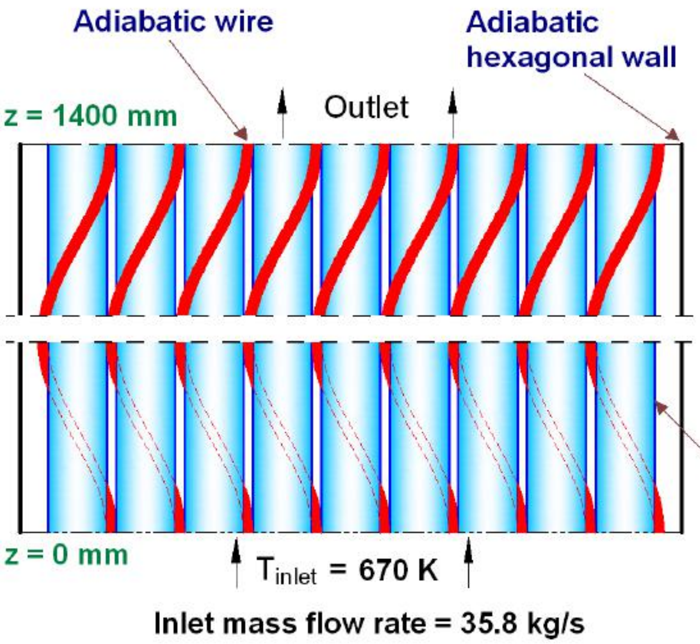

Fig. 3.5a: Boundary conditions considered for the SFR fuel subassembly.

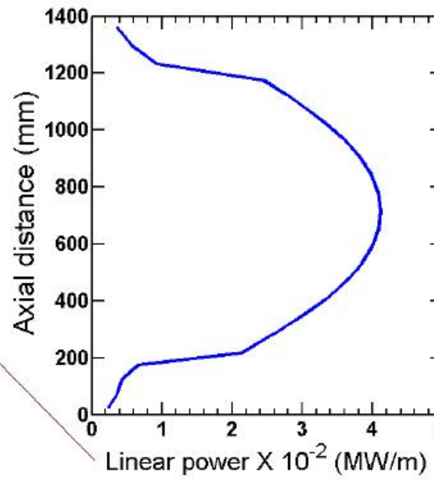

Fig. 3.5b: Cosine power profile considered in fuel pin.

3.5 MESH GENERATION

The structured mesh of the wire wrapped pin bundle has been generated using a customized mesh generator module of CFD-Expert (2009), GridZ^{TM}. To avoid the line contact between the pin and wire, the wire is radially inserted into the pin by 0.05 mm. This value is ~3% of the wire diameter, hence does not change the flow cross section significantly. However, studies have been carried out to understand the influence of wire penetration, where two different levels of wire penetrations (0.025 mm and 0.05 mm) are studied on an ideal fuel pin with helical wire located inside a circular sheath. The predicted temperature field at 0.1 m from the inlet of the bundle in both the cases is depicted in Fig. 3.6. It is found that, in the case of 0.025 mm penetration, the predicted peak temperature is ~ 7 K higher than that in the other. This variation in temperature occurs locally near the pin wire contact region. Globally the temperature profile remains the same.

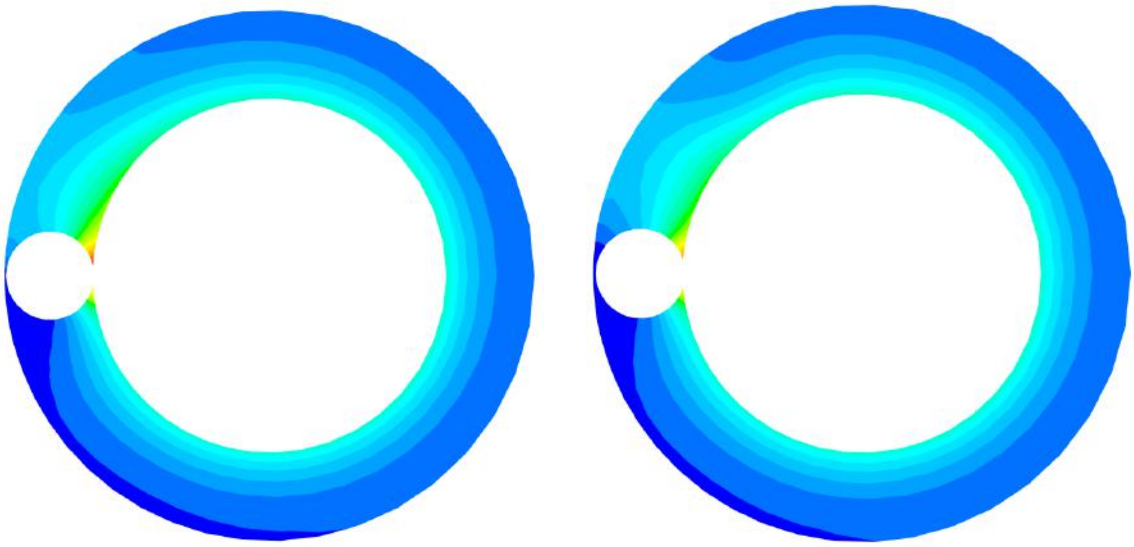

(a) Wire inserted 0.025 mm into the pin (b) Wire inserted 0.05 mm into the pin

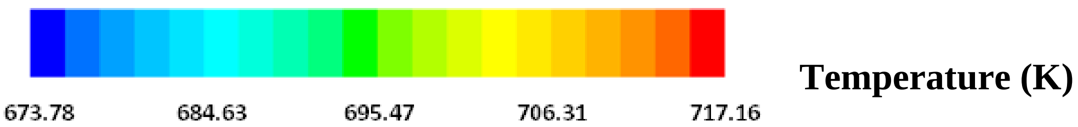

Fig. 3.6: Temperature contour at 0.1 m from the inlet

As fuel pin is assembled in a triangular pitch, a hexagonal boundary can be marked around each fuel pin. The space between the hexagonal boundary and the fuel pin is divided into six topologically distinct blocks each having its own structured mesh for 1/6th pitch length. The same is done for all the pins in the subassembly. Utilizing the geometric periodicity of pin bundle over 1/6th pitch, the structured mesh obtained for the 1/6th axial pitch is rotated over 60° about the axis and patched as the successor for the previous 1/6th pitch. This procedure is repeated to obtain the required length of the axial domain. For the seven helical pitches considered for the prototype fuel subassembly, the entire domain is axially divided into 84 blocks and handled separately by 84 processors on a cluster computer with 48 GB RAM and 131 GFLOPS speed for each node.

3.6 GRID INDEPENDENCE STUDY

Due to the large size of 217 pin bundle and the associated computational time, grid independency study was performed for a 19 pin bundle with 7 helical pitch length. After determining the required mesh density on the small bundle, an equivalent mesh count is adopted for the large prototype 217 pin bundle. The grid independence study was carried out in two steps and pressure drop is taken as the target parameter. First, for a very fine radial mesh (R1), three different axial meshes (A1, A2, A3) were considered, and from this study, the axial mesh division A2 was finalized (Table 3.4). Subsequently, by a similar procedure with the finalized axial mesh division, radial mesh density was optimized and radial mesh R3 was selected (Table 3.5). It can be seen that a mesh with 36 divisions around the circumference of each fuel pin, 12 division around the circumference of each wire and 15 divisions along the axial direction of every 1/6 helical pitch, provides a nearly grid independent solution. This mesh density when adapted to the 217 pin prototype bundle contained 36 million grid cells. The mesh pattern (A2-R3) in one pitch length (200 mm) of 217 pin bundle is depicted in Fig 3.7. Further the mesh density around the inner and the peripheral pins are depicted in Fig 3.8. For the generated mesh, the average near wall $y+$ is 120, whereas standard wall function requires the wall-adjacent cell's centroid to be maintained within the log-law layer, i.e., ($30 < y+ < 300$).

TABLE 3.4: Radial grid configurations in 19 pin bundle.

Radial grid	Cells around pin-wire-gap*	Total No. of Mesh points (millions)	Pressure Drop (Pa) $\times 10^5$	Deviation with respect to fine mesh
R1	60-23-18	22.10	1.816	--------
R2	48-18-14	6.99	1.800	- 0.88
R3	36-12-10	3.63	1.796	- 1.10

* Gap – gap between the fuel pin and hexcan wall

TABLE 3.5: Axial grid configurations in 19 pin bundle.

Axial grid	No. of Mesh Points in axial direction for 1/6 helical pitch	Total No. of Mesh points (millions)	Pressure Drop (Pa) $\times 10^5$	Deviation with respect to fine mesh (%)
A1	29	22.10	1.816	--------
A2	15	11.43	1.818	0.11
A3	8	6.10	1.792	- 1.32

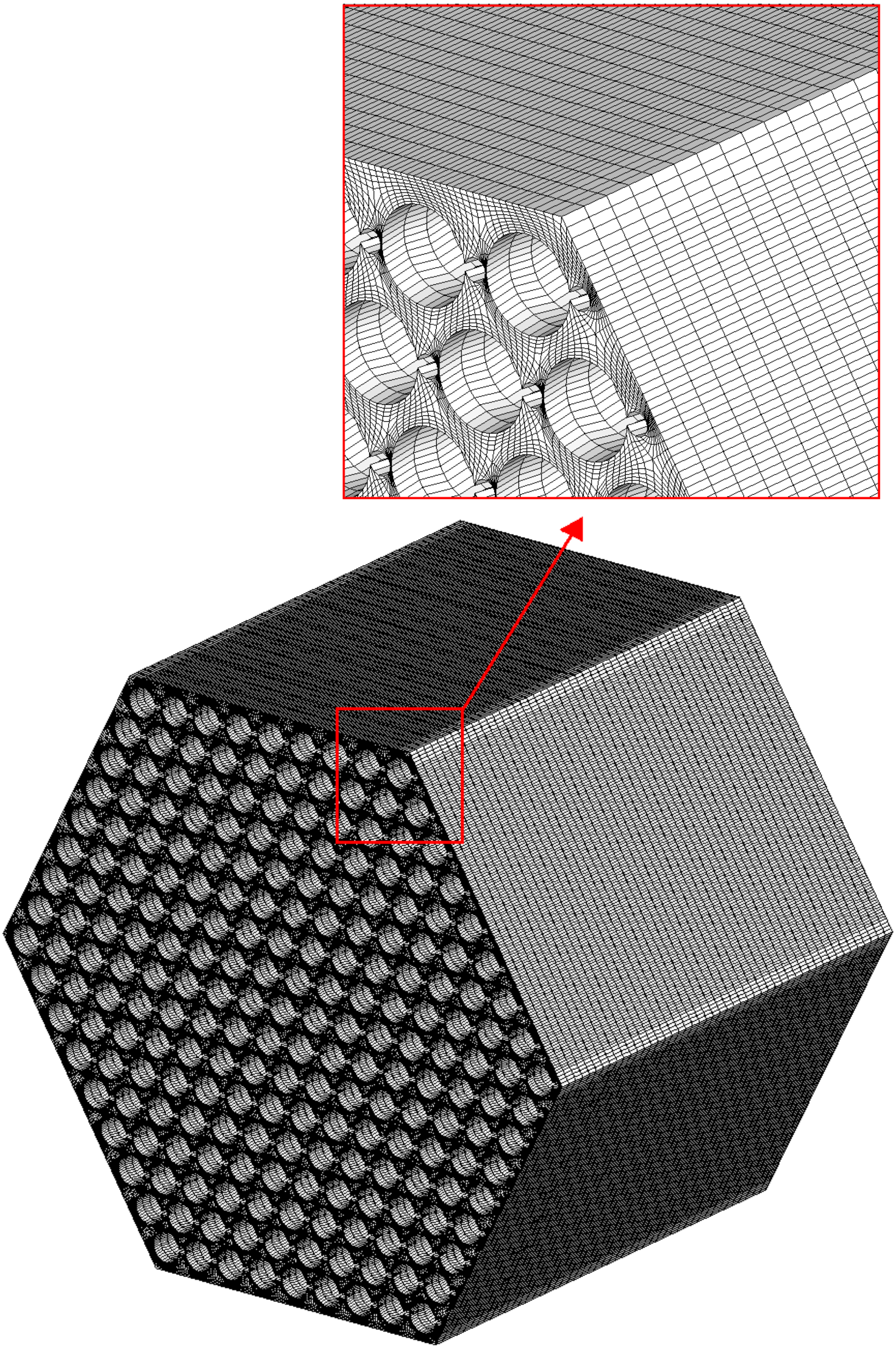

Fig. 3.7: Mesh pattern in one pitch length (200 mm) of 217 pin bundle.

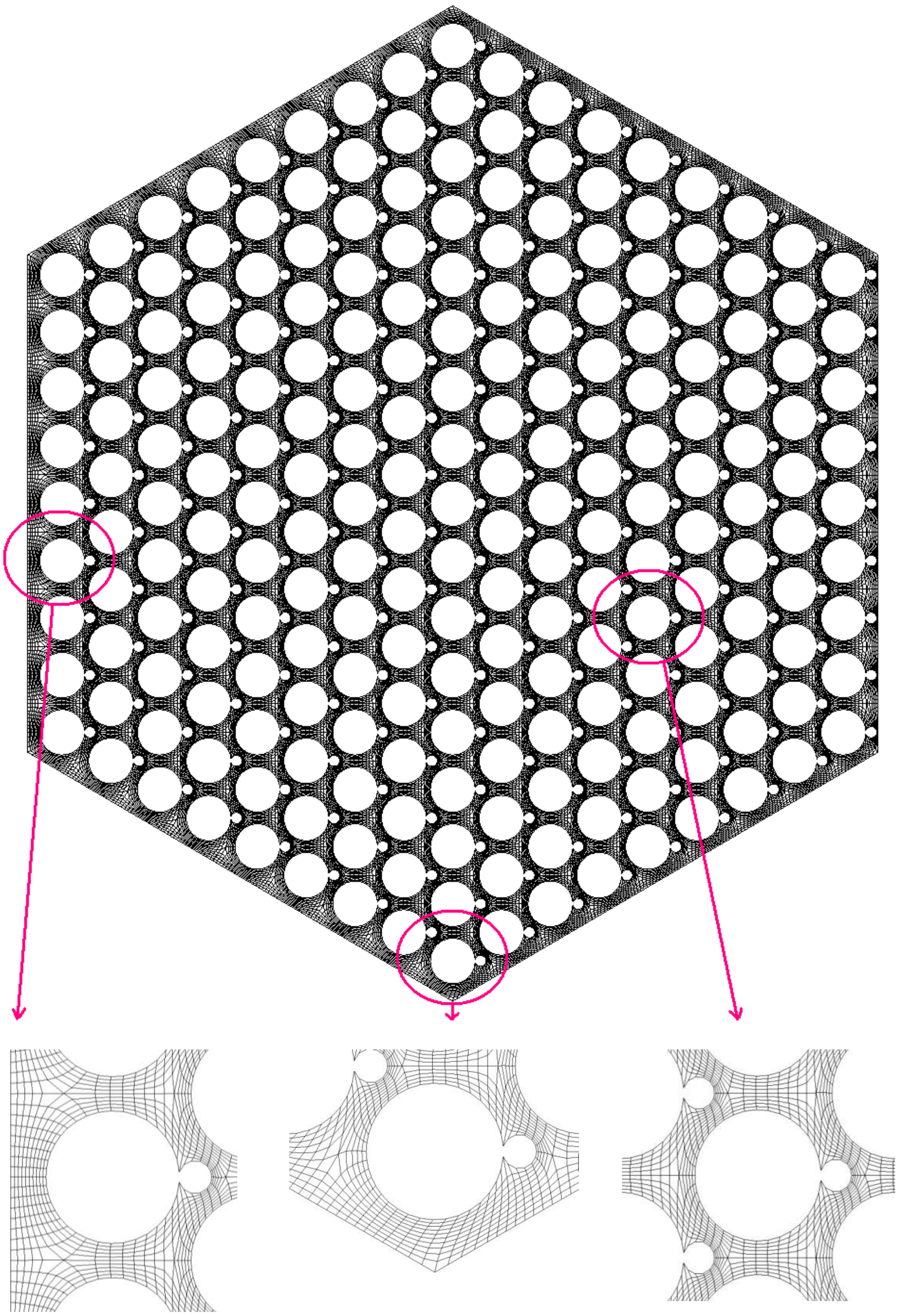

Fig 3.8. Cross section of mesh considered in the present analysis.

In addition to the above grid independence test, a study has been carried out to understand the sensitivity of the 1st grid point in predicting the pin bundle thermal hydraulics. Towards this, the near wall cells are further refined by splitting cells in the first layer (Fig. 3.9) of the original mesh (R3-A2). Friction factor and Nusselt number obtained from the original mesh (average y+ ~ 120) and wall refined mesh (average y+ ~ 58) are depicted in Figs. 3.10a and 3.10b. In the case of both, friction factor and Nusselt number, satisfactory comparison between the two meshes are observed.

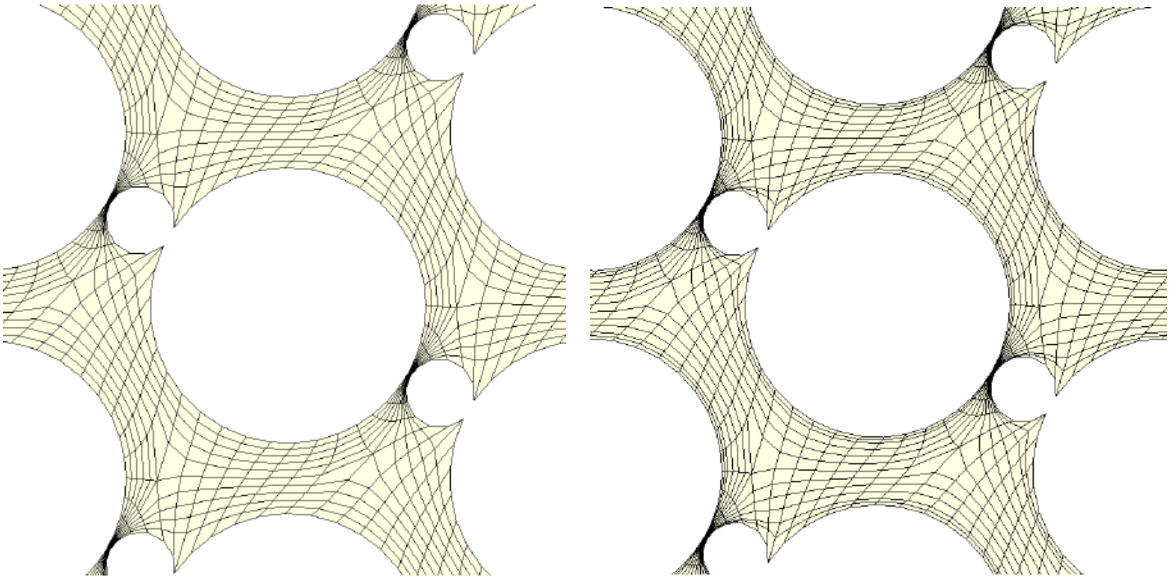

Fig. 3.9: The actual mesh (left) and near wall refined mesh (right) taken for the validation study.

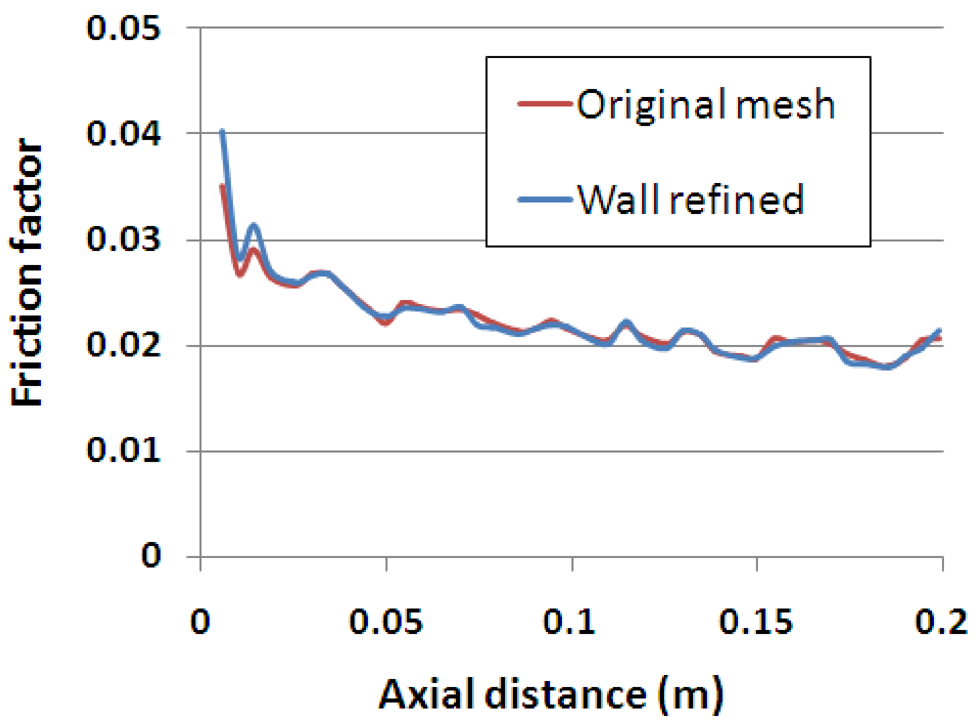

Fig. 3.10a: Comparison of friction factor obtained with original mesh and wall refined mesh.

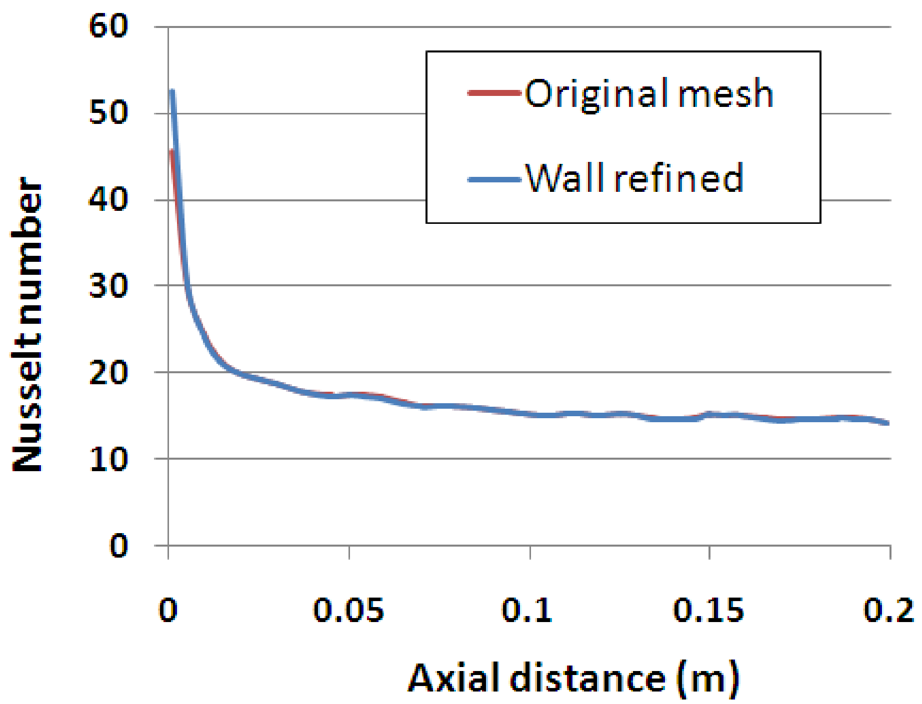

Fig. 3.10b: Comparison of Nusselt number obtained with original mesh and wall refined mesh.

3.7 CLOSURE

The governing equations for simulating the flow and heat transfer of sodium flow in prototype fuel bundle, the model to simulate local blockage within the pin bundle and the justification for choosing the various models were discussed in the present chapter. The results predicted from the CFD simulations are discussed in the subsequent chapters.

4 CHARACTERIZATION OF VELOCITY AND TEMPERATURE FIELDS IN A 217 PIN WIRE WRAPPED FUEL BUNDLE

4.0 INTRODUCTION

As noted in the literature survey, though large volumes of numerical and experimental investigations on pin bundle were reported, most of the studies were devoted to engineering parameters such as friction factor and Nusselt number and their dependence on pin bundle geometrical parameters. The reported understanding of local flow features within a subassembly is still limited. Detailed studies on flow physics to establish appropriate relationships between the local (axial and transverse) flow features and correlations for inter-channel transverse flow have not been reported. Characterization of local flow physics is very important for development of improved subchannel analysis codes. This forms the motivation for the present investigations where the focus is on the local flow features and their effects on the axial and transverse flow patterns within each subchannel and their effect on overall flow and temperature distributions in the subassembly.

4.1 VALIDATION

The computational model used in the present CFD analysis is validated with the in house experiment, published correlations and published data of friction factor and Nusselt number within the SFR fuel pin bundle. In addition, the present transverse flows within the pin bundle are compared with those reported in the literature.

4.1.1 Validation with In-house Experiment

The pressure drop of wire wrapped 217 pin bundle predicted in the CFD analysis is compared with the measured data obtained from an in-house water model experiment. It may be highlighted that hydraulic experiments have been conducted in-house on a full scale 217 pin dummy fuel bundle with water as the working fluid (Padmakumar et al., 2017). Reynolds number similitude is followed to determine the necessary flow rate in the model and Euler number similitude is followed for transposing pressure drop from model (water) to prototype (sodium). The nominal sodium flow through the peak rated fuel subassembly is 36 kg/s. Applying Reynolds number similitude, the water flow rate in the model is estimated as 53.6 kg/s. Pressure drop across the bundle was measured for various flow rates and the data was transposed to reactor operating condition by using Euler number similarity. The pressure drop as a function of sodium flow rate in the pin bundle transposed from the experimental data is depicted in Fig. 4.1. Also shown in the same figure is the pressure drop predicted by the present CFD model for various values of sodium flow rate. It is seen that the agreement between the experimental and CFD data is good in the low flow rate regime. Further, even for the large flow rate of 34.5 kg/s, the deviation is within 10% and is satisfactory.

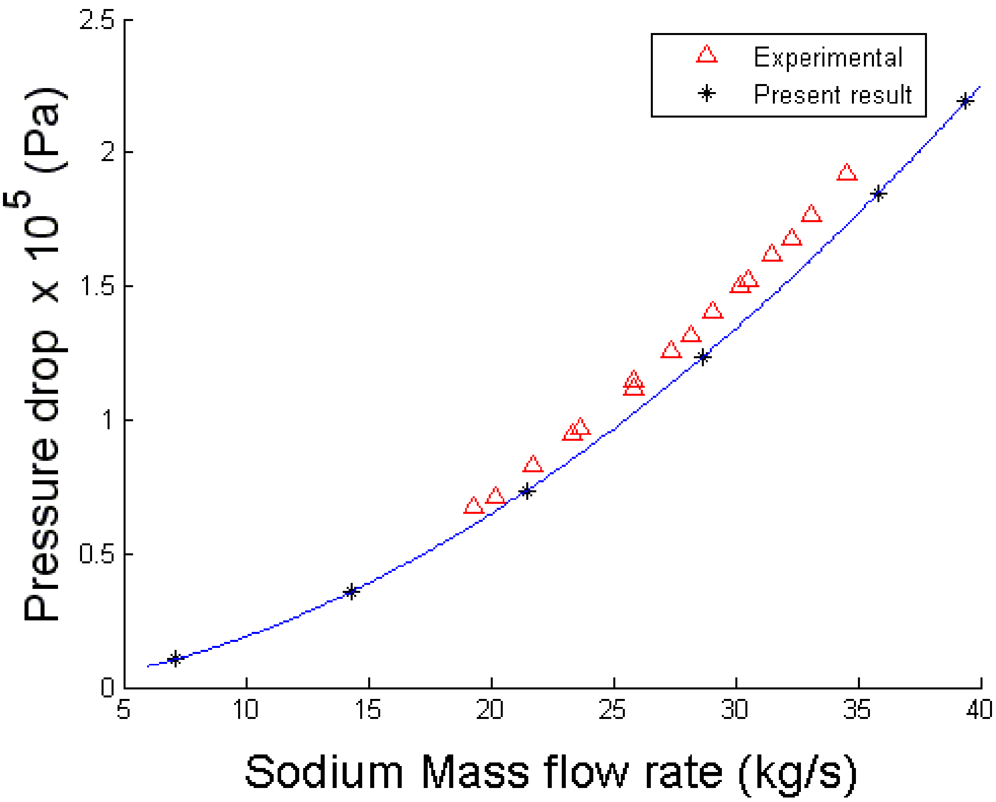

Fig. 4.1: Comparison of predicted pressure drop in fuel pin bundle against in-house experimental data (Padmakumar et al., 2017).

4.1.2 Validation with Published Correlations

The fully developed friction factor predicted by the present study as a function of Reynolds number is compared with correlations proposed by various researches in Fig. 4.2. It can be seen that the present result compares very well with the Novendstern correlation for Reynolds numbers lower than 50000 and beyond which agreement with Modified Engel correlation is good. Quantified deviation of present result from the reported correlations for a particular Reynolds number of 87000 (corresponding to 100% flow condition of reactor) is presented in Table 4.1. It is seen that the maximum deviation is -9%. The CFD predicted Nusselt number at the end of 7 helical pitches is 6.77 for Reynolds number of 87000. The same estimated by Kazimi and Carelli (1976) correlation is 8.04 suggesting a deviation of -19%. The comparison is satisfactory considering the large scatter in the published experimental correlations (Ref. Govinda Rasu et al., 2013).

Friction factor and Nusselt number correlations used for the validation study are given in the Appendix-I.

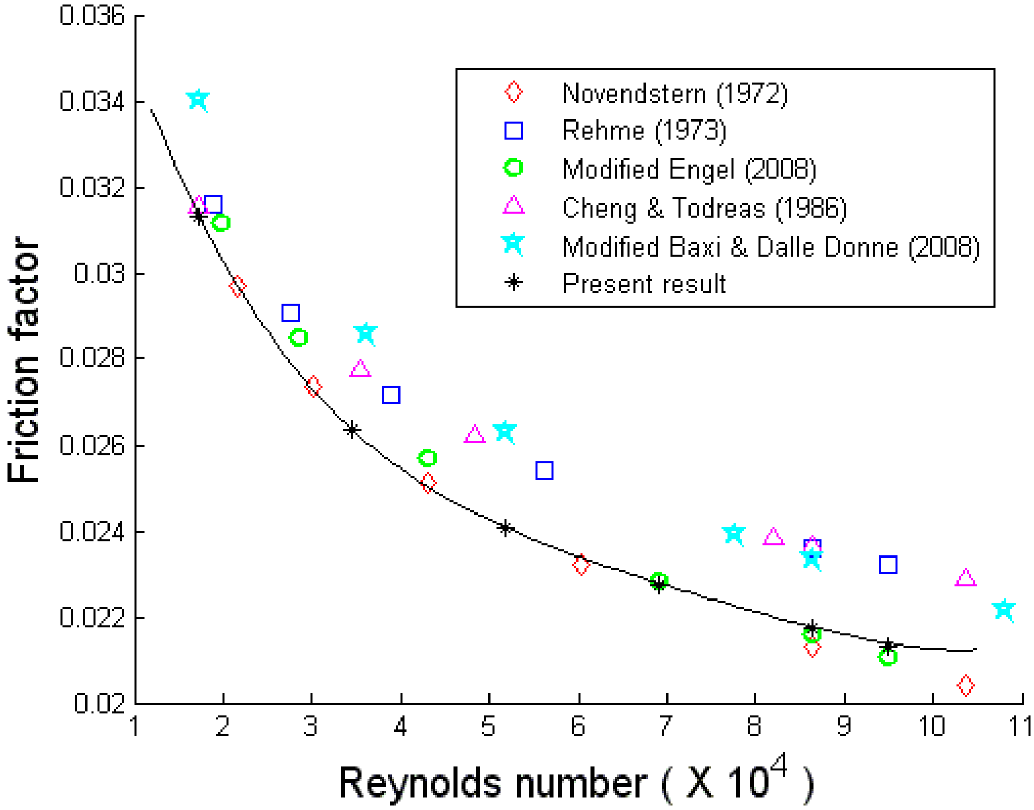

Fig. 4.2: Comparison of computational results with various published friction factor correlations for wire-wrapped pin bundles.

Table 4.1: Comparison of present result with various friction factor correlations for *Re* = 87000.

Reference	Friction factor	% Deviation
Present calculation	0.02175	--------
Novendstern et al. (1972)	0.02131	2.0288
Reheme (1973)	0.02360	- 8.4808
Modified Engel et al. (Bubelis et al. 2008)	0.02159	0.7417
Cheng and Todreas (1986)	0.02363	- 8.6209
Modified Baxi & Dalle Donne (Bubelis et al. 2008)	0.02336	-7.4209

4.1.3 Validation with Published Data

The friction factor obtained from the present CFD simulations of 217 pin wire wrapped bundle is also compared with the experimental data of Wakasugi and Kakehi (1971). The geometrical parameters considered in the CFD simulation (P/D = 1.254, H/D = 30.3) and that of experiments (P/D = 1.221, H/D = 30.2) are very similar. It shall be highlighted that while calculating the friction factor, Wakasugi and Kakehi (1971) neglected the influence of hexagonal wrapper (i) by determining the bundle hydraulic diameter only based on central subchannel region and (ii) flow velocity in the central region. Hence, for the purpose of comparison, a similar methodology is followed now for calculating fiction factor and Reynolds number in CFD simulations also. This comparison is depicted in Fig. 4.3. It can be seen that the CFD data calculated based on the methodology proposed by Wakasugi and Kakehi (1971) compares with the measured data with a maximum deviation of 5%.

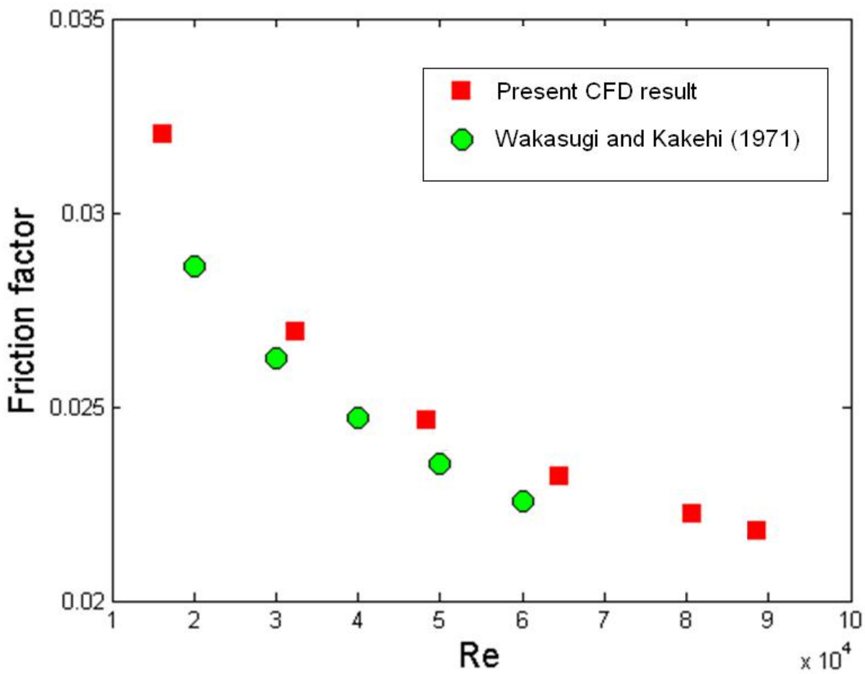

Fig. 4.3. Comparison of friction factor predicted by CFD simulations against measurements of Wakasugi and Kakehi (1971).

4.2 RESULTS AND DISCUSSION

The predicted axial velocity distribution of sodium during passage of one helical pitch length is depicted in Fig. 4.4. These results are for the fourth axial pitch, starting from z = 600 mm to z = 800 mm, where the flow is expected to be fully developed. The peak axial velocity in the bundle (11.4 m/s) is about 1.5 times the mean velocity of 7.4 m/s. It is seen that as sodium flows along the bundle, the location of maximum axial velocity shifts from one sector to subsequent sector for every 1/6th pitch and returns back to the initial position after one helical pitch.

To understand the complex 3-dimensional flow field existing within the subassembly, flow features within each subchannel have to be investigated separately. Towards this, the subassembly has been divided into various parts and the nomenclature adopted for the discussion to be presented in this section is depicted in Fig. 4.5. The subassembly is radially divided into four regions, viz., central, middle, outer and peripheral regions (Fig. 4.5a). All the 217 pins are numbered with pin number 1 starting from the center. Further, the hexagonal subassembly is circumferentially divided into six triangular sectors, named sequentially as sectors I to VI (Fig. 4.5b). The six subchannels, named A – F, surrounding each pin are named after the pin around which the subchannels are located (Fig. 4.5c). As one moves up along the mean flow direction, the spacer wire position moves counter-clockwise. A particular wire orientation denoted as wire angle α corresponds to a particular axial location of investigation lying within a pitch length of 200 mm. Location of wire at the inlet to the pin bundle (i.e elevation = 0 mm) which corresponds to zero wire-angle is also shown in Fig. 4.5d. The circumferential locations around the pin are depicted in Fig. 4.5e.

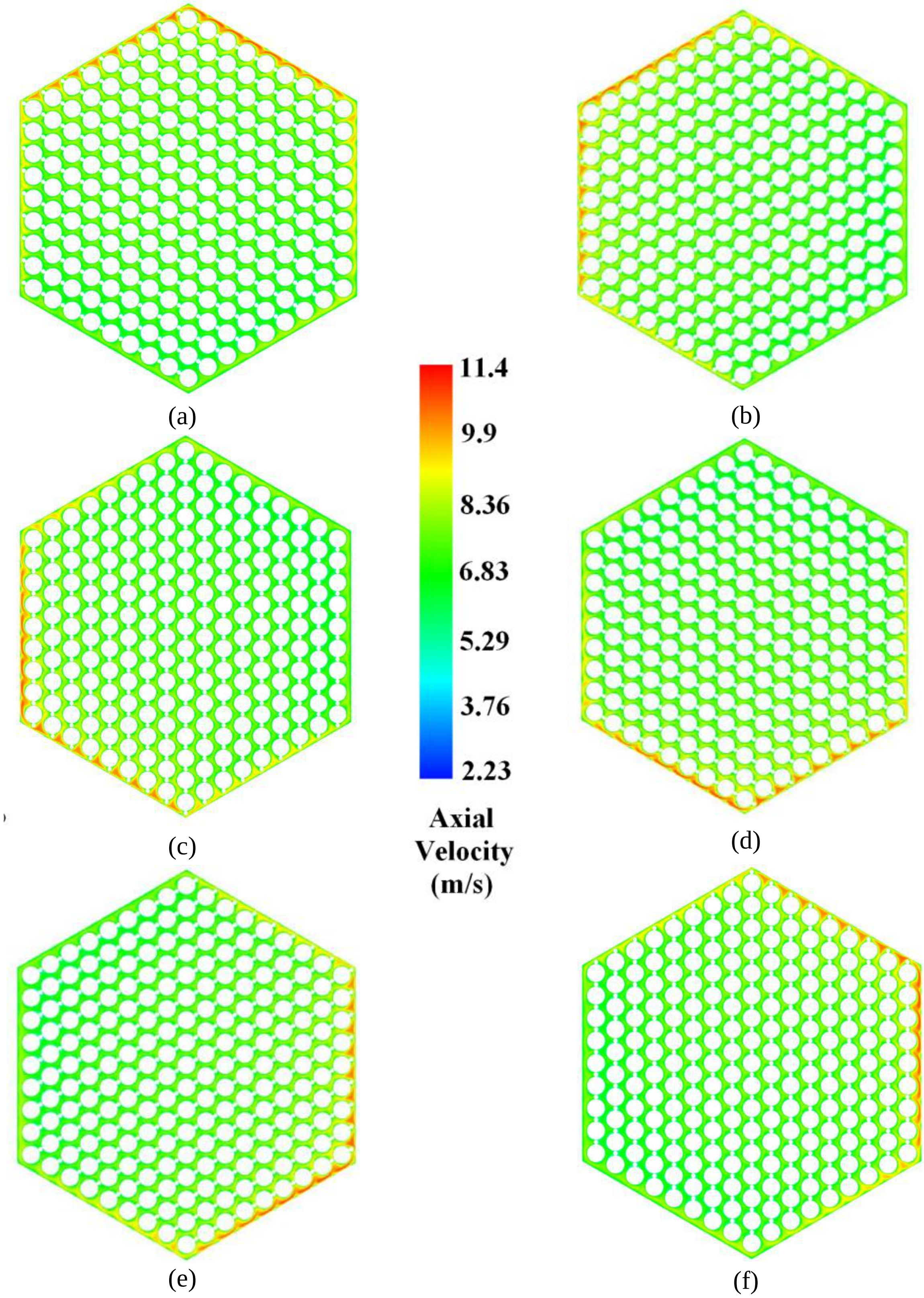

Fig 4.4: Axial velocity contours at various locations (a) z = 600 mm, (b) z = 633.3 mm, (c) z = 666.7 mm, (d) z = 700 mm, (e) z = 733.3 mm and (f) z = 766.7 mm.

Pins grouped into four groups

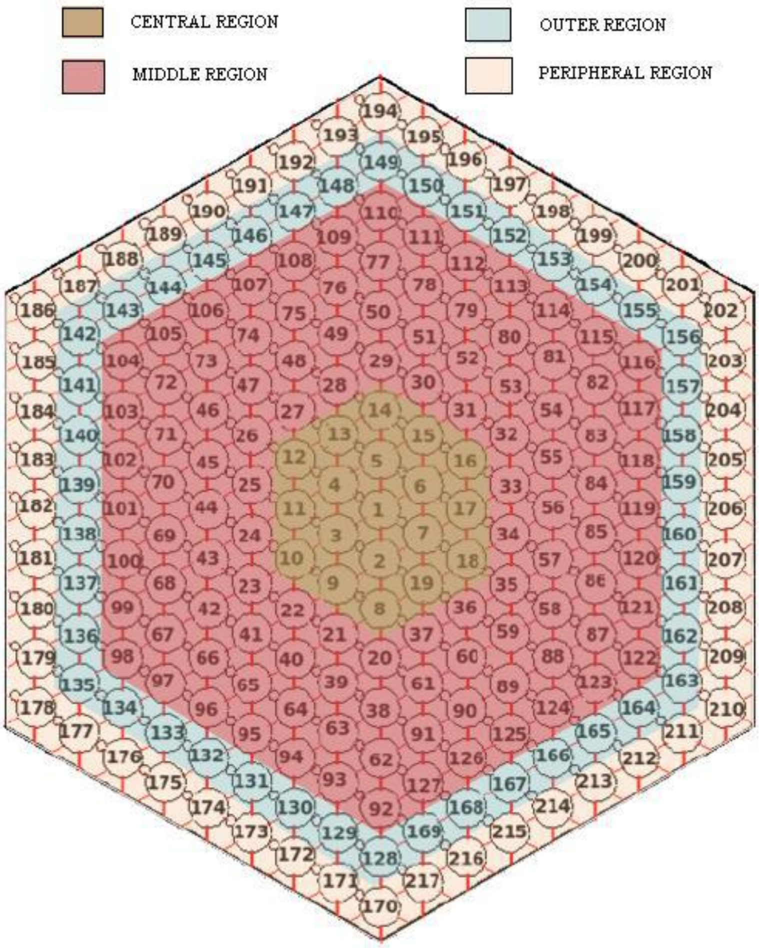

(a) Pin numbering adapted in 217 pin bundle

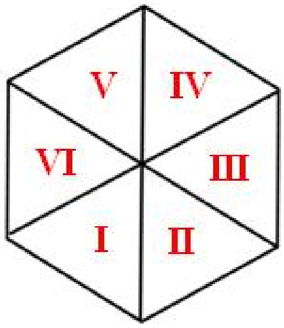

(b) Circumferential division of subassembly into six sectors

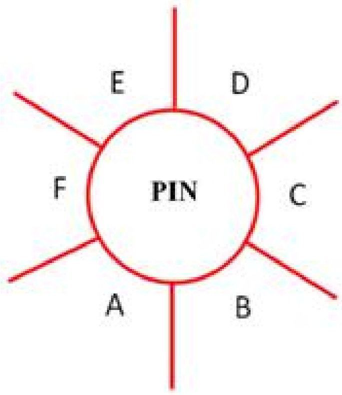

(c) Naming of subchannels around a pin

Location of wire at inlet, which corresponds to α = 0°, it is 30° offset with horizontal.

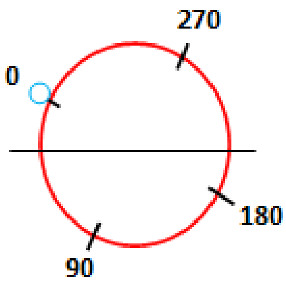

(d) Wire angle (α)

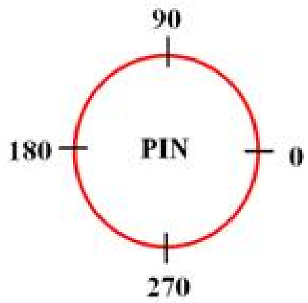

(e) Angle around the pin (θ)

Fig 4.5: Nomenclature adopted for discussion of the present results.

4.2.1 Subassembly Flow Features

Though the predominant flow in a wire wrapped subassembly is in the axial direction (z), presence of helical wire generates significant transverse flow, which results in spatially oscillating axial flow within each subchannel. It is to be highlighted that all the oscillations discussed in the thesis are not temporal oscillations but spatial oscillations. Based on detailed investigation of fully developed flow in wire wrapped pin bundle, the following four characteristics are evident.

(a) Axial flow rate oscillations: The axial flow rate through a subchannel is not constant and is superimposed with a periodic fluctuation. The amplitude and phase shift of axial flow oscillations vary among subchannels in different radial and sectorial locations.

(b) Swirl around hexcan: There exists a unidirectional transverse swirl adjoining the hexcan wall, in the direction same as that of wire rotation around the pin.

(c) Flow bypass: There is diversion of flow towards the gap between the peripheral pin and the hexcan wall, where the resistance is low compared to that of the central region.

(d) Alternate inflow and outflow in peripheral subchannel: Alternate transverse inflow into peripheral subchannel from the center and outflow from peripheral subchannel towards the center persists in the entire length of the bundle.

The influence of helical wire on 3-dimensional flow field existing in the subassembly and the flow oscillation can be divided into,

(i). **Local phenomenon:** This is due to the passage of wire through a subchannel and its influence is localized to that subchannel.

(ii). **Global phenomenon:** This is due to the change in orientation of wire with respect to hexcan wall in the peripheral region and its influence is visible in the whole sector.

Flow features in central and peripheral subchannels are widely different, because the strengths of these two phenomena vary among these two regions. Flow features in middle region are nearly similar to that of the central region and the flow features of outer region are closer to that of the peripheral region. For a quantitative and qualitative understanding of flow features within a subassembly, subchannels located in the various regions are investigated.

4.2.2 Axial Flow Oscillations in Central Subchannels

It shall be indicated that within an axial length of one helical pitch, three helical wires corresponding to the three pins that form the subchannel, pass through the subchannel. The cross section area of a spacer wire is ~17% of the subchannel flow area. Hence, mass flow rate within the subchannel periodically changes attaining three minima. Figure 4.6a depicts the mean axial velocity variation in the subchannel 1A as a function of wire angle (Ref. Fig. 4.5c for nomenclature). It can be seen that the mean axial velocity mildly oscillates with three local minima. However, the peak to peak variation is only ~3.5%. The spatial variation in axial mass flow rate within the same subchannel is depicted in Fig. 4.6b. A large variation in mass flow rate can be seen to the extent of ~21%.

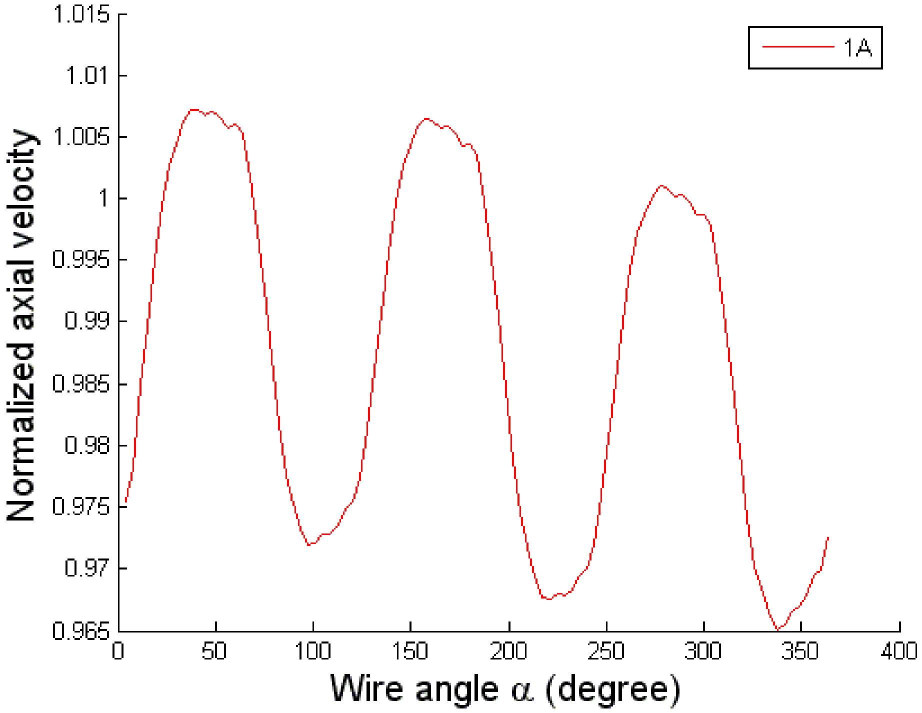

Fig. 4.6a: Variation of area averaged normalized axial velocity in subchannel 1A with increase in wire angle.

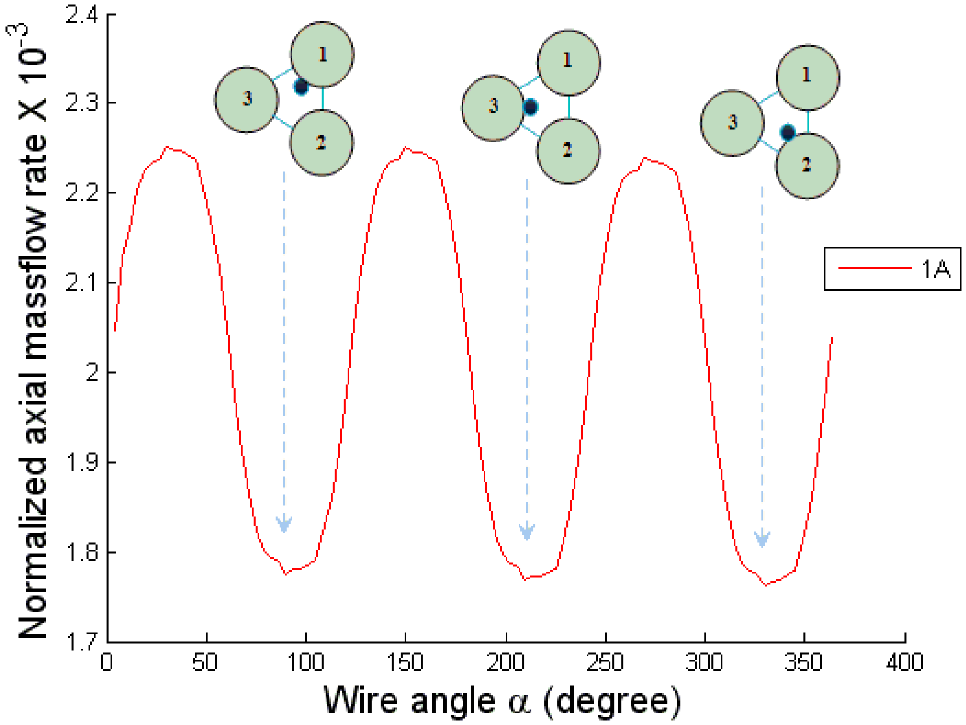

Fig. 4.6b: Variation of area averaged axial mass flow rate in subchannel 1A with increase in wire angle.

The mass flow rate is the maximum when all the three wires that could pass through the subchannel are fully outside the subchannel (at wire angles 30°, 150° and 270°). The mass flow rate is the minimum when a wire is completely inside the subchannel (at wire angles 90°, 210° and 330°). All the three minimum flow rates are identical in magnitude irrespective of which spacer wire is present inside the subchannel. Further, there is a periodicity over 1/3rd pitch. These observations conclude that in a central subchannel, the flow oscillations are predominantly due to passage of wire through that subchannel (local phenomenon). Further, the axial flow oscillations in the neighboring subchannel are identical in amplitude but phase-shifted by 60° (Fig. 4.7).

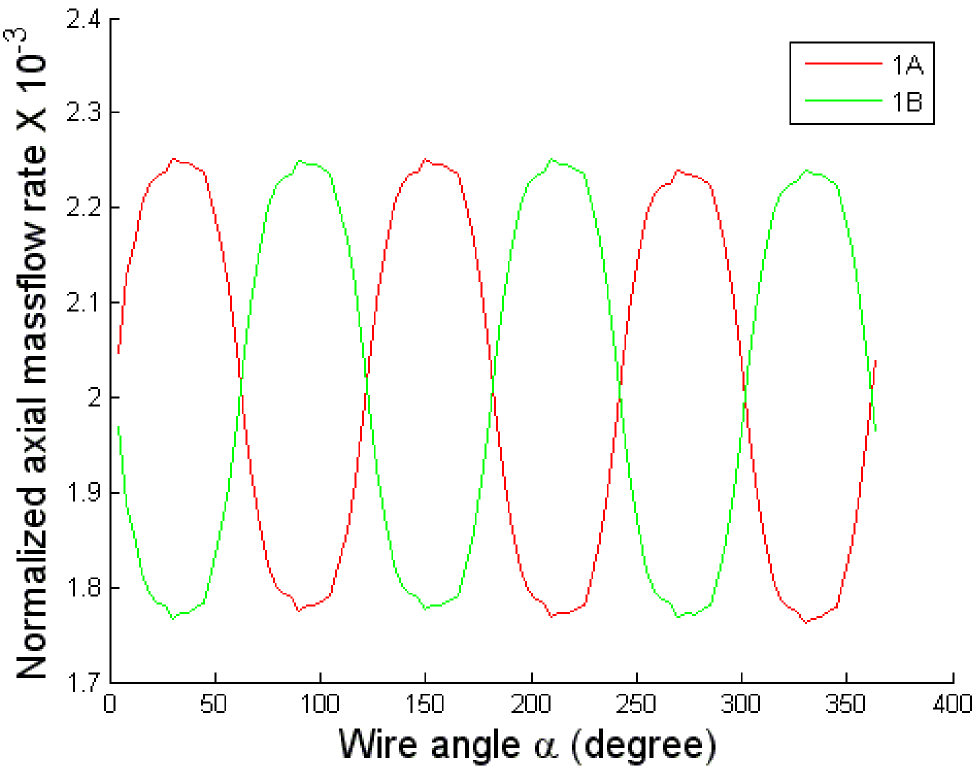

Fig. 4.7: Comparison of normalized axial mass flow rate in two adjacent central subchannels.

4.2.3 Transverse Flow in Central Subchannels

The transverse velocity fields in the central subchannel for four different wire angle positions are depicted in Fig. 4.8. The subchannel under consideration is 1A. At α = 0°, a part of the wire attached to pin 2 is inside the subchannel (Fig. 4.8a). At this position, there is mass influx through face *k* and mass efflux through face *i*. The transverse flux through *j* is nearly zero as it is blocked by the wire. As one moves upward, the angle increases and the wire attached to pin-1 blocks the transverse face *i* (Ref. Fig. 4.8b). During this interval of α = 0 – 60°, the mass efflux through face *i* reduces and attains nearly zero at α = 60°. Simultaneously, the wire of pin-2 moves away, leading to mass efflux from the subchannel through face *j*. Also, mass influx through face *k* reduces. As one moves further up to α = 120° (Fig. 4.8c), the wire attached to pin 1 moves clockwise to block face *k*. This leads to mass influx through face *i* and efflux through face *j*. During α = 120°-180°, the wire withdraws away from face '*k*' resulting in mass efflux through face *k*. The efflux continues till α = 270° and the flow reverses to inflow when the wire attached to pin 2 moves towards face '*k*'. Thus, in one helical pitch length each transverse face encounters two wires. Both the wires move anti-clockwise. But, one wire crosses the face to enter the subchannel while the other wire crosses the face to leave the subchannel. When wire moves away from the subchannel, it leads to mass efflux and when wire moves towards the subchannel, it leads to mass influx. Similar cycle of mass influx and efflux can be observed through other transverse faces *i* and *j* also. The predicted transverse mass flow rates through all the three faces as a function of wire angle are depicted in Fig. 4.9. The algebraic sum of net influx through all the three faces is also depicted in the same figure. In this figure, a positive sign indicates mass influx into the subchannel and negative sign indicates mass efflux.

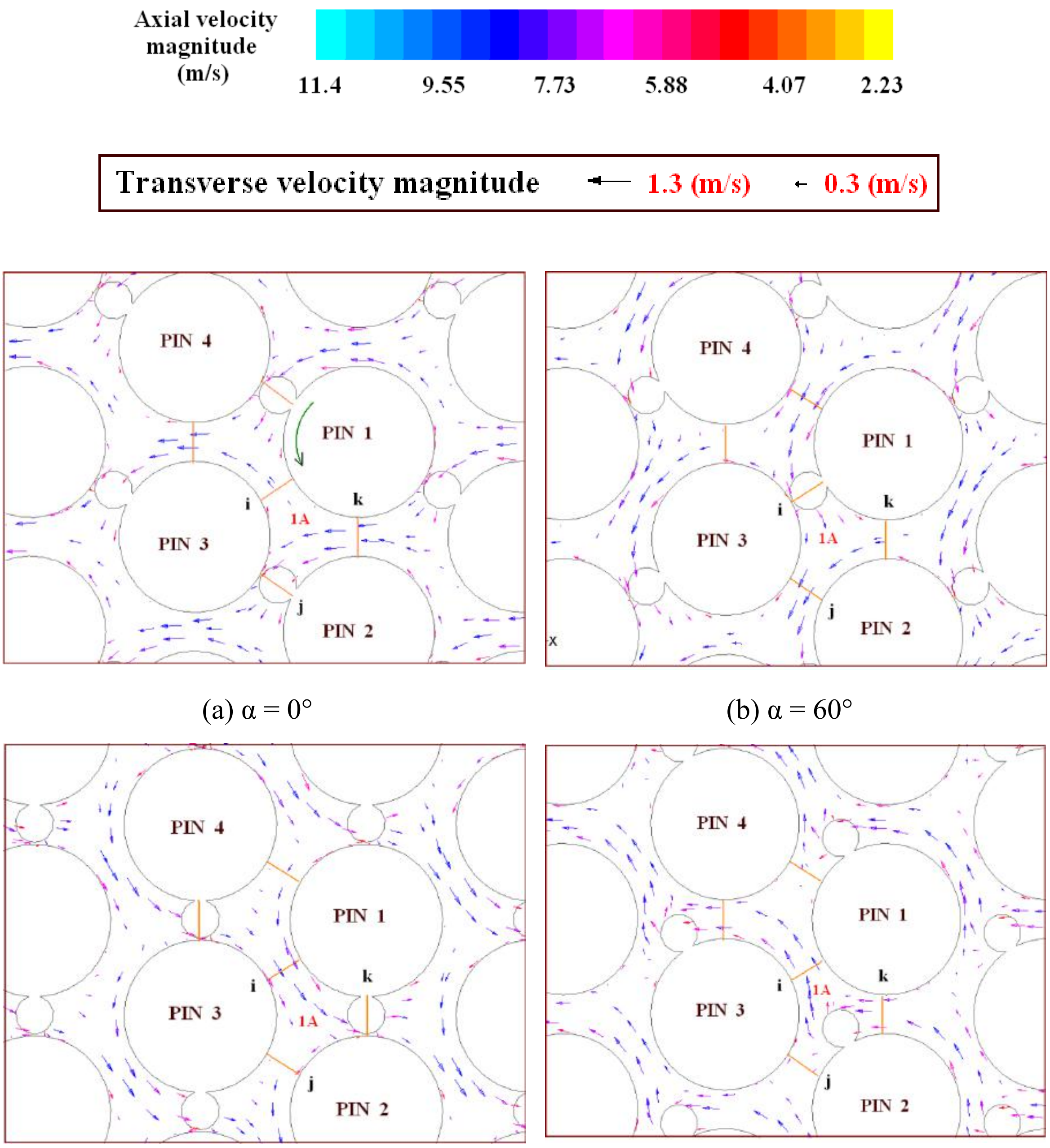

(a) α = 0°

(b) α = 60°

(c) α = 120°

(d) α = 330°

Fig. 4.8: Transverse velocity vector in central subchannels at four different wire angles.

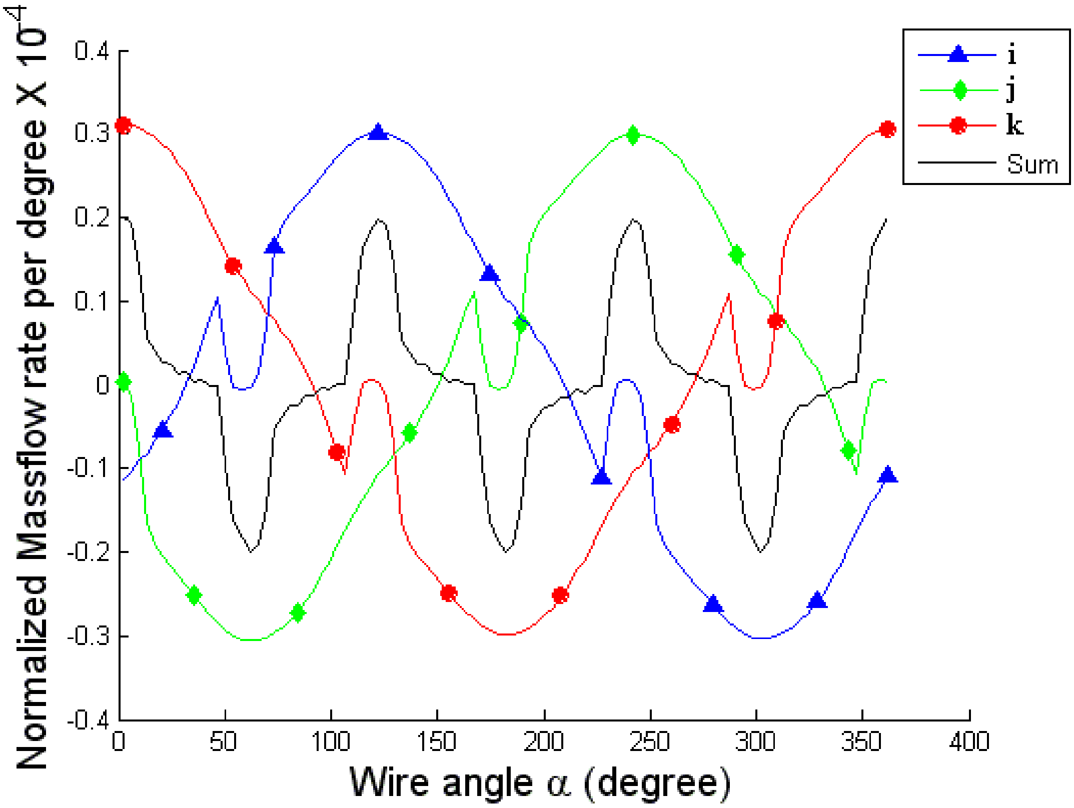

Fig. 4.9:Transverse mass flow rate per degree wire angle in an central subchannel.

For the central subchannel 1A, whenever a wire is about to enter the subchannel (i.e., α = 60°, 180°, and 300°) there is a trough in the cumulative transverse mass flow (cumulative efflux). Similarly, when the wire is about to leave the subchannel (i.e., α = 0°, 120° and 240°) there is a peak in the cumulative transverse mass flow (cumulative inflow). As a consequence of these, there is a periodic change in the axial mass flow rate as expected. When all the wires are fully outside the subchannel (i.e., α = 30°, 150°, 270°), or a wire is fully inside the subchannel (i.e., α = 90°, 210°, 330°) the cumulative transverse mass flow is zero and the axial mass flow is either a maximum or a minimum. It is to be noted that though the flow follows the wire, near the wire the flow is almost zero and it gradually increases and reaches a maximum value at some distance away from the wire. The maximum value reached in the downstream side is higher than that reached in the upstream side. The transverse flow rates through the three faces have identical profiles but with a phase shift of 120°.

4.2.4 Transverse Velocity Correlation for Central Subchannel

As already indicated, for the development of an advanced subchannel model for SFR fuel subassembly, knowledge of transverse flow exchange among the subchannels is important. It is known that the helical wire wrap sweeps the flow along its direction of rotation. If the flow follows the wire exactly, the transverse flow near the wire will be a function of axial velocity and wire helix angle i.e., $\tan^{-1}(\pi^*(D+D_w)/H)$. By splitting the components of velocity vector with respect to wire helix angle and assuming that the flow follows the wire exactly, the non-dimensional transverse velocity is,

$$\frac{V_t}{V_a} = \frac{\pi(D + D_w)}{H} \quad \text{--------------- (Eq.4.1)}$$

Where, V_a is axial velocity of coolant at inlet, V_t is Transverse velocity at a lateral face of the subchannel. From Fig. 4.8, it can be noted that, for every pitch, two wires pass in opposite directions through an inter pin gap (lateral face) in the central subchannel. So a positive and a negative peak of equal magnitude are expected in the transverse flow profile predicted in the lateral face of central subchannel. From the study it was found that, between the peaks the transverse flow follows a cosine profile. This is the motivation to use the cosine profile with velocity ratio predicted by helix angle as its amplitude. For the present condition, the value of (V_t/V_a) works out to be 0.13. But the maximum non-dimensional transverse velocity predicted by the CFD code is about 1.5 times this value (~0.2). This could be attributed to the influence of other wires entering the subchannel. So, it was found that a factor has to be multiplied with the profile to properly fit with the CFD results. For the 217 pin bundle case with reactor dimensions, this multiplication factor (MF) was, thus found to be 1.5. Based on these discussions and the flow characteristics explained in the section 4.2.3, the non-dimensional transverse velocity across the subchannel face can be written in a generalized form as,

$$V_t^* = V_{\max}\cos(\alpha) + N\left(\frac{V_{\max}}{2}\right)\cos(6\alpha) \text{ --------------- (Eq.4.2)}$$

$$\text{Where, } V_{\max} = 1.5\left(\frac{V_t}{V_a}\right) \text{ --------------- (Eq.4.3)}$$

The above expression has two terms. The first term exists throughout the pitch, while the second term comes into picture when wire enters or leaves the subchannel through the corresponding face. For example, when the wire leaves the subchannel 1A through face *k*,

N = 1 for (110° > α > 130°)

Similarly, when the wire enters the subchannel 1A through face *k*,

N = - 1 for (290° > α > 310°)

For other angles N = 0.

Comparison of the CFD results with the proposed function for transverse velocity in the lateral face *k* of central subchannel is shown in Fig. 4.10. Transverses velocity in other two faces (*i* and *j*) can be simply obtained by shifting the curve obtained for face *k* by 120°. Also in the same figure expression of transverse velocity given by Wantland (1974) is plotted. Since he assumes the wire as a vane, maximum cross flow occurs when the face is blocked by the wire. But, the present CFD prediction shows that the maximum flow occurs nearly 60° away from the wire. Further, his model assumes that a wire induces transverse velocity in a face, only when that wire is within ± 60° from the face. And the transverse velocity in a face is influenced only by the wires passing through that face. These assumptions lead to zero transverse velocity in the face during α = 0° - 60° and α =180° - 240°. But CFD predictions show that the transverse flow is not zero in these regions. Except for these differences, the Wantland's function and present results are similar, with inflow when wire enters the subchannel and outflow when the wire leaves the subchannel.

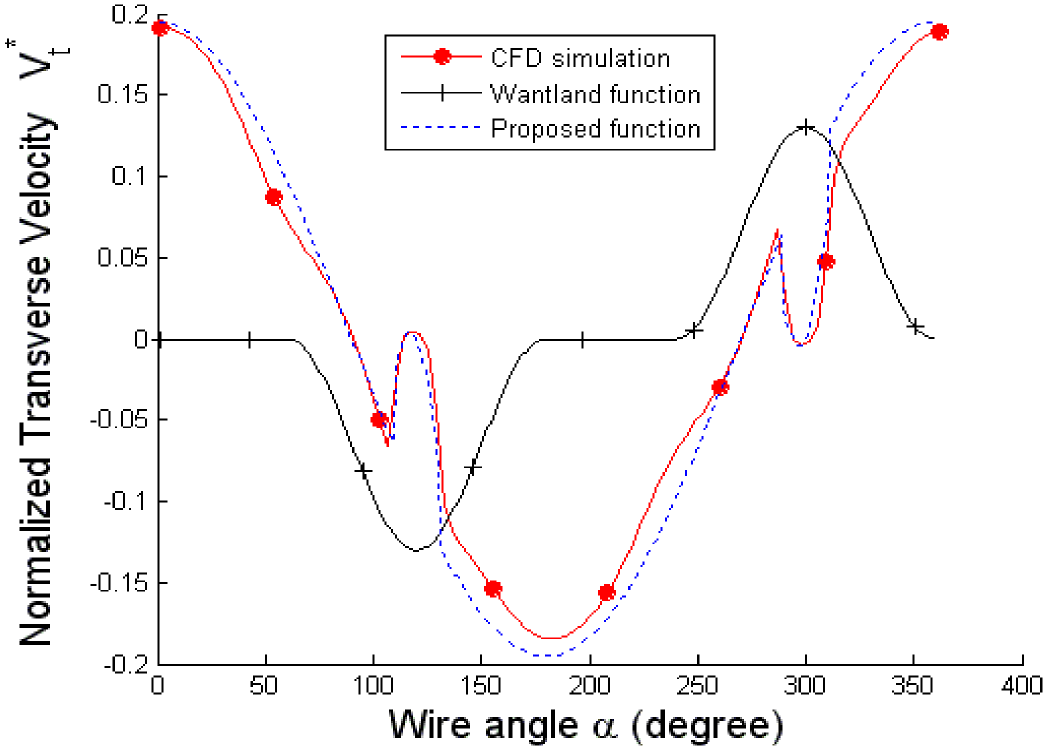

Fig. 4.10: Comparison of transverse velocity estimated by the proposed function with that predicted by CFD simulation for face *k* of central SC in sector I.

Bogolovskaya el al., (2000) reported the measurements of transverse velocity field of liquid metal in a 19 pin wire wrapped bundle. The velocity measurements were carried out using electromagnetic and thermal track techniques. The transverse velocity over 5 axial pitch lengths was measured. The same through the face between the pins 1 and 2 is depicted in Fig. 4.11. The subchannel face 1-2 is equivalent to face *k* in the present study shown in Fig. 4.8. A portion of Fig. 4.11 (z = 20 cm to 34.4 cm), corresponds to $\alpha = 0°$ to 360°, and it compares qualitatively well with the present results (Fig. 4.10). As predicted by the present CFD analysis, the reported experimental results also indicate that the maximum transverse flow does not occur when the wire is present inside the face (A or B in Fig. 4.11), but instead it occurs when wire has passed 60° out of the face.

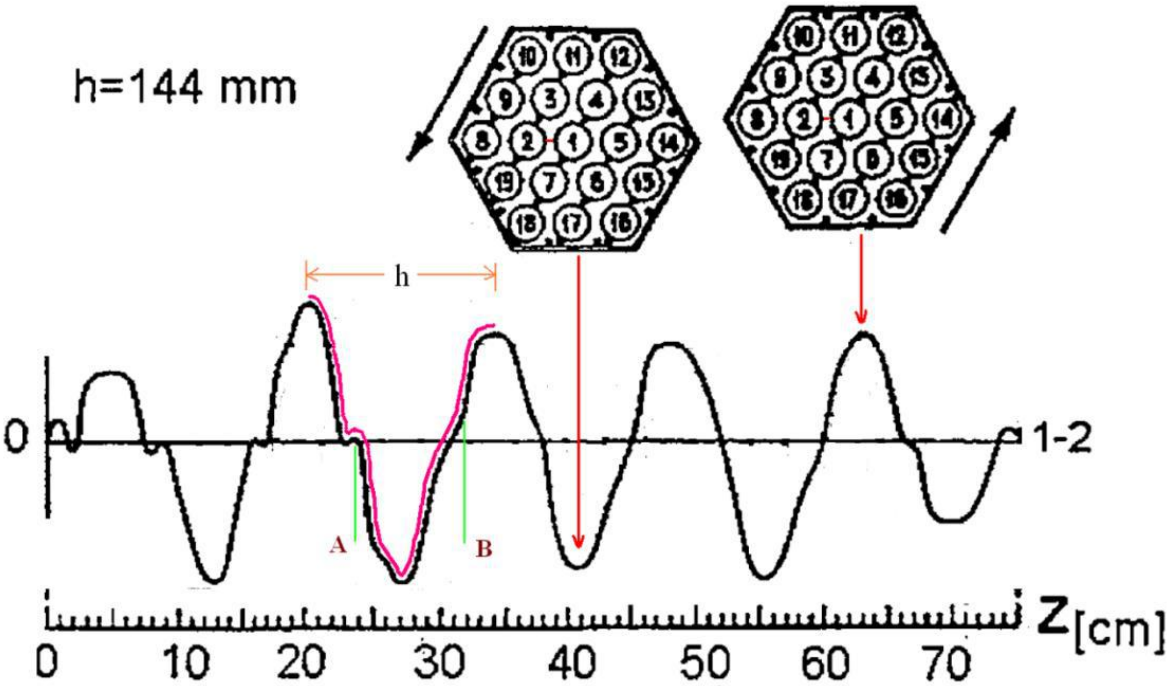

Fig. 4.11: Measured transverse flow through the gap between pins 1 and 2 in a 19 pin fast reactor assembly (Bogolovskaya et al., 2000); at 'A' wire attached to pin 1 passes through face 1-2 and at 'B' wire attached to pin 2 passes though face 1-2.

4.2.5 Central subchannel transverse velocity profile obtained employing periodic boundary condition.

Further studies have been carried out to understand the influence of the actual change in the bundle dimensions on the transverse velocity correlation proposed for the reactor dimensions in the section 4.2.4. In this study periodicity of the bundle has been utilized to greatly reduce the computational effort, where the wire wrapped 217 pin bundle with one helical pitch length is considered and periodic boundary condition is applied to its inlet and outlet (see Fig. 4.12).

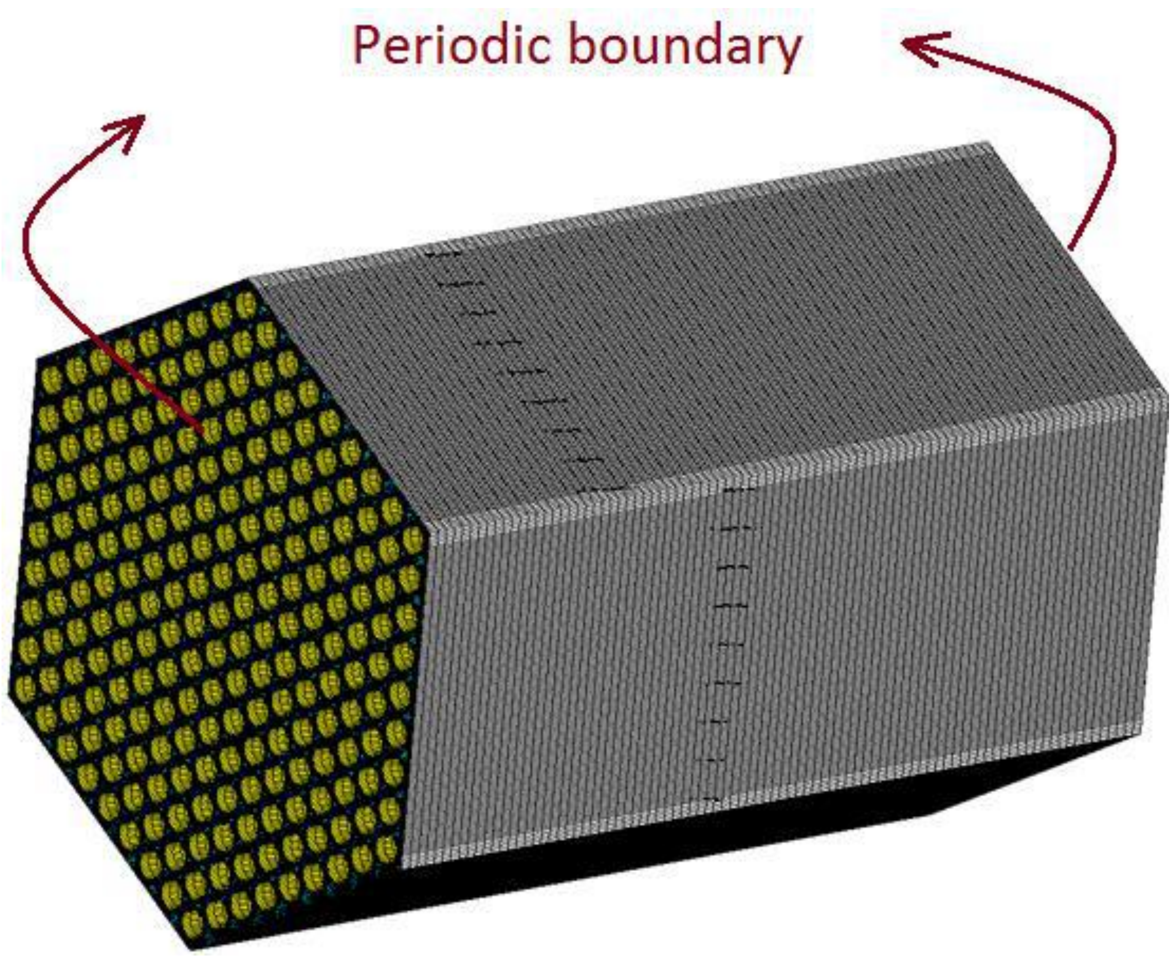

Fig. 4.12: Geometry chosen for simulation with periodic boundary condition.

All the simulations using periodic boundary condition are carried out using commercial code ANSYS-FLUENT. Power law scheme is used to combine the convection and diffusion terms. Except for this all the models and mesh chosen are identical to that used in the full length simulation discussed in Chapter 3. Totally, six different geometries of 217 pin bundle with various pin diameter, wire diameter and wire pitch, have been studied and the details are presented in Table. 4.2. The case B chosen in this study corresponds to actual reactor dimensions. Same bulk mean axial velocity (7.4

m/s) is considered in all the cases and mass flow rate corresponding to this velocity is provided as the periodic condition.

Table 4.2: Comparison of peak normalized transverse velocity obtained from proposed function and periodic model.

Case name	Pin diameter D (mm)	Wire diameter D_w (mm)	Helical Pitch H (mm)	P/D ratio	P/H ratio	H/D_w ratio	Peak normalized transverse velocity	
							Periodic case	Proposed function
A	4.95	1.65	200	1.333	0.0330	121.2	0.154	0.155
B	6.6	1.65	200	1.250	0.0412	121.2	0.188	0.194
C	9.9	1.65	200	1.167	0.0577	121.2	0.228	0.272
D	8	2	200	1.250	0.0500	100	0.228	0.240
E	6.6	1.65	100	1.250	0.0825	60.6	0.345	0.389
F	6.6	1.65	300	1.250	0.0275	181.8	0.1245	0.130

Comparison of the normalized transverse velocity profile obtained for various cases (A-F) with different bundle dimensions is depicted in Fig. 4.13. It can be inferred from this figure that the transverse profiles along the wire angle appear nearly similar in all the cases but they differ only in magnitude of the peak value.

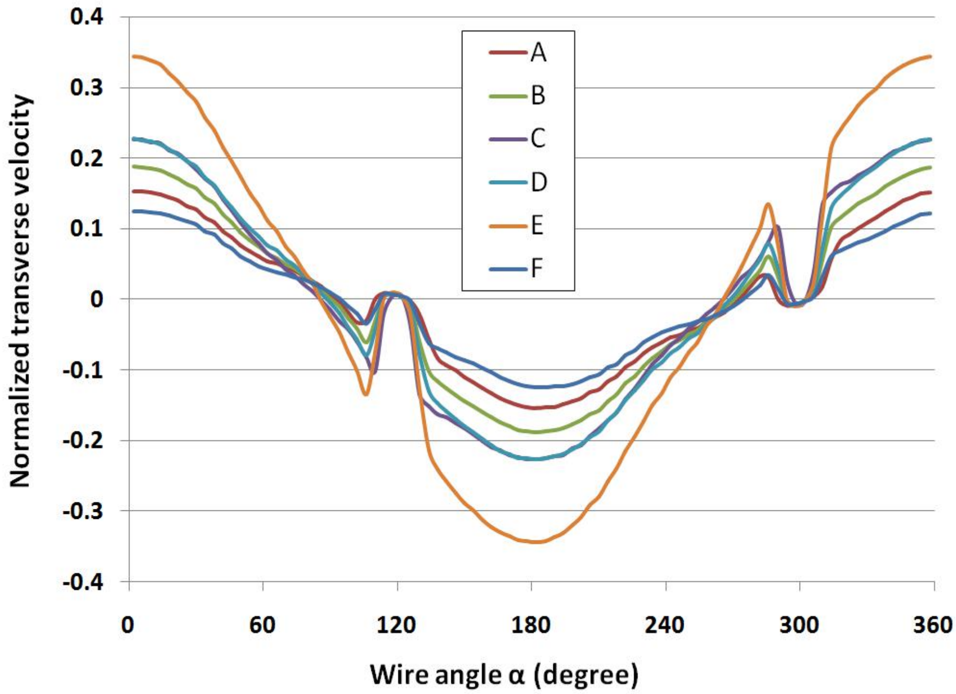

Fig. 4.13: Comparison of normalized transverse velocity profile with different bundle dimensions.

Normalized transverse velocity profile obtained from various cases employing periodic model is compared with those values obtained from proposed function for the corresponding dimensions. These are depicted in Fig. 4.14. In all the cases the profile along the length matches very well with the proposed function. To have a better picture on comparison of the peak magnitude, peak normalized transverse velocity obtained from the proposed function and that obtained from periodic model is presented in Table 4.2. It can be noted that for the actual reactor dimensions (Case B) the difference in the peak normalized transverse velocity between the full length model and periodic model is ~ 3%. In addition, the fully developed fiction of factor (0.02175) for 217 pin bundle reported in the section 4.1.2 compares well (deviation of ~ 2%) with the friction factor (0.0222) obtained from the periodic model. These show that the results obtained from the periodic model compares well with that obtained from the full length model.

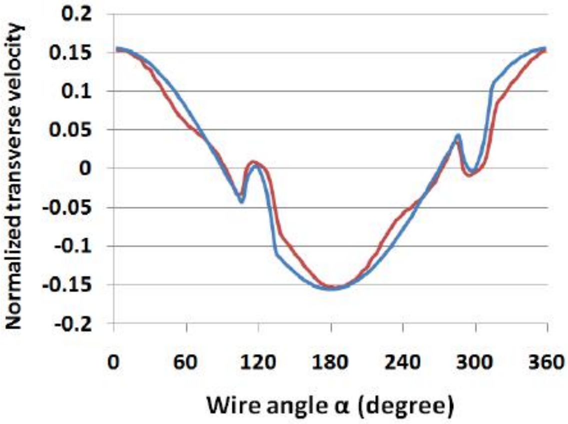

(a) Case A

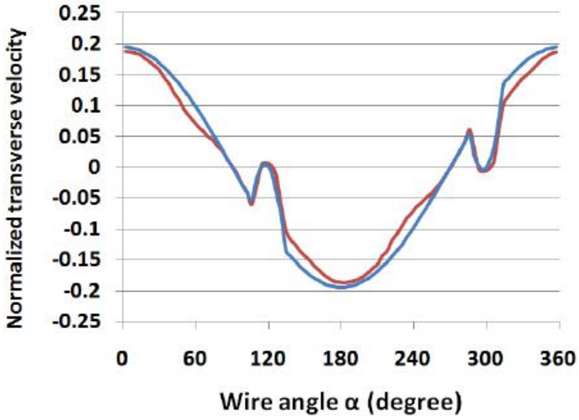

(b) Case B

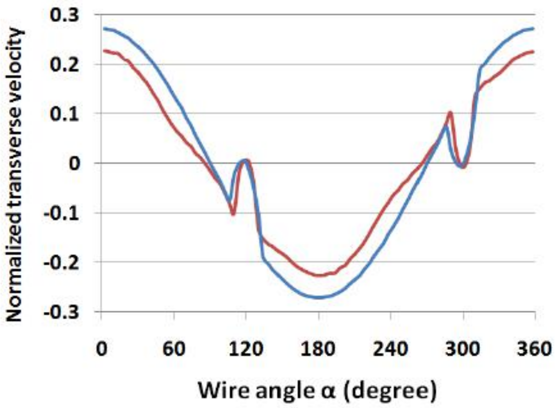

(c) Case C

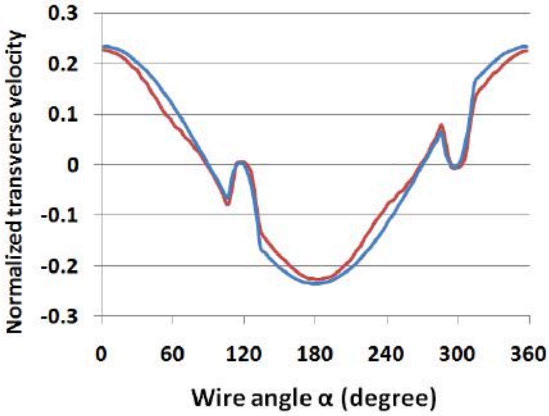

(d) Case D

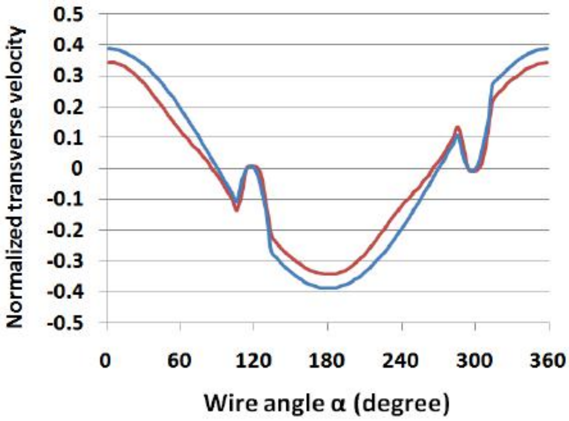

(e) Case E

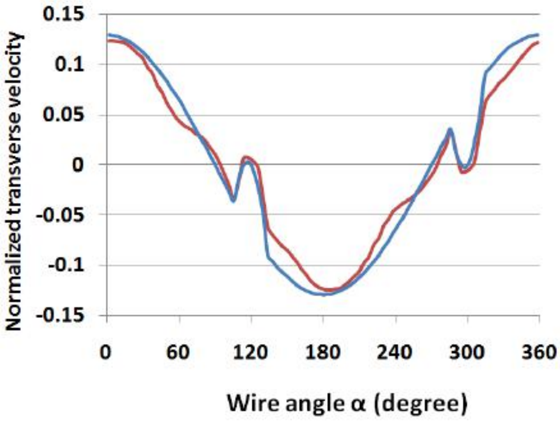

(f) Case F

Periodic case results **Proposed function**

Fig. 4.14: Comparison of the normalized transverse velocity profile obtained from the periodic model and proposed function.

To characterize the influence of the change in the bundle dimensions on the multiplication factor (i.e., factor that is multiplied with the non-dimensional transverse velocity predicted with helix angle to get the actual value) the peak normalized transverse velocity obtained from periodic case and the proposed function is plotted as a function of geometric parameters (Figs. 4.15-4.17). It is to be noted that in the plot for varying P/D ratio, H/D_w ratio is kept fixed at 121.2 and in the plot for different P/H and H/D_w, P/D ratio is kept constant at 1.25. As noted in the previous section, the multiplication factor (MF) in the function proposed for 217 pin bundle is 1.5. It can be seen that though the deviation is very marginal for P/D >1.25, it increases significantly for P/D <1.25. Further, for P/H values lower than 0.06 and H/D_w values greater than 100 the comparison is very good. Hence, for these cases the multiplication factor (MF) remains as 1.5.

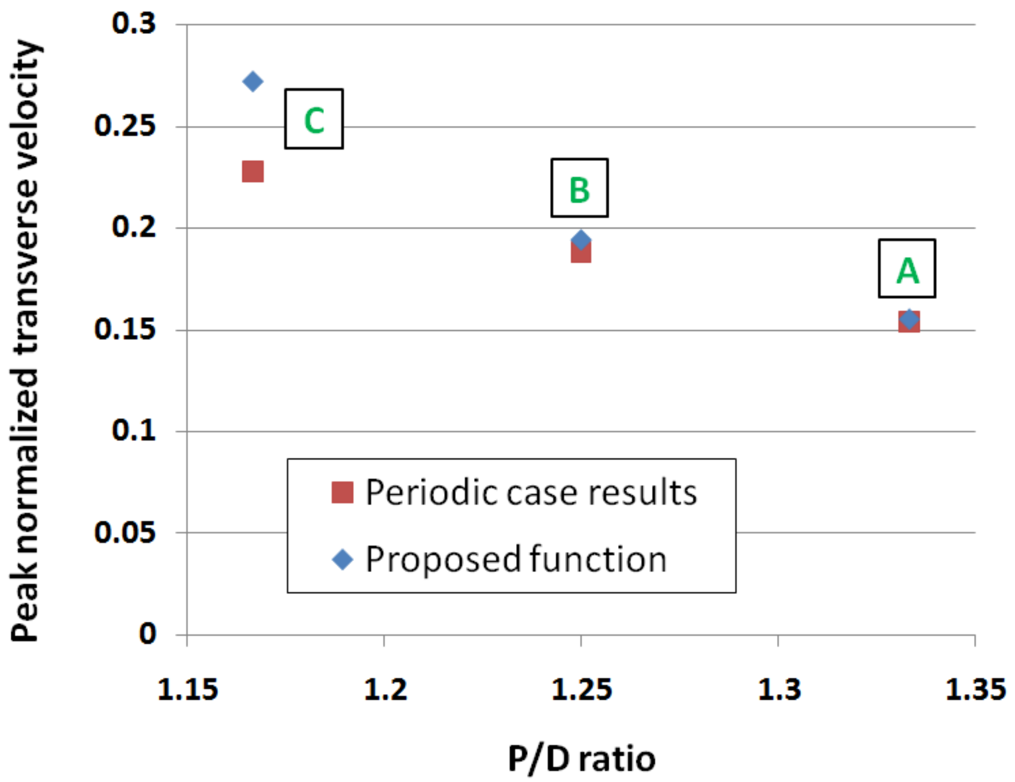

Fig. 4.15: Comparison of the transverse velocity obtained from the periodic model and proposed function for different P/D ratios. (H/Dw = 121.2).

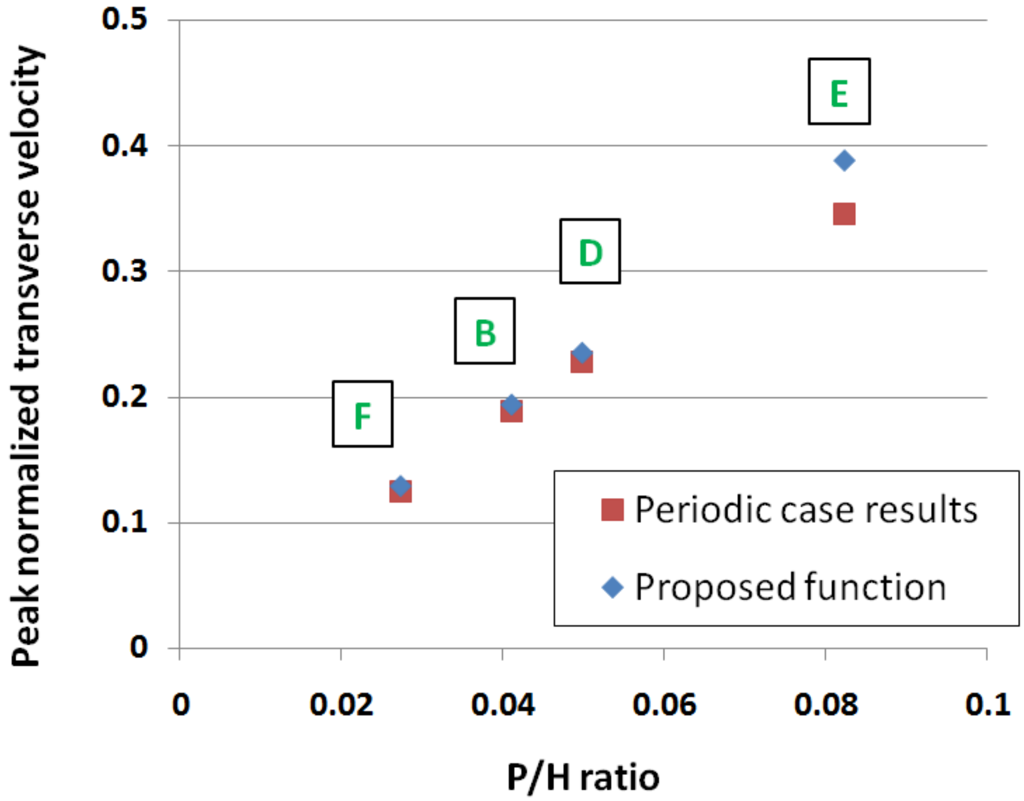

Fig. 4.16: Comparison of the transverse velocity obtained from the periodic model and proposed function for different P/H ratios. (P/D = 1.25).

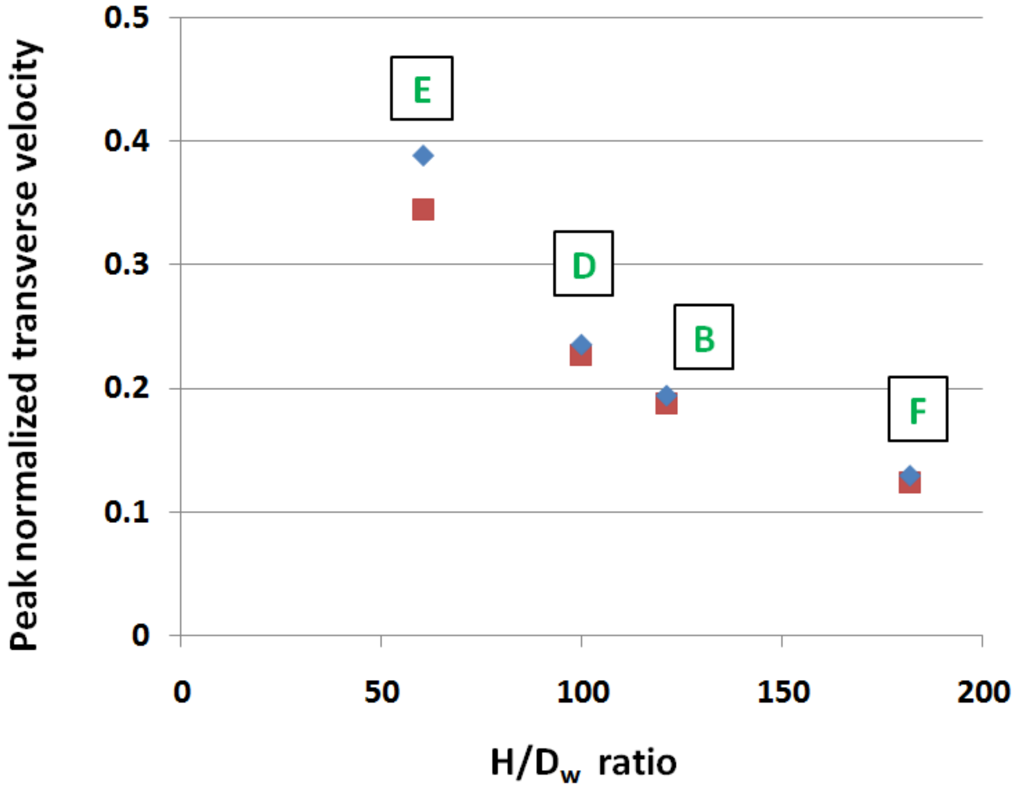

Fig. 4.17: Comparison of the transverse velocity obtained from the periodic model and proposed function for different H/D_w ratios. (P/D = 1.25).

Further, additional cases were studied with lower number of pins (7, 19 and 37) with reactor dimensions (D = 6.6 mm, D_w =1.65 mm H = 200) to identify the influence of multiplication factor (MF) on the number of pins in the bundle. The results obtained are depicted in Fig. 4.18. In addition to periodic model results, the multiplication factor obtained from the full length model is also depicted. Further, to have a comparison, results of LES simulation performed by Poineter et al., (2009) on 7 pin bundle and the experimental findings of Patch et al., (1979) performed on 49 pin bundle are depicted in Fig. 4.18.

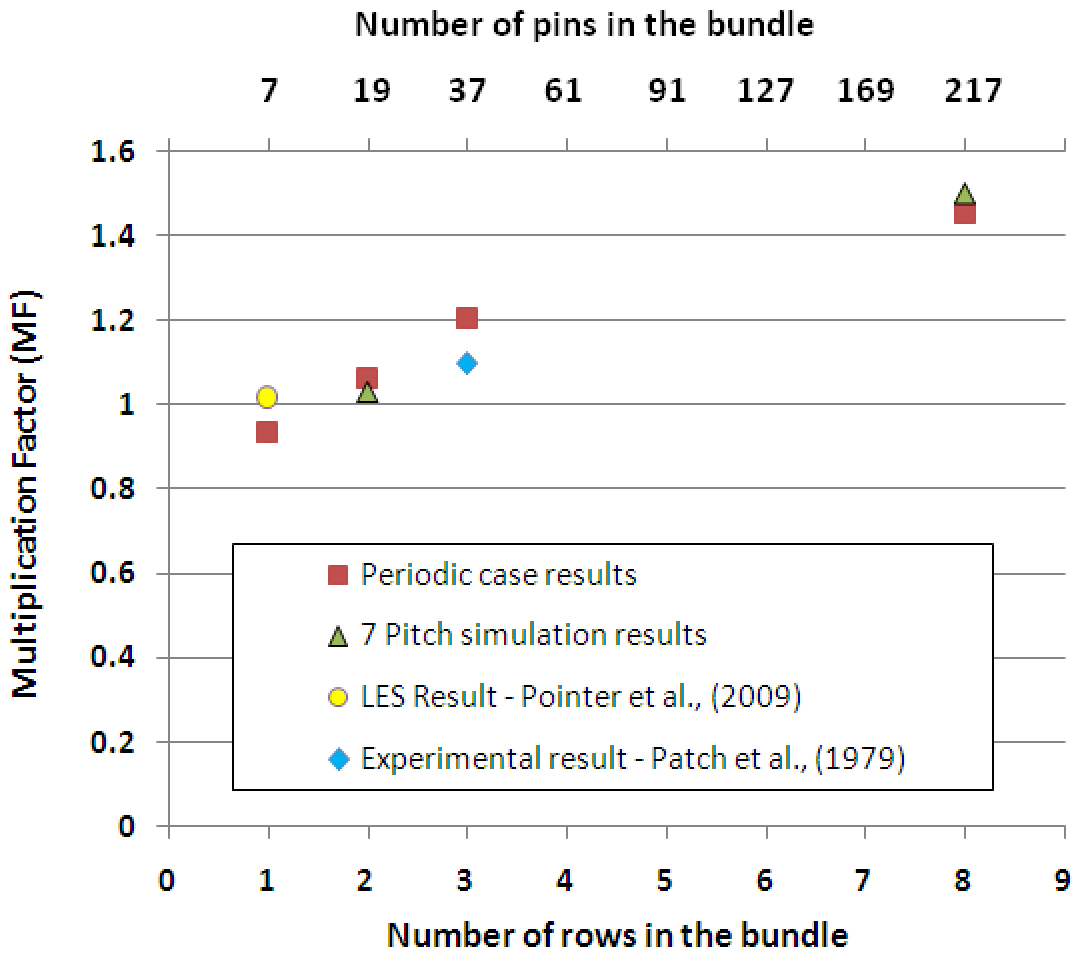

Fig. 4.18: Comparison of the multiplication factor (MF) obtained for pin bundles with different number of rows.

Though the outer geometry taken by Patch et al., (1979) is unsymmetrical, their predictions at central subchannal shall be considered for comparison. It could be seen that the comparison between the experimental, LES data and present simulation is reasonably good. Further, it could be seen that the multiplication factor increases with increase in the number of pins. For 217 pin bundle the value is ~1.5, whereas the value steadily decreases with decrease in number of pins and reaches a value ~ 1 in the case of 7 pin bundle.

4.2.6 Friction factor and Nusselt number obtained employing periodic boundary condition.

Friction factor and the Nusslet number obtained for the various cases studied using periodic model are depicted in Table 4.3. As noted earlier, the friction factor predicted with periodic model (case B in Table 4.3) and the full length model (Table 4.1) compares well with a deviation of ~2%. But the Nusselt number predicted in periodic model is lower than that predicted by the full length model. This is because the Nusselt number is still under developed at the outlet of non periodic case. To highlight similar finding, Govindha Rasu et al., (2013), reported that the flow is developed within an axial length of ~125 hydraulic diameters, but temperature development is achieved only when pin diameter is small or the number of pins are less. They also noted that for bundles with large number of pins, temperature development is not achieved, even after a length of 1000 hydraulic diameters. In the full length model the hydraulic diameter and total length are ~ 4 mm and 1400 mm. But as per Govindha Rasu et al., (2013), more than 4000 mm is required for the Nusselt number to get fully developed. This shows that the results predicted in the periodic case is the fully developed Nusselt number.

Table 4.3: Comparison of Friction factor and Nusselt number among pin bundle with different dimensions.

Case name	Reynolds Number	Friction factor	Peclet number	Nusselt number
A	81046	0.0221	410	4.15
B	87430	0.0222	449	4.20
C	100719	0.0229	509	4.15
D	106865	0.0231	541	5.55
E	88606	0.0332	448	6.46
F	88875	0.0205	450	3.13

4.2.7 Axial flow oscillations in peripheral subchannels

Axial velocity oscillations in various subchannels in sector I, located from center to periphery are shown in Fig. 4.19a for 7 pitch length. Figure 4.19b is an expanded view of Fig. 4.19a for one pitch length. As mentioned earlier, there exists an alternate transverse inflow into the peripheral subchannel from the center of subassembly for one half of pitch and outflow from peripheral subchannel for next half of pitch (This is further elaborated in the next section). This causes continuous increase in axial flow during α = 0° - 180° and continuous decrease in axial flow during α = 180° - 360° within peripheral subchannels located in the sector I. Subchannels located closer to the periphery are more influenced by this effect. The amplitude of flow oscillation also increases while moving towards the periphery. In a typical peripheral subchannel 174A there is mass flow oscillation to the extent of 50% and the axial velocity oscillation of 38%. There are two peaks in the axial velocity oscillation of 174A. The peak occurring at α ~ 180° (Fig 4.19b) is due to the global phenomenon and the trough at α = 90° is due to the passage of wire inside the subchannel (local phenomenon). Since only one wire enters the subchannel 174A, only one trough exists. Oscillations in peripheral, outer and middle subchannels have a periodicity of one pitch length. The peak axial velocity in all the subchannels in sector I occurs around α ~180°. Further, it is found that consecutive sectors have peak in axial velocity at locations with 60° phase shift from the previous sector.

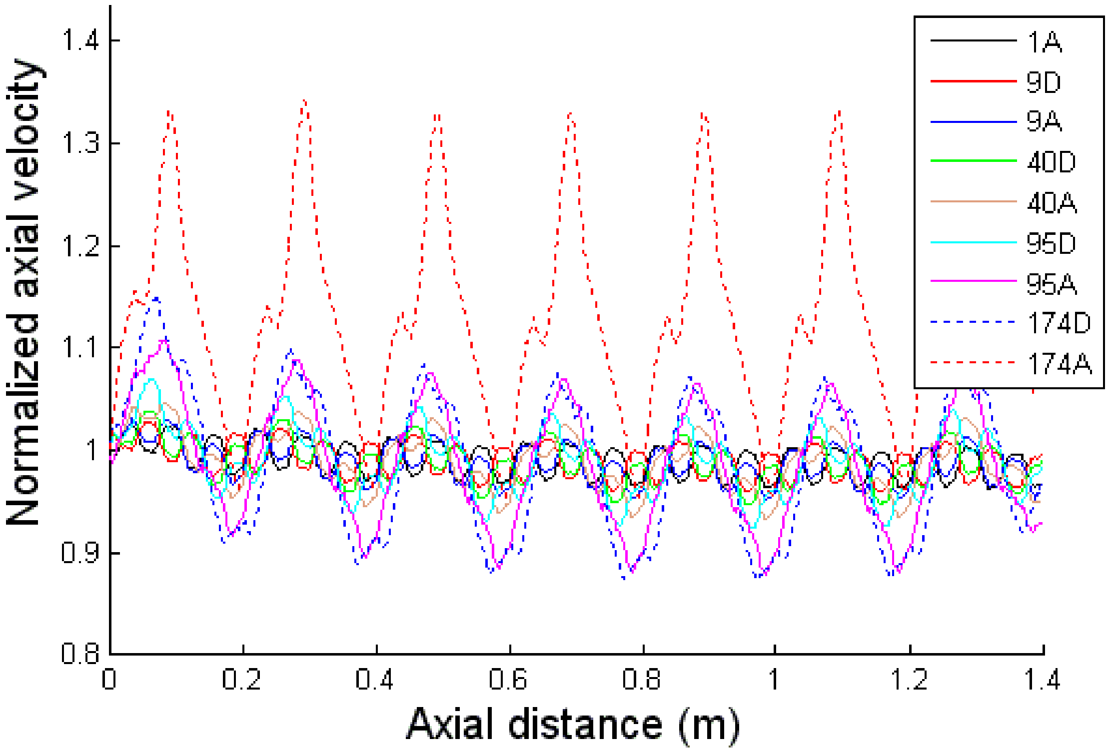

Fig. 4.19a: Normalized axial velocity in various subchannels in sector I, located radially from center to periphery.

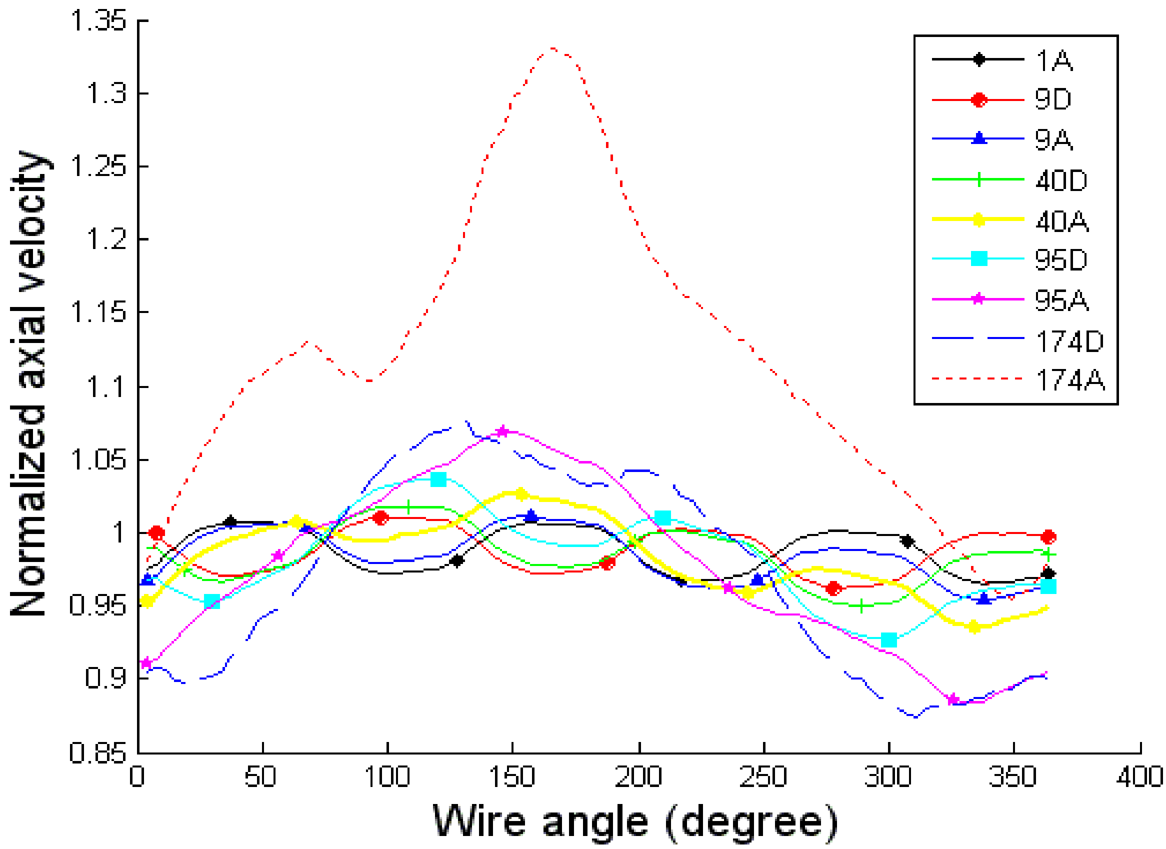

Fig. 4.19b: Expanded view of normalized axial velocity in various subchannels in sector I, for one pitch length.

4.2.8 Transverse Flow in Edge Subchannels

Transverse velocity field around a typical edge subchannel in sector I at various wire orientations is shown in Fig. 4.20. Let us focus our attention on the edge subchannel bounded by pins 174 and 173 with lateral faces *i*, *j* and *k* as marked in Fig. 4.20. For wire angle α = 0° (Fig. 4.20a), the lateral face *k* is blocked by the wire attached to pin 173. Hence, there is nearly no mass transfer through this face. However, there is free passage of transverse flow through the other two faces, with mass influx through face *i* and mass efflux through face *j*. As one moves upwards at α = 90° (Fig. 4.20b) the wire attached to pin 174 moves anticlockwise and offers maximum blockage of face *i*. Similarly, face *j* is blocked by the wire of pin 173.

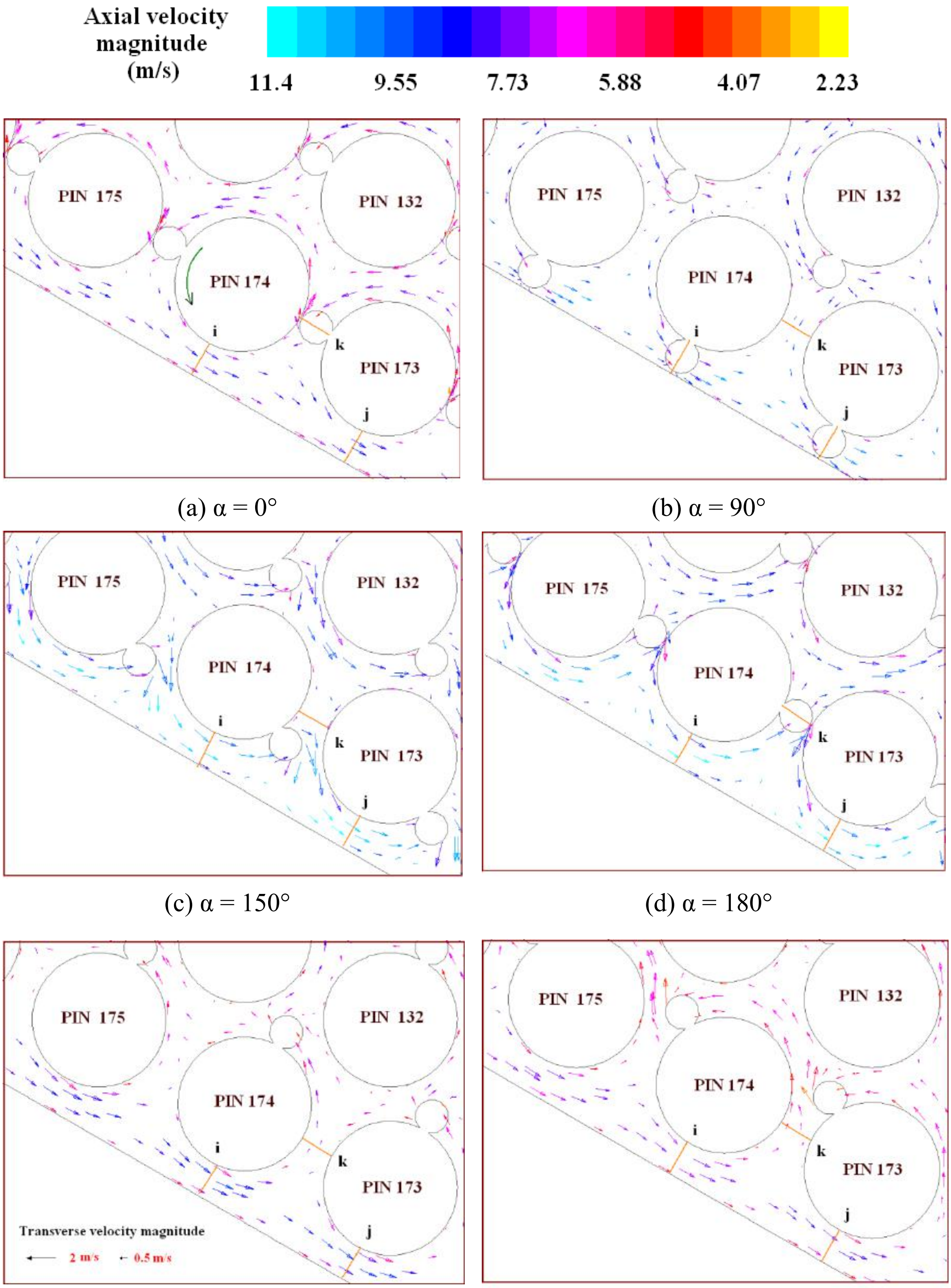

(a) α = 0° (b) α = 90°

(c) α = 150° (d) α = 180°

(e) α = 270° (f) α = 330°

Fig. 4.20: Transverse velocity vector in edge subchannels at six different wire angles.

Hence, at this orientation, there is nearly no influx or efflux through these two faces. However, there is marginal influx through face *k*. At α = 150° (Fig. 4.20c) though the wire attached to pin 174 is about to move out of the subchannel through face *k*, there is an influx through this face. This signifies that this influx is not the flow guided by the wire. Instead, it is from the global phenomenon. Further, at this orientation the mass influx through *i* and mass efflux through *j* are nearly re-established. At α =180° (Fig. 4.20d), transverse flow in face *k* again becomes zero while flow in other two faces remains unaffected. Once the wire attached to pin 174 cross the face *k*, the mass flow becomes efflux through face *k* (α =270°). At 330°, similar to 150° wire angle position, wire attached to pin 173 is about to move into the subchannel through face *k*. But there is an efflux through this face (Fig. 4.20e) without significant changes in the mass flux of faces *i* and *j*.

Transverse mass flow in lateral faces of an edge subchannel is shown in Fig. 4.21. As already explained, a positive flow indicates inflow into the subchannel. It is seen that there exists a unidirectional swirl near the hexcan wall, which locally ceases whenever the faces *i* and *j* are blocked by a wire. The transverse flow magnitude significantly varies in both the faces *i* and *j* throughout the pitch length. But the difference between the inflow through *i* and outflow through *j* is nearly zero throughout the pitch. This denotes that the only source for the axial flow rate oscillation is the influx/efflux through *k*, which faces the center of the subassembly. It is clear that there is a continuous influx through face *k* for wire angle 15° to 165° and a continuous efflux for wire angle 195° to 345°.

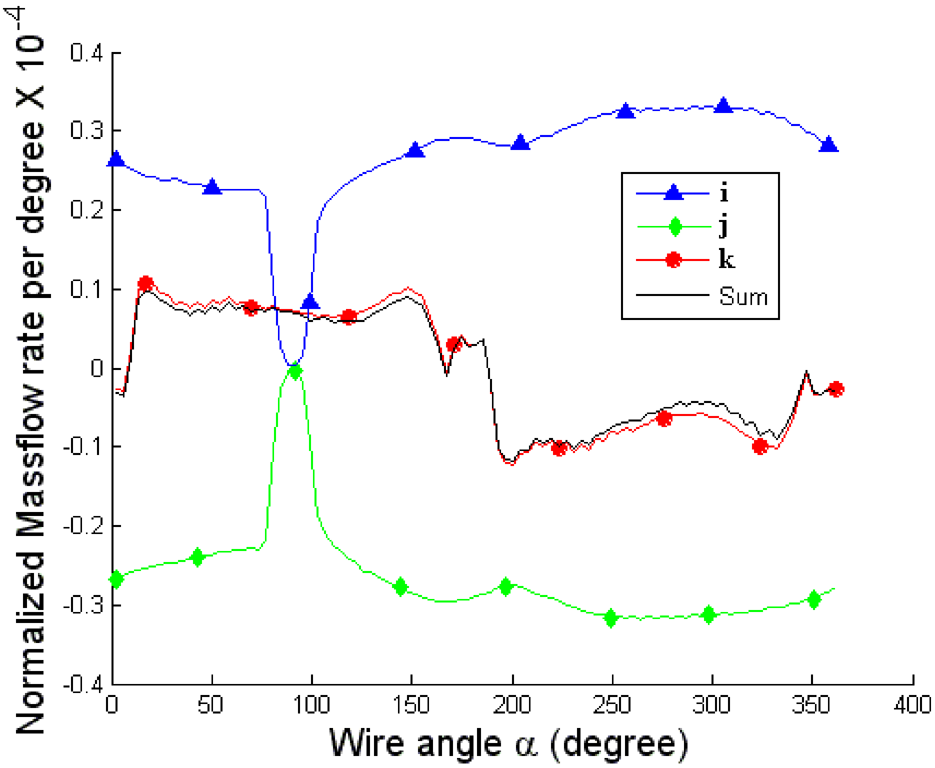

Fig. 4.21: Transverse mass flow rate in an edge subchannel.

4.2.9 Transverse Velocity Correlation for Edge Subchannels

The non-dimensional transverse velocity (which is important for development of subchannel analysis codes) through face '*j*' as function of wire angle is found to be represented by the following correlation,

$$V_t^* = \sum_{i=0}^{3} C_i \alpha^i + 0.135 N \cos(6\alpha) \qquad \text{--------------- (Eq.4.4)}$$

where, C_0 = -0.1528, C_1 = 4.787e-4, C_2 = -4.611e-6 and C_3 = 8.901e-9

When the wire enters the edge subchannel through face *j*

N = - 1 for (75° > α > 105°) and N= 0 otherwise.

The transverse velocity in face *i* is just opposite to that in face *j*. The transverse velocity through face *k* stays almost constant in one half of the pitch, and it gets reversed in the next half. Its magnitude is found to be

$V_t^* = 0.05$ for (15° > α > 165°)

$V_t^* = -0.05$ for (195° >α> 345°)

and it is zero for other values of α.

Comparison of the CFD results with the proposed function for transverse velocity in the lateral face of edge subchannel is shown in Fig. 4.22a. The transverse velocity curves should be phase shifted by 60° for the edge subchannel in the subsequent sectors. Subchannel codes like SUPERENERGY and SUPERENERGY- 2 (Basehore and Todreas, 1980), use the swirl velocity V_θ to model the enhanced mixing induced by the circumferential flow persisting near the hexcan wall. Lorenz and Ginzberg (1976) reported that the average peripheral swirl velocity is nearly 1.2 times that predicted by the helix angle. Chiu et al., (1978a) proposed a generalized correlation for normalized swirl velocity V^*_{Lt}, using local subchannel axial velocity as normalizing parameter. Comparison of the average swirl velocity reported by Lorenz and Ginzberg (1976) and the present result is shown in Fig. 4.22a. In addition, comparison of the correlation proposed by Chiu et al., (1978a) and the present result is shown in the Fig. 4.22b. It can be seen that the earlier models assume a constant velocity while the actual velocity exhibits significant variation along the axial distance. However, the mean, averaged over one pitch distance compare reasonably.

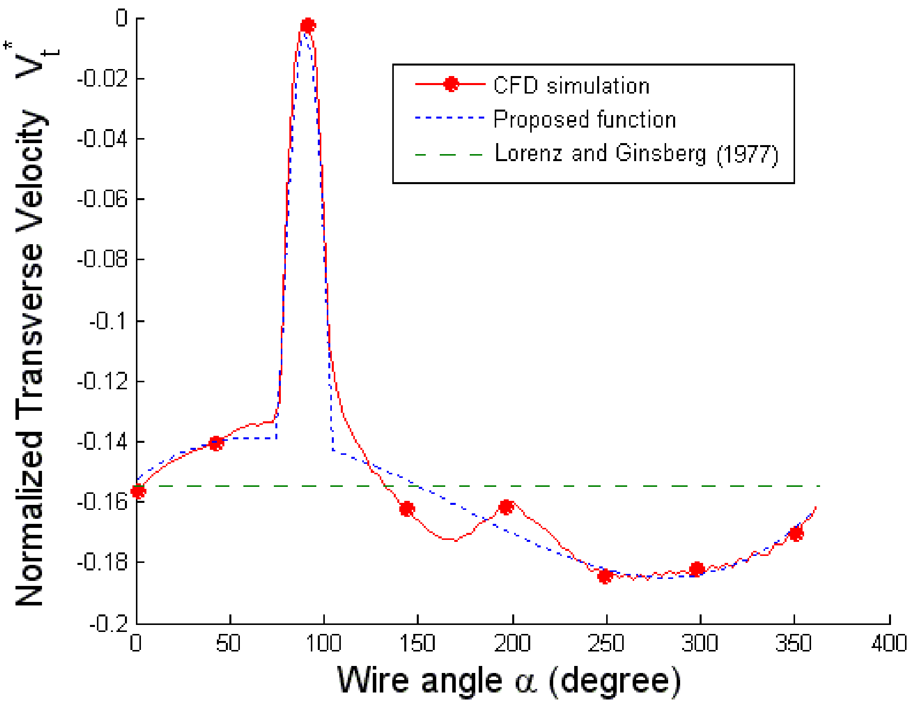

Fig. 4.22a: CFD predicted transverse velocity normalized with bulk average velocity in face *j* of edge SC in sector I. and it's comparison with experimental data of Lorenz and Ginsberg (1977).

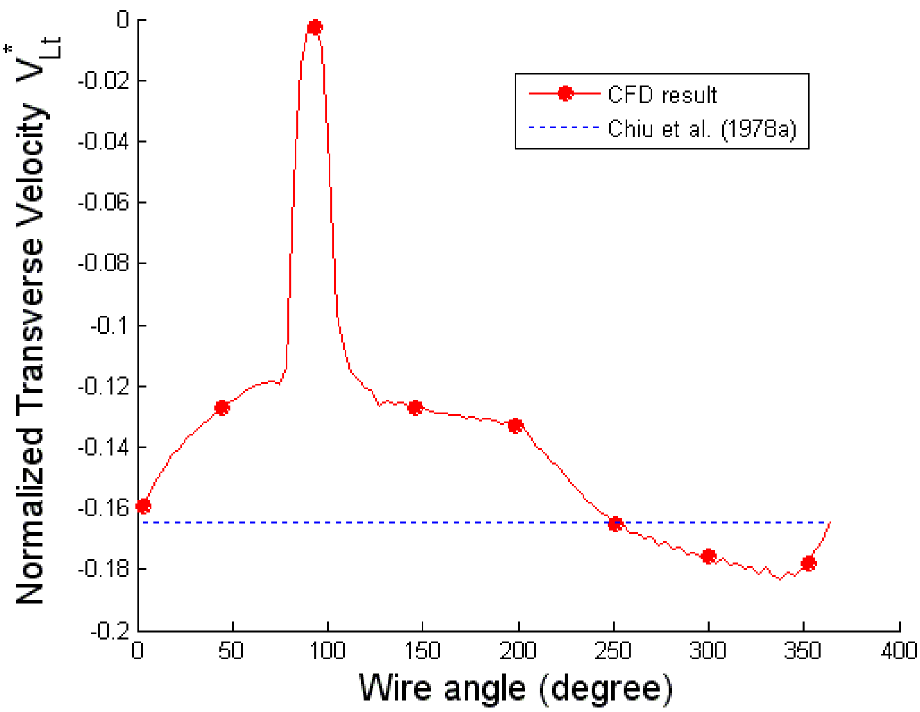

Fig. 4.22b: Comparison of CFD predicted transverse velocity normalized with local axial velocity in face *j* of edge SC in sector I (swirl velocity) with the correlations proposed by Chiu et al., (1978a).

4.2.10 Edge subchannel transverse velocity profile obtained employing periodic boundary condition.

Transverse velocity profile of edge subchannel normalized with bulk average axial velocity (V_t^*) and that normalized with local axial velocity (V_{Lt}^*) for different bundle dimensions (cases A-F, see Table 4.2) are depicted in Figs.4 23a and 4.23b. It could be seen that the profiles largely differ for different bundle dimensions, but the profile obtained for the reactor dimensions (case B) through periodic simulation and that obtained through full length non periodic simulation compare well. Transverse velocity averaged over one helical pitch and normalized with bulk axial velocity (V_t^*) is compared with the value reported by Lorenz and Ginsberg (1976) and the pitch averaged transverse velocity normalized with local axial velocity (V_{Lt}^*) is compared with the Correlation proposed by Chiu et al., (1978a) and the results are depicted in Table 4.4. It could be seen that except for the case E, for all other dimensions, the V_{Lt}^* compares well with deviation < 14 %. Though the maximum deviation in V_t^* is ~16 % for the case C, it compares well in the case B which is with reactor dimensions.

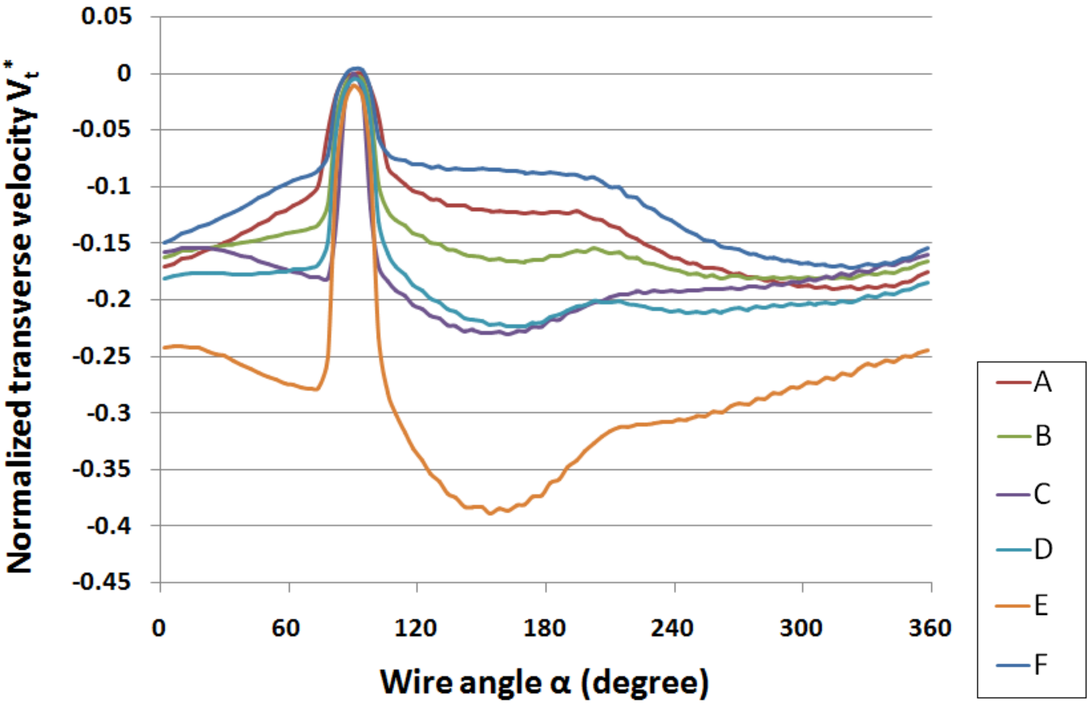

Fig. 4.23a: Comparison of the normalized transverse velocity profile obtained for various cases (A-F) with different bundle dimensions.

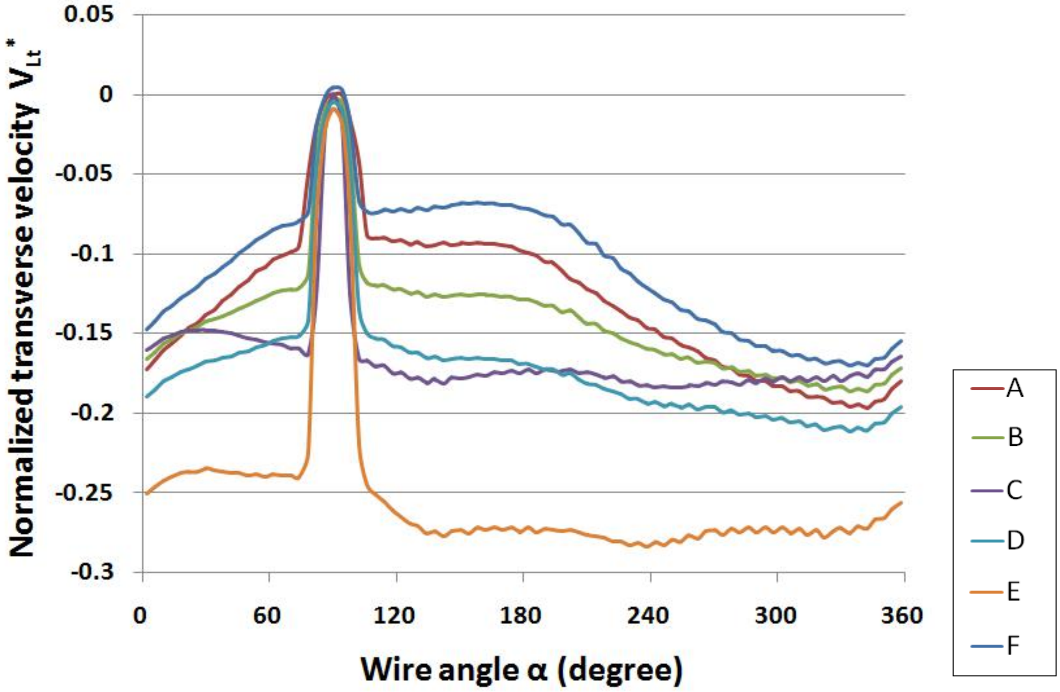

Fig. 4.23b: Comparison of the transverse velocity profile normalized with local axial velocity obtained for various cases (A-F) with different bundle dimensions.

Table 4.4: Comparison of V_t^* and V_{Lt}^* with the published experimental results for different bundle dimensions.

Case name	Pitch averaged transverse velocity in face j of edge SC normalized with bulk axial velocity (Average V_t^*)$^{\#}$	Average swirl velocity reported by Lorenz and Ginzberg (1976)	Pitch averaged transverse velocity in face j of edge SC normalized with local axial velocity (Average V_{Lt}^*)$^{\#}$	Correlation proposed by Chiu et al., (1978a)
A	0.138	0.124	0.129	0.148
B	0.153	0.155	0.142	0.164
C	0.182	0.218	0.165	0.190
D	0.187	0.188	0.172	0.198
E	0.285	0.311	0.252	0.320
F	0.115	0.103	0.107	0.110

- Absolute value

4.2.11 Transverse Flow in Corner Subchannels

Transverse velocity field around a typical corner subchannel located between sector I and sector II is shown in Fig. 4.24. For a corner subchannel there are only two transverse faces and only once in every axial pitch does a wire pass though this subchannel. At α = 0°, the wire is fully outside the corner subchannel and there is an influx through face *i* and efflux through face *j*. At α =90° the face *i* is blocked but still there is efflux through face *j*. This is the cross flow due to flow diversion from subchannel axial flow. Similarly, at α =150°, the face *j* is blocked but there is an influx through face *i*. This gets added to the axial flow within the corner subchannel. At α =300° when the wire is away from the corner subchannel the swirl flow is again reestablished. The transverse flows in lateral faces of a corner subchannel are shown in Fig. 4.25.

Similar to the edge subchannel, unidirectional swirl is observed in corner subchannel. The magnitudes of transverse flow in faces *i* and *j* vary throughout the pitch. The cumulative transverse flow is zero throughout the pitch except when a wire blocks a face.

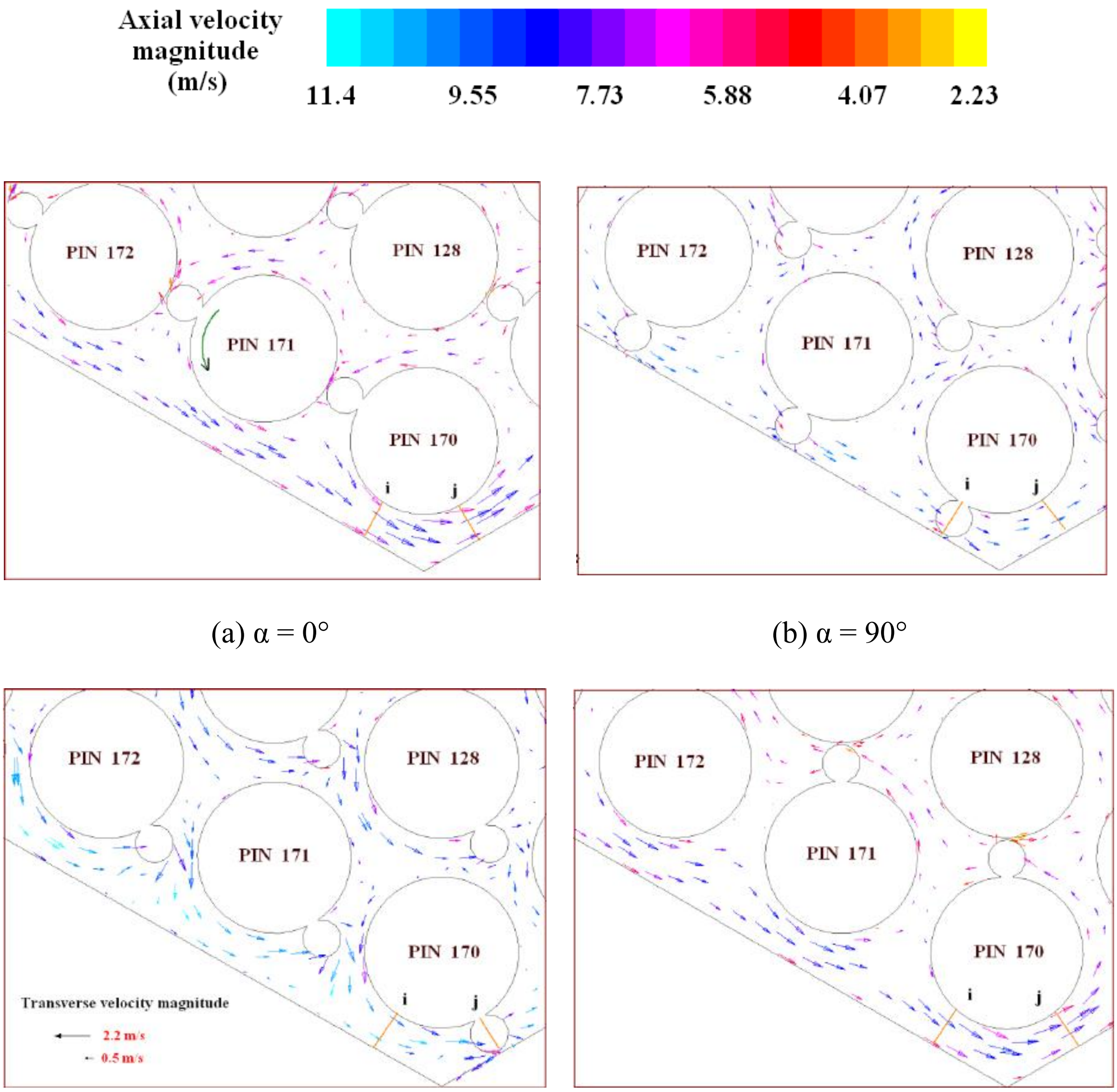

(a) α = 0°

(b) α = 90°

(c) α = 150°

(d) α =300°

Fig. 4.24: Transverse velocity vector in corner subchannels at four different wire angles.

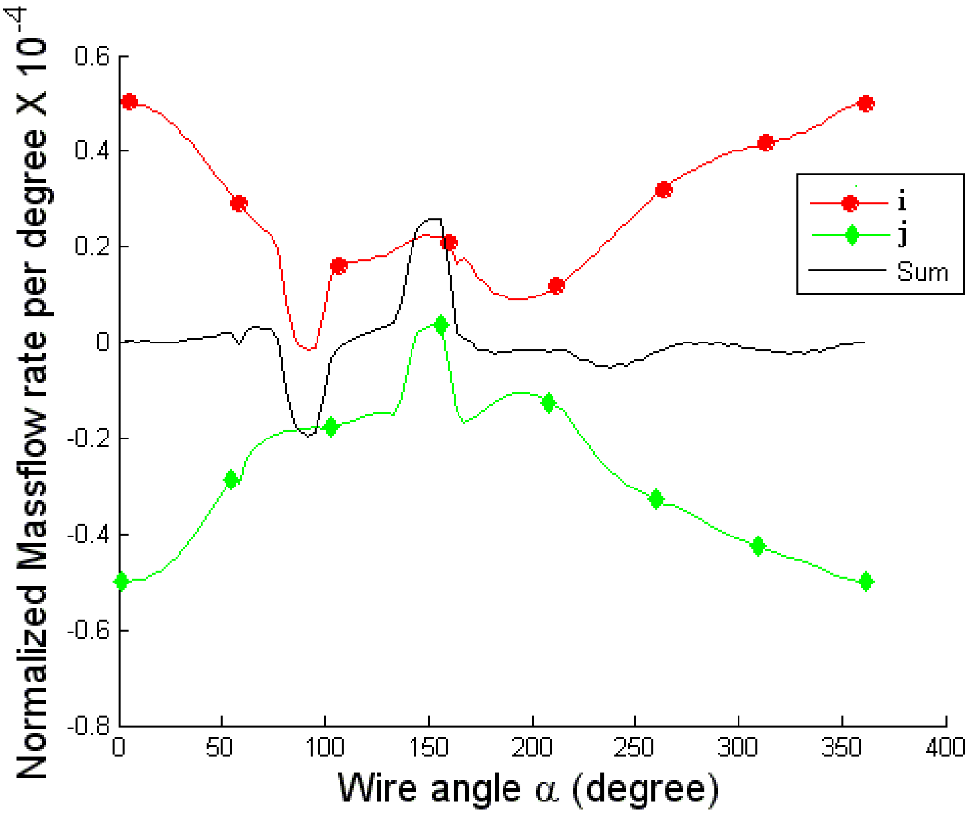

Fig. 4.25: Transverse mass flow rate per degree of wire angle in an corner subchannel.

4.2.12 Transverse Velocity Correlation for Corner Subchannels

The non-dimensional transverse velocity through face '*j*' as function of wire angle is found to be represented by the following equation,

$$V_t^* = \sum_{i=0}^{3} C_i \alpha^i + 0.095 N \cos(6\alpha) \quad \text{--------------- (Eq.4.5)}$$

where, C_0 = -0.3463, C_1 = 4.329e-3, C_2 = -2.0324e-5, C_3 = 2.39719e-8

When wire enters the edge subchannel through face *j*

N = - 1 for (135° > α > 165°)

and otherwise, N= 0.

Transverse velocity in face *i* of the corner subchannel

$$V_t^* = \sum_{i=0}^{3} C_i \alpha^i - 0.095 N \cos(6\alpha) \quad \text{--------------- (Eq.4.5)}$$

When wire enters the edge subchannel through face *i*

N = - 1 for (75° > α > 105°)

and N= 0 otherwise.

Comparison of the CFD results with the proposed function for transverse velocity in the lateral face of corner subchannel is shown in Fig. 4.26. A satisfactory agreement can be seen. The transverse velocity curves should be phase shifted by 60° for the subsequent corner subchannel.

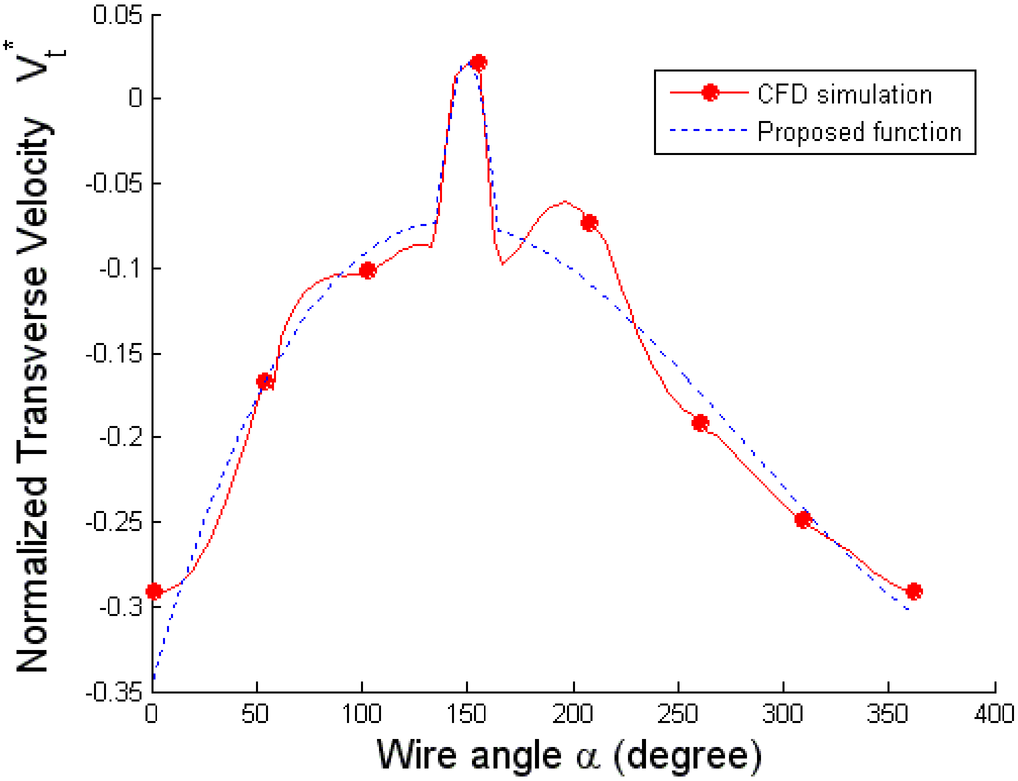

Fig. 4.26: Comparison of transverse velocity estimated by the proposed function with that predicted by CFD simulation for face *j* of corner SC in sector I.

4.2.13 Radial Distribution of axial velocity averaged over one helical pitch

The axial velocity in all the subchannels exhibits periodic spatial oscillations over one pitch length. Hence, to get an understanding of radial variation of stream-wise velocity, one pitch averaged values of normalized axial velocity are plotted in Fig. 4.27a for sector I. It is clear that peripheral subchannel has the highest velocity ~1.12, which is about 12% higher than the mean value. On moving towards the center, there is a small depression in the velocity in interior subchannel adjoining the peripheral subchannel. However, as one moves further inside the subassembly, the velocity recovers to ~0.98. This large difference in velocity is attributed to frictional characteristics of various subchannels which is the minimum for the peripheral subchannel. Further it could be seen that the profile does not change with respect to change in elevation. This shows that the flow field got fully developed by this length.

4.2.14 Radial Distribution of sodium temperature averaged over one helical pitch

To understand the influence of velocity field on the temperature, radial variation of sodium temperature normalized with bulk average temperature and averaged over one pitch length is plotted in Fig. 4.27b along the line connecting subchannels 1A and 174A. It can be seen that the averaged temperature is higher in the central subchannel where the velocity is lower, and the temperature value maintains nearly constant for all the interior subchannels and then sharply falls in the peripheral region. This low value of temperature in the peripheral regions is due to high value of average velocity in this region and a relatively low volumetric heat generation rate (adiabatic wall on one side). Further it is seen that, the averaged temperature in the central region increases with increase in elevation and in the periphery it decreases with increase in elevation. This suggests that thermal development is incomplete.

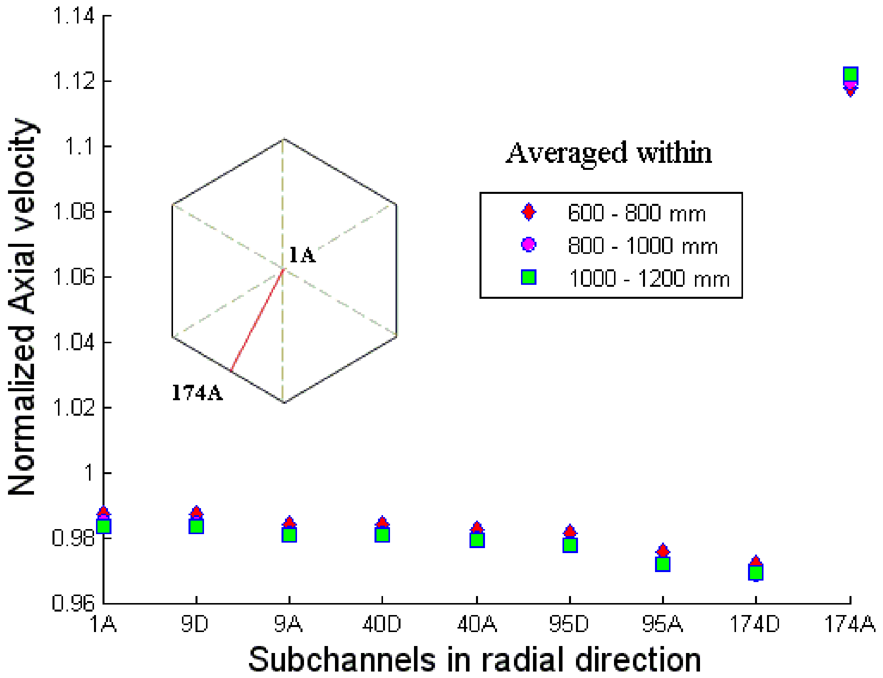

Fig. 4.27a: Average axial velocity in various subchannels in sector I.

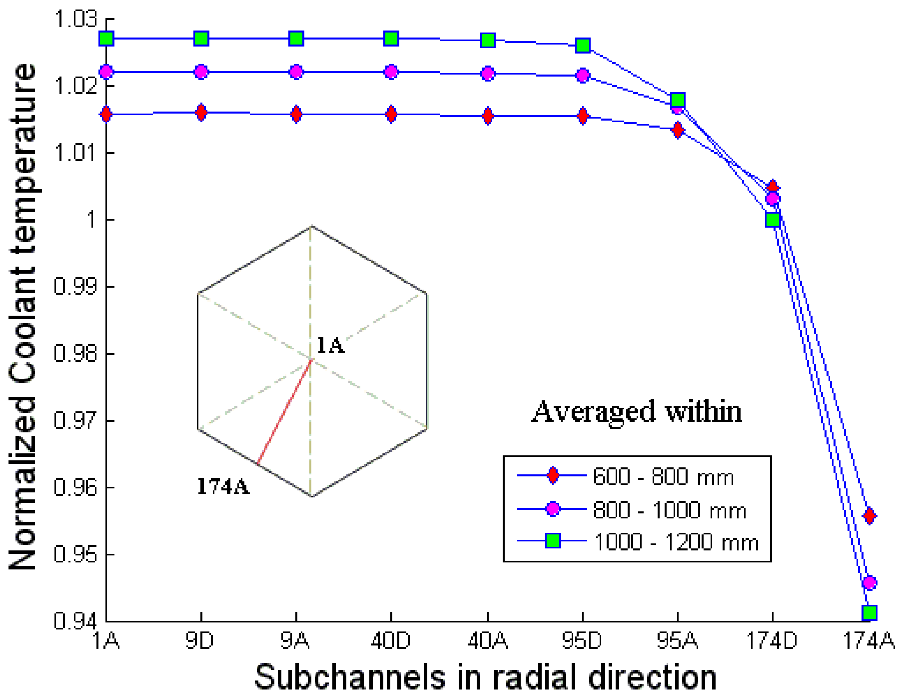

Fig. 4.27b: Average sodium temperature in various subchannels in sector I.

4.2.15 Temperature and axial velocity variations in the inter pin gap

The variation of the temperature and axial velocity field in the inter pin gap when the wire is away from the gap is plotted in the Figs.4.28a and 4.28b. It is observed that as expected the flow field shows a turbulent velocity profile with sharp gradient near the clad walls and a maximum value of 8 m/s at the center. On the other hand, the temperature profile exhibits a gradual variation in the gap, as expected for a liquid metal. The maximum difference in the temperature between the wall and the center is ~ 6 K.

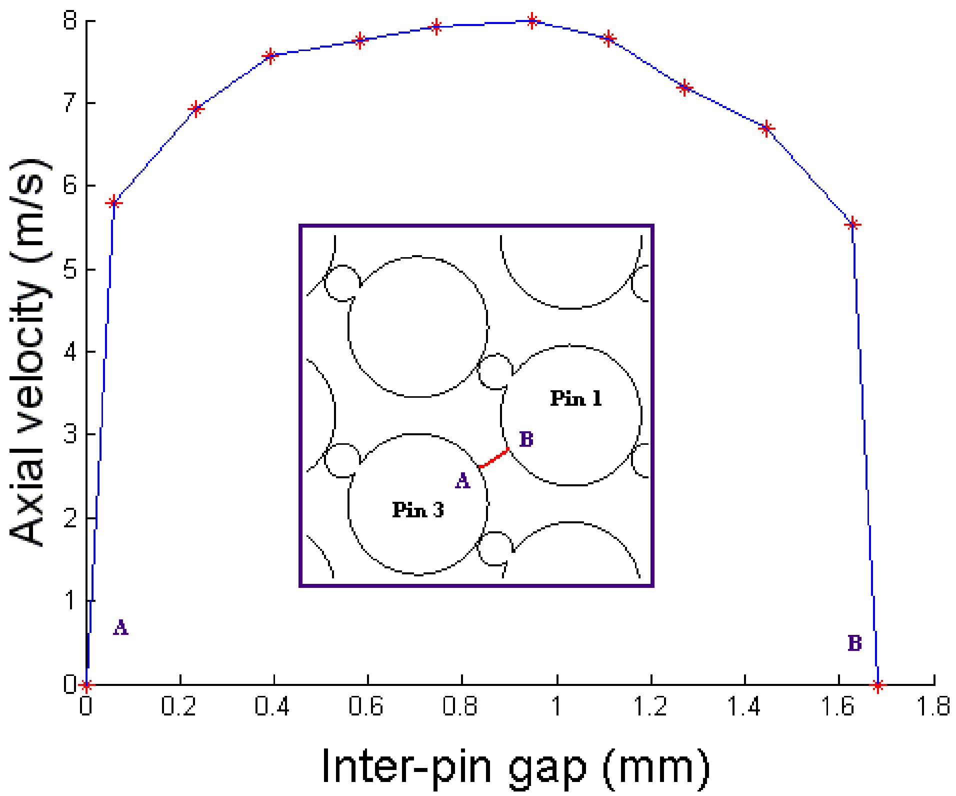

Fig. 4.28a: Velocity profile in the inter pin gap.

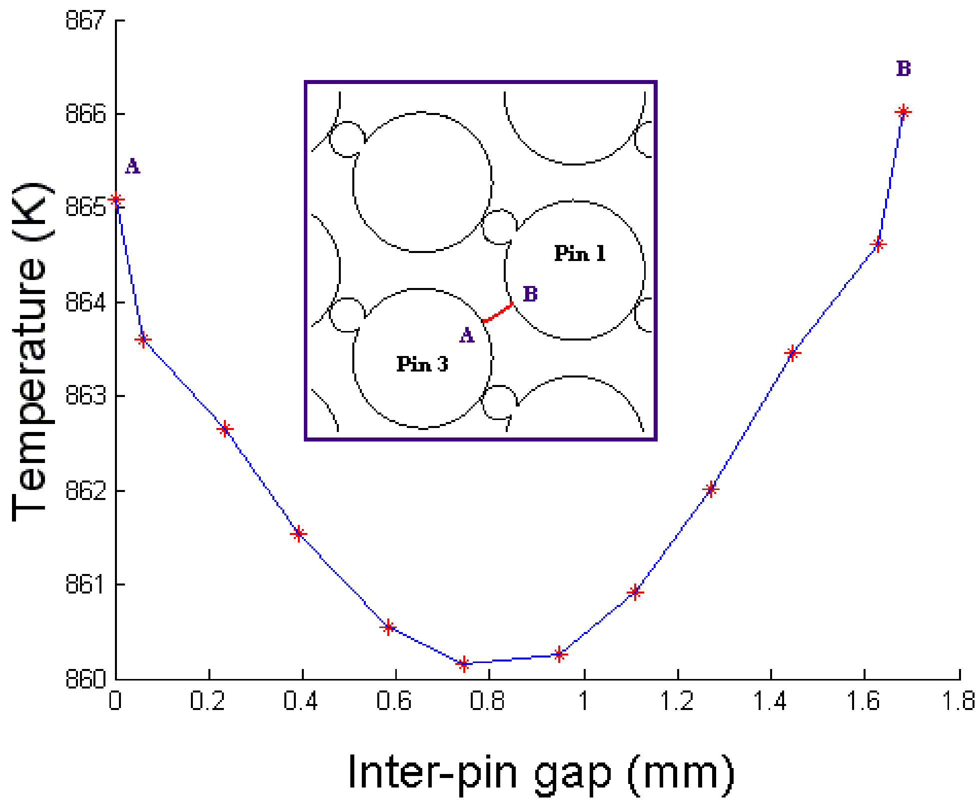

Fig. 4.28b: Temperature profile in the inter pin gap.

4.2.16 Subassembly Heat Transfer Features

In the present study two different heat fluxes are applied on the pin walls. The first one is a traditional cosine heat flux profile occurring in the actual reactor given in Fig. 3.5b. The second one is a constant heat flux throughout the length of the subassembly and in all the pins. In both the cases the total heat supplied is 7.92 MW.

4.2.17 Axial Profile of Clad and Coolant Temperature

The predicted mean coolant temperature and mean clad temperature at any cross section are depicted in Fig. 4.29a for the case of cosine heat flux profile. For the initial 200 mm and final 200 mm, the changes in sodium and clad temperatures are marginal, due to very small value of heat flux in the axial blanket zones. At the beginning of fuel zone, z =200 mm, the temperature difference between the clad and coolant is low and it increases downstream, due to (i) change in heat flux and (ii) continuous development of Nusselt number. The corresponding axial variation of clad temperature in various pins is shown in Fig. 4.30a.

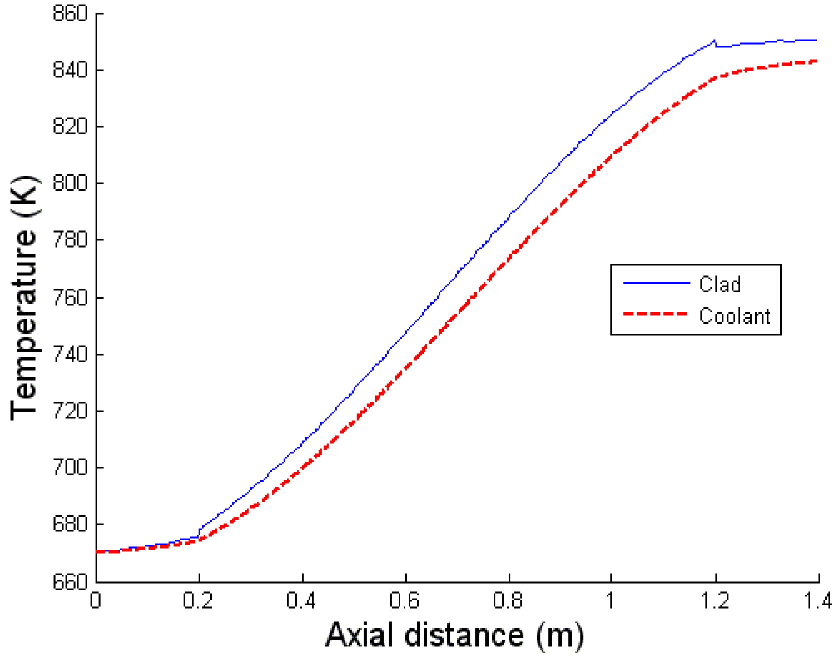

Fig. 4.29a: Mean clad and coolant temperature variations along the axial distance for Cosine power profile.

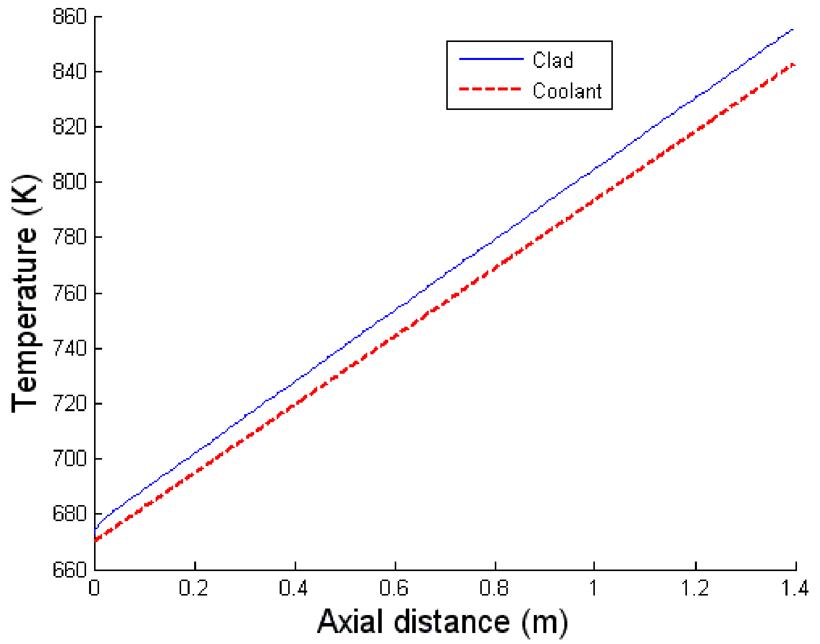

Fig. 4.29b: Mean clad and coolant temperature variations along the axial distance for a uniform power profile.

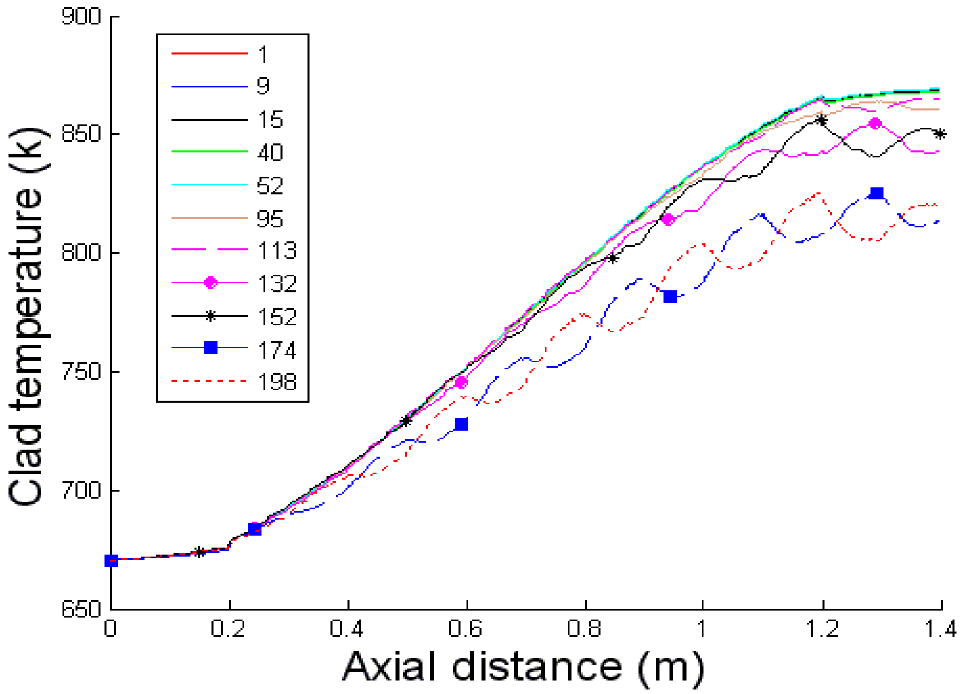

Fig. 4.30a: Clad temperature variation along the axial distance for various pins subjected to a Cosine power profile.

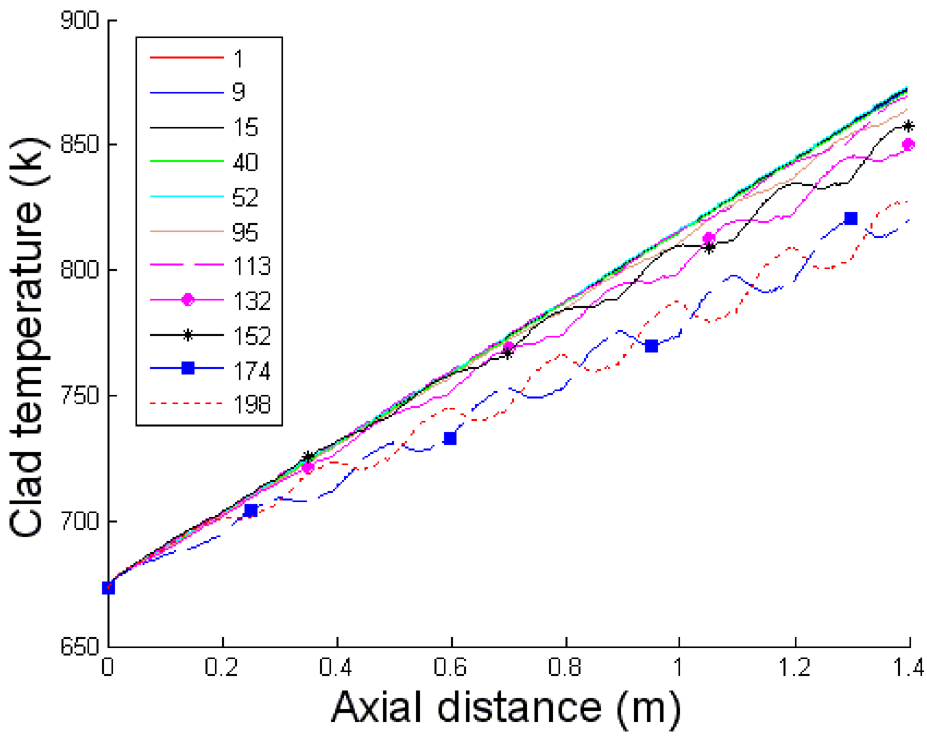

Fig. 4.30b: Clad temperature variation along the axial distance for various pins subjected to a uniform power profile.

It is seen that the pins in the central and middle regions do not exhibit any spatial oscillation in clad temperature (Fig. 4.30a). But, pins in the outer and peripheral regions exhibit prominent oscillations with amplitude increasing in downstream direction. As seen in the transverse flow in the edge subchannel (Fig. 4.21), there is a continuous influx of coolant into the edge subchannel from the core of the subassembly for $\alpha = 15°$- $165°$. The hot sodium coming from the central region flows over the peripheral pins keeping the clad at a comparatively high temperature. Similarly, there is a steady efflux in the edge subchannel for $\alpha = 195°$ to $345°$. As a result of this, cold sodium from the vicinity of hexcan wall flows over the peripheral pins, keeping the clad temperature to be low in these wire orientations. A similar phenomenon influences the subchannel in the outer region. In the case of constant heat flux, there is uniform increase in overall clad and bulk coolant temperature (Ref. Fig. 4.29b), with a monotonic increase in their difference in the downstream direction due to thermal development and the associated reduction in Nusselt number. Further the oscillations in the clad temperature of pins are similar to that observed in the case of cosine heat flux (Ref. Fig. 4.30b).

4.2.18 Circumferential Variation of Clad Temperature

The CFD predicted circumferential variations of clad temperatures in various pins are shown in Fig. 4.31a at the middle of the active zone, z = 700 mm. At this value of z, the wire occupies $\alpha = 180°$. It is found that the pins in the peripheral region have large temperature variations in circumferential direction compared to pins in the interior region. The variation is as high as 35 K for the peripheral pins and it is as small as 10 K for the central pins. The large circumferential variation in peripheral pins is attributed to the fact that they are exposed on one side to neighboring pin with high heat flux and on other side to an adiabatic hexcan. It is seen that side of the pin 174 facing the center ($\theta = 330° – 150°$) of the subassembly has temperature closer to that of the middle region, while the other side facing hexcan ($\theta = 150° – 330°$) has a comparatively lower temperature. A similar trend is seen in pin 198. In Fig. 4.31b, the circumferential variation of clad temperature in pin 174 along seven axial planes is depicted. It is seen that though the profile changes while moving downstream, the position of maximum temperature lies always facing the center. Also, it is found that the same circumferential profile gets repeated after one pitch with an elevated mean temperature, i.e., the profile of pin 174 at 700 mm elevation is similar to that at 900 mm elevation with mean value increased by 35 K. But, for similar wire orientation ($\alpha = 180°$), circumferential temperature variation is higher in 900 mm compared to that in 700 mm elevation. This shows that temperature in the center of subassembly increases with axial length at a higher rate compared to that in the periphery. These temperature features indirectly validates the CFD model.

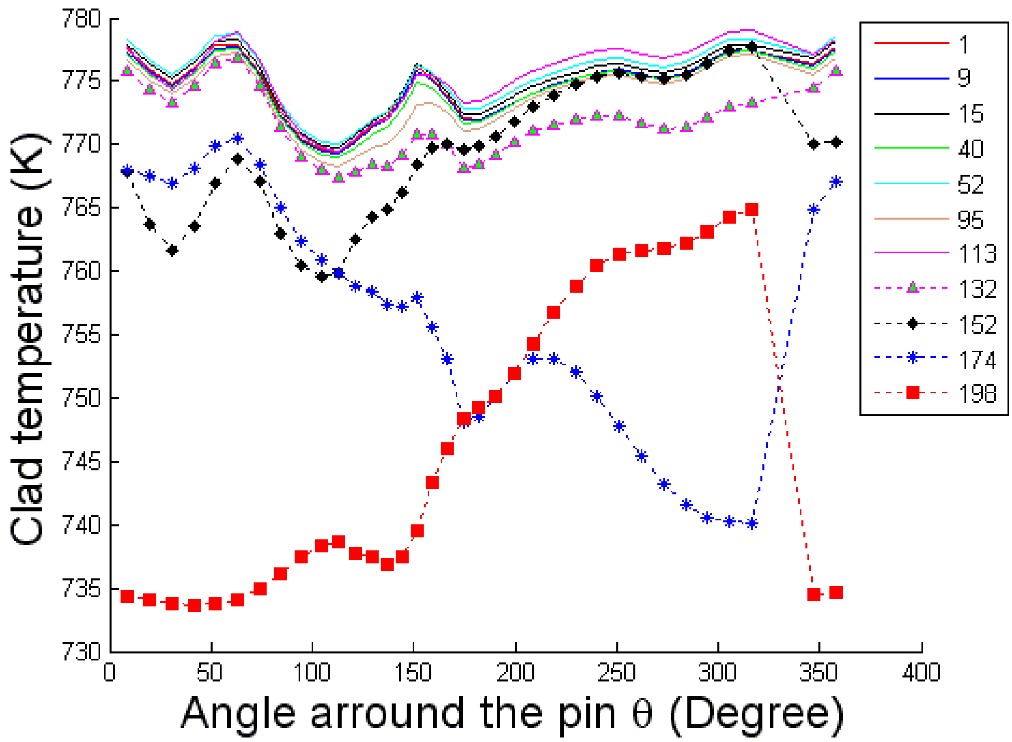

Fig. 4.31a: Circumferential variation of clad temperature at an axial distance 700 mm. (Cosine power profile).

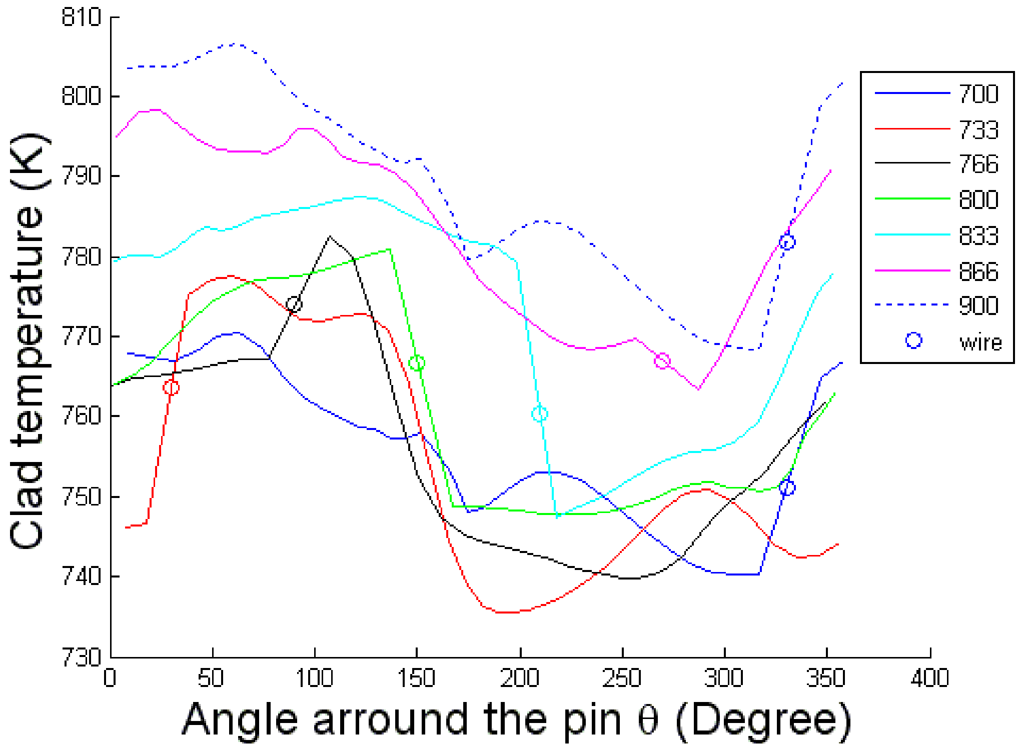

Fig. 4.31b: Circumferential variation of clad temperature at pin 174 at various axial positions within one pitch.

4.3 CLOSURE

Local flow pattern and heat transfer characteristics of sodium in a 217 pin wire-wrapped fuel bundle were predicted. The axial mass flow rate in any subchannel exhibits periodic oscillations in the fully developed region of the bundle. The periodicity of axial flow in central subchannel is 1/3rd pitch, whereas it is over one pitch in peripheral subchannel. For the central subchannel, the origin of these periodic oscillations has been traced to be due to the change in flow area and hydraulic resistance of the subchannel due to the passage of wire. For the central subchannel, the transverse flows crossing the subchannel lateral faces nearly follow a Cosine profile. These flows in different faces are identical but with a phase shift. Through the lateral face of the edge subchannel facing the subassembly centre, a continuous inflow prevails for one half of the pitch while a continuous outflow prevails for the other half of the pitch. This causes larger amplitude axial flow oscillations in the peripheral subchannels compared to that in the central subchannels.

Correlations have been proposed for non-dimensional transverse velocity as a function of wire orientation, for various types of subchannels and for a wide range of bundle dimensions. These correlations can be adopted for development of advanced subchannel models for subassembly thermal hydraulic design. A comparison of results from a full length fuel subassembly model and a periodic model suggests that thermal development is incomplete in fuel pin bundle of practical length. Prominent oscillations in clad temperature along the axial direction are seen in the peripheral and outer pins. These oscillations are due to transverse flow from center to the periphery and vice versa occurring in the vicinity of peripheral region. Peripheral pins show large circumferential variation in clad temperature. This is due to the fact that one side of the peripheral pin is facing the heat generating pins while the other side is facing the adiabatic wall. Pins in central and middle regions do not show such large variation. Further, circumferential temperature profile of pins repeats for every pitch, while the mean value continuously increases.

5 THERMAL HYDRAULIC INVESTIGATIONS ON POROUS BLOCKAGE IN PIN BUNDLE

5.0 INTRODUCTION

In the last chapter, flow features in a nominal fuel pin bundle without any blockage were investigated. The present chapter deals with thermal hydraulic features with partial flow blockage in the active region of the fuel pin bundle. Though many experimental and numerical studies have been reported for model fuel bundles with small number of pins, blockage study for a prototype fuel bundle with large number of pins is rather limited. Further, thermal hydraulic features obtainable through 3-D CFD simulations for a 217 pin wire wrapped bundle have not yet been examined. In addition, most of the studies related to model pin bundles deal with impermeable blockage, which is less likely to occur. A parametric study of porous heat generating blockage has been conducted by Marr and Crawford (1972) with one dimensional model. It may be highlighted that the derbies which clog the fuel pin bundle before any fuel subassembly failure do not generate any heat. Knowledge of safe and unsafe domains of blockage parameters for non heat generating blockages is very essential. Further, experimental (or) subchannel based models cannot capture 3 dimensional temperature and velocity distributions within the bundle, specifically behind the blocked zone. Clear understanding of these thermal hydraulic features is important for improving the detectability of blockage and to propose improvements in subassembly design. These form the inspiration for the study reported in this chapter. The major focus of the study is determination of permissible axial length of porous blockage that excludes the risk of sodium boiling as a function of blockage parameters. This is essential for blockage characterization and the subsequent safety analysis.

5.1 VALIDATION OF POROUS BLOCKAGE MODEL

The models adopted in the present analysis are validated with a physically similar experiment on a 19 pin wire wrapped bundle with porous blockage, SCARLET II reported by Olive and Jolas (1990). The cross-sectional layout of the bundle with blockage in SCARLET II and the present CFD model are illustrated in Fig. 5.1a. Bundle dimensions adopted in the experiment are, pin diameter = 8.5 mm, pin pitch = 9.79 mm, helical wire pitch = 180 mm and wire diameter = 1.29 mm. Six central subchannels are blocked with a sintered material of particle diameter 0.5 mm with porosity of 0.32, and effective thermal conductivity of 36 W/mK. Each fuel pin is supplied with electric power of 45 kW over the heated length of 1 m. The base of the blockage is located at 587 mm from the beginning of heated zone and extends up to 647 mm downstream. The sodium inlet temperature and flow rate are 245.8 ºC and 3.3 kg/s. The hexcan wall in the computational mesh has straight faces, whereas the experimental model has dummy pins at its periphery. These dummy pins are modeled as blockages with very low porosity, filling the corresponding dummy pin locations. Mesh density selected in the grid independence study is used in the validation study also.

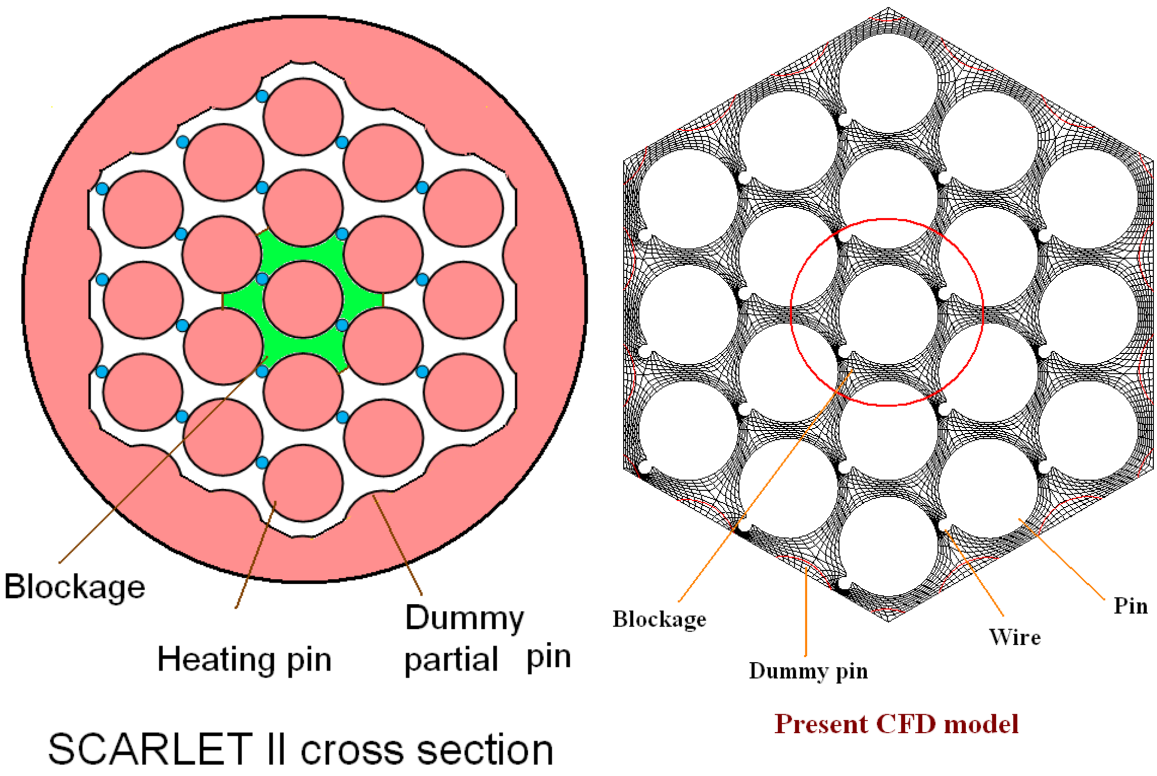

Fig 5.1a: Cross sectional layout of SCARLET II bundle with blockage and present CFD model.

All the blockage parameters and bundle dimensions are represented in the computational model. In the experiment, totally 44 thermocouple were employed in the blocked zone. Thermocouples were located both upstream and downstream of the blockage as well as within the blockage. Within the blockage, thermocouples were placed at 3 circumferential locations 120^{o} out of phase and at different axial planes. However, details of subchannels inside the blockage where thermocouples are placed are not explicitly provided in Olive and Jolas (1990). Hence, the circumferential average of thermocouple readings at any plane within the blockage is compared with the corresponding computational results and presented in Fig. 5.1b. Further, in both the upstream and downstream sides of blockage, only wire temperature is available in the experimental data and hence, average of the three wire temperatures within the blockage length is compared with this data. The comparison shows an over-prediction in the peak temperature by < 11 % of ΔT across blockage (210 °C). Considering the uncertainties in the proximity of the thermocouples with respect to wire (temperature is high near wire), the observed deviation is judged to be satisfactory. In addition, though there is deviation inside the blocked region, the wire temperature in wake region compares well with the experimental data.

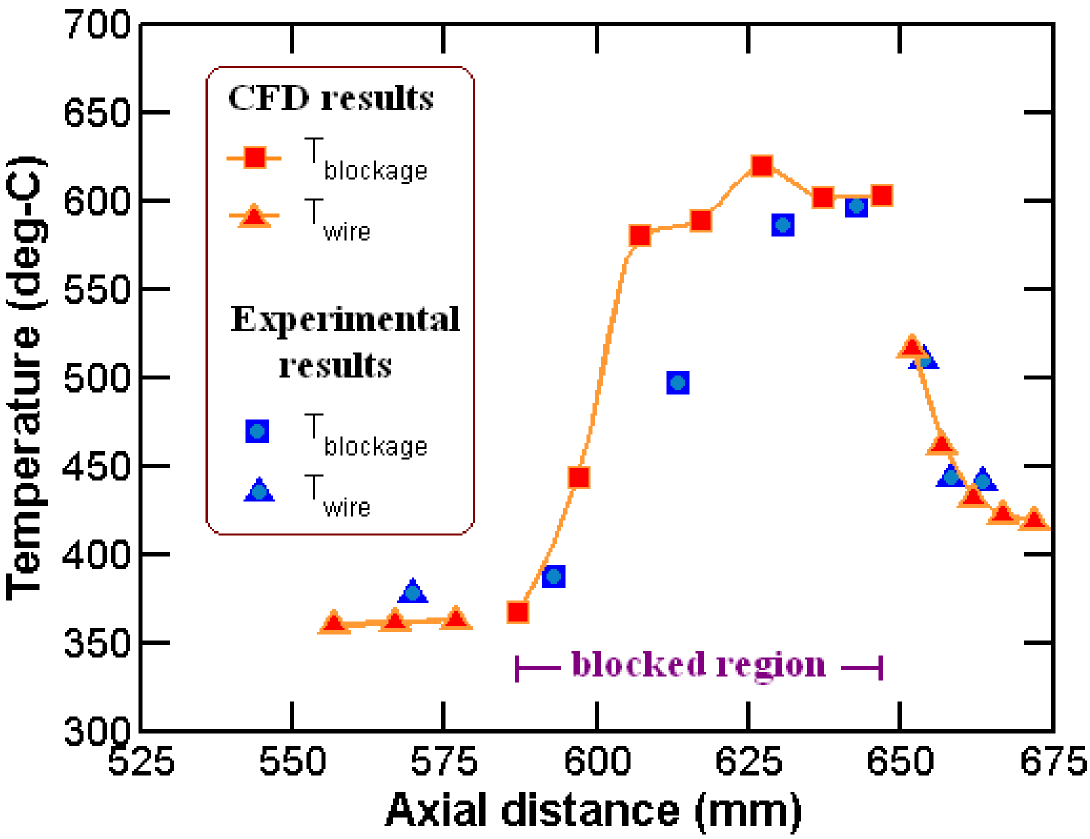

Fig 5.1b: Comparison of predicted sodium temperature with SCARLET II measurements.

5.2 RESULTS AND DISCUSSION

As stated before the focus of the present study is to estimate the critical length of blockage that would lead to sodium boiling, as a function of various blockage parameters such as radial extent, porosity and mean particle diameter. The critical length may be considered as the blockage height at or above which the subcooled sodium boiling occurs in the bundle with the consequent reactivity changes in the core. The ranges of various parameters considered in the present study are given in Table 5.1a. Sixteen different blockage cases with various configurations are studied as detailed in Table 5.1b. To have a conservative analysis, all the blockages in the present study are assumed be axially centered at 700 mm from the inlet to the bundle (i.e., mid-height of active core), where the cosine power profile peaks (Ref. Fig. 3.3b). Boiling superheat values in the range of 40 – 125 ºC are reported by Schleisiek (1970) for large heat flux and low Peclet number regimes. But for the present analysis with peak heat flux and Peclet number as 190 W/cm^2 and 460 respectively, the superheat value found from Schleisiek's results is less than 20 ºC. Further, Uotani and Haga (1984) reported that boiling superheat is nearly zero in blocked bundles when the bundle averaged sodium velocity exceeds 2.5 m/s. In the present study, the bundle averaged velocity is ~ 7.56 m/s. Hence, in all the present analysis sodium is assumed to boil when the clad temperature reaches sodium boiling point (i.e., 1155 K). Hence, attention is focused on the peak clad temperature (hot spot) for fixing the critical blockage length for initiation of sodium boiling. This critical length for different types of blockages is found on the basis of trail calculations. The pin number and nomenclature for measuring pin angle are provided in Fig. 5.2.

TABLE 5.1a: Ranges of the various parameters considered in the present analysis.

Parameter	Range
Radius of blockage	8.28-33.12 (mm)
Porosity	5-60 %
Mean particle diameter	0.25-0.75 (mm)
Location	Central, single and double subchannel
Sodium mass flow rate	35.8 kg/s

TABLE 5.1b: Details of blockage cases investigated in the present study.

Blockage case	Type of blockage	Length (mm)	Radius (mm) /Extent/Type		% Porosity	Mean Practical Diameter (mm)	Location
B0	unblocked	---	unblocked		---	---	---
B1	1-row	80	8.28	(1-row)	40	0.5	Center
B2	2-row	35	16.56	(2-row)	40	0.5	Center
B3	3-row	14.5	24.84	(3-row)	40	0.5	Center
B4	4-row	14.5	33.12	(4-row)	40	0.5	Center
B5	5% porosity	6.25	8.28	(1-row)	5	0.5	Center
B6	10% porosity	10.5	8.28	(1-row)	10	0.5	Center
B7	20% porosity	19	8.28	(1-row)	20	0.5	Center
B8	60% porosity	400	8.28	(1-row)	60	0.5	Center
B9	d_p = 0.25*	25	8.28	(1-row)	40	0.25	Center
B10	d_p = 0.75*	200	8.28	(1-row)	40	0.75	Center
B11	1-subchannel	200	1-subchannel		5	0.5	SC:1-5-6 *
B12	1-subchannel	200	1-subchannel		20	0.5	SC:1-5-6
B13	1-subchannel	200	1-subchannel		40	0.5	SC:1-5-6
B14	2-subchannel	200	2-subchannel		40	0.5	SC:1-5-6 SC:1-6-7
B15	2-subchannel	200	2-subchannel		40	0.5	SC:1-5-6 SC:1-7-2
B16	2-subchannel	200	2-subchannel		40	0.5	SC:1-5-6 SC:1-2-3

* SC = Subchannel and refer Fig. 5.2 for identification of the subchannel based on the pins surrounding it (e.g. 1-5-6 corresponds to pin1 - pin5 - pin6).

d_p* = Mean particle diameter within blockage

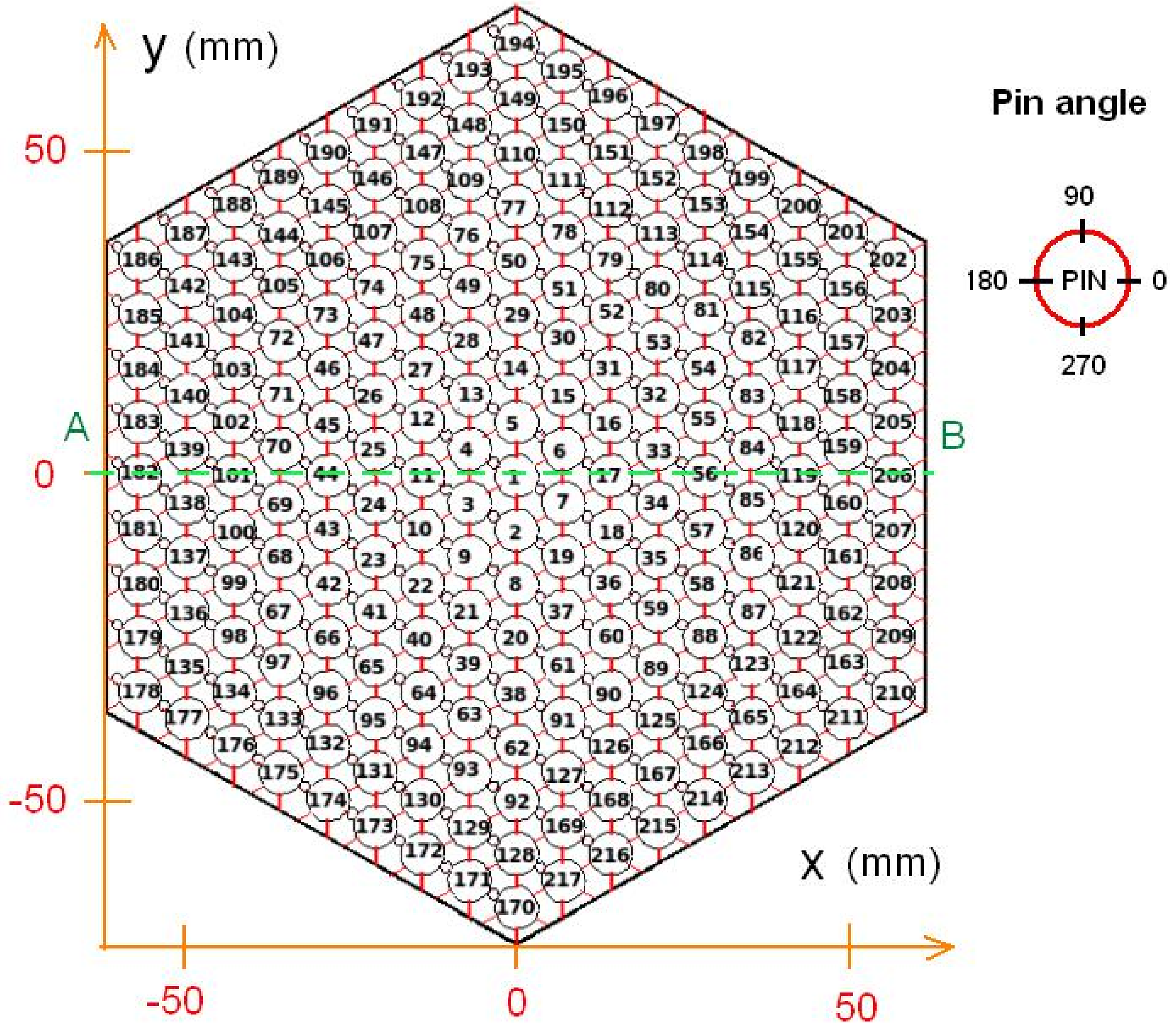

Fig 5.2: Numbering system for pins and angle around the pin adopted in the present investigations.

5.2.1 Flow and Temperature Fields in Sodium

Predicted temperature contours and velocity field of sodium in a vertical section (AB shown in Fig. 5.2) from an elevation of 500 mm to 900 mm of unblocked pin bundle are depicted in Fig. 5.3. Velocity and temperature fields at various horizontal cross sections are depicted in Fig. 5.4. The corresponding results for central blockages having radial extents of 1 row and 4 rows are shown in Figs. 5.5 to 5.8 respectively.

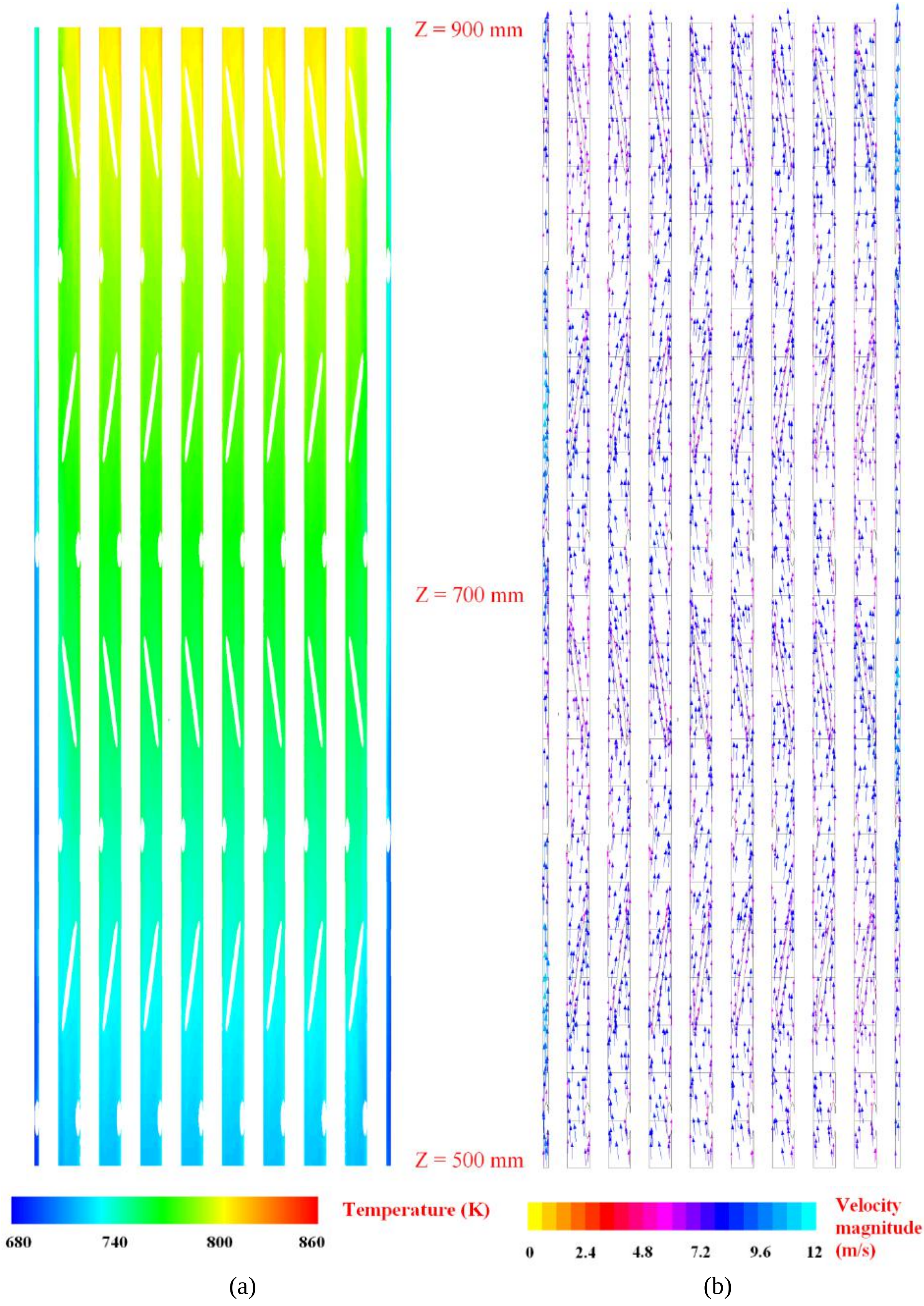

Fig 5.3: Temperature (a) and velocity fields (b) along the vertical cross section (A-B) from elevation 500 – 900 mm of unblocked bundle (B0).

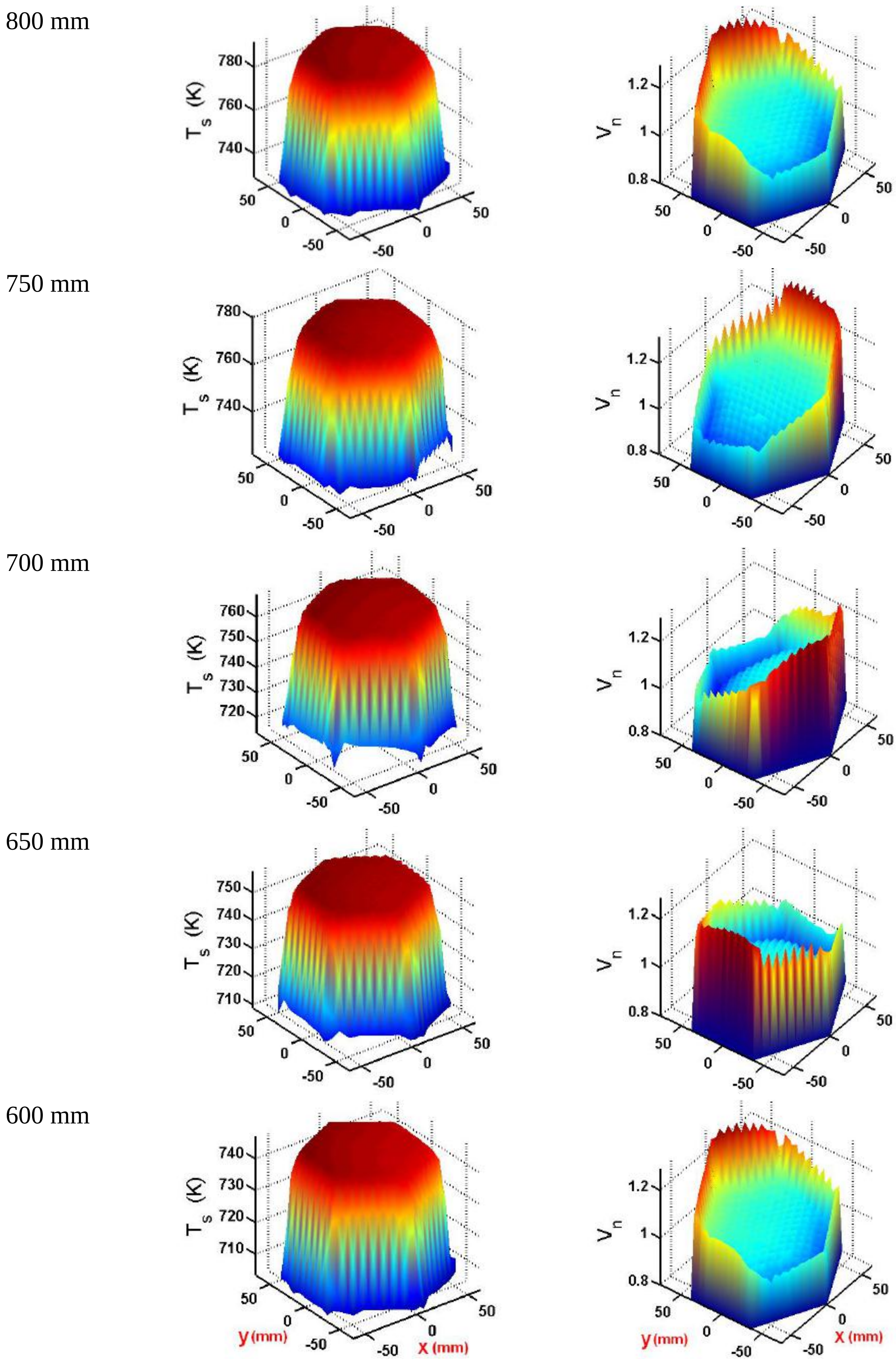

Fig 5.4: Temperature (left) and velocity profiles (right) at various elevations of unblocked bundle (B0).

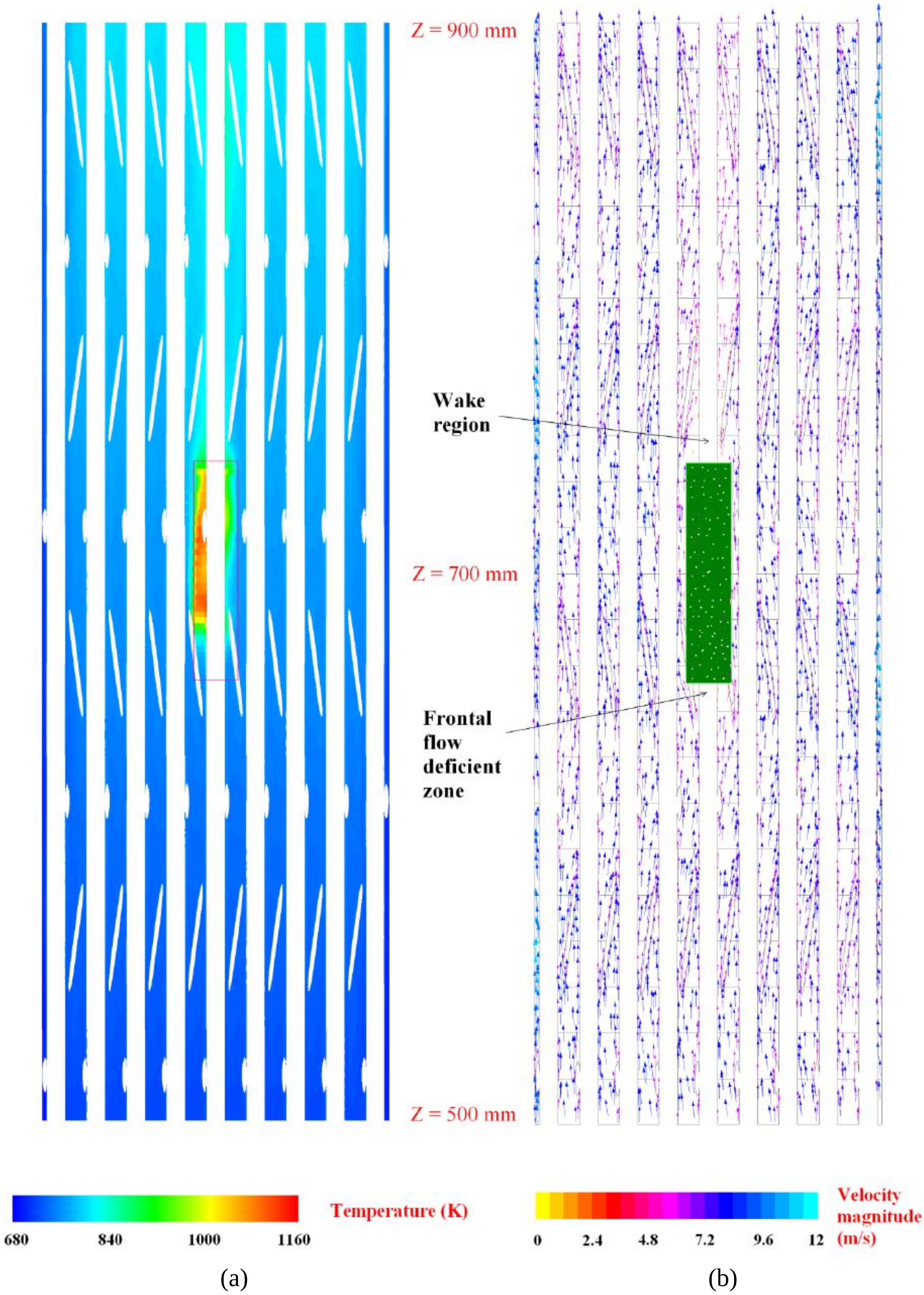

Fig 5.5: Temperature (a) and velocity fields (b) along the vertical cross section (A-B) from elevation 500 – 900 mm of in the case of single row (B1) blockage.

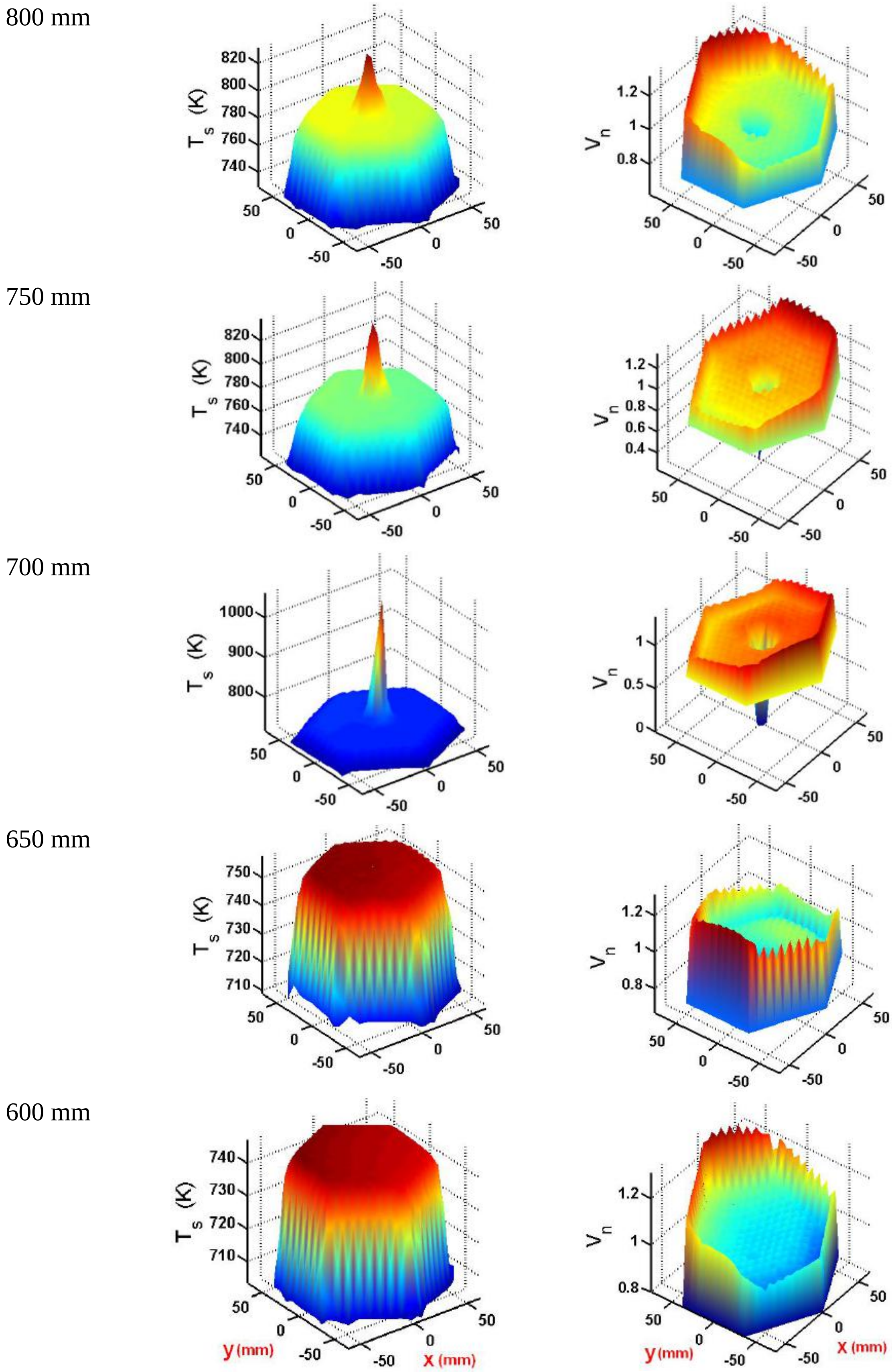

Fig 5.6: Temperature (left) and velocity profiles (right) at various elevations of single-row (B1) blockages case.

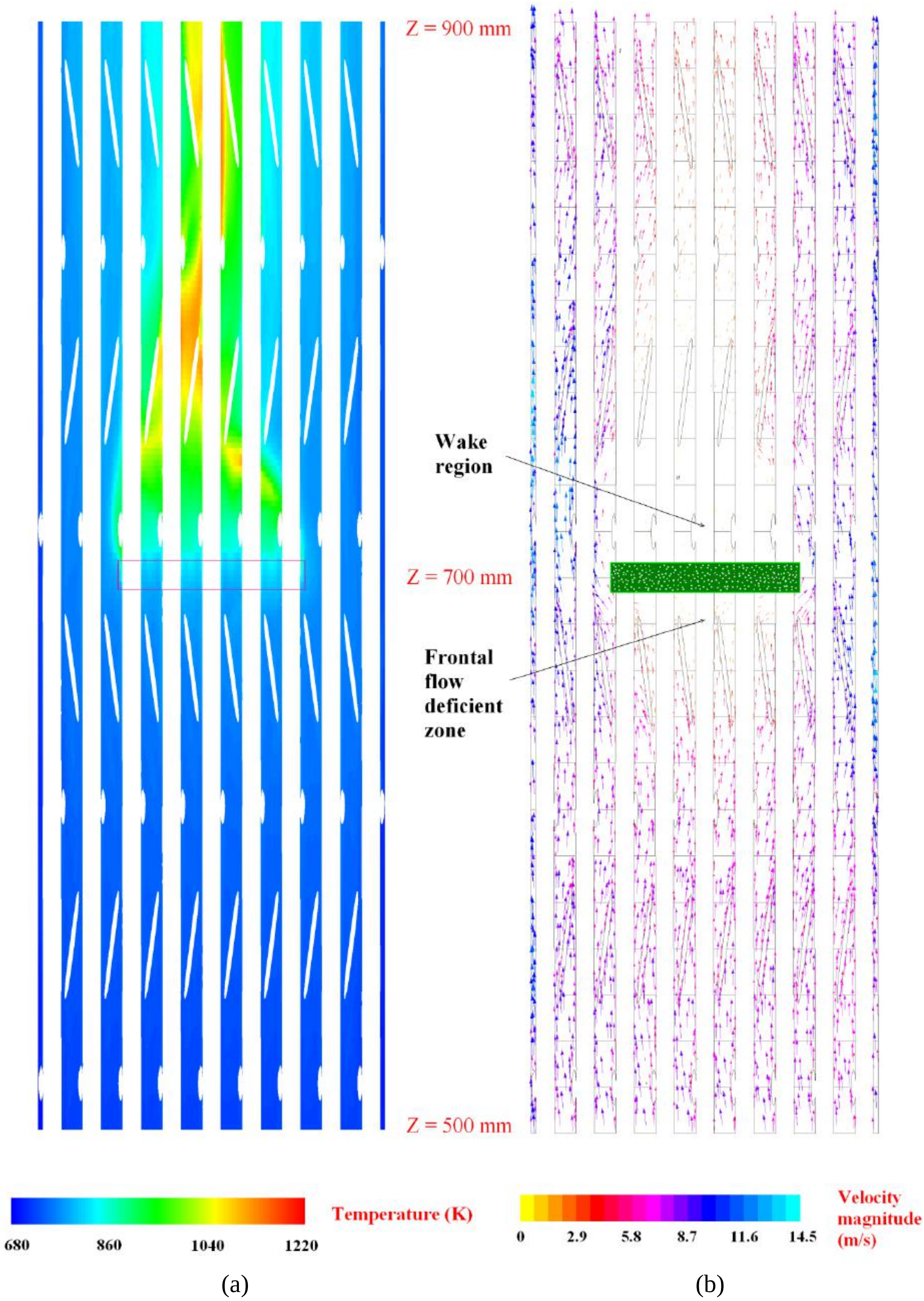

Fig 5.7: Temperature (a) and velocity fields (b) along the vertical cross section (A-B) from elevation 500 – 900 mm of 4-row (B4) blockage case.

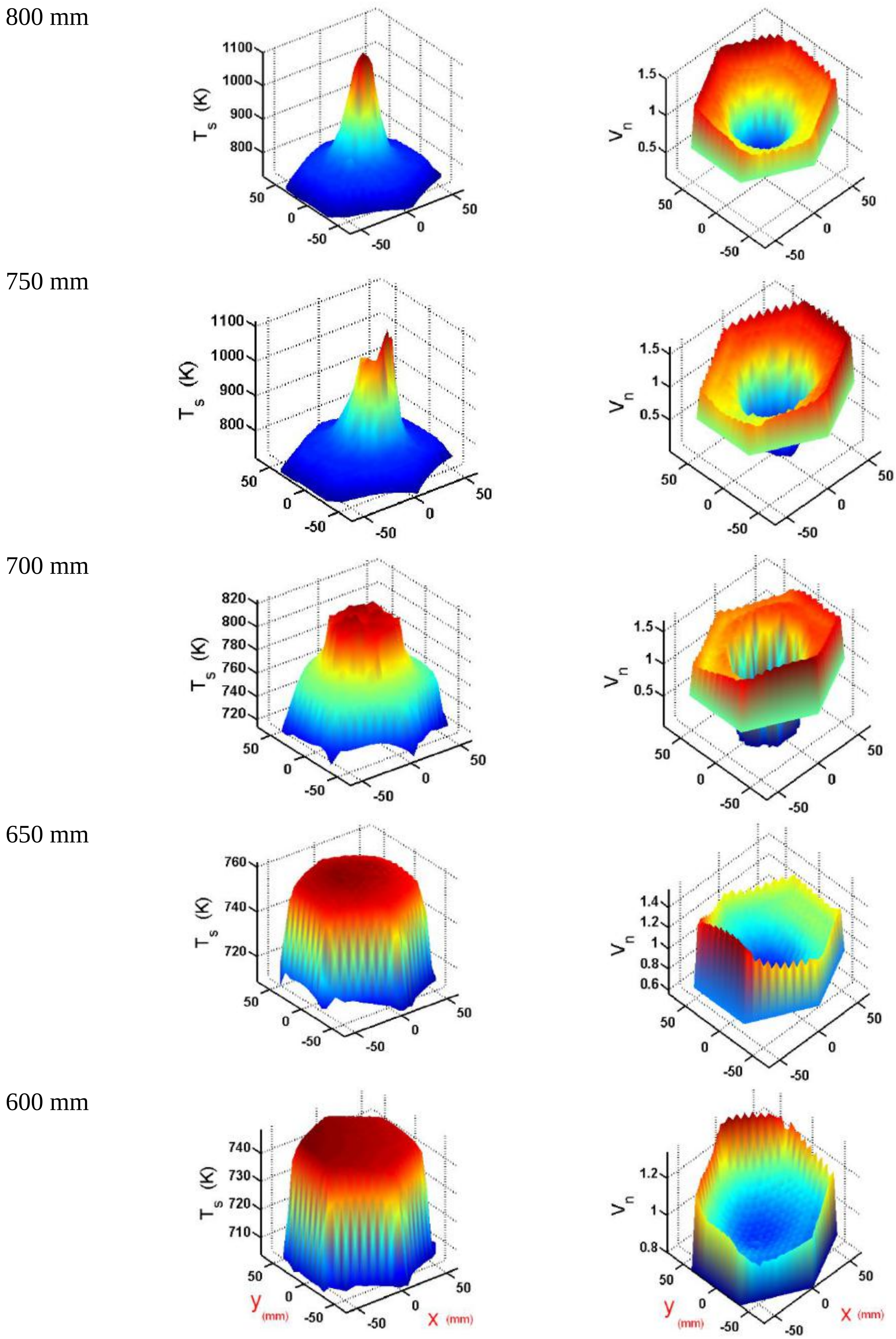

Fig 5.8: Temperature (left) and velocity profiles (right) at various elevations of 4-row (B4) blockages case.

In unblocked bundle, though there is a periodic change in location of peripheral peak velocity along the circumference of the subassembly (Ref. Fig. 5.4), the flow gets fully developed within about two helical pitch lengths. The perfect repetition in the periodic flow oscillation confirms this fact. But, this is not true in the downstream side of blockage. It is seen from Fig. 5.5 that even for one row blockage, the flow disturbed by the blockage never gets fully developed and a large radial temperature variation behind the blockage continue to persist till the outlet. It is seen that in the wake zone, immediately downstream of blockage (elevation ~750 mm), peak sodium temperature does not occur at the center, and instead it occurs at the edge of the blockage. Similar findings were seen in the experimental investigations of blockage in FBR bundle by Huber and Peppler (1985), Krisch (1973), and subchannel analysis on FBR blockage by Jeong et al., (2009). On moving further downstream of the blockage, the peak sodium temperature shifts towards the center and this sharp non uniformity in temperature stays almost un-damped till the exit of the bundle.

It could be seen that for small radial extents of blockage, the peak clad temperature lies within the porous blockage (Fig. 5.5), whereas as for large extents such as 4 row blockage, the peak clad temperature occurs in the wake zone far behind the blockage (Fig. 5.7). Compared to single-row blockage, the smaller height of 4-row blockage aids in good axial conduction, and preventing the occurrence of hotspot within the blockage. But the sustained low velocity stream in the wake region downstream of blockage results in large rise in sodium and clad temperatures. The same effect is also visible in other large radial extents of blockage with small length. As expected, the flow diversion towards the periphery in a 4 row blockage is large and the resulting maximum velocity in the blockage cross section is 14.5 m/s in periphery, whereas it is 12 m/s in single row blockage and 11.4 m/s in unblocked bundle. But even in a 4 row blockage no reverse flow is found to occur behind the blockage. This could be attributed to the large porosity of the blockage. It is clear from Figs. 5.5 and 5.7 that a flow deficient zone is formed before the blockage (on the upstream of the blockage). This zone extends to an axial length equal to half the diameter of the blockage zone. On the downstream side the wake hydraulic effect is strongly felt to an axial length equal to four times diameter of the blockage.

5.2.2 Subassembly Flow Reduction due to Blockage

As the pressure head available with the coolant pump is fixed, the excess pressure drop due to blockage in a single subassembly within a prototype core having ~ 300 subassemblies (180 fuel subassemblies + 120 blanket subassemblies; only through these subassemblies predominant coolant flow occurs) will result in flow reduction in the blocked subassembly. This reduction in flow is calculated with available in house experimental data on pressure drop and flow rate for various components along the length of the subassembly. Pressure drop in various components for the nominal full power at a rated flow rate of 35.8 kg/s is given in Table 5.2 and details of the location of the pressure tapings are depicted in Fig. 5.9. The maximum pressure drop due to blockage (0.13 bar) is small compared to the total pressure drop (5.15 bar). The pressure drop across the length of bundle, the percentage flow reduction in the subassembly due to blockage, and the associated bulk coolant temperature rise are presented in Table 5.3. It is clear that for most of the cases, the flow reduction due to blockage is <1% and the associated bulk temperature increase is < 1 K. The maximum flow reduction is < 3%. Hence, in the present calculations no flow reduction is accounted.

TABLE 5.2: Sodium pressure drop in various components of the subassembly for nominal flow rate of 35.8 kg/s.

Components	Pressure drop (bar)
Grid plate (0-1)	0.28
Subassembly foot (1-2)	0.85
Bundle entry (2-3)	0.9
Pin bundle (3-4)	2.52
Bundle exit (4-5)	0.35
Shielding bundle (5-6)	0.25
Total	5.15

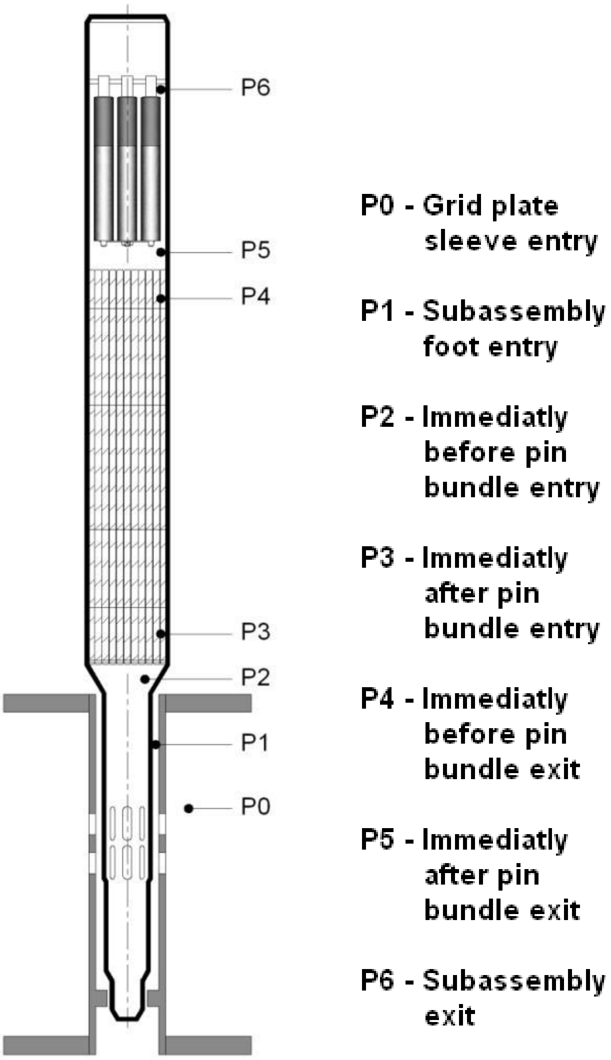

Fig 5.9: Locations for pressure tapping in the experiment.

TABLE 5.3: Pressure drop across the pin bundle, resulting percentage flow reduction, rise in bulk outlet sodium temperature and rise in peak sodium outlet temperature.

Blockage case	**Pressure drop (bar)**	**% flow reduction**	**Bulk sodium temperature rise K**	**Maximum temperature at outlet K**	**Peak sodium temperature rise**
B0	1.837	---	---	867	---
B1	1.847	0.12	0.22	885	18
B2	1.870	0.40	0.71	920	53
B3	1.929	1.09	1.93	951	84
B4	1.966	1.50	2.66	1027	160
B5	1.843	0.07	0.13	878	11
B6	1.843	0.07	0.13	878	11
B7	1.844	0.09	0.15	879	12
B8	1.862	0.30	0.53	917	50
B9	1.843	0.07	0.13	880	13
B10	1.852	0.18	0.32	899	32
B11	1.849	0.15	0.26	873	6
B12	1.840	0.04	0.06	873	6
B13	1.840	0.04	0.06	873	6
B14	1.850	0.16	0.28	875	8
B15	1.851	0.17	0.30	878	11
B16	1.851	0.17	0.30	879	12

5.2.3 Critical Length for Different Radial Extents of Blockage

To understand the effect of radial extent of blockage on critical length, four different central cylindrical blockage cases, with radii increasing in multiples of pin pitch, are studied. The cases are named such that, a cylindrical blockage with one pin pitch radius is referred as single row blockage and so on. All the cases studied under radial extent of blockage have 40% porosity and 0.5 mm mean particle diameter. Peak clad temperature (T_{cp}, hotspot) at any axial section in whole bundle and in pin 1, for different cases are shown in the Fig. 5.10. It is seen that in all the cases, the maximum global hotspot increases beyond sodium boiling point. However, when the height of blockage is reduced, the peak clad temperature reduced below the limit for subcooled boiling. Detailed parametric studies are carried out varying the blockage height to identify the exact blockage height that leads to subcooled boiling. From such studies for various blockage extents, the boiling and non boiling zones have been identified and are depicted in Fig. 5.11. It is to be noted from Fig 5.10 that in all the cases, the global hotspot almost coincides with central pin (pin 1) hotspot, except for a small axial zone near blockage. The (i) hotspot clad temperature, (ii) maximum circumferential clad temperature variation, along with the elevation where it occurs and (iii) pin experiencing the hot temperature in different types of blockages are presented in Table 5.4. Only for single row blockages the maximum hot-spot occurs within the blockage region. For larger radial extents of blockages (2, 3, 4 rows) the hot spot lies in the downstream wake of blockage. Further it was found that, larger the radius of the blockage, longer is the axial distance of hot spot from the center of blockage. As expected, single row blockage tolerates a large critical length of 80 mm compared to that of 14.5 mm for three row blockage. But, it was found that with increase in the radial extent of blockage beyond 3 rows, the critical length required to produce boiling becomes nearly insensitive to the radial extent.

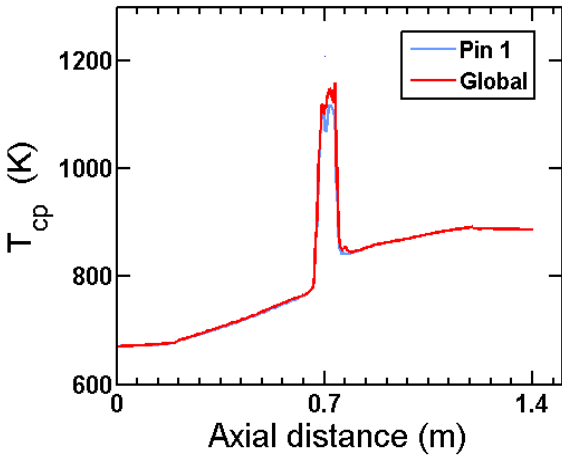

a) Blockage-B1 (R = 8.28 mm)

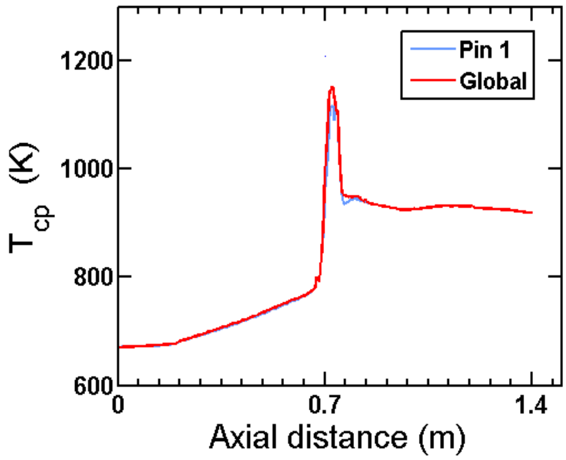

b) Blockage-B2 (R = 16.56 mm)

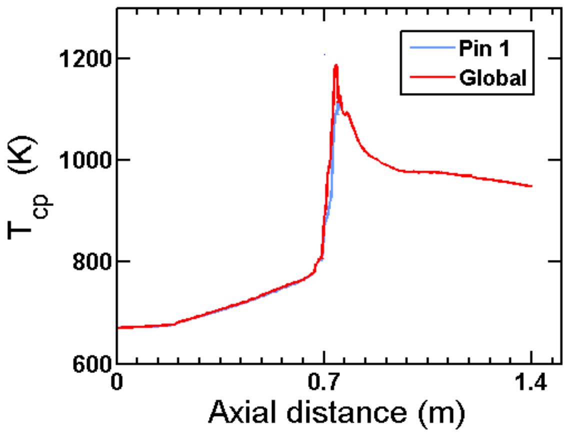

c) Blockage-B3 (R = 24.84 mm)

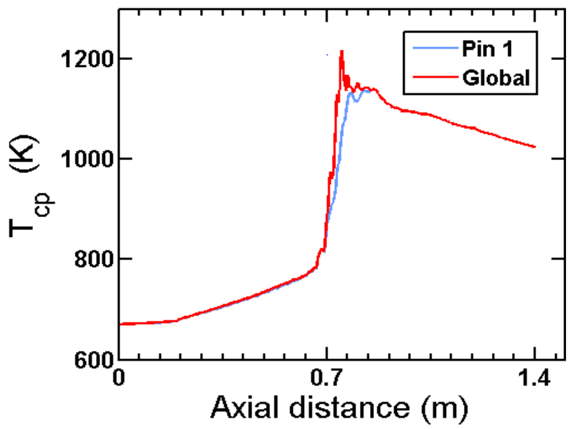

d) Blockage-B4 (R = 33.12 mm)

Fig 5.10: Peak clad temperature (T_{cp}) at any axial section in the whole bundle and in central pin (pin 1).

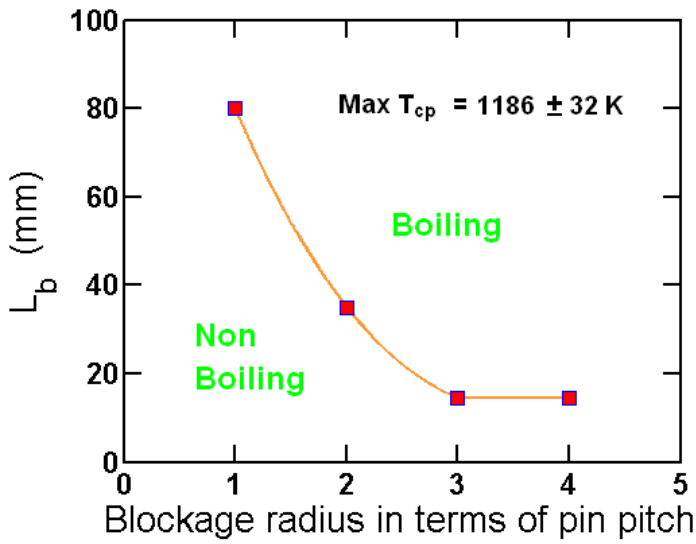

Fig 5.11: Critical lengths as a function of blockage radius (R) (porosity = 40 % and mean particle diameter = 0.5 mm).

TABLE 5.4: Maximum circumferential temperature variation in pin and peak clad temperature in different blockage cases, along with the location and pin number.

Blockage case	Maximum circumferential temperature variation in pin			Peak clad temperature K		
	Pin No *	Axial location (mm)	ΔTc max (K)	Pin No *	Axial location (mm)	Tcp max (K)
B0	---	1070	58	---	1400	878
B1	6	735	372	6	735	1160
B2	17	723	368	17	723	1155
B3	18	737	312	17	738	1187
B4	57	737	316	36	747	1218
B5	5	698	419	1	698	1213
B6	5	703	442	1	702	1229
B7	7	705	425	7	705	1203
B8	6	718	260	6	898	1070
B9	6	705	394	6	705	1172
B10	5	713	391	6	713	1173
B11	6	737	240	6	737	1026
B12	5	738	150	5	770	945
B13	5	770	88	5	770	881
B14	6	672	245	1	772	1028
B15	5	770	137	5	770	931
B16	5	745	93	1	1083	885

* Refer Fig: 5.2 for details

5.2.4 Critical Length for Single Row Blockage: Effect of Porosity

Suhultheiss (1987) has reported that axial growth of blockage is found to be predominant in wire wrapped bundle, where as radial growth is predominant in grid spaced bundle. From this it is judged that six subchannel blockage (i.e., single row) has a larger probability of occurrence compared to larger radial extents of blockages, Hence, additional parametric studies are considered for this case. In this section five different porosities (5%, 10%, 20%, 40%, and 60%) are investigated and the critical length is determined by varying the blockage length. Global and central pin (Pin -1) hotspot temperatures as a function of axial length are shown in Fig. 5.12.

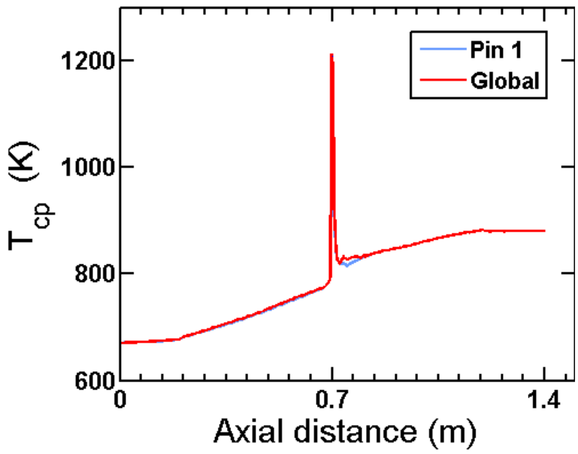

a) Blockage-B5 (β = 5%)

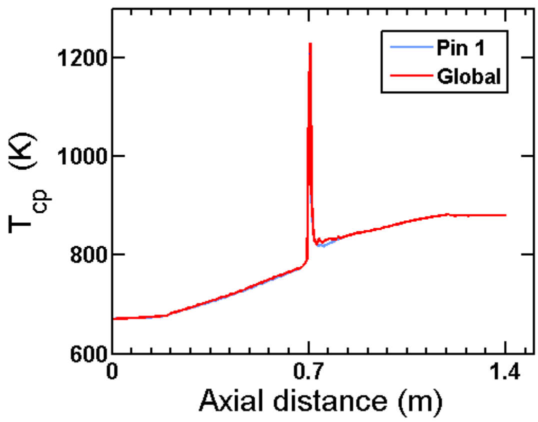

b) Blockage-B6 (β = 10%)

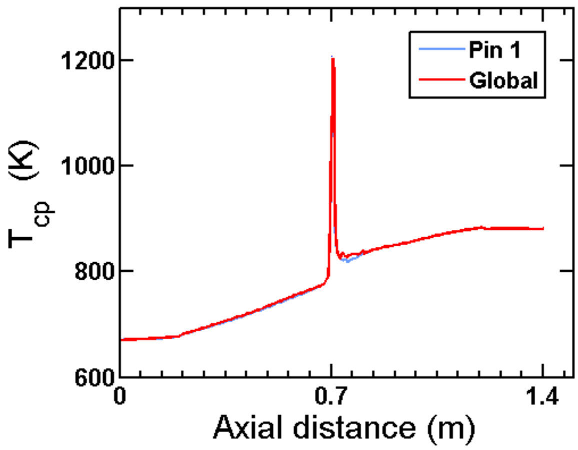

c) Blockage-B7 (β = 20%)

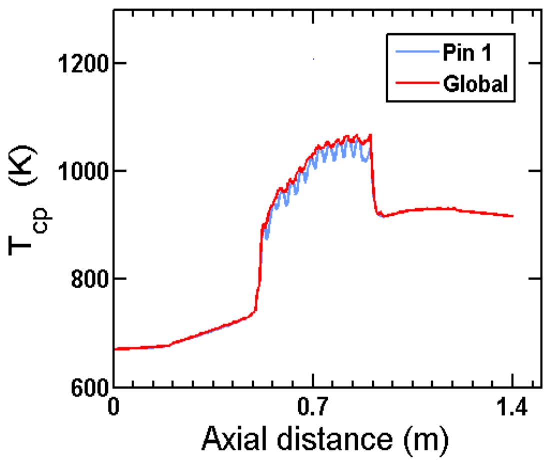

d) Blockage-B8 (β = 40%)

Fig 5.12: Peak clad temperature (T_{cp}) at any axial section in the whole bundle and in central pin (pin 1).

The critical length as a function of porosity along with boiling and non boiling zones is depicted in Fig. 5.13. It is seen that in low porosity blockages, the peak hotspot lies within the blockage (Ref. Table 5.4) and central pin and global hotspots almost nearly coincide. As expected, large flow reduction in the low porosity blockage leads to shorter critical length in such blockages. For the single row blockage with 60 % porosity, boiling is not reached even for a large axial length of blockage, viz., 2 helical pitches, (400 mm). It is further found that though critical lengths of low porosity blockage are short, the peak clad temperature sharply falls in the immediate downstream of the blockage, due to narrow wake zone.

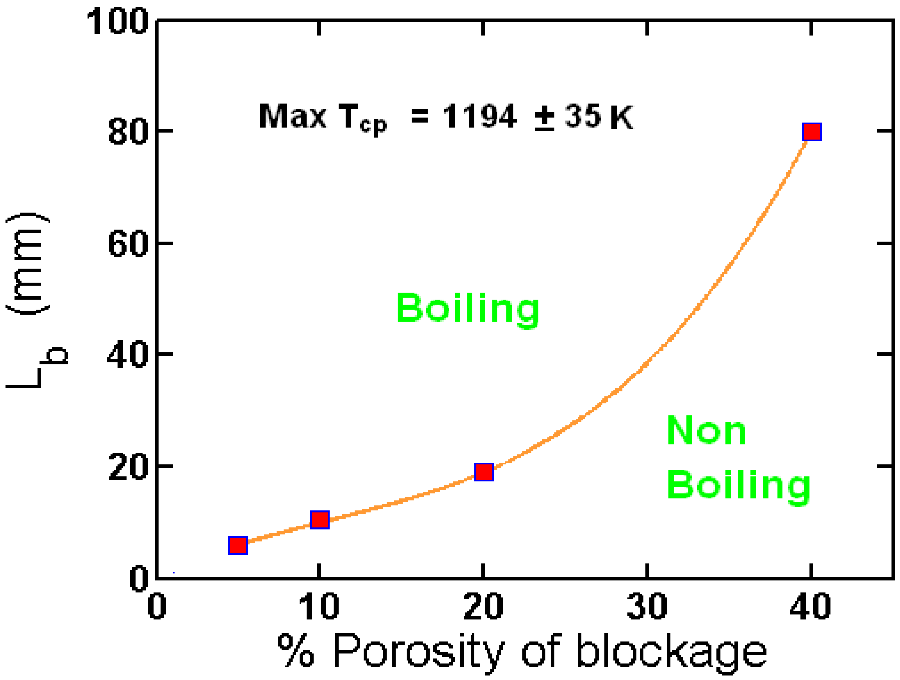

Fig 5.13: Critical lengths of the 1-row blockage as a function of porosity (mean particle diameter = 0.5 mm).

5.2.5 Critical length for Single Row Blockage: Effect of Mean Particle Diameter

In the present study, the reference value of mean particle diameter considered is 0.5 mm. But to understand its effect on critical length, two more particle diameters, viz., 0.25 mm and 0.75 mm are also studied with single row blockage. Though the porosity remains the same (40%), the compactness of blockage and tortuousness of flow path increase with reduction in the particle diameter, leading to enhanced flow resistance and reduced flow through the blockage. Hence, it could be seen that as the particle size reduces to 0.25 mm from 0.5 mm, the critical length reduces to 25 mm from 80 mm, (Fig. 5.14. Global and central pin hotspots along the flow direction for various particle diameters are shown in the Fig 5.15. For blockages with particle size greater than 0.75 mm, the permissible length is larger than one helical pitch.

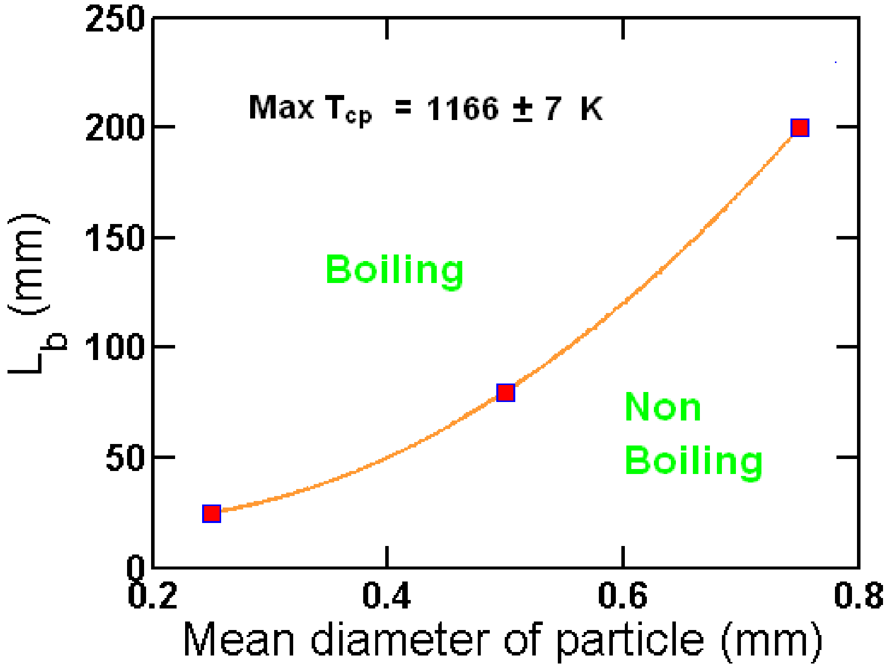

Fig 5.14: Critical lengths of the 1-row blockage as a function of mean particle diameter (porosity =40%).

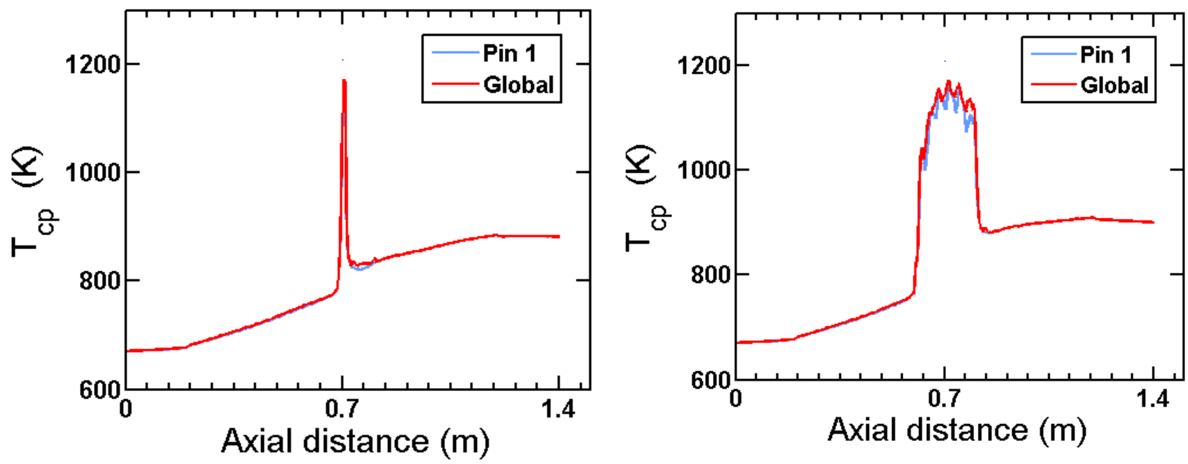

a) Blockage-B9 (d_p = 0.25 mm) b) Blockage-B10 (d_p = 0.75 mm)

Fig 5.15: Peak clad temperature (T_{cp}) at any axial section in the whole bundle and in central pin (pin 1).

5.2.6 Single Subchannel Blockage

It is of interest to study a single subchannel blockage as a lower bounding case. Towards this, the case of single subchannel blockage near the central pin with different porosities is studied. The pins surrounding the selected subchannel are denoted in Table 5.1b. All the cases are studied with identical length of blockage, viz., 200 mm. Porosity values of 5%, 20%, and 40% with particle diameter 0.5 mm are studied. The corresponding results of global hotspot temperatures are shown in Fig. 5.16.

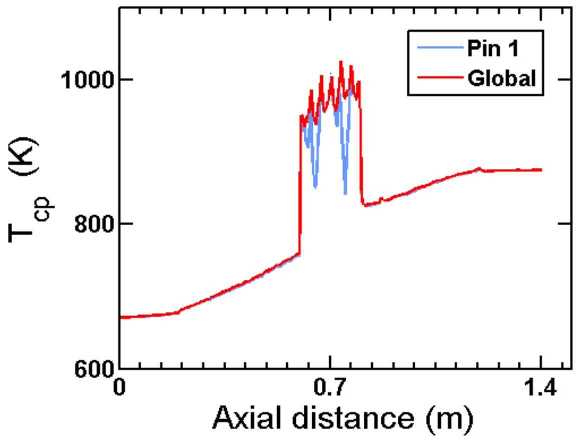

a) Blockage-B11 (β = 5%)

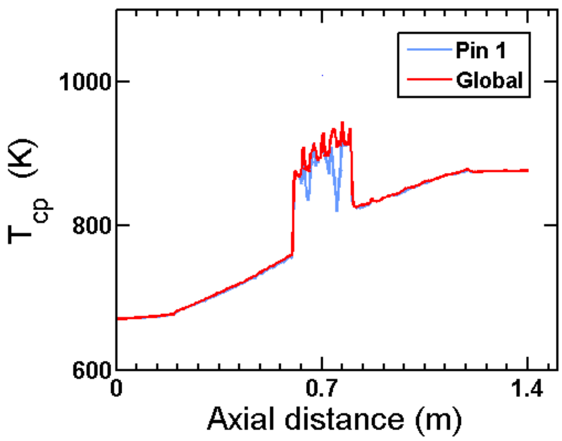

b) Blockage-B12 (β = 10%)

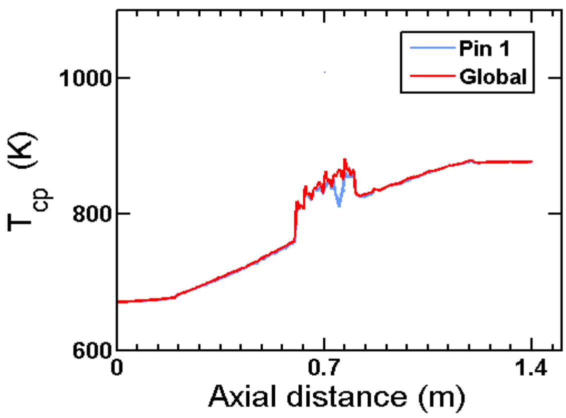

c) Blockage-B13 (β = 20%)

Fig 5.16: Peak clad temperature (T_{cp}) at any axial section in the whole bundle and in central pin (pin 1).

It was found that even for a low porosity of 5% and 200 mm of blockage length the peak clad temperature was below the sub-cooled boiling limit. This shows that occurrence of sodium boiling with single sub-channel blockage is most unlikely for any porosity (Fig. 5.17).

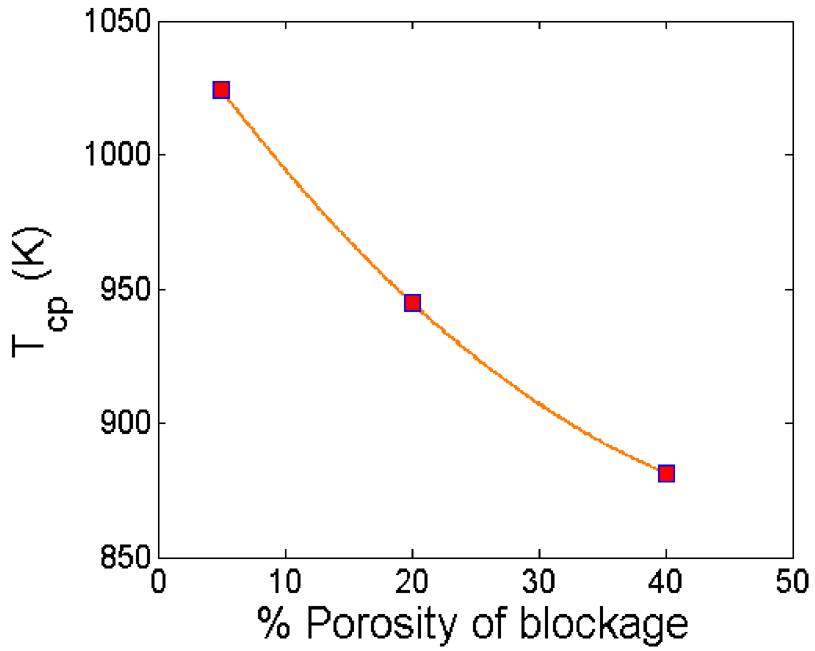

Fig 5.17: Maximum clad temperature reached in single subchannel blockage for different blockage porosity (mean particle diameter = 0.5 mm and blockage length = 200 mm).

5.2.7 Double Subchannel Blockage

Since subcooled boiling is not possible in single subchannel blockage, the next higher level of two subchannel blockage is also studied. To understand the interaction of two single subchannel blockages in the same vicinity, three different arrangements of double subchannel blockage cases are considered. The pins surrounding the selected subchannels are denoted in Table 5.1b. All the cases are studied with 40% porosity, 0.5 mm mean particle diameter and 200 mm blockage length. The corresponding clad hotspot temperatures are shown in Fig. 5.18. The maximum value of hotspot for different configurations of double subchannel blockage are compared with that of single subchannel blockage in Fig. 5.19. It is clear that the hottest clad temperature is reached when the two adjacent subchannels are blocked. Further, the peak clad temperature reduces largely as the two blocked subchannel are spatially separated. More interestingly, when the blockages are three subchannels apart, the peak clad temperature attained is almost similar to that of single sub channel blockage (Fig. 5.17). This suggests that the blockages do not interact when they are separated by three or more subchannels. Further, none of the double subchannel blockages resulted in sodium boiling. But, reducing the porosity further may induce boiling.

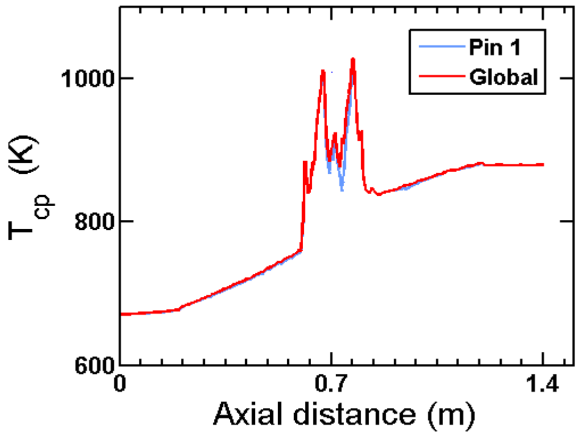

a) Blockage-B14

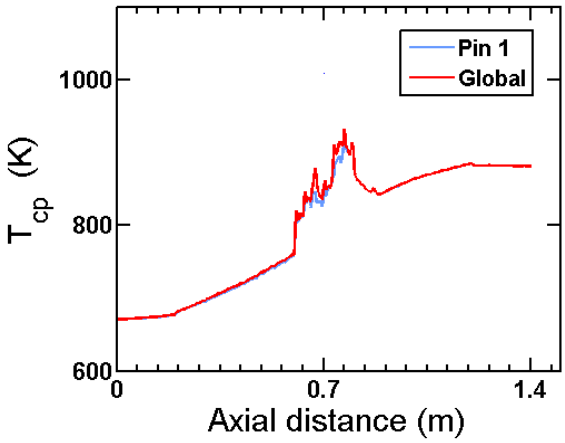

b) Blockage-B15

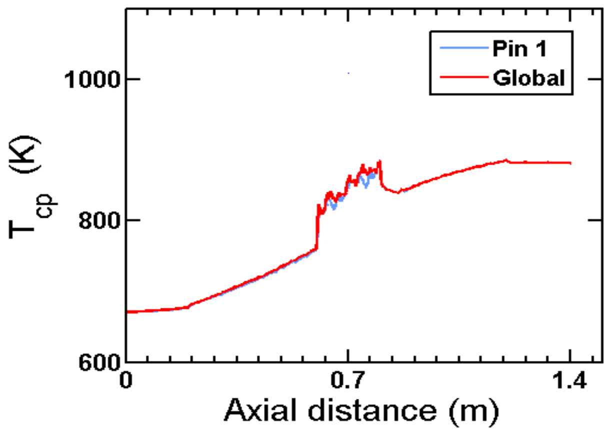

c) Blockage-B16

Fig 5.18: Peak clad temperature (T_{cp}) at any axial section in the whole bundle and in central pin (pin 1).

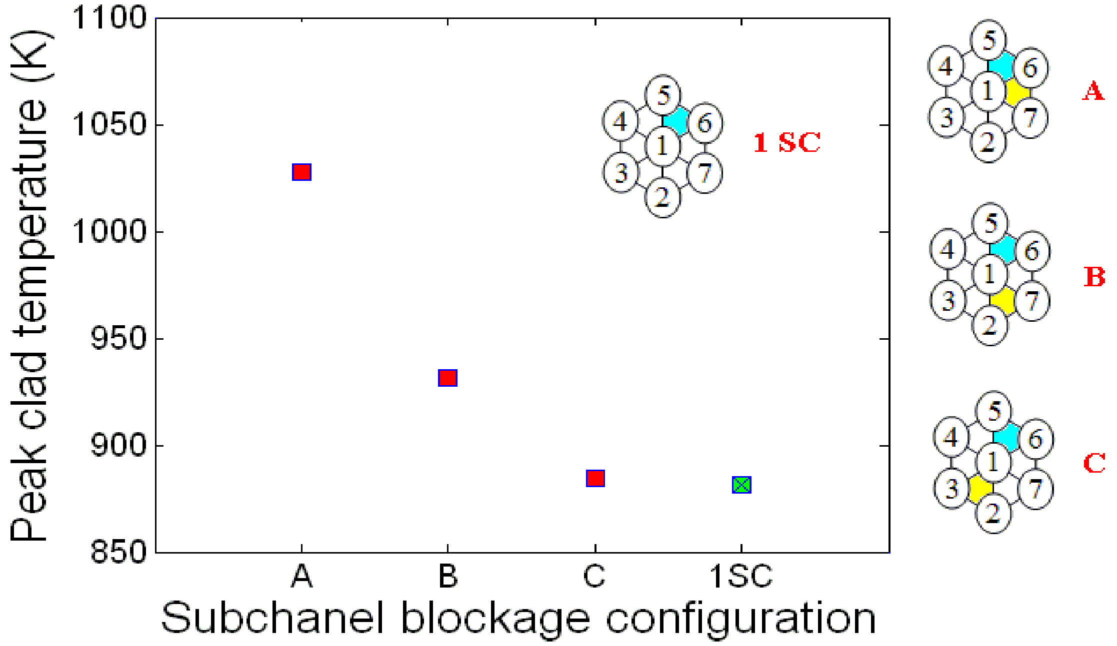

Fig 5.19: Maximum clad temperature in double subchannel blockage (porosity = 40 %, mean particle diameter = 0.5 mm and blockage length = 200 mm).

5.2.8 Circumferential Clad Temperature Variation in Blocked Bundles

The maximum circumferential clad temperature variation, along with the elevation where it occurs is presented in Table 5.4. The maximum circumferential clad temperature variation in an unblocked bundle is 58 ºC, whereas in blocked bundle approaching boiling, the circumferential clad temperature variation is ~ 300 to 450 ºC. Large circumferential pin temperature variation could adversely affect the integrity of clad. Typical clad temperature around its circumference, where the circumferential variation is maximum in the case of single row and 4 row blockage is depicted in Fig. 5.20. It could be inferred with the help of Fig. 5.2 that in both, single row and 4 row blockages cases, the peak clad temperature on the pin occurs on its side facing the subassembly center. Though peak clad temperature is higher in the 4 row blockage, circumferential clad temperature variation is larger in single row blockage. This could be attributed to the location of maximum circumferential clad temperature variation inside the blockage region in the case of single row blockage, compared to its location in the wake zone in the case of 4 row blockage.

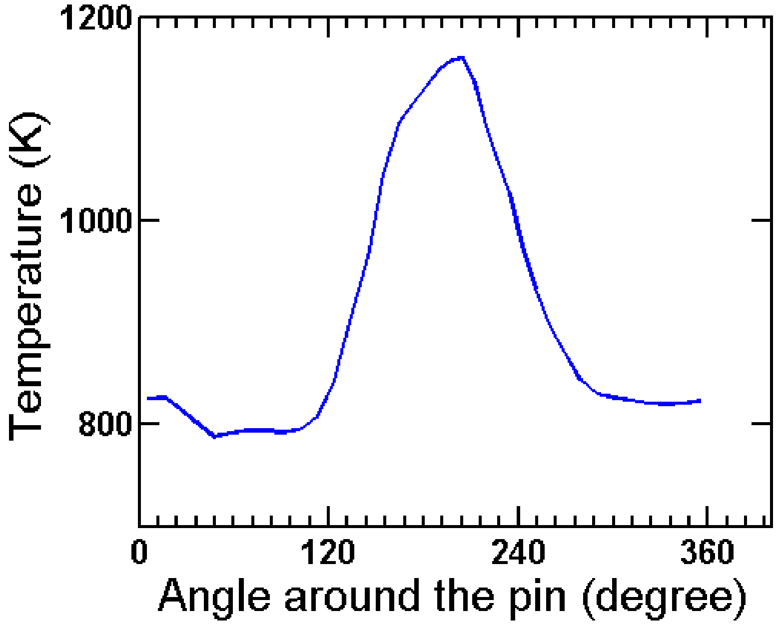

a) Blockage B1, pin 6, at elevation 675 mm.

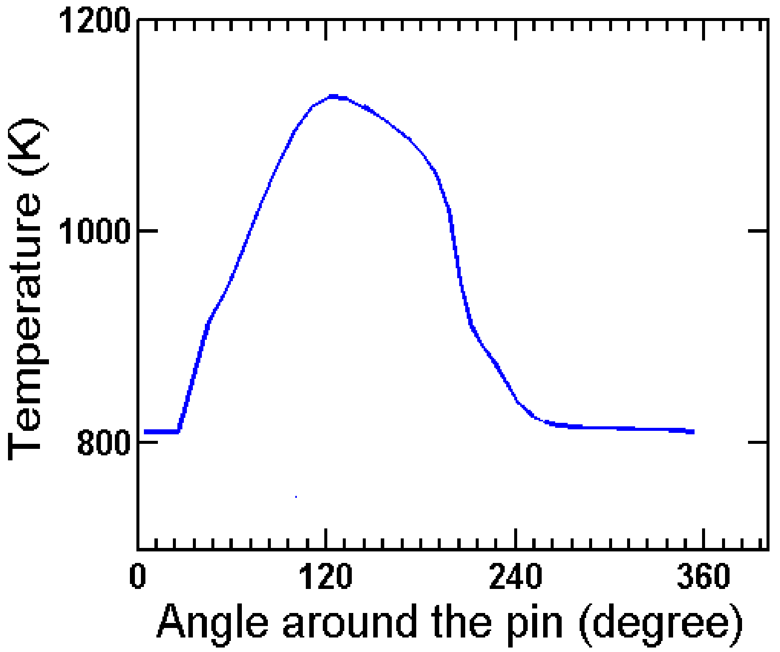

b) Blockage B4, pin 57, at elevation 737 mm.

Fig 5.20: Circumferential temperature variation around the pin in blocked subassembly at location where the variation is maximum.

5.2.9 Detectability of Blockage

It is desirable that, even after a possible detection of local blockage in any fuel subassembly, the reactor operation can be continued till the scheduled shutdown, if the consequences of the blockage are known and manageable (Roychowdhury et al., 2000). Only if the blockage is detected, its size and consequences can be discussed based on the intensity of the parameter used for detection. In a typical SFR, the sodium temperature exiting from every fuel subassembly is continuously monitored online. A 10 ºC rise in the sodium temperature orders automatic reactor trip, while a 5 ºC rise provides alarm to the operators. From heat balance calculations, these global rises in outlet sodium temperature correspond to flow reduction of 6 % and 3 % respectively. From the increased bundle pressure drop due to the blockage, the reduction in overall subassembly flow rate and the resulting rise in the bulk subassembly outlet temperature are presented in Table 5.3. It is clear that, the maximum reduction in flow rate is < 3 % among the various cases analyzed. Thus, presence of internal porous blockages cannot be detected by global subassembly outlet temperature monitoring, before onset of boiling.

Figure 5.21 shows, sodium temperature and axial velocity profiles at the exit of the bundle for unblocked and blocked bundles. It could be seen that for an unblocked case the temperature profile is almost uniform throughout the section, whereas a large peak in sodium temperature occurs in all the cases with internal blockage. Larger the radial extent of blockage, higher is the magnitude of the peak temperature. The rise in the peak outlet sodium temperature for various blockage cases compared to that of unblocked case is presented in Table 5.3. The peak outlet temperature in a 4 row blockage is 160 K higher than that in unblocked case. This large local peak in the outlet sodium temperature could be used as a source for early deduction of the blockage, even though bulk outlet temperature could not be differentiated. Admittedly this calls for sophisticated instrumentation for subassembly outlet sodium temperature monitoring.

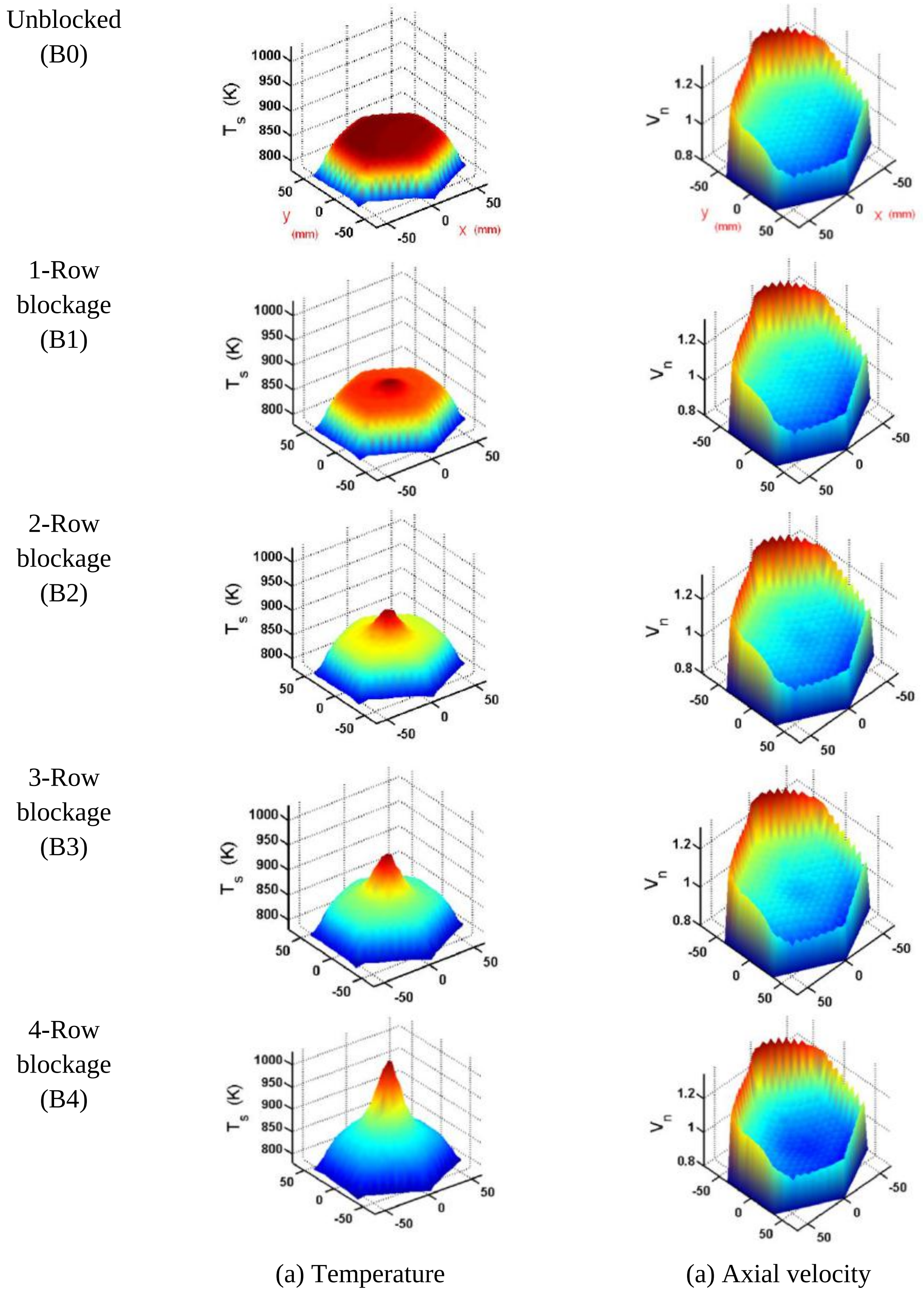

Fig 5.21: Comparison of temperature and velocity profiles at an elevation of 1300 mm from the inlet for unblocked and blocked cases.

5.3 CLOSURE

Thermal hydraulic features of a prototype subassembly with various porous blockage configurations have been investigated for a wide range of blockage radius, porosity and mean particle diameter. The critical length of blockage that would result in local sodium boiling as a function of blockage parameters and the parametric zone posing risk of sodium boiling have been determined. It is seen that a large non-recirculating wake zone prevails in the downstream side of the blockage, with the extent of the wake zone increasing with blockage radius. The peak clad temperature occurs in the wake zone for large radius blockages and it does not occur in the central pin. The total flow reduction in the subassembly as a result of blockage is found to be < 3 % for all blockages that can lead to local sodium boiling. This suggests, that global bulk sodium temperature monitoring at the outlet of the subassembly is unlikely to detect slowly growing blockages. The wake induced temperature non-uniformity persists even upto 3 helical pitch lengths suggesting that the sodium temperature non-uniformity at the bundle exit can serve as an efficient blockage indicator, provided that the cross section temperature is mapped by a proper instrumentation. Six subchannel blockage with 60% porosity and 0.5 mm mean particle diameter, does not induce boiling even up to a blockage height of 400 mm. Fuel-clad that are partly exposed to blockage are subjected to large circumferential temperature variation and the resulting thermal stress. For a single subchannel blockage there is no risk of sodium boiling, even upto 200 mm of length and porosity as low as 5%. Even in the adverse case of two adjoining subchannel blockage, sodium boiling does not occur.

6 THERMAL HYDRAULIC INVESTIGATIONS ON PLANAR BLOCKAGE IN PIN BUNDLE

6.0 INTRODUCTION

In the previous chapter, thermal hydraulics in a prototype subassembly with porous internal blockage was investigated. The flow characteristics of wake region behind an impervious planar blockage are significantly different from that behind a porous columnar blockage. The pressure loss induced by planar blockage is also different from that by a porous blockage. Further, the radial location of blockage will greatly influence the flow pattern behind the blockage, which in turn influences the peak clad temperature downstream of the blockage. Knowledge on permissible radial extent of planar blockage that avoids the risk of sodium boiling and the possibility of blockage detection by core monitoring thermocouple is essential in the safety analysis of a SFR. This forms the main focus of the studies presented in this chapter.

6.1 VALIDATION

The computational methodology and models used in the planar blockage analysis are validated with FFM-3A experimental data (Test-2, Run-101) reported by Fontana et al., (1973). A 19 pin wire wrapped bundle with dimensions and boundary conditions presented in Table 6.1 is adopted in the experiment. A 6.35 mm thick steel plate blocking the central 6 subchannels is placed at 381 mm from the beginning of heat generating region. The detailed geometry of test bundle is modeled and meshed to render a grid independent solution. The cross-sectional layout of 19 pin wire wrapped FFM-3A bundle and the mesh used in the present CFD model are presented in Fig. 6.1. Local wire temperatures in the bundle both upstream and downstream of the blockage are measured by thermocouples present in the spacer wire. In addition, subchannel sodium temperatures at 76 mm downstream of the heat generating region are also measured. These temperature data are taken for validation purpose. Comparison of the predicted CFD results of wire wrap temperature at various elevations with the corresponding measured values is depicted in Fig. 6.2a. Comparison of the predicted subchannel sodium temperature at 76 mm downstream of the heat generating region with the corresponding measured values is depicted in Fig. 6.2b. The maximum deviation between computational and experimental results, in both cases is found to be < 15 %. Further, the comparison is very close in the upstream and far downstream of the blockage.

TABLE 6.1: Dimensions and boundary conditions adopted in CFD simulations of FFT-3A experiment (Fontana et al., 1973).

Parameters	**Value**
Wire diameter	1.4 mm
Pin diameter	5.84 mm
Helical pitch	304.8 mm
Pin pitch	7.26 mm
Upstream unheated length	457.2 mm
Heated length	533.4 mm
Downstream unheated length	228.6 mm

Boundary conditions	**Value**
Inlet flow rate	0.00341 m^3/s
Inlet temperature	714.3 K
Heat supplied	17.5 kW/rod

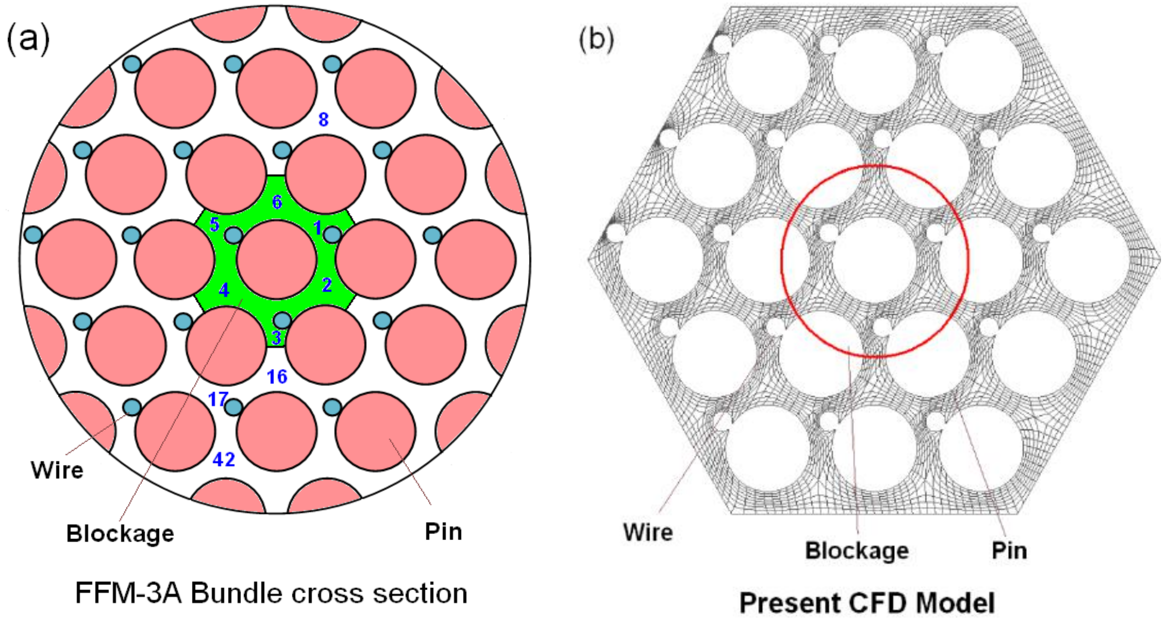

Fig 6.1 (a) Cross-sectional layout of FFM-3A bundle (marked with subchannel numbers) and (b) Present CFD model.

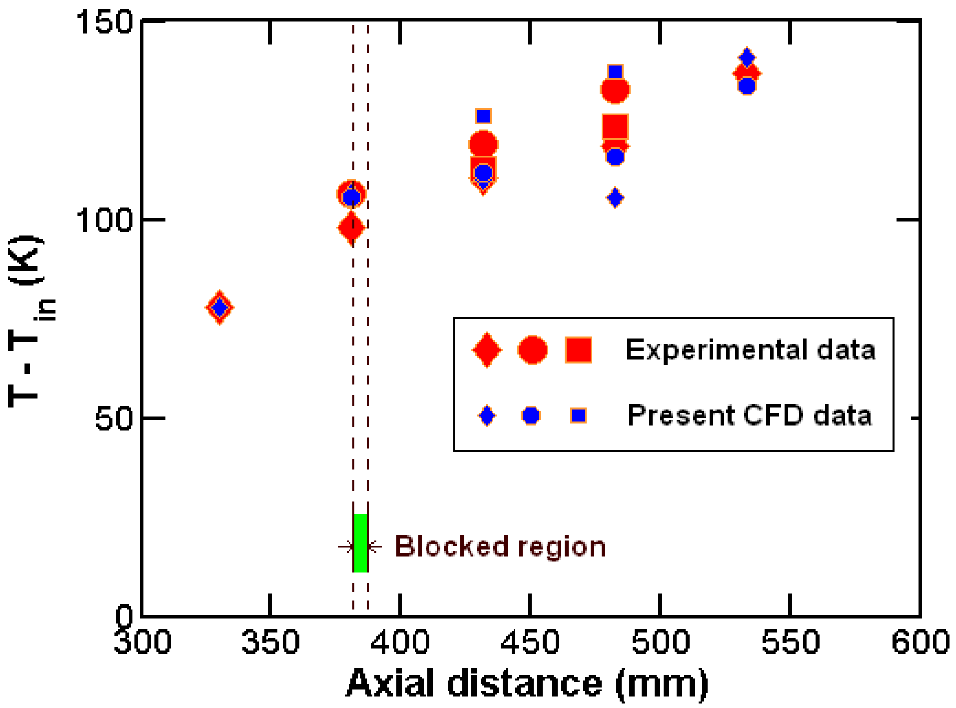

Fig. 6.2a: Comparison of temperature measured (Fontana et al., 1973) by wire wrapped thermocouples with present CFD simulation. (Symbols represent thermocouples on different wires at identical axial distance).

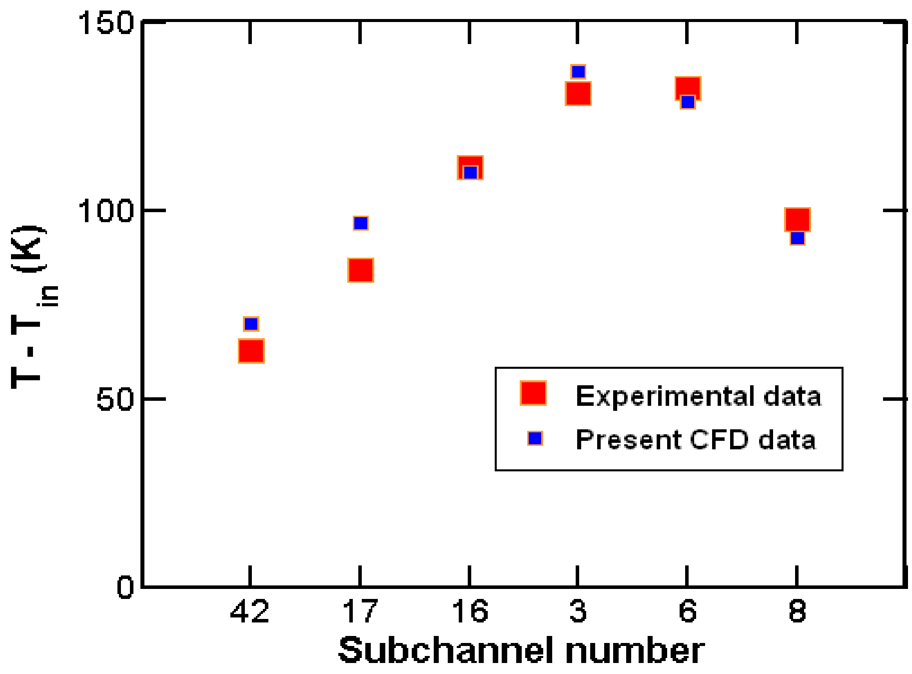

Fig. 6.2b: Comparison of measured subchannel temperature at 76 mm downstream of the heat generating region (Fontana et al., 1973) with the corresponding CFD data.

6.2 RESULTS AND DISCUSSION

In the present study, totally nine cases of planar blockages within a 217 pin prototype fuel bundle are considered (Ref. Table 6.2). The thickness of solid blockages is 4 mm. In what follows, B0 refers an unblocked case used for comparison purpose. In cases P1 to P8, the planar blockage is axially located at 700 mm from inlet (where heat flux peaks). Further, in cases P1 to P4, the blockage surrounds the central pin (the pin 1, shown in Fig. 6.3) and in cases P5 to P8, blockage surrounds a corner pin in the bundle (pin 170, shown in Fig. 6.3). Blockage case P9 is same as P4, but in the former, blockage is axially located at 800 mm from inlet. Additional details of various cases, regarding the blockage radius are given in Table 6.2.

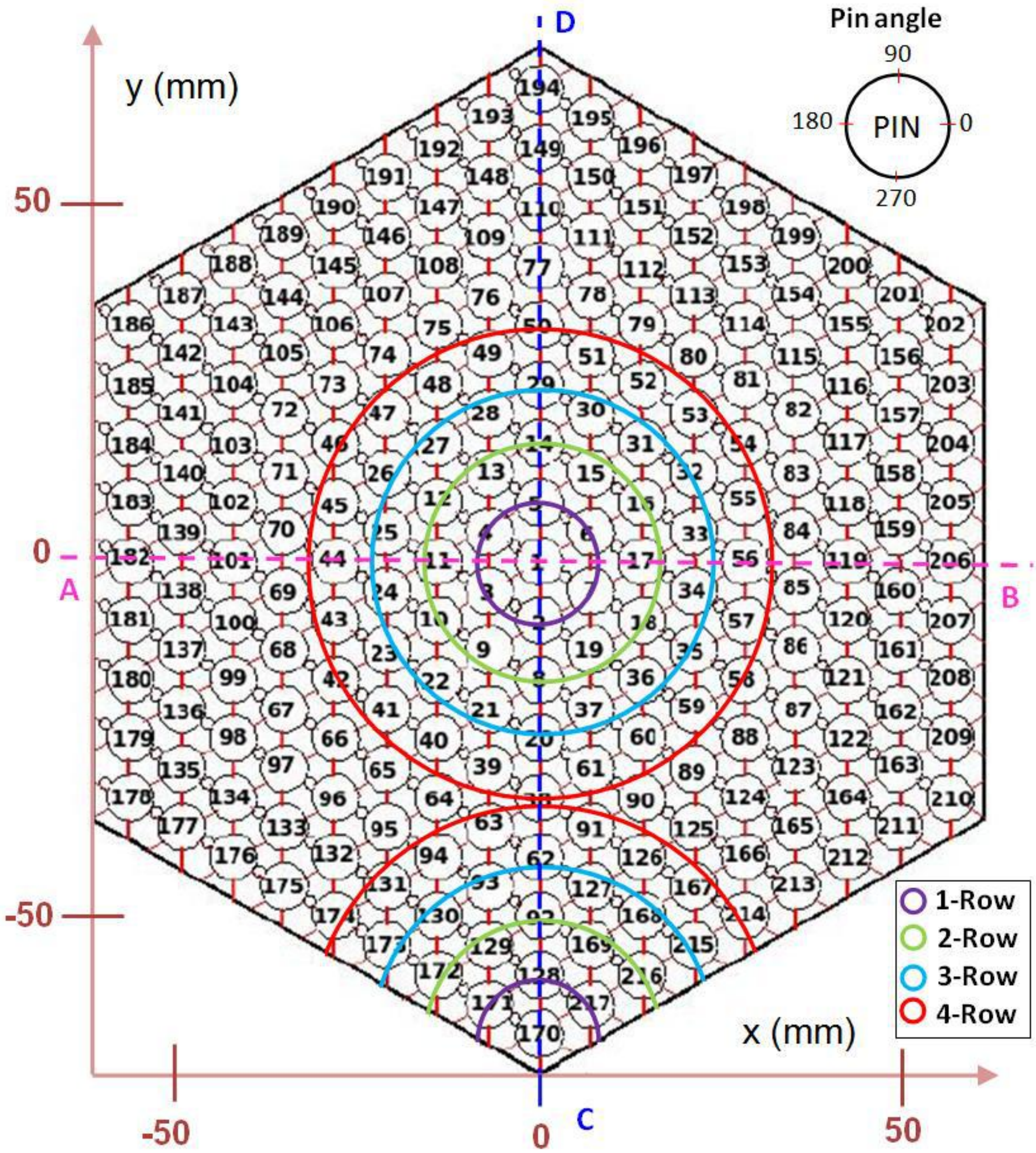

Fig. 6.3: Nomenclature to identify the pin location along with extents of various blockages.

TABLE 6.2: Nomenclature of planar blockages studied in the present analysis.

Blockage case	Type of blockage	Axial location (mm)	Blockage radius (mm)
B0	Unblocked	---	---
P1	1-row	700	8.28
P2	2-row	700	16.56
P3	3-row	700	24.84
P4	4-row	700	33.12
P5	1-row-corner	700	8.28
P6	2-row-corner	700	16.56
P7	3-row-corner	700	24.84
P8	4-row-corner	700	33.12
P9	4-row-top	800	33.12

The focus of the present study is to investigate the possibility of local sodium boiling during a planar blockage and detectability of such blockages before reaching coolant boiling. Towards this, the peak clad temperature exceeding the saturation temperature of sodium (1155 K) is taken as an important parameter. Further discussions are focused towards the difference in the thermal hydraulic consequences among blockages located in central and corner of the subassembly.

6.2.1 Flow and Temperature Fields in the Vicinity of Blockage

Critical attention is paid to velocity fields and temperature contours in two vertical cross sections A-B and C-D, depicted in Fig. 6.3. These features, in the vicinity of central and corner blockages are presented in Figs. 6.4-6.7. A strong reverse flow region is found behind all the cases of blockages (Figs. 6.4 and 6.6). This reverse flow zone is seen to disturb the velocity field in the bundle for a long length. The axial extent of the reverse flow zone in the case of central blockages is typically equal to diameter of the blockage. Beyond the reverse flow zone, the disturbance in velocity takes about 5 times the diameter to die down. In the case of single row corner blockage, the axial extent of the reverse flow zone is ~ 4 times the blockage diameter. But in other corner blockage cases, it is ~ 2 times the diameter of blockage. In general, reverse flow zone behind corner blockage is larger than that of central blockage. This effect could be attributed to the presence of hexcan walls, which inhibits flow redistribution in the downstream of corner blockage. Another possible reason for this behavior can be explained by referring to the pin bundle hydraulics discussed in chapter 4. It is noted that, compared to the central region of subassembly, the flow resistance in the periphery is relatively low. Further, the normalized axial velocity in central and peripheral regions of an unblocked bundle is 0.98 and 1.12 respectively. Since the flow diverted by a corner blockage will find a lesser resistance path, (nearby peripheral regions) compared to path available in the blockage downstream, the reattachment of flow in the case of corner blockage will be less rapid compared to that of central blockage. In addition, it may be highlighted that in the case of porous columnar blockage, no reverse flow zone was observed. It is noticed that small flow through the porous blockage annihilated the formation of any recirculation zone.

Effect of recirculation zone is also reflected in the temperature field behind the blockage (Figs. 6.5 and 6.7). From Fig. 6.7 it can be seen that, in the case of corner blockage of any radius, the peak temperature within blockage lies radially towards the center of the subassembly. This is due to radial non uniformity in heat applied near the wall (pin with heat flux on one side and adiabatic wall on other side).

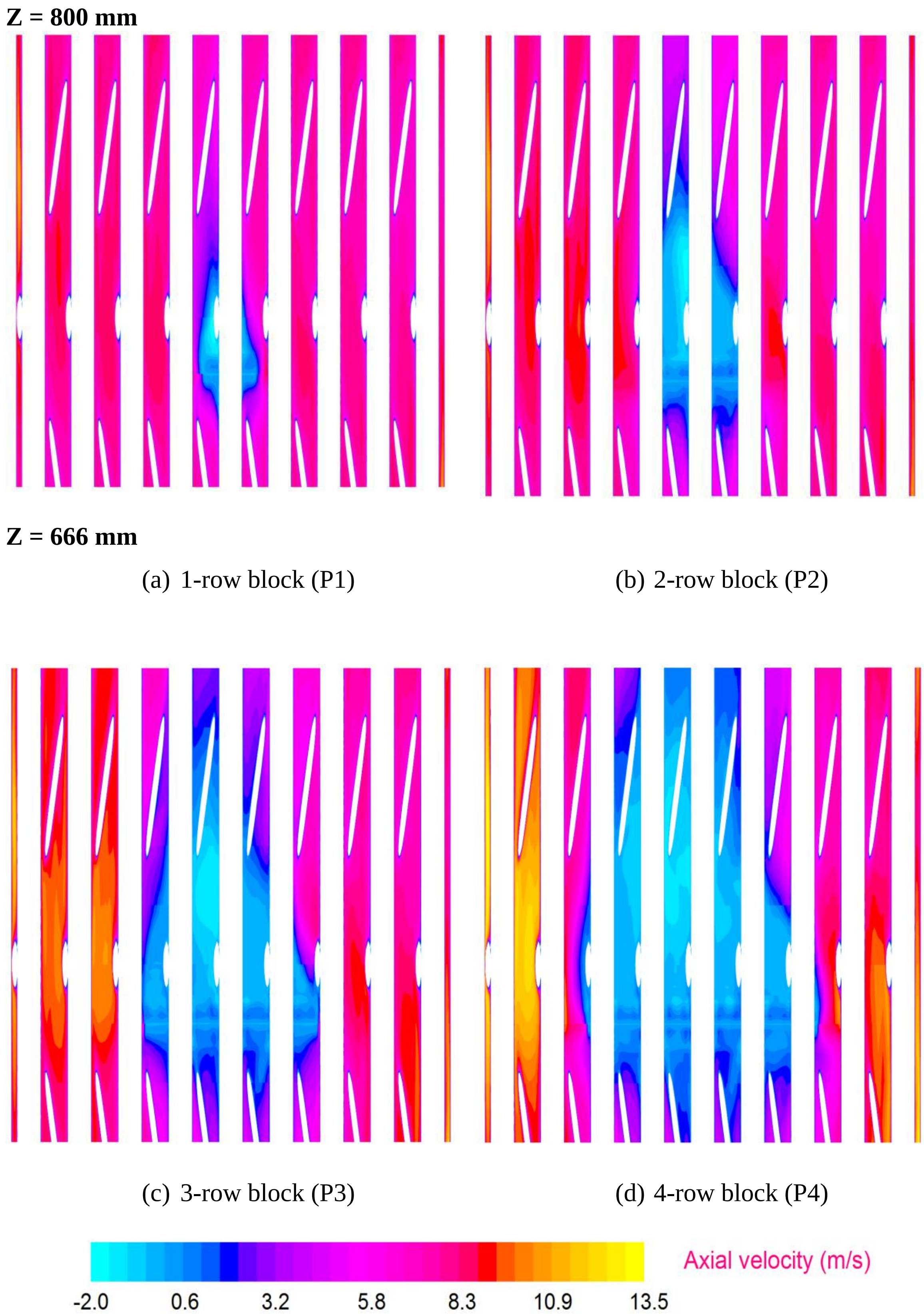

Fig. 6.4: Axial velocity field along section A-B from elevation 666 – 800 mm; Blockage around central pin.

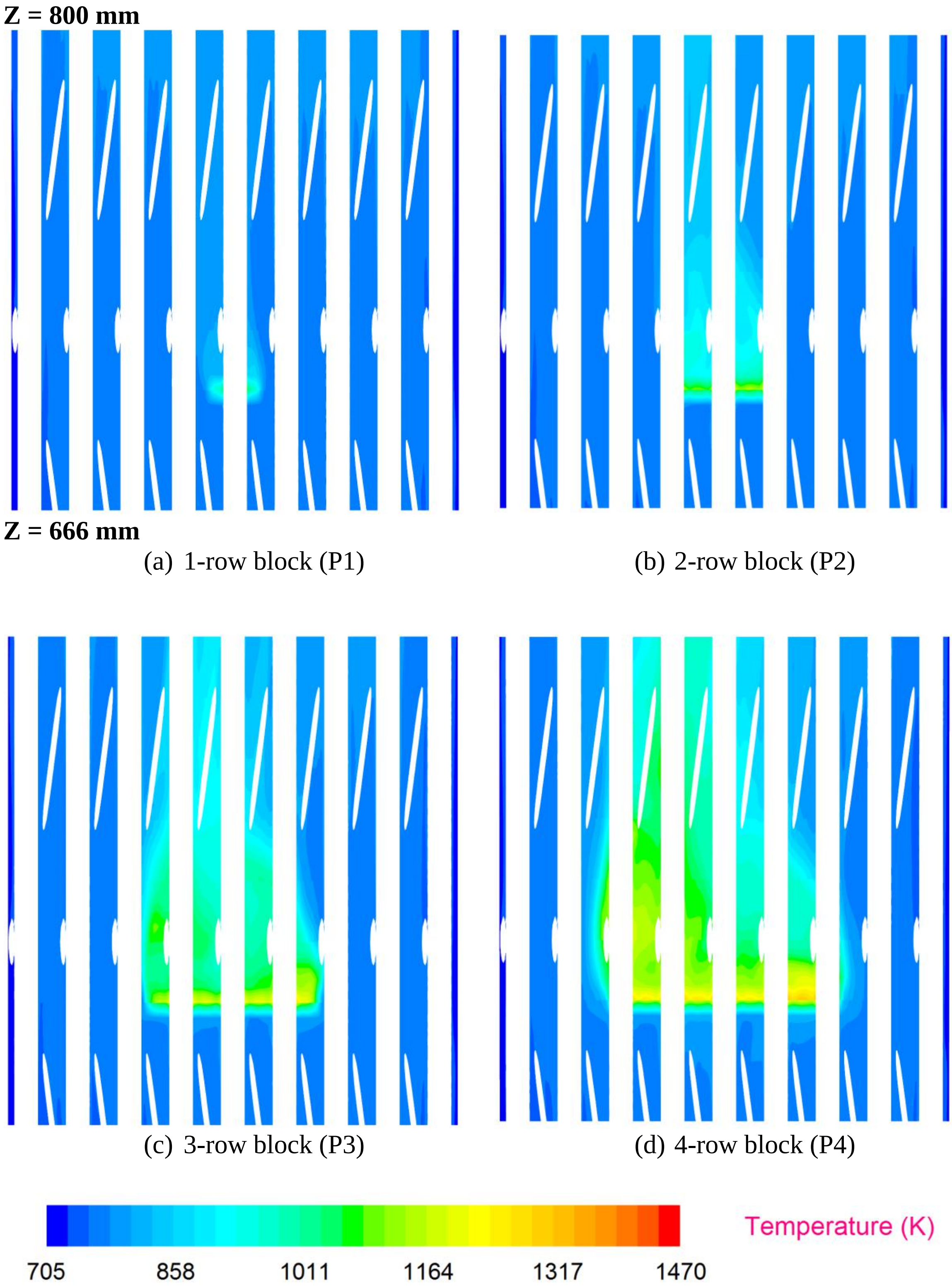

Fig. 6.5: Temperature field along section A-B from elevation 666 – 800 mm; Blockage around central pin.

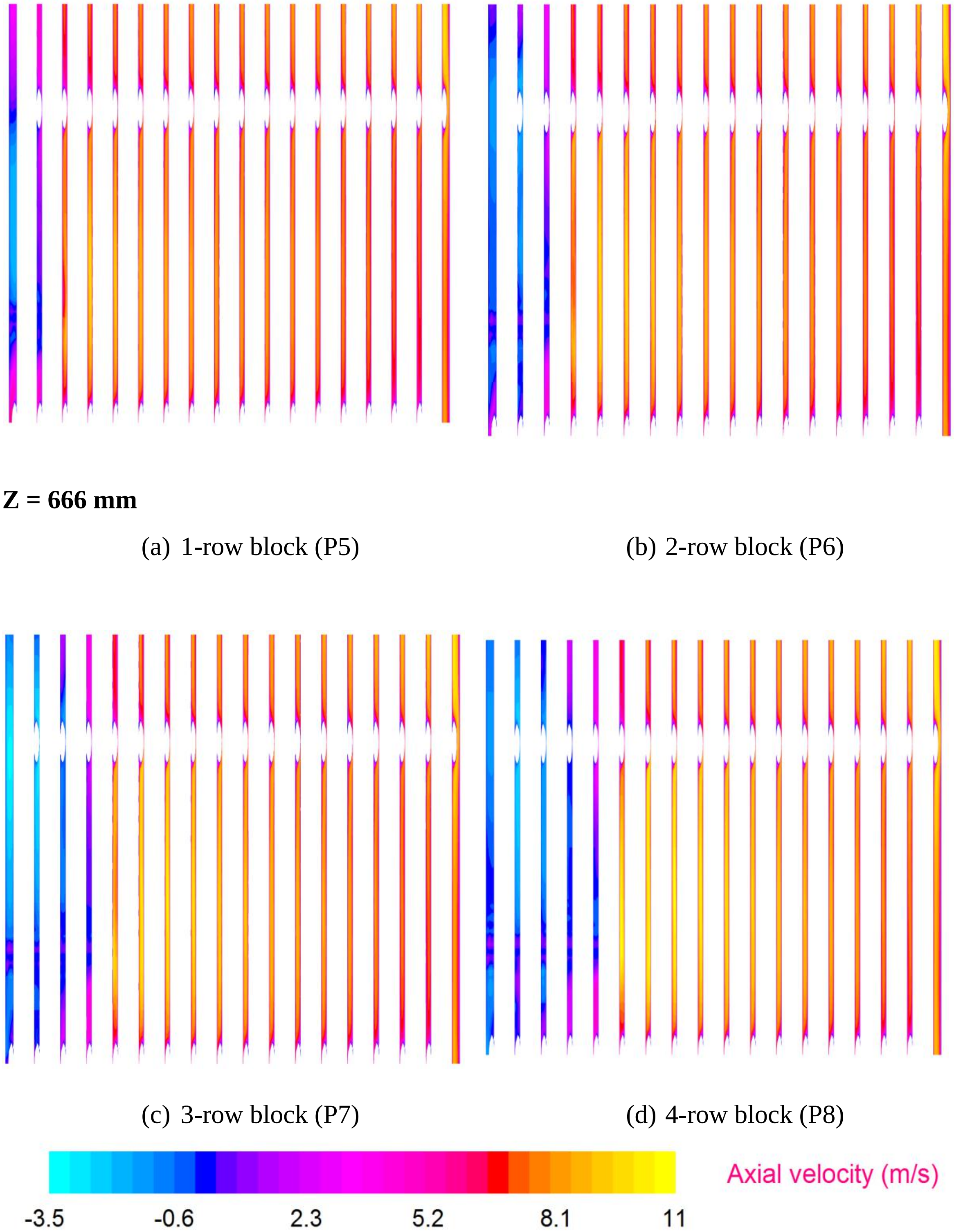

(a) 1-row block (P5)

(b) 2-row block (P6)

(c) 3-row block (P7)

(d) 4-row block (P8)

Fig. 6.6: Axial velocity field along section C-D from elevation 666 – 800 mm; Blockage around corner pin.

Z = 800 mm

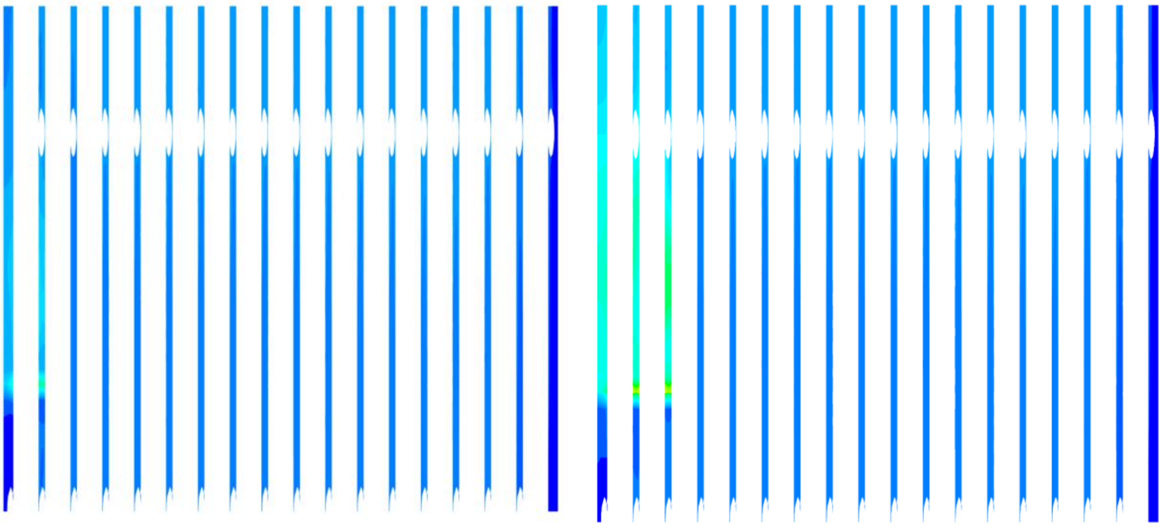

Z = 666 mm

(a) 1-row block (P5) (b) 2-row block (P6)

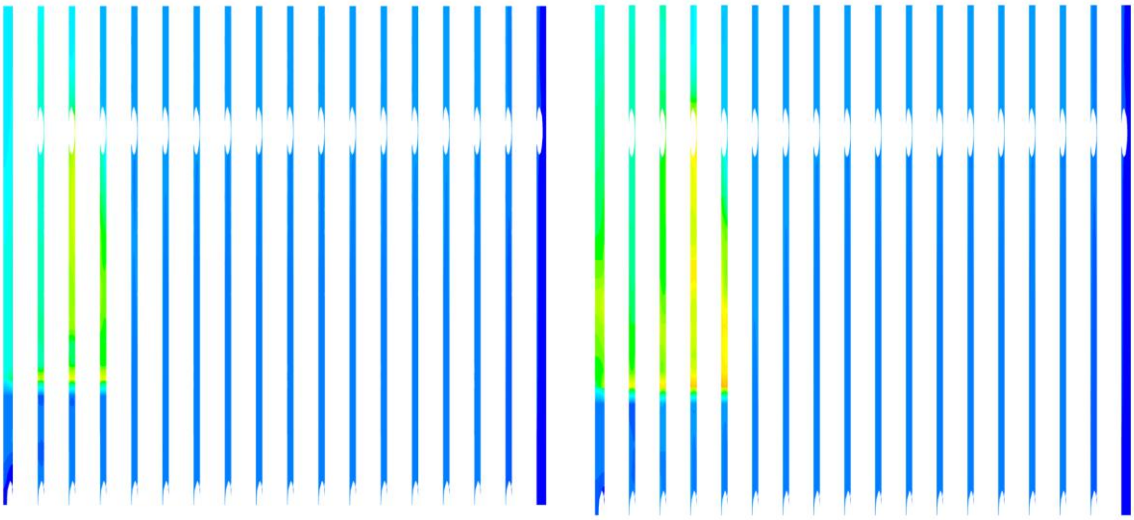

(c) 3-row block (P7) (d) 4-row block (P8)

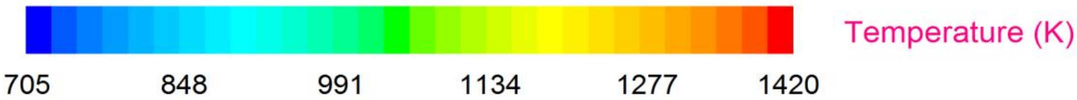

Fig. 6.7: Temperature field along section C-D from elevation 666 – 800 mm; Blockage around corner pin.

Temperature fields in the axial cross section for 4 row blockage located at elevation of 700 mm and 800 mm are presented in Fig. 6.8. Large asymmetry in temperature field within the blockage is observed, with the peak temperature lying near the periphery of the blockage. Further, the temperature distribution within the blockage is found to be strongly dependent on the wire wrap orientation in the upstream of blockage. This is evident in Fig. 6.8, where, if the blockage is at 700 mm, the maximum temperature region occurs in the lower half, whereas in a similar case of blockage located at 800 mm, the maximum temperature region lies in the upper half. This is due to the fact that the wires play an important role in inducing inter-channel cross flows. In typical orientations, there is flow of hot sodium from the center of the blockage to the periphery of the blockage, leading to an increase in the sodium temperature in the periphery of the blockage. Further, in a planar blockage experiment on a grid spaced bundle, Huber and Peppler (1985) observed that the peak temperature occurs in the vortex center of recirculating zone in the downstream of the blockage. In the case of grid spaced bundle though the peak temperature occurs in the periphery of the blocked region, the temperature field is symmetric about the axis. Similar findings were also reported by Krisch (1973) and Jeong et al., (2009). But, the temperature field becomes asymmetric in the case of wire wrapped bundle.

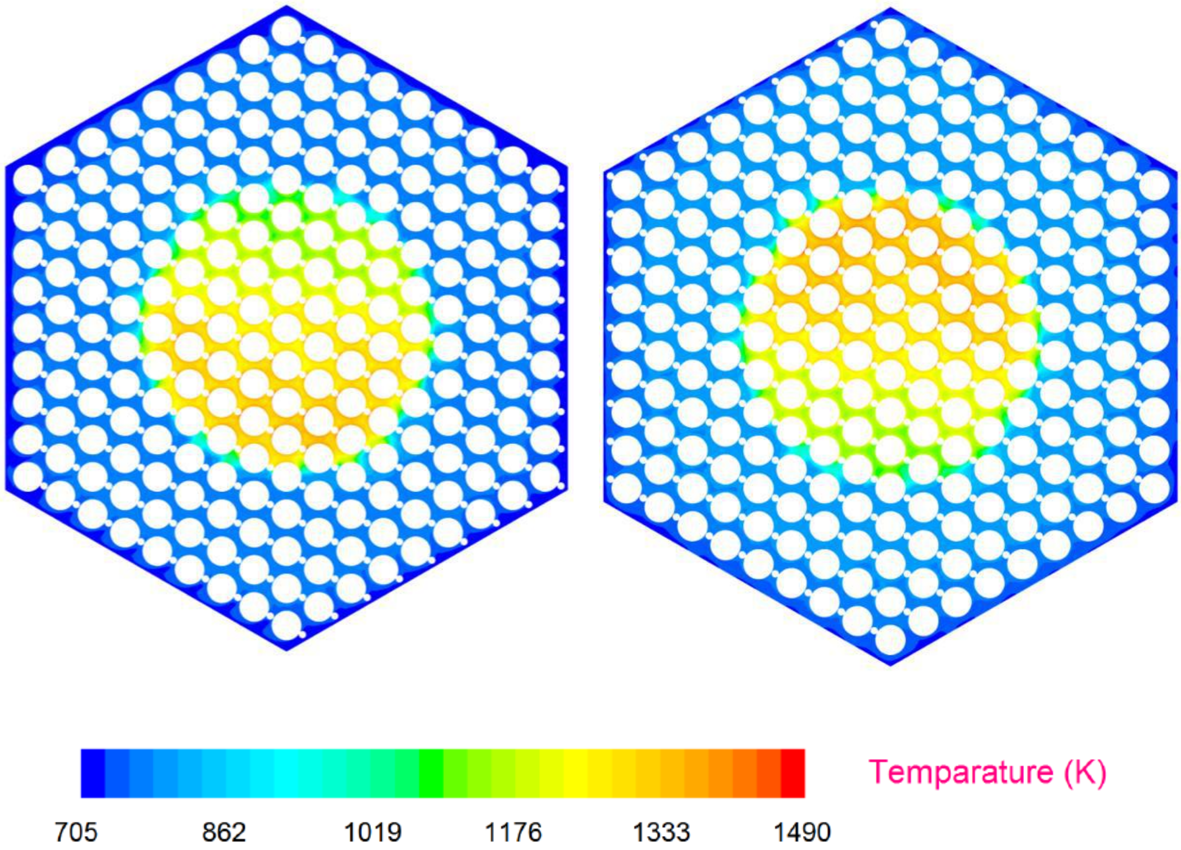

(a) 4-row blockage at 700 mm from inlet (P4)

(b) 4-row blockage at 800 mm from inlet (P9)

Fig. 6.8: Temperature field in the axial cross-section.

6.2.2 Peak Temperature in Central Blockage

Peak clad temperature (Tcp) as a function of axial location, in various cases of central blockage is shown in Fig. 6.9a. Further, the value of peak clad temperature within the blockage and outside the blockage for various cases of blockage is presented in Table 6.3. It can be seen that as expected the peak clad temperature in all the cases lies within the blockage and temperature drops drastically in the region behind the blockage. But further downstream, considerable rise in peak temperature is visible. Though in all the cases, peak clad temperature within blockage (steel region) is above saturation temperature, only in 3-row and 4-row blockage cases, the temperature of clad which is in contact with sodium (clad lying outside the blockage) rises above saturation temperature. Hence, the possibility of boiling prevails only in the cases of 3 and 4 row central blockages.

6.2.3 Peak Temperature in Corner Blockage

The peak clad temperature as a function of axial location, in different cases of corner blockage is shown in Fig. 6.9b. Similar to the central blockage cases, in all the corner blockage cases the peak clad temperature lies within the blockage zone and it drops drastically in the region behind the blockage. This is followed by a gradual rise in the downstream of blockage. The peak clad temperature within blockage is lower in the case of corner blockage compared to the central blockage (Ref. Fig. 6.9 and Table 6.3).

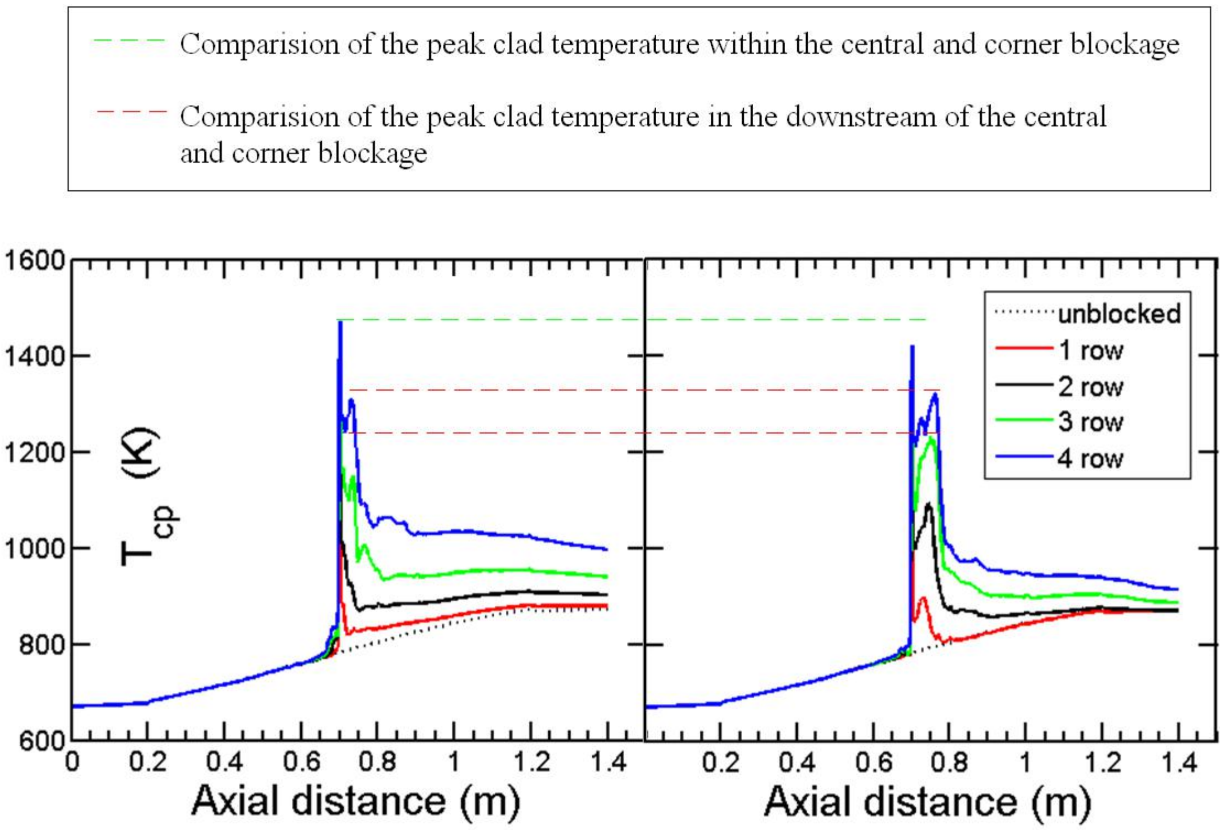

(a) Central blockage cases. (b) Corner blockage cases.

Fig. 6.9: Peak clad temperature at various axial sections along the length.

On the other hand, the clad temperature outside the blockage is more in corner blockage than that in central blockages (Ref. Fig. 6.9 and Table 6.3). This shows that, there is a marginally higher risk of sodium boiling in the case corner blockage compared to central blockage. As noted in section 6.2.1, this is due to the large reverse flow zone in the downstream of the corner blockage compared to that in the case of central blockage. For both 3 and 4 row corner blockage cases the clad temperature outside the blockage exceeds the saturation temperature, which would lead to sodium boiling.

TABLE 6.3: Peak clad temperature (K) within and outside blockage and peak circumferential clad temperature variation in different blockage cases, along with the location and pin number.

Blockage case	Peak clad temperature inside blockage (K) (Pin No.)		Peak clad temperature downstream of blockage (K) (Pin No)		Peak circumferential clad temperature variation (K) (Pin No)	
B0	872	---	872	---	57	---
P1	1170	(1)	886	(3)	360	(7)
P2	1288	(2)	1020	(11)	482	(19)
P3	1392	(8)	1174*	(37)	596	(36)
P4	1471	(60)	1310*	(34)	645	(61)
P5	1116	(170)	897	(171)	306	(128)
P6	1262	(128)	1093	(172)	422	(129)
P7	1318	(92)	1229*	(92)	466	(93)
P8	1418	(127)	1320*	(130)	570	(91)
P9	1491	(30)	1324*	(25)	638	(47)

* – Temperature crossing boiling criteria

6.2.4 Circumferential Profile of Clad Temperature in Blocked Bundles

Large temperature variation around the circumference of the pin will result in thermal stress and pose an increased threat to clad integrity. The peak circumferential clad temperature variation in different cases of blockage is extracted and reported in Table 6.3 along with its location in the bundle. The temperature profiles along the circumference of the pin where circumferential variation peaks for 1-row (P1) and 4-row (P4) blockages are depicted in Fig. 6.10. The maximum variation in the case of unblocked bundle is 58°C, whereas it increases up to 650 °C in the case of large radius planar blockage cases (4-row blockage). It should be noted that in the case of porous blockage, the maximum variation in clad temperature observed is ~450 °C. It can be seen from the Table 6.3, that larger the radius of blockage, large is the circumferential temperature variation. Further, circumferential variation in the case of central blockage is larger than that of the corner blockage. It can be noted that the largest variation occurs on the pin which lies in the periphery of the blockage, where major portion of the pin, lies within blockage (hot), and a minor portion is exposed to sodium flow outside blockage (cold).

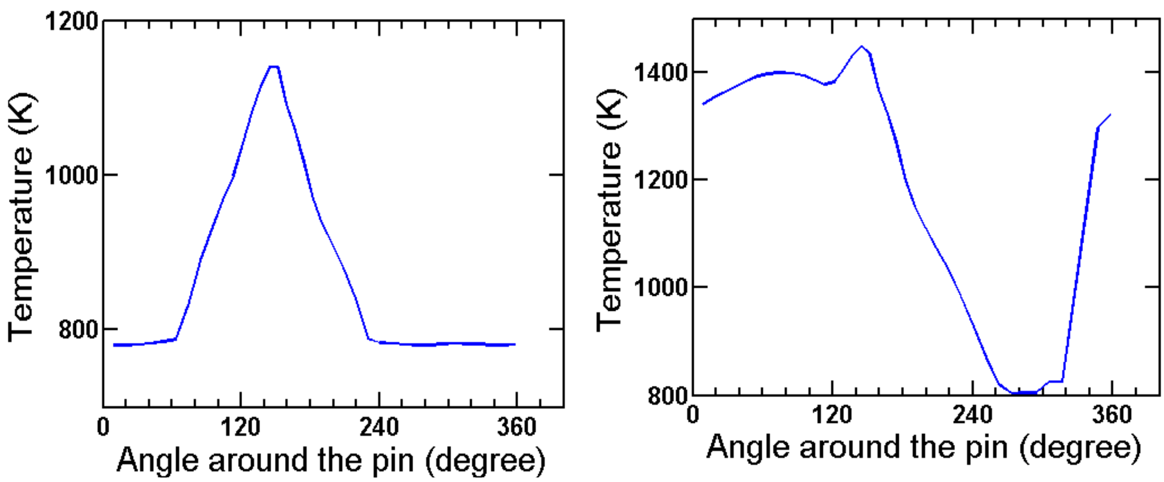

(a) pin 7 of 1 row blockage (P1) (b) pin 61 of 4 row blockage (P4)

Fig. 6.10: Circumferential temperature variation around the pin at an axial location it is maximum.

In addition, studies have been carried out to understand the influence of clad conduction modeling on existing circumferential temperature variation. Towards this, a 2-dimentional conduction study is carried out for the clad with inner radius 2.8 mm and outer radius of 3.3 mm. Here, heat flux boundary condition is applied at the inner surface of clad and the fluid temperature and heat transfer coefficient profile obtained from the CFD study of an adverse blockage case are applied at the outer surface of clad. An interior wall is defined for every 60° sector. In one case, the circumferential heat transfer is allowed, while in another it is restricted. It was found that compared to the case that allowed circumferential conduction, the case without conduction over predicts the circumferential temperature variation by < 2% (Refer Fig. 6.11). This value in the former is 565 K, while that in the later is 575 K. This shows that the circumferential temperature variation would persist even if the clad conduction is considered.

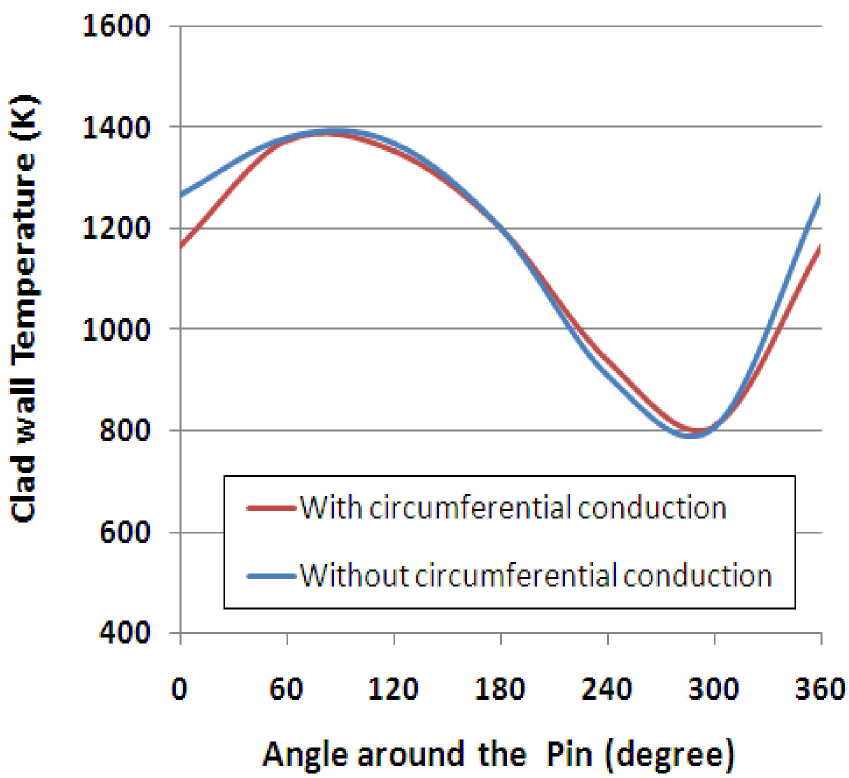

Fig. 6.11: Circumferential temperature variation around the pin.

6.2.5 Detectability of Blockage

As discussed in the chapter 5, an increase in the bulk sodium temperature at fuel subassembly outlet by 10 ºC will initiate automatic reactor trip, while a 5 ºC rise provides alarm to the operators. It was determined from heat balance calculations, that 6 % and 3 % subassembly reductions are necessary for flow bulk sodium temperature increase of 10 °C and 5 °C respectively. The maximum bulk temperature rise, calculated based on bundle pressure drop due blockage predicted in the present analysis is < 4.5 °C (Refer Table 6.4). This shows that, blockage detection before sodium boiling is not possible.

TABLE 6.4: Pin bundle pressure drop, percentage flow reduction, bulk and peak temperature rise at outlet due to blockage.

Blockage case	Pressure drop (bars)	Flow reduction (%)	Bulk sodium temperature rise at outlet (K)	Maximum sodium temperature at bundle outlet (K)	Peak sodium temperatur e rise (K)
B0	1.837	-	-	868.6	-
P1	1.854	0.21	0.4	876.3	7.7
P2	1.878	0.50	0.9	900.8	32.2
P3	1.935	1.16	2.1	939.6	71.0
P4	2.062	2.50	4.5	997.4	128.8
P5	1.854	0.21	0.4	867.0	-1.6
P6	1.869	0.39	0.7	868.8	0.2
P7	1.896	0.71	1.2	887.1	18.5
P8	1.943	1.25	2.2	916.0	47.4
P9	2.061	2.49	4.5	1005.0	136.4

In contrast to bulk sodium temperature rise, the peak sodium temperature rise at the bundle outlet due to blockage is found to be more rapid (Table 6.4). As expected, outlet peak sodium temperature rise is lower in corner blockage compared to that in the central blockage. But in the case of 1-row corner blockage (P5) there is marginal drop in the outlet peak sodium temperature compared to that of unblocked bundle case. This is because the 1-row corner blockage has actually promoted mixing of cold peripheral sodium and hot central sodium. But in the case of corner blockage with large radial extent, a positive rise in peak sodium temperature at outlet is observed. Pictorial representation of the temperature distribution near the outlet (1300 mm form inlet) for different blocked and unblocked bundle is shown in Fig. 6.12. It could be inferred that the temperature distribution is appreciably disturbed by the presence of blockage. Monitoring of subassembly outlet distribution for any major anomaly in temperature profile would offer a possible way for early detection of blockage.

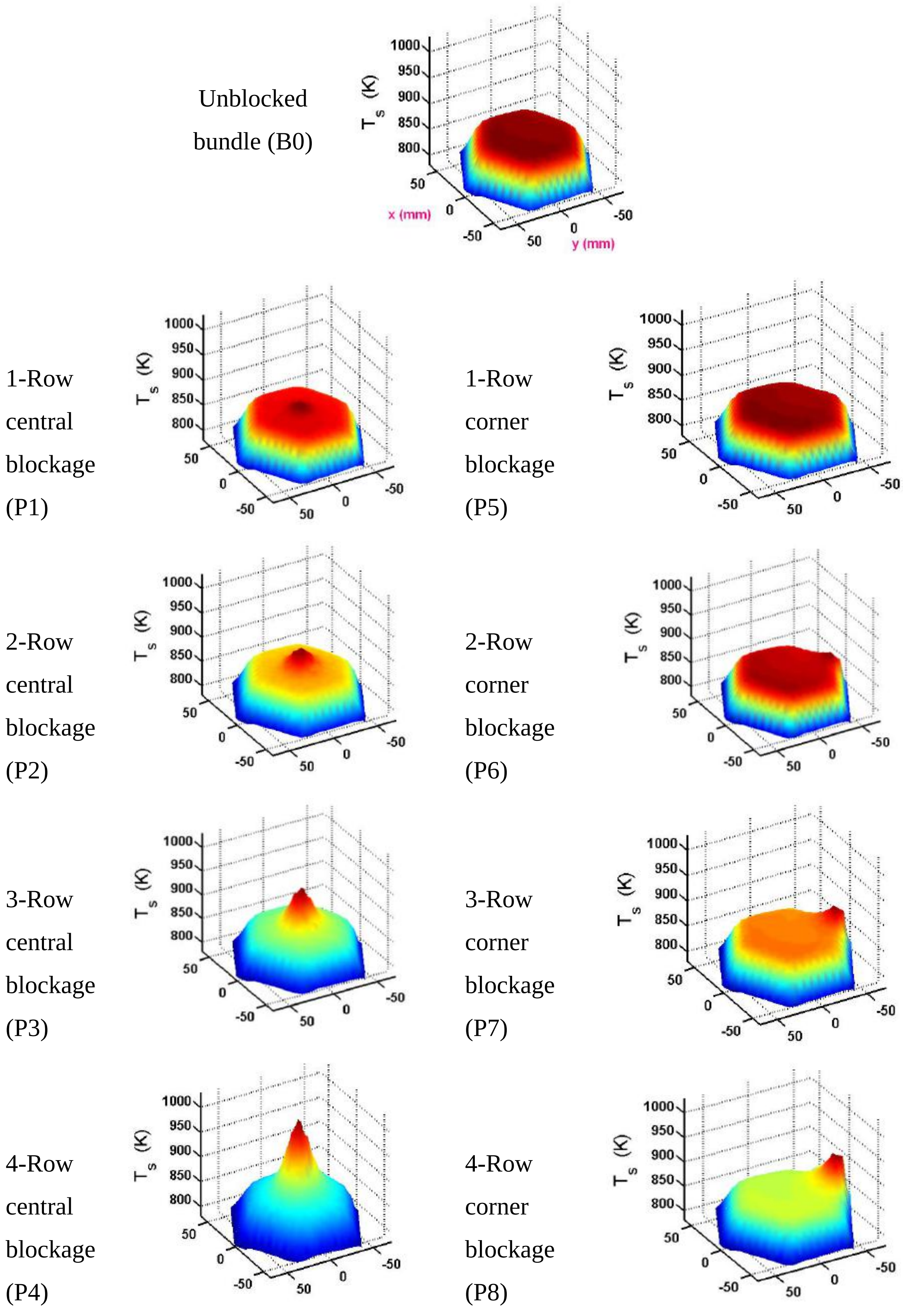

Fig. 6.12: Comparison of temperature profile at 1300 mm from inlet for different cases of blocked and unblocked bundles.

6.3 CLOSURE

Three dimensional CFD based investigation has been carried out to understand the thermal hydraulic consequences of planar blockage within a prototype fuel subassembly. It is seen that in the cases of central and corner blockages with 3 or more rows blocked, the peak clad temperature outside of blockage exceeds the saturation temperature of sodium, highlighting the risk of sodium boiling. Unlike the case of porous blockage, large reverse flow zone is observed in the case of planar blockage. The extent of wake zone is ~ 2 to 4 times the diameter of blockage in corner blockage, whereas it is roughly equal to the diameter of blockage in the case of central blockage. Large circumferential temperature variation up to 650 °C is observed in the case of 4-row blockage. The pins in the periphery of the blocked zone are prone to peak circumferential temperature variation around them. None of the blockage cases studied in the present analysis gave rise to outlet bulk sodium temperature exceeding alarm limit of 5 °C. Hence detecting these blockages using outlet bulk temperature monitoring system is not possible. The disturbance in temperature field created by any blockage is felt up to outlet. Hence, monitoring the discrepancies in outlet temperature profile will be a possible approach for early detection of blockage.

7 CONCLUSIONS AND SCOPE FOR FUTURE RESEARCH

7.0 INTRODUCTION

The present thesis is focused towards (i) flow and temperature characteristics in a prototype fuel subassembly during normal operating condition, (ii) thermal hydraulic consequences of porous internal blockage in the active region, (iii) critical length of the internal blockages that would lead to local sodium boiling, (iv) thermal hydraulic consequences of planar internal blockage and (v) detectability of flow blockages by core monitoring thermocouple.

For these purpose, RANS based CFD simulation of flow and temperature fields in a wire wrapped 217 pin fast reactor fuel subassembly has been carried out. Structured mesh and parallel processing have been adopted to reduce the computational time for a 7 pitch full length fuel subassembly. The CFD models have been validated against the published correlations of Nusselt number and friction factor and benchmark blockage experiments on a 19 pin bundle reported in literature. Further, to understand the boiling phenomena of sodium, a simplified case of flow boiling through pipe is studied. Detailed validation of the various models used in the present study is performed with the published results in the open literature. Major conclusions of the present research are highlighted in the following sections.

7.1 VELOCITY AND TEMPERATURE FIELDS IN A 217 PIN WIRE WRAPPED FUEL BUNDLE

At the outset, local flow pattern and heat transfer characteristics of sodium in a 217 pin wire-wrapped fuel bundle under normal conditions have been investigated by 3 dimensional steady state CFD simulation. Subchannel axial mass flow rate, inter-subchannal cross flow, influence of bundle dimensions on cross flow, circumferential swirl generated as a result of wire-wrap, clad temperature distribution etc were studied in detail. Major findings of these investigations are,

- The axial mass flow rate in any subchannel exhibits periodic spatial variations in the fully developed region of the bundle. The periodicity of axial flow in a central subchannel is 1/3rd pitch of helical wire. The origin of these periodic variations has been traced to be due to the change in flow area and hydraulic resistance of the subchannel due to the passage of helical wire in the subchannal.
- In the central subchannels, the transverse flows crossing the subchannel lateral faces follow a cosine profile in the axial direction. These flows in different faces are identical but with a phase shift of 120°. Through the lateral faces of the edge subchannels facing the subassembly centre, a continuous inflow prevails for one half of the pitch while a continuous outflow prevails for the other half of the pitch. This causes larger amplitude axial flow oscillations in the peripheral subchannels compared to that in the central subchannels.
- Based on the predicted CFD results, correlations have been proposed for non-dimensional transverse velocity as a function of wire orientation, for various types of subchannels. These correlations can be adopted for development of advanced subchannel models for subassembly thermal hydraulic design. The present CFD

results can be used as a reference data to assess the models adopted to compute transverse velocity in the subchannel codes.

- The normalized peak transverse velocity in central subchannels is found to be proportional to the tangent of helix angle of the wire wrap. The proportionality constant (MF) is found to be a function of number of pins in the bundle. It is found to be 1 for 7 pin bundle and 1.5 for 217 pin bundle.
- A comparison of results from a full length fuel subassembly model and a periodic model suggests that thermal development is incomplete in fuel pin bundle of practical length.
- Prominent non monotonic clad temperature variations along the axial direction are seen in the peripheral and outer pins. Such variations are found to be due to transverse flow from center to the periphery and vice versa occurring in the vicinity of peripheral region.
- Peripheral pins experience large circumferential variation in clad temperature. This is due to the fact that one side of the peripheral pin is facing the heat generating pins while the other side is facing the adiabatic hexcan wall. Pins in central and middle regions do not show such large variation. Further, circumferential temperature profile of pins repeats for every pitch, while the mean value continuously increases.

7.2 THERMAL HYDRAULIC INVESTIGATIONS ON POROUS BLOCKAGE IN PIN BUNDLE

Thermal hydraulic features of blocked fuel subassemblies with various porous blockage configurations have been investigated through computational fluid dynamics approach. A wide range of blockage radius, porosity, mean particle diameter and location of blockage has been considered in this parametric analysis. The critical length of blockage that would result in local sodium boiling as a function of aforementioned blockage parameters has been estimated. Subsequently, the parametric zone posing risk of sodium boiling has been determined. Critical attention is paid to coolant mixing and flow and temperature fields downstream of the blockage zone. Important conclusions from the present investigations are:

- A large non-recirculating wake zone prevails in the downstream side of the porous blockage, with the extent of the wake zone increasing with blockage radius. The peak clad temperature occurs in the wake zone for large radius blockages and it does not always occur in the central pin.
- For a prototype subassembly with other pressure drop sections, the total flow reduction due to porous blockage is found to be < 2.5 % for all blockages that can lead to local sodium boiling. This suggests, that global bulk sodium temperature monitoring at the outlet of the subassembly is unlikely to detect slowly growing internal porous blockages.
- Comparing the sodium flow and temperature fields in unblocked and blocked bundles, it is found that the wake induced temperature non-uniformity persists even upto 3 helical pitch lengths. This suggests that the sodium temperature non-uniformity at the bundle exit can serve as an efficient blockage indicator, provided the cross section temperature is mapped by a proper instrumentation.
- Fuel-clad that are partly exposed to blockage are subjected to large circumferential temperature variation and the associated risk of thermal stress.
- Six subchannel blockage with 60% porosity and 0.5 mm mean particle diameter, does not induce boiling even up to a blockage length of 400 mm.

- For a single subchannel blockage there is no risk of sodium boiling, even upto 200 mm of length and porosity as low as 5%. Even in the adverse case of two adjoining subchannel blockage, sodium boiling does not occur.

7.3 THERMAL HYDRAULIC INVESTIGATIONS ON PLANAR BLOCKAGE IN PIN BUNDLE

Thermal hydraulic consequences of non porous planar blockage within a 217 pin wire wrapped prototype fuel subassembly is studied. Influence of the radial/axial locations and radius of the blockage is ascertained. The following are the major findings from the analysis:

- In the cases of central and corner planar blockages with 3 or more rows blocked, the peak clad temperature outside of blockage exceeds the saturation temperature of sodium, highlighting the risk of sodium boiling.
- Large asymmetry in temperature distribution within the blockage is observed, which is found to be a strong function of wire orientation in the upstream of blockage.
- Unlike the case of porous blockage, large reverse flow zone is observed in the case of planar blockage. The extent of wake zone is ~ 2 to 4 times the diameter of blockage in the case of corner blockage, whereas it is roughly equal to the diameter of blockage in the case of central blockage.
- For similar conditions of blockage, the possibility of sodium boiling is marginally higher in the corner blockage than in the central blockage.
- Large circumferential temperature variation up to 650 °C is observed in the case of 4-row blockage. The pins in the periphery of the blocked zone are prone to experience peak circumferential temperature variation around them.

- None of the blockage cases studied in the present analysis gave rise to outlet bulk sodium temperature exceeding alarm limit of 5 °C. Hence, detecting these blockages using outlet bulk temperature monitoring system is not possible.
- Larger the radial extent of blockage, longer is the reverse flow zone behind the blockage. The disturbance in temperature field created by any blockage is felt up to outlet. Hence, monitoring the discrepancies in outlet temperature profile will be a possible approach to detect blockage at an early stage.

7.4 SCOPE FOR FUTURE RESEARCH

- Computational simulation can be performed to identify the possible sodium temperature fluctuation in the upper plenum as a consequence of flow blockage, to decide the thermocouple characteristics.

- Suitable CFD based sodium boiling models have to be developed and validated against appropriate sodium experiments.

- Sodium boiling simulations in SFR fuel subassemblies can be performed to understand thermal hydraulic characteristics of pin bundle with blockage.

- Thermal hydraulics model shall be integrated with and reactor physics model to account for the possible change in the reactivity due to sodium voiding.

- Large scale experimental investigation and LES based computational investigations shall be conducted to further validate the cross flow and temperature fields.

APPENDIX-I: DETAILS OF CORRELATIONS AND THEIR APPLICABLE RANGES FOR PIN BUNDLE

Reference	Pe	X = P/D	Fluid	Nusselt number correlation
Kazimi and Carelli (1976)	20-1000	1.2-1.3	Na, Hg and Na-Hg	$Nu = 4 + \left[0.33(X)^{3.8}\left(\frac{Pe}{100}\right)^{0.86}\right] + \left[0.16(X)^{5}\right]$

Reference	Re	X = P/D	No. of pins	H/D	Friction factor correlations
Novendstern (1972)	2600 - 10^5	1.06 – 1.42	19 - 217	8 - 96	$f = f_1 (X_1)^2 \left(\frac{D_{eb}}{D_{e1}}\right)$ $f_1 = M(f_s)$ $f_s = 0.316 / \mathrm{Re}_1^{0.25}$ $M = \left(\frac{1.034}{(X)^{0.124}} + \frac{29.7(X)^{6.94}\mathrm{Re}_1^{0.086}}{(H/D)^{2.239}}\right)^{0.885}$ $\mathrm{Re}_1 = X_1 (D_{e1}/D_{eb})\mathrm{Re}$ $X_1 = A_b / \left(\begin{array}{c} N_1 A_1 + N_2 A_2 (D_{e2}/D_{e1})^{0.714} \\ + N_3 A_3 (D_{e3}/D_{e1})^{0.714} \end{array}\right)$
Rehme (1973)	200 – 2.5×10^5	1.125 –	7 - 217	8 - 50	$f = \left(\frac{64}{\mathrm{Re}}F^5 + \frac{0.0816}{\mathrm{Re}^{0.133}}F^{50.9335}\right) Nr\pi \frac{D+D_w}{P_{wb}}$

		1.417			$F = X^{0.5} + \left(7.6(X)^2 (D+D_w)/H\right)^{2.16}$
Cheng and Todreas (1986)	50–10^6	1.025 –1.42	19–217	8 - 50	For Re > Re_T $Re_T = 10000\left(10^{0.7(P/D-1)}\right)$ $C_{ft} = (0.8063 - 0.9022(\log(H/D)) + 0.3526(\log(H/D))^2) \times (P/D)^{9.7} (H/D)^{1.78-2(P/D)}$ $f = C_{ft} / Re^{0.18}$
Modified Engel (Bubelis et al. 2008)	50–10^5	1.067 – 1.082	19-61	7.7 -8.3	For Re > 5000 $f = 0.37 / Re^{0.25}$
Modified Baxi and Dalla Donne (Bubelis et al. 2008)	50–10^5	1.06 – 1.42	19 - 217	8 - 96	For Re > 5000 $f = M(f_s)$ $f = 0.316 / Re_1^{0.25}$ $M = \left(\frac{1.034}{(X)^{0.124}} + \frac{29.7(X)^{6.94} Re_1^{0.086}}{(H/D)^{2.239}}\right)^{0.885}$

Reference	Correlation for swirl flow normalized with local axial velocity
Chiu et al., (1978)	$$V_{Lt}^{*} = 10.5\left(\frac{P-D}{P}\right)^{0.35}\left(\frac{A_{r2}}{A_{s2}}\right)^{0.5}\frac{D+D_w}{\sqrt{\pi^2(D+D_w)^2+H^2}}$$ Where, $$A_{s2} = P\left(\frac{D}{2}+D_w\right)-\frac{\pi}{8}D^2$$ $$A_{r2} = \frac{\pi}{4}\left(\frac{D}{2}+D_w\right)^2-\frac{\pi}{16}D^2$$

REFERENCES

Ahmad, I., Kim, K.Y., 2006. Flow and Convective Heat Transfer Analysis Using RANS for a Wire-Wrapped Fuel Assembly. Journal of Mechanical Science and Technology 20 (**9**), 1514-1524.

Amgad, S., Salah, E.D.E.M, 2012. CFD simulation of flow blockage through a coolant channel of a typical material testing reactor core. Annals of Nuclear Energy 41, 26-39.

Amit, K.C., Prasad, B.V.S.S.S., Patnaik, B.S.V., 2013. Thermal hydraulics of rod bundles: The effect of eccentricity. Nuclear Engineering and Design 263, 218-240.

Basehore, K.L., Todreas, N.E., 1980. SUPERENERGY-2: A Multiassembly Steady-State Computer Code for LMFBR Core Thermal–Hydraulic Analysis, PNL-3379. Pacific Northwest Laboratory, Richland, WA.

Baxi, Dalle-Donne, 1981. Heat Transfer and Fluid Flow in Nuclear Systems. Pergamon Press, ISBN 0-08-027181-2.

Bogoslovskaya, G.P., Zhukov, A.V., Sorokin, A.P., 2000. Models and characteristics of interchannel exchange in pin bundles cooled by liquid metal, XA0055052.

Blasius, P.R.H., 1913. Das Aehnlichkeitsgesetz bei Reibungsvorgangen in Flussigkeiten Forschugsheft 131, 1-141.

Bubelis, E., Schikorr, M., 2008. Review and proposal for best fit of wire-wrapped fuel bundle friction factor and pressure drop predictions using various existing correlations. Nuclear Engineering and Design 238, 3299–3320.

Central Electricity Authority, 2017. Growth of electricity sector in India from 1947-2017. Retrieved from CEA Website http://www.cea.nic.in/reports/others/planning/pdm/growth_2017.pdf.

CFD Expert, 2009. Zeus Numerix Pvt. Ltd., Mumbai-400076.

Chang, W.P., Ha, K.S., Suk, S.D., Jeong, H.Y., 2011. A comparative study of the MATRA-LMR-FB calculation with the SABRE result for the flow blockage accident in the sodium cooled fast reactor. Nuclear Engineering and Design 241, 5225–5237.

Chen, S.K., Todreas, N.E., Nguyen, N.T., 2014. Evaluation of existing correlations for the prediction of pressure drop in wire-wrapped hexagonal array pin bundles. Nuclear Engineering and Design 267, 109-131.

Cheng, S.K., Todreas, N.E., 1986. Hydrodynamic models and correlations for bare and wire-wrapped hexagonal rod bundles - bundle friction factors, sub-channel friction factors and mixing parameters. Nuclear Engineering and Design 92, 227-251.

Chiu, C., Rohsenow, W. M., Todreas, N. E., October 1978a. Turbulent sweeping flow mixing model for wire wrapped LMFBR assemblies. C00-2245-55TR, Revision 1, Massachusetts Institute of Technology, Cambridge, MA.

Choi, et al., 2003. Measurement of pressure drop in a full-scale fuel assembly of a liquid metal reactor. Journal of Pressure Vessel Technology 125, 233-238.

Cole, R., 1960. A Photographic Study of Pool Boiling in the Region of the Critical Heat Flux. AIChEJ, 6, 533–542.

Di Piazza., Fabrizio, M., Mariano, T., Alessandro A., 2014. A CFD analysis of flow blockage phenomena in ALFRED LFR demo fuel assembly. Nuclear Engineering and Design 276, 202–215.

Engel, F. C., Markley, R. A., Bishop, A. A., 1979. Laminar, transition and turbulent parallel flow pressure drop across Wire-wrap-spaced rod bundles. Nuclear Science and Engineering 69, 290-296.

Ergun, S., 1952. Fluid flow through packed columns. Chem. Eng. Prog. 48, 89–94

Fanning, T.H., Pointer, W.D., Thomas, J.W., 2009. Multi-resolution modeling of subassembly pin bundles for advanced fast reactor safety simulations. M&C 2009, Saratoga Springs, USA.

Fernandez, E. F., Carajilescov, P., 2000. Static Pressure and Wall Shear Stress Distributions in air Flow in a Seven Wire-Wrapped Rod Bundle. Journal of the Brazilian Society of Mechanical Sciences 22 (2).

Fontana, M.H., Kress, T.S., Parsly, L.F., Thomas, D.G., Wantland, J.L., 1973. Effect of partial blockages in simulated LMFBR fuel assemblies, ORNL/TM-4324. Oak Ridge National Laboratory, Oak Ridge, Tennessee-37830.

Gajapathy, R., Velusamy, K., Selvaraj, P., Chellapani, P., Chetal, S.C., 2009. A comparative CFD investigation of helical wire-wrapped 7, 19 and 37 fuel pin bundles and its extendibility to 217 pin bundle. Nuclear Engineering and Design 239, 2279–2292.

Gajapathy, R., Velusamy, K., Selvaraj., Chellapandi, P., 2015. CFD investigation of effect of helical wire-wrap parameters on the thermal hydraulic performance of 217 pin bundle. Annals of Nuclear Energy 77, 498-513.

Gast, K., Smidt, D., 1970. Cooling disturbances in the core ofsodium-cooled fast reactors as causes of fast failure propagation. Nuclear Engineering and Design 14, 12-22.

Gopala, V.R., Doolaard, H., Sanna, V., Roelofs, F., 2014. Detailed investigation of flow through wire-wrapped fuel assemblies using computational fluid dynamics. THINS 2014 International Workshop, Modena, Italy.

Govindha Rasu, N., Velusamy, K., Sundararajan, T., Chellapandi, P., 2013. Investigations of flow and temperature field development in bare and wire-wrapped reactor fuel pin bundles cooled by sodium. Annals of Nuclear Energy 55, 29–41.

Govindha Rasu, N., Velusamy, K., Sundararajan, T., Chellapandi, P., 2014a. Simultaneous development of flow and temperature fields in wire-wrapped fuel pin bundles of sodium cooled fast reactor. Nuclear Engineering and Design 267, 44– 60.

Govindha Rasu, N., Velusamy, K., Sundararajan, T., Chellapandi, P., 2014b. Thermal hydraulic effect of porous blockage in fuel subassembly of sodium cooled fast reactor. Annals of Nuclear Energy 70, 64–81.

Han, J.T., 1977. Blockage in LMFBR fuel assemblies-A Review of experimental and theoretical studies, ORIL/TM1-5839. Oak Ridge National Laboratory, Oak Ridge, Tennessee-37830.

Hisashi Ninokata and Taka aki Okano, 1990. SABENA: Subassembly Boiling Evolution Numerical Analysis. Nuclear Engineering and Design 120, 349-367.

Hicks, E.P., Menzies, D.C., 1965. Theoretical studies on the fast reactor maximum accident. Proceedings of the conference on safety, Fuel and Core Design in Large Fast Power Reactors, ANL-7120, Argonne National Laboratory, Argonne/ IL 654-670.

Holtz, R. E., and Fauske, H. K., 1971. The prediction of incipient boiling superheats in liquid metal cooled reactor systems. Nuclear Engineering and Design 16, 253-265.

Huber, F., Peppler, W., 1985. Summary and Implications of Out-of-pile Investigations of Local Cooling Distributions in LMFBR Subassembly Geometry under Single-phase and Boiling Conditions. KfK 3927, Kernforschungszentrum Karlsruhe.

IEA, 2017. Key world energy statistics. Retrieved from IEA Website: https://www.iea.org/publications/freepublications/publication/KeyWorld2017.pdf

Ishii, M., 1979. Two-fluid model for two-phase flow. 2nd International Workshop on Two-phase Flow Fundamentals. RPI, Troy, NY.

Jeong, H.Y., Ha, K.S., Kwon, Y.M., Lee, Y.B., Hahn, D., 2009. Analysis of three different types of blockage in a sodium flow path with the MATRA-LMR-FB code. Annals of Nuclear Energy 36, 583-589.

Kazimi, M.S., Carelli, M.D., 1976. Heat transfer correlation for Analysis of CRBRP Assemblies. CRBRP-ARD-0034.

Kim, W.S., Kim, Y.G., Kim, Y.J., 2002. A subchannel analysis code MATRA-LMR for wire wrapped LMR subassembly. Annals of Nuclear Energy 29, 303–321.

Kleijn, H.R., 1970. Reactivity change associated with sodium voiding of large liquid metal fast breeder reactors. Tripartite USSR – Belgian – Dutch Symposium on Fast Reactor Physics, Melekess.

Krisch, D., 1973. Investigations on the flow and temperature distribution downstream of local coolant blockages in rod bundle subassemblies. Nuclear Engineering and Design 31, 266-279.

Kurul, N. and Podowski, M.Z., 1991. On the Modeling of Multidimensional Effects in Boiling Channels. Proc. of the 27th National Heat Transfer Conference, Minneapolis, MN.

Lafay, J., Menant, B. and Barroil, J., 1975. Local pressure measurements and peripheral flow visualization in a water 19-rod bundle compared with FLICA II B calculations: influence of helical wire-wrap spacer system. AIChE/ASME Heat Transfer Conf., Paper 75-HT-22, Cal.

Launder, B.E., and Spalding, D.B., 1974. The numerical computation of turbulent flows. Computer Methods in Applied Mechanics and Engineering 3(2), 269-289.

Liu, X.J., Scarpelli, N., 2015. Development of a sub-channel code for liquid metal cooled fuel assembly. Annals of Nuclear Energy 77, 425–435.

Lopez de Bertodano, M., 1991. Turbulent Bubbly Flow in a Triangular Duct. Ph.D. Thesis. Rensselaer Polytechnic Institute, Troy, New York.

Lorenz, J. J., Ginsberg, T., 1977. Coolant mixing and subchannel velocities in an LMFBR fuel assembly. Nuclear Engineering and Design 40, 315-326.

Marie, N., Marrel, A., Seiler, J.M., Bertrand, F., 2015. Physico-statistical approach to assess the core damage variability due to a total instantaneous blockage of SFR fuel sub-assembly. Nuclear Engineering and Design 297, 343-353.

Marr, W.W., Crawford, R.M., 1972. Porous, Heat-Generating Blockage in a Fuel Subassembly. Transactions American Nuclear Society 15, 350-351.

Memmott, M., Buongiorno, J., Hejzlar, P., 2010. On the use of RELAP5-3D as a subchannel analysis code. Nuclear Engineering and Design 240, 807–815.

Moraga, F. J., Bonetto R. T., and Lahey R. T., 1999. Lateral forces on spheres in turbulent uniform shear flow. International Journal of Multiphase Flow 25. 1321–1372.

NEA - IAEA, 2016. Uranium 2016: Resources, Production and Demand. Retrieved from OECD-NEA Website, https://www.oecd-nea.org/ndd/pubs/2016/7301-uranium-2016.pdf.

Novendstern, E. H., 1972. Turbulent flow pressure drop model for fuel rod assemblies utilizing a helical wire-wrap spacer system. Nuclear Engineering and Design 22, 19-27.

Olive, J., Jolas, P., 1990. Internal blockage in a fissile super-phenix type of subassembly: the SCARLET experiment‘s and their interpretation by the CAFCA-NA3 code. Nuclear Energy 29, 287–293.

Padmakumar, G., Velusamy, K., Prasad, B.V.S.S., Rajan, K.K., 2017. Hydraulic Characteristics of a fast reactor fuel Subassembly: An experimental investigation. Annals of Nuclear Energy 102, 255-267.

Pointer, W.D., Thomas, J., Fanning, T, Fischer, P., Siegel, A., Smith, J., Tokuhiro, A., 2009. RANS-based CFD simulations of sodium fast reactor wire-wrapped pin bundles. M&C 2009, Saratoga Springs, USA.

Patankar, S.V., 1980. Numerical Heat Transfer and Fluid Flow. McGraw-Hill Book Co, New York.

Patch, L., Roidt, R. M., Carelli, M.D., Markley, R.A., 1979. Experimental Studies of Flow Distribution in a Wire Wrapped LMFBR Blanket Assembly. Report on the International Meeting on Reactor Heat TYRansfer, Karlsruhe.

Peniguel, C., Rupp, I., Rolfo, S., Guillaud, M., 2010. Thermal-hydraulics and conjugate heat transfer calculation in a wire-wrapped SFR assembly. ICAPP 2010, San Diego, USA.

Ravi, L., Velusamy, K., Chellapandi, P., 2013. A robust thermal model to investigate radial propagation of core damage due to total instantaneous blockage in SFR fuel subassembly. Annals of nuclear energy 62, 342-356.

Raza, W., Kim, K.Y., 2008. Comparative analysis of flow and convective heat transfer between 7-pin and 19-pin wire-wrapped fuel assemblies. Journal of Nuclear Science and Technology 45, 653–661.

Rehme, K., 1973. Pressure drop correlations for fuel element spacers, Nuclear Technology 17, 15-23.

Rensen, Q., 1981. Experimental investigation of turbulence heat transfer to liquid sodium in the thermal entrance region of an annulus. Nuclear Engineering and Design 68, 397-404.

Roelofs, F., Gopala, V.R., Chandra, L., Viellieber, M., Class A., 2012. Simulating fuel assemblies with low resolution CFD approaches. Nuclear Engineering and Design 250, 548– 559

Roelofs, F., Shams, A., Doolaard, H., Gopala, V.R., 2013. Application of CFD approaches to the Simulation of LMFR Fuel Bundles and the Reactor Pool. Fluid Mechanics and Chemistry for Safety Issues in HLM Nuclear Reactors, SEARCH-MAXSIMA Lecture Series, Von Karman Institute, Sint-Genesius-Rode, Belgium.

Roidt, R.M., Carelli, M.D.,Markley, R.A., 1980. Experimental investigation of the hydraullic field in wire wrapped LMFBR core assemblies. Nuclear Engineering and Design 62, 295-321.

Roychowdhury, D.G., Govindarajan, S., Chetal, S.C., Bhoje, S.B., 2000. Design approach to local blockages, LMFBR core thermal hydraulics: status and prospects, IAEA-TECDOC-1157.

Schleisiek, K., 1970. Heat transfer and boiling during forced convection of sodium in an induction-heated tube. Nuclear Engineering and Design 14, 60–68.

Schultheiss, G.F., 1987. On local blockage formation in sodium cooled reactors. Nuclear Engineering and design 100, 427-433.

Seung H. S., Won D. J., Seok K. C., and Seong O. K., 2006. Establishment of the design requirements for a flow blockage detection system through a LES analysis of the temperature fluctuation in the upper plenum. Annals of Nuclear Energy 33, 62-70.

Sreenivasulu, T., Prasad, B.V.S.S.S., 2009. Flow and heat transfer characteristics in an annulus wrapped with a helical wire. International Journal of Thermal Sciences 48, 1377-1391.

Syeilendra Pramudiya and Minoru Takahashi, 2013. Thermal-hydraulic analysis of wire-wrapped SFR test subassemblies by subchannel analysis method. Annals of Nuclear Energy 54, 109-119.

Tomoyuki, U., Masahiro, I., Tomoyasu M., 2008. Irradiation performance of Fast Reactor MOX fuel assemblies irradiated to high burnups. Journal of Nuclear Science and Technology 49 (11), 1183–1192.

Unal, H. C., 1976. Maximum Bubble Diameter, Maximum Bubble Growth Time and Bubble Growth RateDuring Subcooled Nucleate Flow Boiling of Water Up To 17.7MN/m2. International Journal of Heat Mass Transfer 19. 643–649.

Uotani, M. and Haga, K., 1984. Experimental investigation of sodium boiling in partially blocked fuel subassemblies. Nuclear Engineering and Design 82, 319-328.

Venkataraman, G., 1994. Bhabha and his magnificent obsessions. University press, India Limited.

Wakasugi, k., Kakehi, I., 1971. Pressure dorp performance of fuel pin bundle with spiral wire spacer. Journal of Nuclear science and Technology 8(3), 167-172.

Waltar, A.E. and Reynolds, A.B., 1981. Fast Breeder Reactors, Pergamon Press.

Wantland, J.L., 1974. Orrible - A computer program for flow and temperature distribution in 19-rod LMFBR fuel subassemblies. Nuclear Technology 24, 168–175.

Wu, Y.W., Xin Li, Xiaolei Yu, Qiu, S.Z., Su, G.H., Tian, W.X., 2013. Subchannel thermal-hydraulic analysis of the fuel assembly for liquid sodium cooled fast reactor. Progress in Nuclear Energy 68, 65-78.

Yao, W., Morel, C., 2004. Volumetric interfacial area prediction in upward bubbly two-phase flow. International Journal of Heat Mass Transfer 47, 307-328.

Yoshihiro Kikuchi, Kazuo Haga, Tadao Takahashi, 1975. Experimental study of steady state boiling of sodium flowing in a single pin annual channel. Journal of Nuclear Science and Technology 12(2), 83-91.

NOMENCLATURE

English alphabets

A_i	Interfacial area
C	turbulent model constants
Cp	specific heat
d_p	Mean particle diameter in blockage
D	Diameter of fuel pin
D_e	Equivalent diameter of the bundle (=4 × flow area/heated perimeter)
D_h	hydraulic diameter of the bundle (=4 × flow area/wetted perimeter)
D_w	Diameter of helical spacer wire, bubble detachment diameter
f_z	Friction factor at any axial distance
g	Acceleration due to gravity (9.81 m/s)
g_{hex}	Gap between subassembly wall and pin
h_z	Heat transfer coefficient at any axial section
H	Helical pitch of spacer wire, enthalpy
k	Turbulent kinetic energy
Nu	Nusselt number
P	Pressure (or) fuel pin pitch
Pe	Peclet number
Pr	Prandtl number
Pr_t	Turbulent Prandtl number
q''	Heat flux at any axial section.
R	Blockage Radius
Re	Reynolds number

S_{por}	Momentum sink for blocked region
t	time
T	Temperature
T_{bz}	Bulk mean coolant temperature at any axial section
T_{cz}	Mean clad temperature at any axial section
T_{cp}	Peak clad temperature
T_l	Liquid temperature
T_{sat}	Saturation temperature
T_w	Wall temperature
v	velocity
u^+	Non-dimensional velocity
u_s	Superficial velocity
u_τ	Friction velocity or shear velocity
V_a	Axial velocity of coolant at inlet
V_t	Transverse velocity
V^*_{Lt}	Non dimensional transverse velocity, normalized with local axial velocity
V^*_t	Non dimensional transverse velocity, normalized with bulk axial velocity
x	Spatial coordinates
y^+	Wall distance
z	Axial coordinates (stream wise coordinates)

Greek symbols

α	Wire angle, phase volume fraction
β	Porosity of blockage

ΔP, dP	Pressure drop
Δz, dz	Change in axial coordinate
ΔT_{sub}	Degree of sub cooling
ε	turbulent dissipation rate
λ	Thermal conductivity
λ_b	Thermal conductivity of blockage material
λ_m	Mean thermal conductivity
λ_s	Thermal conductivity of sodium
μ	Laminar viscosity
μ^{eff}	Effective viscosity
μ_t	Turbulent (or eddy) viscosity
υ	Kinematic viscosity
ρ	density of coolant
σ_k, σ_ε	Turbulent Prandtl numbers of k and ε
θ	Angle around the pin
τ_w	Wall shear stress

Acronyms

CEA	Central Electricity Authority
CFD	Computational Fluid Dynamics
FBR	Fast Breeder Reactor
IAEA	International Atomic Energy Agency
IEA	International Energy Agency
LES	Large Eddy Simulation

MF	Multiplication Factor
NEA	Nuclear Energy Agency
OECD	Organization for Economic Co-operation and Development
PHWR	Pressurized Heavy Water Reactor
RANS	Reynolds Averaged Navier Stokes equation
RNG	Re-Normalization Group
SC	Subchannel
SFR	Sodium Cooled Fast Reactor